UNIVERSITY OF OKLAHOMA

GRADUATE COLLEGE

MICROWAVE FILTERS FOR NEXT GENERATION RADIO FREQUENCY
TRANSCEIVERS

A DISSERTATION

SUBMITTED TO THE GRADUATE FACULTY

in partial fulfillment of the requirements for the

Degree of

DOCTOR OF PHILOSOPHY

By

Gokhan Ariturk Norman, Oklahoma

2023

MICROWAVE FILTERS FOR NEXT GENERATION RADIO FREQUENCY
TRANSCEIVERS

A DISSERTATION APPROVED FOR THE
SCHOOL OF ELECTRICAL AND COMPUTER ENGINEERING

BY THE COMMITTEE CONSISTING OF

Dr. Hjalti H. Sigmarsson, Chair

Dr. Jorge L. Salazar-Cerreño

Dr. Shahrokh Saeedi

Dr. Nathan A. Goodman

Dr. Alberto Marino Valle

For a world of fairness, peace, and global prosperity. For a society of fair and sincere human rights where people truly care about each other. For a life driven by the principles of science and logic.

Acknowledgments

Progressing in my research and completing this Ph.D. was only possible with the important support of certain people. I would like to express my sincere gratitude and appreciation for their support in developing my career and sustaining my well-being during my studies.

Having a Ph.D. or temporarily living in a country other than one's birthplace is always difficult due to various reasons, including cultural differences, feelings of loneliness, financial stability, and missing one's home country. In that regard, I would like to express my deepest appreciation to my Ph.D. supervisor, Prof. Hjalti H. Sigmarsson, for the incredible support he provided in every aspect during my studies. Not only has he been a great supervisor, but he has also treated me like a family member, with whom I could discuss personal or academic issues. He has consistently been there for me whenever I needed him, while also giving me the space I needed. This, I believe, is a very difficult balance to achieve. I am immensely grateful that he is genuinely invested in his students' success and takes pride in their achievements. I couldn't have asked for a better supervisor during my studies.

I would like to express my deep gratitude to my mentors at Texas Instruments Inc., namely, Dr. Adam Fruehling, Dr. Ernest Ting-Ta Yen, and Dr. Yao Yu. Their significant impact has guided my research path and shaped the direction of my dissertation. I also want to show my appreciation for their efforts in establishing a collaborative project between the Advanced Radar Research Center (ARRC) and Texas Instruments.

Table of Contents

ix

List of Figures

xvi

xix

Abstract

Increased data rates in wireless communications enforce unprecedented performance metrics on the front-end filters to operate in crowded spectral bands. These requirements include strong selectivity, low insertion loss, and good out-of-band (OOB) rejection in addition to the applicability in complementary metal oxide semiconductor (CMOS) integrated circuit layouts. The acoustic wave (AW) resonator based filter design technology has gained a very important role in the on-chip filter design techniques due to chip-scale physical resonator sizes and the ability of achieving high quality factor values at microwave frequencies. However, conventional synthesis methods used in the design of AW resonator based microwave filters suffer from limited achievable fractional bandwidth (FBW) and weak out-of-band rejection. The origin of these issues is the limitations on increasing the electromechanical coupling coefficient (k_t^2) of the resonators, which is an intrinsic property of the piezoelectric material in its design. This dissertation proposes a new class of hybrid acoustic-electromagnetic (Hybrid-ACEM) filters to overcome both of the aforementioned limitations of AW resonator-based filters. In other words, the main goal of this new topology is to maximize the ratio between the achievable FBW and the required k_t^2. This is achieved by employing one or two electromagnetic (EM) resonators that are placed at purposefully selected stages within the design. In addition, cross-coupling mechanisms are systematically used to reduce the required electromechanical coupling coefficient in certain filter orders. Altogether, the proposed method can achieve much larger FBW values and stronger OOB

rejection compared to the conventionally synthesized ladder acoustic wave filters. The effect of finite quality factor of the EM resonators is analyzed. A new algorithm to convert extracted-pole sections to Butterworth-Van-Dyke (BVD) model for large FBW values is also presented. It has been shown in the simulations that FBW-to-k_t^2 ratios of four or above is achievable with this method. As a proof-of-concept, a sixth-order hybrid canonical prototype with a center frequency of 2.67 GHz and 11.2% FBW is designed and fabricated. The acoustic wave resonators used in the fabrication have k_t^2 values of 3.5%. The fabricated prototype proves the validity of the proposed method for achieving FBW values of 30% with required k_t^2 values of 7.5%, which is available with the common aluminum nitride (AlN) based bulk acoustic wave resonator technologies of today. The developed technique opens a new pathway to reduce the limitations of integrating microwave filters for future fully on-chip microwave transceivers.

Chapter 1

Introduction

1.1 Background

The last decade saw a significant improvement in the devices that require wireless data transfer. The enhancements in social media platforms, wireless communication systems including 5g, development of better imaging devices, and the advancement of radar technologies rely heavily on wireless transceivers. The result is the increased data rates that require the RF transceivers to occupy larger bandwidths in the frequency spectrum. That requires the adjacent wireless bands to overlap or become dangerously close in frequency that they start to interfere with each other.

The next generation RF transceivers that operate in crowded spectral bands, for example the S-band (2GHz–4GHz), will require an unprecedented frequency selectivity in order to protect themselves from the interference from adjacent bands. An example of an RF receiver front end module for communication systems is depicted in Fig. 1.1. Considering this architecture, a common dilemma is the order of the band-select-filter and the low-noise-amplifier (LNA) components. Placing the LNA directly after the antenna (as in (i)) results in the lowest noise figure in the entire system, however, it makes the system vulnerable to out-of-band interferences. This means that an RF signal that has a carrier frequency at an adjacent band can easily saturate the LNA and

cause the desired signal to be rendered undetectable by the receiver.
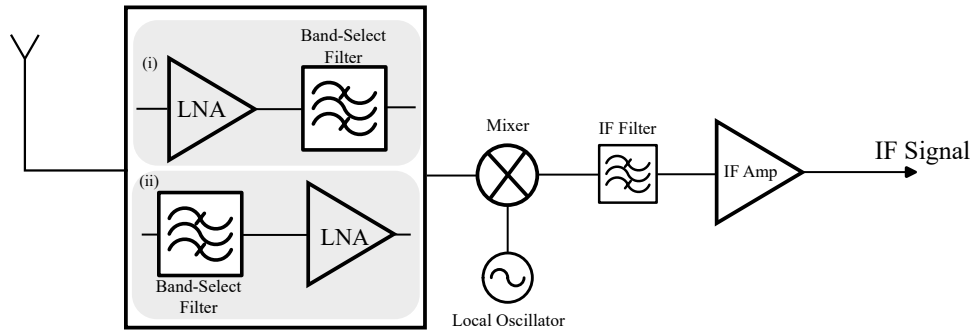
Figure 1.1: The front end block diagram of an RF downconverting receiver.

Placing the band-select filter after the antenna as in (ii) is, therefore, the safer and the preferred design procedure as it rejects the out-of-band interferences. However, in this configuration, the bandpass filter needs to have a very strong out-of-band rejection performance and a steep roll-off (selectivity) in order to be able to prevent the leakage from the adjacent channels. In addition to that, the insertion loss of the filter needs to be as low as possible in order to prevent the overall noise figure of the system from growing.

The need for low insertion loss and strong roll-off enforces stringent requirements on the design of the filters for the receiver front-end architectures. For instance, Table 1.1 depicts some of the common wireless bands that are in or close to the S-band frequencies. As observed, the uplink of the n40 band has a band edge at 2.4 GHz while the lower-end band edge of the n41 band is at 2.496 GHz [1]. Due to such close band edges, the receiver of an RF system operating at the n41 band is required to have a rejection of 30 dB at 2.4 GHz while the required insertion loss of the front-end microwave filter should be around 1 dB or less [1]. In addition to these stringent requirements, these bands correspond to the wireless communication bands which are used extensively in mobile devices such as smartphones. Due to the size restrictions in such devices, the front-end filters should be designed as integrated circuits (IC).

Table 1.1: The uplink and downlink frequencies of several bands at and around the S-band [1].

Band	f (MHz)	Uplink (MHz)	Downlink (MHz)
n3	1800	1710-1785	1805-1880
n39	1900	1880-1920	1930-1995
n40	2300	2300-2400	n/a
n41	2500	2496-2690	n/a

The difficulty in achieving the growing demands of the wireless industry can be theoretically described in this chapter in a way to emphasize the needs for frequency-agile and more enhanced filters for the next generation RF transceivers. The insertion loss, selectivity, and the out-of-band rejection of the filters are dependent on multiple factors including the order of the filter, the quality factor of the resonators that are used to design it, and the polynomial function which is used as a basis for the design procedure. The filter response can be characterized in terms of its S-parameters which include the reflection coefficient (S_{11}) and the transmission coefficient (S_{21}). The effect of these parameters on the filter response is depicted in Fig. 1.2.
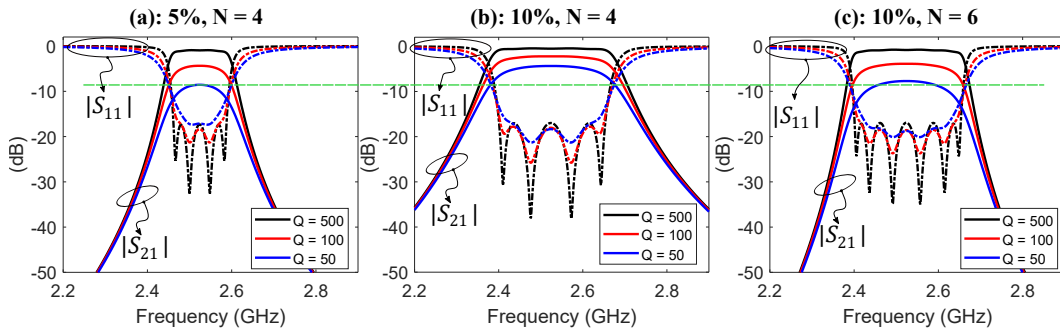
Figure 1.2: The effect of filter order, fractional bandwidth, and quality factor of the resonators on the filter response. (a): Fourth order response with 5% FBW, (b): Fourth order response with 10% FBW, and (c): Sixth order response with 10% FBW. All graphs demonstrate the responses when the designs have resonators with Q-factor values of 500, 100, and 50, respectively.

A fourth-order inline filter response at a center frequency of 2.524 GHz and a frac-

tional bandwidth (FBW) of 5% is depicted in Fig. 1.2 (a), when the quality factor of the four coupled resonators are set as 500, 100, and 50, respectively. As observed, the insertion loss of the filter increases from 0.94 dB to 8.55 dB when the resonator quality factor values reduce from 500 to 50, respectively. In addition to the increased insertion loss, the band edges of the response also get rounded, which reduces the selectivity and the band flatness of the filter. In Fig. 1.2 (b), the same filter responses are depicted for a fractional bandwidth of 10%, again for a filter order of four. As observed, the wider bandwidth improves the filter response in terms of selectivity and insertion loss for each quality factor value. Finally, Fig. 1.2 (c) demonstrates the filter responses of a sixth-order design for a FBW of 10%. Comparing the graphs in Fig. 1.2 (b) and (c) also gives the indication that increased filter order for the same fractional bandwidth worsens the filter response (in the presence of resonators with low Q values). The corollary of these findings is that achieving narrow-band and higher-order filters require the coupled resonators to have high quality factor values to provide acceptable insertion loss and selectivity values.

There are multiple paths to design better filters. One of the most important methods of such is to work on the resonator technologies in order to create higher-Q, miniaturized, and power-resilient resonators. The second pathway is to develop the methodology to use these resonators in a way to design filters that meet the specifications for specific applications. This dissertation will include discussions on both methods with a particular emphasis on the proposed synthesis and design methodologies. In contrast to developing new resonator technologies, the aim is more on achieving significantly better filter responses compared to the current state-of-the-art by developing novel theoretical synthesis background for such filters.

1.2 Filter Design Methodologies

The concept of filter design methodologies refers to the entire process of designing a filtering function in the normalized frequency and impedance domain, denormalizing it for a desired actual center frequency (f_0), a particular fractional bandwidth (FBW), and for desired source and load termination impedances. Finally, one can obtain the physical network or structure that realizes the desired response.

The most common filtering responses include the Butterworth (maximally flat), Chebyshev, and elliptic function based responses. The Butterworth response provides the flattest passband response because the derivatives of the filter function vanishes at $\Omega = 0$ and $\Omega \to \infty$. It is a commonly used response, however, the selectivity of this function is not as good as the Chebyshev response. The Chebyshev response, however, has nonzero derivatives at $\Omega = 0$ and has a constantly fluctuating response, which is the in-band ripple, which is adjustable. In addition, one can have predefined transmission zeros out of the passband with the Chebyshev response, which is commonly used to improve the rejection performance of the filter. The elliptic filter, on the other hand, is a subcategory of the generalized Chebyshev response which has fixed transmission zero positions. The low-pass circuit network of Chebyshev and Butterworth function based filters can be obtained directly from the *g-coefficients*, the insertion loss method [2], or the image parameter method [3]. On the other hand, more advanced responses including the design of filters realizing generalized Chebyshev responses with finite transmission zeros, the polynomial-based filter synthesis methodologies and the coupling matrix approach become very important [2, 4, 5].

In order to be able to design filters using the resonators at the required frequency band, one needs to be able to connect/couple them with each other and also with the source and the load terminations of the network. This should be done in a methodolog-

ical way in order to be able to scale the design for any required center frequency and the fractional bandwidth. Furthermore, this design should be able to realize a mathematical filtering function such as a Butterworth or a Chebyshev prototype in order to be able to achieve the best input matching, band flatness, specified selectivity, and strong out-of-band rejection performance [2].

1.2.1 The Method of g-coefficients

The method of g-coefficients are valid for both Butterworth and Chebyshev responses, however, this dissertation mainly includes the Chebyshev functions and the readers are suggested to read [2] for the Butterworth responses.

To get the g-coefficients of a response, one needs the order of the filter (N) and the ripple constant ($\epsilon = \sqrt{10^{R/10} - 1}$) where R is the ripple level in the linear scale (non-dB). For both the odd and the even order cases, $g_0 = 1$. For the odd-orders, $g_{N+1} = 1$. On the other hand, the last coefficient for even-order is found as:

$$g_{N+1} = \begin{cases} (\epsilon + \sqrt{1 + \epsilon^2})^2 & S_{11}(0) > 0, \\ \frac{1}{(\epsilon + \sqrt{1+\epsilon^2})^2} & S_{11}(0) < 0. \end{cases} \tag{1.1}$$

The remaining g-coefficients are found as follows:

$$g_{r+1} = \frac{1}{g_r} \cdot \frac{4 \sin\left[\frac{\pi(2r-1)}{2n}\right] \sin\left[\frac{\pi(2r+1)}{2n}\right]}{\eta^2 + \sin^2\left(\frac{r\pi}{n}\right)} \tag{1.2}$$

where

$$\eta = \sinh\left[\frac{1}{N} \sinh^{-1}\left(\frac{1}{\epsilon}\right)\right] \quad \text{and} \quad g_1 = \frac{2}{\eta} \sin\left(\frac{\pi}{2N}\right), \tag{1.3}$$

The g-coefficients can be found for a filter of an arbitrary order and ripple value.
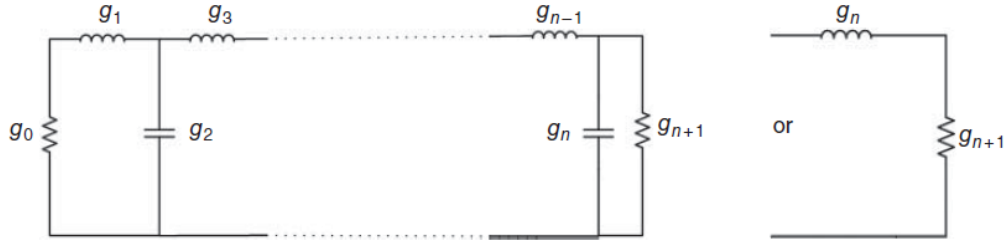
Figure 1.3: The normalized lowpass prototype network that is characterized by the g-coefficients. This figure is taken from [2].

They represent the inductance and the capacitance values of a lowpass ladder network that is depicted in Fig. 1.3. The frequency response of this network has a cutoff frequency of 1 rad/s and the source and the load terminations are found from g_0 and g_{N+1}, as observed.

Using the lowpass prototype of Fig. 1.3, one can design a lowpass, highpass, bandpass, or a bandstop filter by performing the transformations on the inductors and the capacitors in the network in Fig. 1.4. In that figure, Δ refers to FBW whereas ω_0 corresponds to the actual angular center frequency.

On the other hand, the method of g-coefficients is only valid for filters with no transmission zeros. It cannot give an insight into dual band filters, filters with transmission zeros, or on the design of filters with acoustic-wave resonators. Therefore, the more comprehensive generalized Chebyshev function and coupling matrix synthesis methodology is required for the realization of advanced filter responses.

1.2.2 Generalized Chebyshev Function and Coupling Matrix Based Filter Synthesis

The polynomial-based synthesis in conjunction with the extracted pole and the coupling matrix methods provide the designer the following abilities:
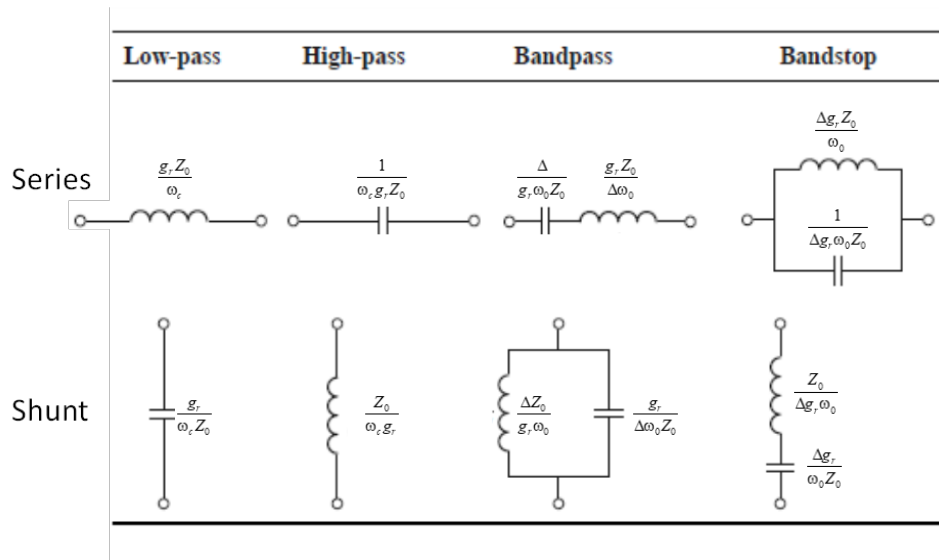
Figure 1.4: Conversion of the normalized lowpass prototype in Fig. 1.3 to a filter with either a lowpass, highpass, bandpass, or bandstop filter network at the denormalized frequency domain. For the lowpass and highpass prototype, ω_c corresponds to the angular cut-off frequency while for the bandpass and bandstop prototypes, ω_0 and Δ correspond to the center frequency and the fractional bandwidth, respectively. This figure is adapted from [6].

- Synthesize the filter response in the normalized frequency domain for any arbitrary filtering function,

- Being able to observe the effect of the finite quality factor of the resonators that are used in the design of the filter,

- Switch between different filter topologies that can realize the same filtering function for the specified fractional bandwidth and center frequency,

- Design more advanced filters with dual-band responses,

- Design filters for different source and load terminations than 50 Ω.

- Design of filters with acoustic-wave resonators.
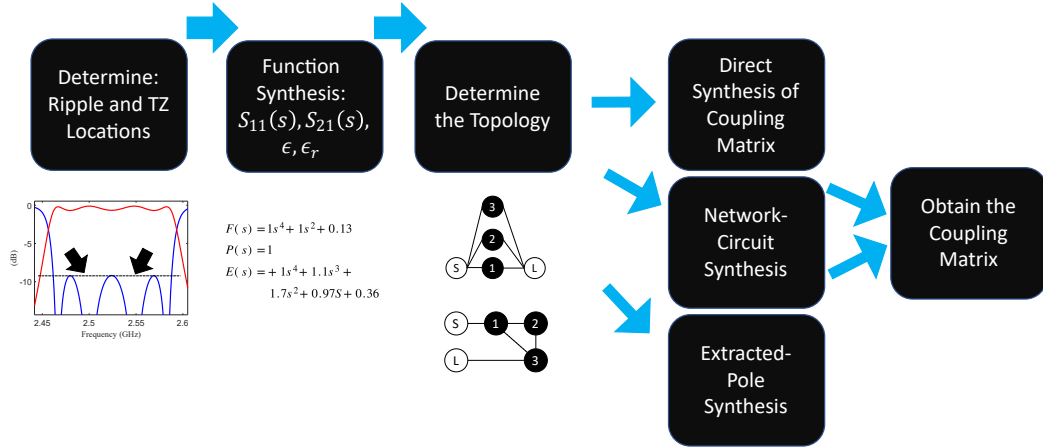
Figure 1.5: Filter synthesis-based design methodology is illustrated. The synthesis starts with determining the ripple value and the transmission zero positions, continues with the extraction of the S-polynomials and according to them, determining which filter topology is desired. According to that, there are multiple solutions to the approach.

A specified filtering function of order N with N_{TZ} finite-frequency transmission zeros can be synthesized based on the required ripple value and the normalized-frequency transmission zero locations with the use of the recursive algorithm given in [2]. This filtering function specifies the reflection and the transmission coefficients of the filter in normalized-frequency domain as:

$$S_{11}(s) = \frac{F(s)/\epsilon_r}{E(s)} \quad \text{and} \quad S_{21}(s) = \frac{P(s)/\epsilon}{E(s)},$$

$$\text{where} \begin{cases} \epsilon_r = 1, & N_{TZ} < N \\ \epsilon_r = \epsilon/\sqrt{\epsilon^2 - 1} & N_{TZ} = N, \end{cases} \quad (1.4)$$

$F(s)$ and $P(s)$ are the numerator polynomials of $S_{11}(s)$ and $S_{21}(s)$, respectively, $E(s)$ is the common denominator polynomial, ϵ_r is the normalization coefficient, and ϵ is the ripple constant. Here, $s = j\Omega$ is the frequency variable with Ω being the normalized angular frequency.

Once the filtering function for the lowpass (normalized-frequency) prototype is syn-

thesized, the design of the filter proceeds as depicted in Fig. 1.5. In particular, one needs to determine the topology of the filter to be synthesized. Depending on both the used resonator technologies and/or the overall geometry of the filter, i.e., whether it will be a cavity-based filter or an on-chip AW resonator based filter, this topology can be chosen. According to the chosen topology, the coupling matrix of the design can be synthesized using either the direct synthesis method, the network-circuit synthesis approach, or the extracted-pole synthesis method [2, 4, 5].

Once the coupling matrix of the desired topology is obtained, the designer can obtain all of the parameters of the physical filter topology from that. For instance, if the filter will be a cavity resonator based filter, the designer can extract the resonant frequency of each cavity as well as the required inter-resonator coupling strengths to obtain the desired response. On the other hand, if the design will be a lumped-element based design, the designer can extract the required component values.

The coupling matrix based filter design approach is a revolutionary method that unified the design methodology of filters with several different resonator technologies. This study will be extensively using this approach in order to solve the common problems of the microwave filters using different technologies.

1.3   Resonator Technologies

The design and synthesis methodologies of the RF filters, as mentioned in Section 1.2 is able to determine the resonant frequencies, inter-resonator coupling coefficients, and inductance/capacitance values of each coupled resonator in a filter network. On the other hand, all these methods assume that the coupled resonators are lossless, which corresponds to a quality factor of infinity. However, one of the most important concerns in a filter network is the ability of obtaining high-Q resonators.
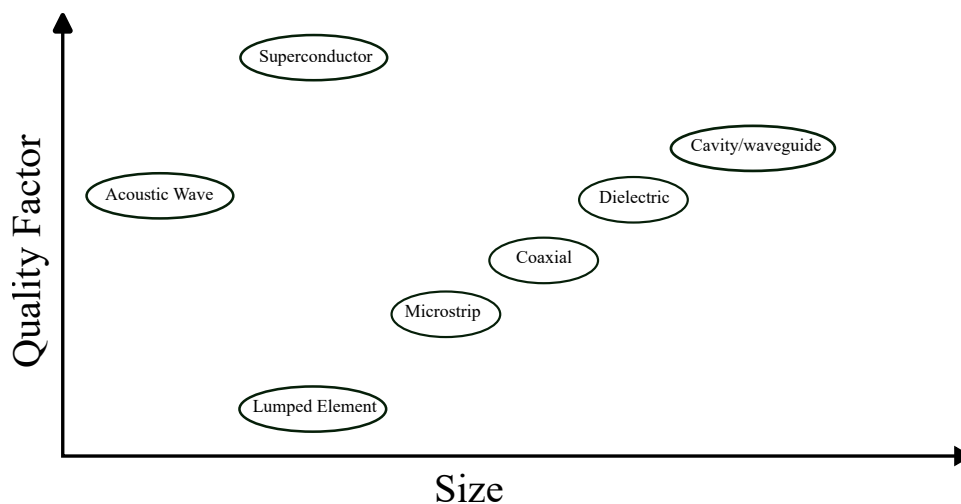
Figure 1.6: Relation between the physical size and the achievable quality factor using several resonator technologies.

There are several resonator technologies that are commonly used in the design of microwave/millimeter-wave (mmWave) filters. These can be classified as electromagnetic (cavity, dielectric, transmission line) based, lumped element based, micro electromechanical systems (MEMS) and acoustic-wave (AW) based, and superconductor based resonators. Fig. 1.6 depicts a general view on the relationship between the size and the quality factor of several resonator technologies.

The resonators that can provide the highest quality factor values are the ones that are based on superconductors, however, they work at cryogenic temperatures and are not practical to be used in commercial applications such as cell phones [2, 7]. Another important technology that can provide high quality factor values are the electromagnetic cavity resonators including air- or dielectric-filled cavities. Such cavities are sections of waveguides and can achieve quality factor values of 3,000–30,000 at frequencies around 1 GHz [3]. The substrate integrated waveguide (SIW) technology has been an important application technique in the design of such cavities, especially in their integration to the printed circuit board (PCB) based applications. Despite their high

quality factor, their sizes are on the order of one wavelength, which makes them large and bulky and not convenient for on-chip applications for the lower frequencies of the microwave band. Other technologies such as dielectric, coaxial, or microstrip line based resonators provide Q values of approximately 3000-5000, 1000, and 100-300 at frequencies around 1 GHz, respectively [3]. Even though these technologies can be implemented with smaller sizes compared to the cavities, it is still difficult to use them for on-chip applications at low frequencies.

1.3.1   Miniaturized Electromagnetic Resonators (Lumped and Distributed)

There are numerous approaches in the literature aiming at miniaturizing the cavity or transmission line based resonators. One such technology is the *evanescent-mode cavity* technology, which uses the waveguides at frequencies below their cut-off frequency. The miniaturization can be accomplished using multiple techniques. One of those is to capacitively terminate, or in other words, *heavily load* the lines or cavities to shorten their physical length [8–14]. An example of such a cavity is depicted in Fig. 1.7 (a) which can be characterized by the coaxial line as in Fig. 1.7 (b). This coaxial line, for instance, is capacitively loaded to reduce the length of the line. The use of capacitive termination has the added benefit of tunability as long as the value of the terminating capacitance is tunable. This has been accomplished by using MEMS based capacitors in [8–10]. On the other hand, the disadvantage of hysteresis and weak durability of these structures were also discussed in these studies. Using solid-state varactors is another option to change the terminating capacitance for tuning, however, the varactors can bring significant losses to the system, causing the resonators to have low quality factors [12].
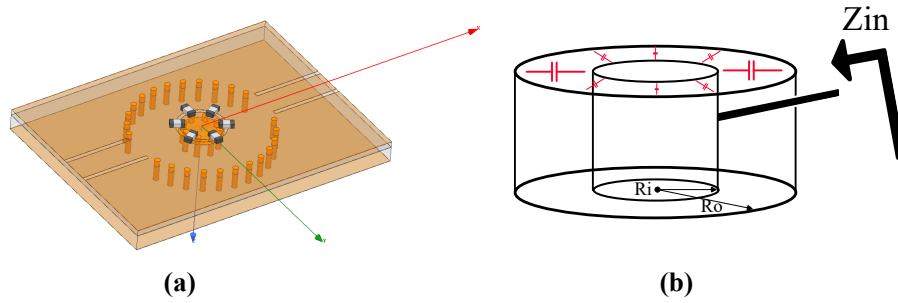
Figure 1.7: A capacitively loaded evanescent-mode cavity resonator. (a): The HFSS drawing of the resonator. (b): The coaxial transmission line model of it.

Other approaches in the design of miniaturized microwave cavity resonators include the folded SIW based resonators [15–17] and half-mode [18, 19] or quarter-mode [20–23] cavities. The folded SIW technology reduces the width of the SIW by increasing the height to twice the original value and placing a conductive obstacle between the top and bottom half-width cavities. In other words, it is based on literally *folding* the cavity to reduce the size of it, however, it has been reported in [15–17] that this technique introduces significant losses to the resonator. The fractional-mode (half, quarter, 1/32) cavities divide the cavity area to a desired fraction and leave certain cavity walls open-ended which act like perfect magnetic conductors. These boundaries fulfill the remainder of the fields according to image theory and act as if the cavity has the desired full mode. These methods are also effective in reducing the physical size of the resonators, however, the achievable cavity sizes are still too large for on-chip implementation.

A different approach than miniaturizing the cavities is the concept of *active resonators*, which can be used to incorporate microwave/mmWave resonators to on-chip applications. An active resonator is accomplished by coupling an active loss compensation network to a resonator with a finite quality factor, as observed in Fig. 1.8. This negative resistance network can either be a two-port RF amplifier as in [24, 25], or can be accomplished as a single-port transistor network using the base impedance of a

common collector bipolar transistor as in [26].
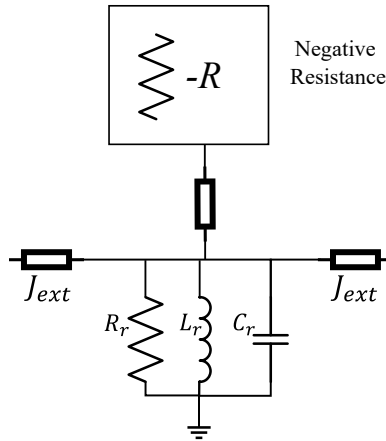
Figure 1.8: Circuit schematic of an active resonator with negative resistance.

Using active resonators to enhance the quality factor of low-Q on-chip lumped-element resonators has been an extensively studied subject in the late 90s. In [26–29], coupled negative resistance approach with the use of field-effect transistors (FET) are used. To have a negative resistance effect, parametric amplification is used for loss compensation in [30] and a further coupling manipulation is used for shape and selectivity enhancement in [31] for narrow-band filter realization.

As the major origin of the loss is identified as the lumped inductors, the concept of active inductor design for narrow-band MMIC filter applications was performed with FET transistors in [32] and [33] and with the inverted collector technique based bipolar transistors in [34] and [35]. Furthermore, dynamic range and nonlinearity considerations of active inductors were presented in [36] and [37]. In [38–40], GaAs FETs are used to link the resonant structures to not only compensate for the loss, but to produce gain within the passband. Finally, the transversal active MMIC filter topology is used in [41] and [32] to improve the shape of the response.

The negative resistance based active resonators are a good solution to improve the quality factor of the low-Q resonators, however, they suffer significant drawbacks in-

cluding high noise figure, low power handling performance and the design complexities. The design complexities include the reluctance to implementing a passive filter with active amplifier networks.

1.3.2   Acoustic Wave Resonators

A very important resonator technology that has been used extensively in the design of microwave filters and low-phase-noise oscillators is the acoustic wave (AW) based resonators [42].

These resonators take the advantage of comparatively lower mechanical phase velocity and hence, lower mechanical wavelength within the mechanical substrates. For the mechanical waves, the same relation between the wavelength and the phase velocity applies as in:

$$\lambda_{mech} = \frac{v_p^{mech}}{f},$$
(1.5)

where λ_{mech} and v_p^{mech} are the mechanical wavelength and the mechanical phase velocity, respectively.

Considering that the mechanical phase velocity is 11340 m/s in AlN substrate for instance [42], the mechanical wavelength for an operating frequency of 2 GHz is 5.67 μm compared to the electrical wavelength in air at the same frequency, being 15 cm. The outcome of that is the multiple order of magnitude smaller physical resonator size compared to the electromagnetic resonators.

There are two types of acoustic wave resonators. The surface acoustic wave (SAW) based resonators, as illustrated in Fig. 1.9 (a), have wave propagation that is parallel to the piezoelectric substrate [43, 44]. The electrical (RF) signal is converted into mechanical waves with the inter-digital transducers (IDT) and the resonance frequency of this device is determined by the spacing of the IDT fingers. Finger spacing of one mechan-

ical wavelength is used in many applications [45]. Piezoelectric materials of LiTaO$_3$ or LiNbO$_3$ are commonly used in the design of the SAW resonators, which is not compatible with CMOS process integration. Typically, the resonance frequency of SAW resonators have an upper limit around 2.5 GHz [42] due to structural stability problems while miniaturizing the resonator fingers. Compared to the BAW resonators, they have lower quality factor values and less power handling performance, which is typically around 31 dBm (The BAW resonators can tolerate upto 36 dBm of RF power[42]). On the other hand, the SAW resonator fabrication is relatively simpler compared to the BAW devices.

(a) SAW Resonator
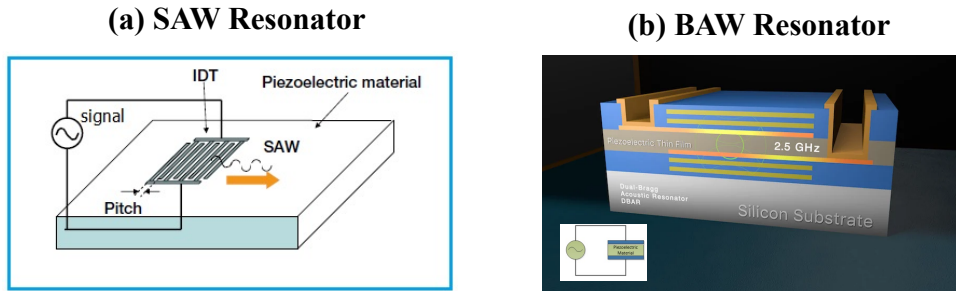
(b) BAW Resonator

Figure 1.9: Schematic drawing of the surface acoustic wave (SAW) and the bulk acoustic wave (BAW) based resonators are depicted in (a) and (b), respectively. The image is taken and adapted from [46].

The BAW resonators, as depicted in Fig. 1.9 (b), are designed as a piezoelectric material being sandwitched between two metallic electrodes. The wave propagation direction is the vertical direction, therefore, the thickness of the piezoelectric material determines its resonant frequency. With the BAW resonators, going towards higher resonant frequencies is dependent on the developments on the thin film growth technology. It has been reported in [42] that the maximum resonant frequency of BAWs are usually limited to 10 GHz, however, recent developments in [47] and [48] demonstrate very promising results at 14 GHz and 33 GHz, which suggests a good future for the use of BAW resonators in mmWave applications as well. Compared to the SAW resonators,

they can have stronger power handling capabilities ($\approx$36 dBm), higher quality factors, and the advantage of being CMOS compatible, which is a very important feature in the system-on-chip (SOC) applications [42].
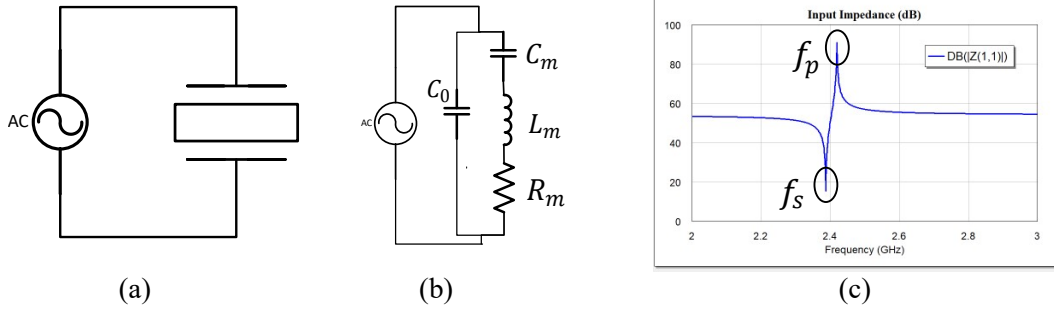
Figure 1.10: (a): An acoustic-wave resonator connected to a voltage source. (b): The Butterworth-Van-Dyke model, and (c): The input impedance of the acoustic-wave resonator in (a).

The input impedance of an acoustic-wave resonator, when connected to a voltage source, as in Fig.1.10 (a), reveals the presence of a series and a parallel resonance frequency, as depicted in Fig. 1.10 (c). This behavior can be modeled with the Butterworth-Van-Dyke (BVD) model as given in Fig. 1.10 (b) or the Mason model which will be described in Chapter 2. The capacitance C_0 originates from the dielectric properties of the piezoelectric material that is between the conductive electrodes whereas the motional branch (C_m and L_m) can only be understood considering the Mason model.

The distance between the series and the parallel resonances in Fig. 1.10 (c) is proportional to the electromechanical coupling coefficient (k_t^2), which is an intrinsic property of the piezoelectric material that is used in the design of the AW resonators [42]. As also depicted in Table 2.1, different materials can achieve different k_t^2 values and this coefficient is a very important parameter in the utilization of the AW based resonators for microwave filter design. Indeed, it gives an upper limit to the achievable fractional bandwidth while using the AW based resonators in microwave filter design.

1.4 Problem Definition and the Hypothesis

The main problem definition in this dissertation is the inability of obtaining *high-performance on-chip* RF/mmWave filters that can meet the growing demands of the wireless industry. The phrase "high-performance" corresponds to strong selectivity, low insertion loss, small size, strong power handling, and the ease of fabrication and integration in system-on-chip applications.

The lumped-element based resonators have the sizes that can fit into an integrated circuit, however, they provide weak quality factor values, being in the range of 10–50 at lower frequencies of the S-band [2]. This produces significant insertion loss and poor selectivity performance, if used for on-chip filter integration.

The acoustic wave resonator technology has gained a very important popularity due to its ability of achieving exceptionally high quality factor values at the lower frequencies of the microwave spectrum, while maintaining a physical size that can fit on a chip. However, they still face multiple challenges. The intrinsic property of the piezoelectric substrate, which enforces the electromechanical coupling coefficient k_t^2 to be limited, has direct consequences on the design of filters using AW based resonators. These include the limited achievable fractional bandwidth, weak out-of-band rejection performance, and the difficulty of achieving a flat passband.

The earliest design methods for the filters based on AW resonators use the ladder based architecture, as depicted in Fig. 1.11 (a). In this network, the series- and shunt-connected AW resonators are connected in an alternating order. Since each of the AW based resonators have a series and a parallel resonance frequency, both of them are responsible for creating a peak and a transmission zero [49]. A passband using them can therefore only be achieved by enforcing them to define the band edges. As depicted in Fig. 1.11 (b), the shunt resonators in the design should all have the same

18

series-resonance frequency and define the lower band edge while the series-connected resonators should all have the same parallel resonance frequency and define the upper band edge.
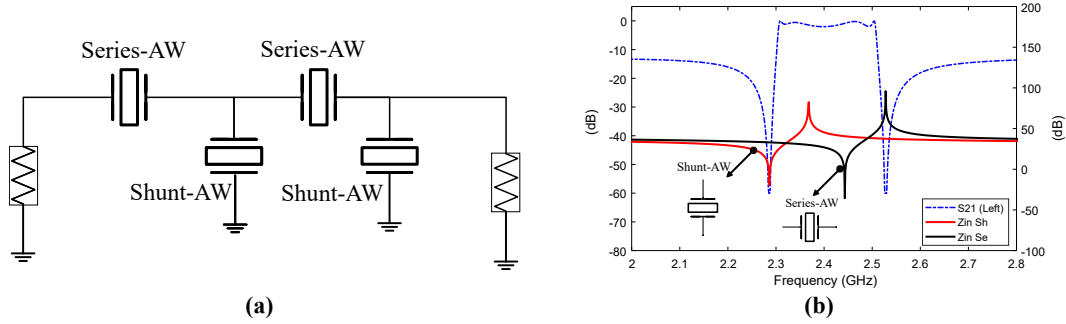
Figure 1.11: (a): The conventional ladder based acoustic-wave microwave filter topology. (b): The frequency response of the filter in addition to the input impedances of the series- and shunt- connected resonators.

The challenge of using AW based resonators with a specific k_t^2 arises at this point. In an effort to enlarge the fractional bandwidth of the filter by increasing the frequency separation of the resonators, an increase in the insertion loss (also known as "midband dip") is observed at center frequencies of these wideband acoustic filters, as depicted in Fig 1.12 (a). This is because there is no resonance in the middle of the passband in order to elevate and flatten the passband. Additionally, the out-of-band rejection of the filter shows a constant, and non-decreasing transmission coefficient at the out-of-band region.

Several methods have been proposed to design AW based filters with wide fractional bandwidth values. The most straightforward method is the AW resonator technology development to achieve larger electromechanical coupling values. In literature, k_t^2 values of 20% – 40% have been reported using lithium niobate substrate [51]. However, it has also been reported that they have many spurious modes and suffer weak temperature stability.

19
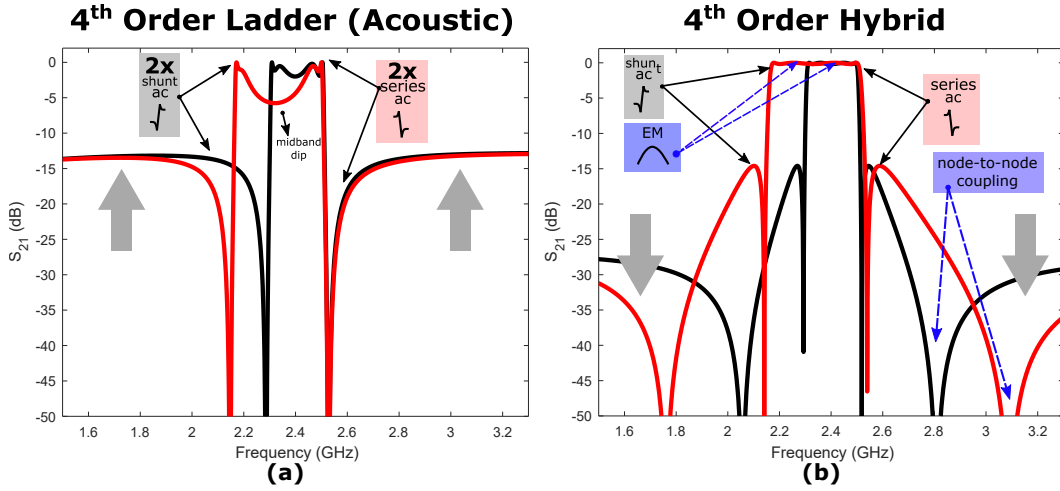
Figure 1.12: (a) Conventional 4th order ladder acoustic filters with various bandwidths. Midband dip is present at wider band filters. (b) The explanation of the proposed method. EM resonators lift the midband dip while providing better rejection at out-of-band frequencies. This image is taken from the publication of the author in [50].

Other methods include connecting parallel transmission lines or lumped elements to manipulate the position of the parallel resonance of the resonator [52, 53], which creates a new transmission zero on the opposite side of the passband. That effectively increases the achievable bandwidth, however, the filter bandwidth is now limited by the created transmission zero.

Another intriguing approach uses inverting sections (coupled lines) to connect ladder-AW sections, which achieved filters with 20%–30% FBW with k_t^2 values of approximately 10% [54]. The inverting sections enlarge the bandwidth of the resonant peak of the acoustic resonators, compensating for the midband dip, however, the required admittance inverters cause weak out-of-band rejection performance as wider bandwidths are desired [52, 54]. This idea is improved in [55] to separately control the upper and lower band edges using transmission line sections in addition to the coupled lines and the FBAR components. Very sharp roll off performance is achieved with very good insertion loss performance, proving the capabilities of using external microwave

elements in AW based filter design. On the other hand, these methods again do not provide solutions for on-chip designs.

Chebyshev functions have also been used to get the best performance metrics from AW-resonator-based filters [56]. That study synthesizes an Nth order topology with N AW resonators whose corresponding BVD models are synthesized using the extracted-pole (EP) synthesis method [2]. As a result, the k_t^2 for each AW resonator for a desired FBW is dictated by the sythesis process.

In order to increase the out-of-band rejection performance, transversal sub-networks have been incorporated to the ladder architecture in [57–59]. A different method in [60] uses an attenuating phase-shifter between the input and output for out-of-band rejection enhancement. In [61], an impressive transversal AW filter topology is introduced to achieve significantly larger bandwidths with acoustic resonators of almost arbitrary k_t^2 values. However, the resulting topology requires a differential output (or input) due to the circuit extraction processes and needs a balanced-unbalanced converter (Balun) on either side of the network.

The current state-of-the art methods for AW resonator based bandwidth enhancement are able to obtain FBW values of almost three times the k_t^2 value of the AW based resonators with reasonable out-of-band rejection [61]. On the other hand, the demand for wider fractional bandwidth values increase for the new applications such as 5 to 7 GHz WiFi. With the increased data rates, FBW values of 30-40% are getting necessary with AW based resonators that have k_t^2 values of 4% to 9%. Furthermore, this should be accomplished on-chip and with the minimum possible process updates for chip manufacturing.

Hypothesis

The hypothesis in this dissertation is based on the design of acoustic-wave filters. The hypothesis statement is given in the next paragraph.

The current achievable bandwidth problem of filters based on acoustic wave resonators can be resolved using a hybrid extracted pole approach in a way to incorporate EM resonators (lumped- or distributed- element based) within the design. In other words, the claim is that significantly wider fractional filter bandwidths and stronger out-of-band rejection performance compared to the state-of-the art in literature can be achieved using a hybrid combination of EM and AW based resonators within the design. Furthermore, this can be achieved without the need for a new resonator technology development or creating additional steps in the fabrication processes.

The basic logic in the proposed method in this dissertation can be summarized in Fig. 1.12 (b). The sharp upper and lower band edges are defined by series and shunt acoustic resonators, whereas the passband flatness is achieved using electromagnetic resonators, as shown in Fig 1.12(b). Using electromagnetic (EM) resonators in the prototype provides four advantages over the pure acoustic design: flat passband, better out-of-band rejection, wide bandwidths that are beyond the limits dictated by k_t^2, and most importantly, the ability to achieve a specific bandwidth using a wide range of k_t^2 values, which will be referred to as k_t^2 scaling.

Starting with a thorough mathematical analysis to understand the relationship between the k_t^2 dictated by each EP section, the effect of using canonical or non-canonical functions, and the achievable FBW, this study gives the foundations of introducing EM resonators for bandwidth achievement, strong OOB rejection, and low insertion loss. Discussions are provided to determine how many and which AW resonators in an inline full-EP based topology can be replaced with an EM resonator for maximum bandwidth

22

and minimum k_t^2. Additional proposed architectures on the use of cross-coupling in a Hybrid-ACEM topology are also provided. For the prototypes of significantly wide bandwidths such as 20%, a modified extracted-pole-to-BVD model is proposed for better accuracy. Overall, this study provides new and novel topologies for achieving significantly wider bandwidths and strong out-of-band rejection with fixed or arbitrary AW resonator k_t^2 values. This study can also be applied in the front-end modules of future on-chip RF transceivers.

1.5   Organization of the Dissertation

This dissertation starts with examining several contemporary microwave resonator technologies in Chapter 2. That includes lumped-element based resonators, electromagnetic resonators including resonant cavities, substrate integrated waveguide (SIW) technology, and the evanescent-mode cavities. In the same chapter, (MEMS) based acoustic-wave resonators are introduced with an emphasis on the BAW resonator technology and circuit equivalent models.

Chapter 3 examines the design of a generalized Chebyshev function with an arbitrary order and number of transmission zeros. This is the initial step for designing a microwave filter at a desired center frequency and having a desired fractional bandwidth.

Chapter 4 examines the contemporary coupled-resonator filter design methodologies with a special emphasis on the coupling matrix method. This includes the analysis and the synthesis of the coupling matrix to characterize a filter. Examples of the use of SIW based resonators for integrated microwave filters for the "Horus" fully-digital active electronically scanned antenna array (AESA) system is described with the coupling matrix-based design methods, as published in [62]. In addition, the lossy microwave

filters and the lossy coupling matrix is introduced in this chapter.

Chapter 5 introduces the role of extracted poles in filter design, the circuit- and network- synthesis methodologies, and the extracted-pole synthesis method. In that context, the synthesis of fully-canonical filters and their corresponding coupling matrices are also described.

Chapter 6 describes the coupling matrix based synthesis and design of ladder-acoustic-wave based filters and the challenges in their design.

Proceeding with the design considerations for on-chip filters, Chapter 7 introduces the novel "hybrid acoustic-electromagnetic filters" for wideband and on-chip applications, as submitted in [63]. A thorough analysis of using the extracted-pole method to maximize the achievable passband with limited electromechanical coupling coefficient is made with the use of the hybrid extracted-pole method and the coupling matrices. An on-chip hybrid acoustic-electromagnetic filter for S-band applications is designed utilizing the BAW resonator of Texas Instruments.

Finally, the impact of this study on the design of future SOC applications, the contributions to the filter design community and the future work are discussed in Chapter 8.

Chapter 2

Microwave/mmWave Resonators

This chapter introduces and examines several microwave resonator technologies that are used in the design of microwave/mmWave networks. Resonant networks have a wide range of applications including filters, tuned amplifiers, antennas, resonator-based oscillators, and biomedical applications (including magnetic resonance imaging (MRI)). In terms of their working principle, it is possible to classify the resonators in two categories, namely electromagnetic (EM)-based and acoustic-wave (AW) based. These two main categories include multiple types of resonators that are widely used in the design of the modern RF transceiver systems.

To characterize, understand, and simplify the behavior of the microwave resonators and to use them in the design of more complex systems, their lumped-element (RLC) equivalents are commonly used. Therefore, this chapter will start with the analysis of the lumped element based resonators and continue with the design and analysis of EM based structures and further consider the AW based resonators in detail.

2.1 Series and Parallel RLC Resonators

2.1.1 Series Tank Circuits

Since many RF resonators can be modeled as lumped resonators near their resonant frequency, it is important to consider the several parameters of the series- and parallel-tank circuits. In Fig. 2.1 (a), a series RLC network is depicted. The input impedance looking into the series-tank circuit is calculated as:

$$Z_{in}^{SE} = R + j\omega L + \frac{1}{j\omega C}.$$ (2.1)
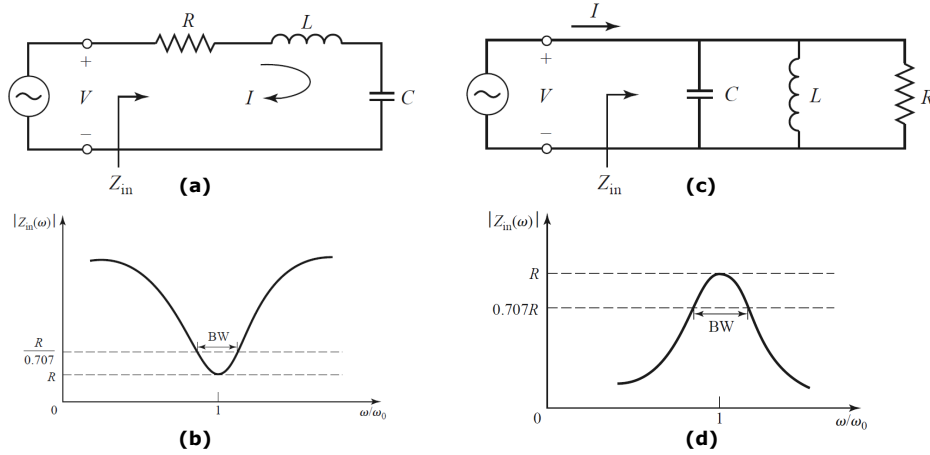
Figure 2.1: (a): A series-connected RLC network. (b): The normalized input impedance of this network near its resonance frequency. (c): A parallel-connected RLC network, and (d): The normalized impedance of this network near its resonance frequency. This image is taken and adapted from [3].

For the series-tank circuit, the dissipated power (P_{loss}), the stored magnetic energy (W_m), and the stored electric energy (W_e) are calculated as follows:

$$P_{loss} = \frac{|I^2|R}{2}, \ W_m = \frac{|I^2|L}{4}, \text{ and } W_e = \frac{|I|^2}{4\omega^2 C}.$$ (2.2)

The resonance condition is defined as the frequency at which the stored magnetic and electric energies are equivalent and given as:

$$\omega_0 = \frac{1}{\sqrt{LC}}, \tag{2.3}$$

and the unloaded quality factor of the resonator is defined as[3]:

$$Q_U^{SE} = \omega \frac{W_m + W_e}{P_{loss}} = \frac{1}{\omega_0 RC}. \tag{2.4}$$

The unloaded quality factor can also be obtained using the input impedance and the half-power bandwidth of the resonator in Fig. 2.1 (b) as:

$$Q_u = \frac{1}{BW}. \tag{2.5}$$

On the other hand, it should be noted that the bandwidth in (2.5) denotes the normalized-frequency bandwidth and for a resonator whose input impedance in de-normalized frequency is measured, this equation should be modified as:

$$Q_u = \frac{1}{FBW}, \text{ where } FBW = \frac{BW_{denormalized}}{\omega_0}. \tag{2.6}$$

In most circuits, on the other hand, the resonator is connected or coupled to either different resonators or to another load with a resistance given by R_L. This resistance changes the measured or the overall quality factor and can be considered to contribute an external quality factor of Q_e, which can be calculated as $\omega_0 L / R_L$. The overall quality factor of the series resonator, in the presence of the external quality factor is

denoted as the loaded quality factor and is given by:

$$Q_L = \left[\frac{1}{Q_u} + \frac{1}{Q_e}\right]^{-1}. \tag{2.7}$$

2.1.2 Parallel Tank Circuits

A sample parallel tank circuit is depicted in Fig.2.1 (c) with the input admittance look-ing into the network as follows:

$$Y_{in} = \frac{1}{R} + j\omega C + \frac{1}{j\omega L}. \tag{2.8}$$

The stored electric energy, magnetic energy, and the dissipated power in this net-work are provided as follows:

$$W_e = \frac{|V|^2 C}{4}, \ W_m = \frac{|V|^2}{4\omega^2 L}, \text{ and } P_{Loss} = \frac{|V|^2}{2R}. \tag{2.9}$$

Similarly, the resonant frequency is obtained for the condition when $W_e = W_m$, which is attained at $\omega_0 = 1/\sqrt{LC}$. The quality factor of the parallel resonator in Fig. 2.1 (c) can be calculated as:

$$Q_0 = \omega_0 \frac{2W_m}{P_{loss}} = \frac{R}{\omega_0 L} = \omega_0 RC, \tag{2.10}$$

or again, from the half-power bandwidth as: $Q_0 = 1/BW$ in normalized-frequency scale and $Q_0 = 1/FBW$ in denormalized bandpass frequency scale.

The definition of the aforementioned quality factor values are calculated using only the parameters of the series or tank RLC networks given in Fig. 2.1. On the other hand, a microwave/mmWave resonator in a network is usually connected or coupled to either

a source, load, or other resonators which have internal dissipative components. In this case, the dissipative elements of the load produces a quality factor that is external to the resonator and is denoted as Q_e.
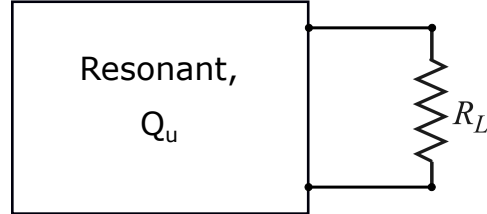
Figure 2.2: A resonator with an unloaded Q of Q_u, which is connected to a load with a resistance of R_L. This image is taken from [3].

The external quality factor is calculated as $Q_e = \omega_0 L/R_L$ for series resonant circuits and $Q_e = R_L/\omega_0 L$ for the parallel resonant circuits. The external quality factor can be interpreted as the quality factor that the load resistance produces with the lossless LC network.

Including the external quality factor, the overall quality factor of the network is referred to as the *loaded quality factor* and is calculated as:

$$Q_L = \left[\frac{1}{Q_u} + \frac{1}{Q_e}\right]. \tag{2.11}$$

Therefore, a passively loaded resonator has a lower loaded quality factor compared to its unloaded quality factor value.

2.2 Transmission Line Resonators

A distributed-element transmission line can have an arbitrarily desired input impedance based on the impedance that it is terminated with [3]. In addition to the ease of fabrication of transmission lines, this property is utilized to design resonators for

microwave/mmWave applications. Transmission lines can be characterized as either series- or parallel-connected RLC resonators based on the impedances they are terminated with. A transmission line of physical length l, a phase constant β, an attenuation constant α, and a characteristic impedance of Z_0 is depicted in Fig. 2.3.
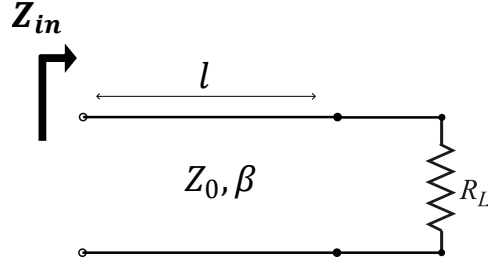
Figure 2.3: A transmission line terminated with a load resistance of R_L.

The input impedance looking into the transmission line given in Fig. (2.3) is given as:

$$Z_{in} = Z_0 \frac{Z_L + jZ_0 \tan((\alpha + j\beta)l)}{Z_0 + jZ_L \tan((\alpha + j\beta)l)}. \tag{2.12}$$

This impedance can be approximated as either the input impedance of a series- or a parallel-connected RLC network under several conditions as follows:

2.2.1 Half-Wave Shorted Transmission Line

For the case of a short-circuit termination (when $Z_L = 0$), (2.12) can be approximated as:

$$Z_{in} = Z_0 \tanh(\alpha + j\beta)l = Z_0 \frac{\tanh \alpha l + j \tan \beta l}{1 + j \tan \beta l \tanh \alpha l}. \tag{2.13}$$

For the case of a low-loss line, $\alpha l \ll 1$, which implies $\tanh \alpha l \cong \alpha l$, and letting $\omega = \omega_0 + \Delta\omega$ for a small ω_0 compared to ω_0, the electrical length of the line can be

30

written in terms of the phase velocity, v_p, as:

$$\beta l = \frac{\omega l}{v_p} = \frac{\omega_0 l}{v_p} + \frac{\Delta \omega l}{v_p}. \tag{2.14}$$

Considering that the transmission line is of half wavelength at the center frequency, the electrical length can be rewritten as:

$$\beta l = \pi + \frac{\Delta \omega \pi}{\omega_0} \tag{2.15}$$

and considering $\tan(\frac{\Delta \omega \pi}{\omega_0}) \cong \frac{\Delta \omega \pi}{\omega_0}$, the input impedance to the shorted half-wave line can be approximated as:

$$Z_{in} = Z_0 \left(\alpha l + j \frac{\Delta \omega \pi}{\omega_0} \right), \tag{2.16}$$

which has the form of the input impedance of a series-connected RLC resonant circuit, given by $Z_{in} = R + 2jL\Delta\omega$. Therefore, the short-circuited half wave line can be approximated as a series resonant circuit with the distributed RLC parameters given by:

$$R = Z_0 \alpha l, \ L = \frac{Z_0 \pi}{2\omega_0}, \ \text{and} \ C = \frac{1}{\omega_0^2 L}. \tag{2.17}$$

Therefore, the unloaded quality factor of the network can be written as: $Q_0 = \pi/2\alpha l = \beta/2\alpha$.

2.2.2 Half-Wave Open Ended Transmission Line

This type of transmission line resonators is a practical one due to its ease of fabrication. Just as in the shorted version, as Z_L is set to infinity in (2.12), the input impedance of the network can be written as:

31

$$Z_{in} = Z_0 \frac{1 + j \tan(\beta l) \tanh \alpha l}{\tanh \alpha l + j \tan \beta l}. \tag{2.18}$$

Similarly to the case in shorted version, one can set $\omega = \omega_0 + \Delta\omega$, assuming $\tanh \alpha l \approx \alpha l$, which results in the input impedance of the network given as:

$$Z_{in} = \frac{Z_0}{\alpha l + j(\Delta\omega\pi/\omega_0)}, \tag{2.19}$$

which is indeed the equivalent of a parallel-connected RLC network with the parameters given by:

$$R = \frac{Z_0}{\alpha l}, \ C = \frac{\pi}{2\omega_0 Z_0}, \text{, and } L = \frac{1}{\omega_0^2 C}. \tag{2.20}$$

Using these parameters, the unloaded quality factor of the network can be obtained as follows:

$$Q_u = \omega_0 RC = \frac{\beta}{2\alpha}. \tag{2.21}$$

2.3 Waveguides and Cavity Resonators

Waveguides can be used with certain boundary conditions to construct resonating cavities, which are preferred due to their high quality factor values and strong power handling. Depending on how the cavity is constructed, these can be rectangular, cylindirical, or coaxial cavity resonators and can support transverse electric (TE), transverse magnetic (TM), or transverse-electromagnetic (TEM) modes. In order for a guiding structure to support TEM modes, it requires at least two conducting surfaces.

To understand the field distributions in the cavity resonators, it is important to understand the field distributions in waveguides. Therefore, this section will begin with a brief examination of the field configurations (modes) in rectangular and coaxial waveg-

uides and then will switch to the rectangular and coaxial cavity resonators. Then, minia-turization of the resonators will be considered with the examination of the evanescent-mode, half-mode, and quarter-mode resonators. The use of such resonators design of filters will be analyzed in the following chapters after the synthesis of the coupling matrix.

To begin with the electromagnetic fundamentals, the starting point is, (as always) the phasor-domain Maxwell's equations, given by:

$$
\begin{aligned}
\nabla \times \vec{E} &= -j\omega\mu\vec{H} \quad \text{(Faraday's Law)}, \\
\nabla \times \vec{H} &= \vec{J} + j\omega\epsilon\vec{E} \quad \text{(Ampere's Law)}, \\
\nabla \cdot \vec{D} &= \rho_s \text{ (Gauss Law)}, \\
\nabla \cdot \vec{B} &= 0, \text{ (Gauss Law for Magnetism)}
\end{aligned}
\tag{2.22}
$$

where $\epsilon = \epsilon_0\epsilon_r$ is the permittivity and $\mu = \mu_0\mu_r$ is the permeability of the media. Furthermore, $\vec{E}$ and $\vec{H}$ are the electric- and magnetic-field vectors. According to the geometry of the guiding structure, the method of finding the field distributions is based on writing the fields in terms of transverse- and longitudinal components. In that case, the initial structure to be considered is the coaxial transmission line, which is considered in the following subsection.

2.3.1 Coaxial Transmission Lines, Waveguides, and Cavity Resonators

A coaxial transmission line comprises two concentric conducting cylinders of radii a and b, and the region between these two conductors is filled with a dielectric material of permittivity ϵ and permeability μ, as shown in Fig. 2.4.
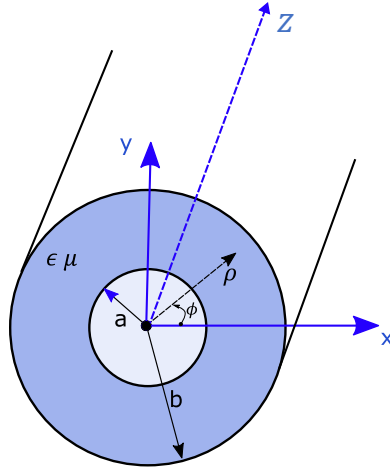
Figure 2.4: A coaxial transmission line of inner radius a, outer radius b, and a filling material of permittivity ϵ and a permeability of μ.

With the two conductors, a coaxial line can support TEM waves although it also supports TE and TM modes, which are of higher order.

The electric and magnetic fields inside the coaxial line can be denoted as:

$$\vec{E} = \frac{V_0 \hat{\rho}}{\rho \ln b/a} e^{-\gamma z}$$
$$\vec{H} = \frac{I_0 \hat{\phi}}{2\pi\rho} e^{-\gamma z}$$

(2.23)

with $\gamma = \alpha + j\beta$ being the propagation constant including the loss of the line. The aim at this point is to obtain the RLC parameters of the coaxial transmission line based on its geometry. This can be found from the stored magnetic and the electric energy in the unit lenght of a coaxial line. The time-averaged stored magnetic energy can be found from the magnetic fields as follows:

$$W_m = \frac{\mu}{4} \int_S \vec{H} \cdot \vec{H}^* ds \triangleq \frac{I_0^2 L_{coax}}{4}.$$

(2.24)

As the magnetic energy is stored within the dielectric substrate between the conductors,

34

this surface integral should be within the region where $\rho \in [a, b]$, which is calculated as:

$$L_{coax} = \frac{\mu}{(2\pi)^2} \int_{\phi=0}^{2\pi} \int_{\rho=a}^{b} \frac{1}{\rho^2} \rho d\rho d\phi$$
$$\Rightarrow \boxed{L_{coax} = \frac{\mu}{2\pi} \ln \frac{b}{a} \text{ H/m}}.$$

(2.25)

Similarly, the electric-field energy within the region can be calculated as:

$$E_e = \frac{\epsilon}{4} \int_S \vec{E} \cdot \vec{E}^* ds \triangleq \frac{V_0^2 C_{coax}}{4},$$

(2.26)

which can be used for the derivation of the capacitance per unit length of the coaxial line as:

$$C = \frac{\epsilon}{(\ln b/a)^2} \int_{\rho=a}^{b} \frac{1}{\rho^2} \rho d\rho d\phi \Rightarrow \boxed{C_{coax} = \frac{2\pi\epsilon}{\ln b/a} \text{F/m}}$$

(2.27)

2.4 Evanescent-Mode Cavities

Waveguides can be used to transmit EM wave modes as long as the cut-off frequency of the desired mode is lower than that of the operating frequency [3]. If the operating frequency is lower than the cut-off frequency of the corresponding mode ($f_{op} < f_c$), that mode is an evanescent mode which quickly attenuates and dissappears. However, the waveguides can be used below their cut-off frequencies for the purpose of designing cavity resonators by capacitively loading them [8, 64]. One of the most common methods of doing so is to introduce a capacitive post inside a coaxial waveguide. This produces a capacitive effect, which, as a consequence, acts like a capacitively loaded transmission line and effectively shortens the physical length of the resonator.
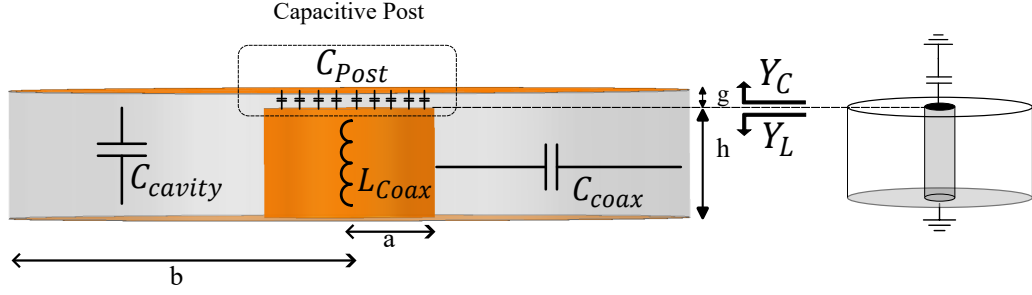
Figure 2.5: An evanescent-mode cavity resonator with a capacitive top post.

Fig. 2.5 depicts a coaxial evanescent-mode cavity resonator showing the capacitances and the inductance of the structure. As observed, the structure is a heavily loaded coaxial transmission line with a length of h, an inner radius of a, and an outer radius of b. In order for this evanescent-mode cavity to resonate, the total admittances looking into the cavity should vanish as follows:

$$Y_c + Y_L = 0$$
$$\Rightarrow j\pi f_0 C_{post} = j\frac{\cot(\frac{2\pi f_0}{v_p}h)}{Z_0},$$

(2.28)

where v_p is the phase velocity in the coaxial line and f_0 is the center frequency and C_{post} is the capacitance of the top post of the line. Using this model and considering the top post as a parallel-plate capacitor which uses air as the dielectric material ($\epsilon_r = 1$), the resonant frequency of this cavity can be approximated as follows:

$$f_0 = \frac{c}{\pi\sqrt{2a^2\frac{h}{g}\ln\frac{b}{a}}},$$

(2.29)

where c is the speed of light in free space. This approximation was based on the transmission line model of the coaxial cavity. Instead of that, one can approximate this structure as a parallel L-C resonator in which the inductance originates from the coax-

ial line, as derived in the previous section given by:

$$L_{coax} = \frac{\mu_0}{2\pi} \ln\left(\frac{b}{a}\right) h, \tag{2.30}$$

and the capacitance of the resonator is obtained as the total capacitance by the cavity, coaxial line, and the post capacitance, which is obtained as:

$$C_{total} = C_{post} + C_{cavity} + C_{coax}, \tag{2.31}$$

where

$$C_{post} = \epsilon_0 \frac{A_{post-top}}{g},$$
$$C_{cavity} = \epsilon_0 \frac{A_{cavity-top} - A_{post-top}}{h + g}, \text{ and} \tag{2.32}$$
$$C_{coax} = \frac{2\pi\epsilon_0}{\ln\frac{b}{a}} h,$$

where $A_{cavity_{top}}$ is the total area of the cavity using the outer radius and $A_{post-top}$ is the area of the top of the capacitive post. Regarding the total capacitance and the inductance of the cavity, one can obtain the resonance frequency of the structure using:

$$f_0 = \frac{1}{2\pi\sqrt{L_{coax}C_{tot}}}. \tag{2.33}$$

This approximation for the resonant frequency does not include the effect of the fringing field capacitances on the top post and more accurate calculations for the resonant frequency of a coaxial evanescent-mode cavity resonator is included in [65].

The most common methodology of designing these structures is to use full-wave simulations with one of the commercially available simulation software, such as Ansys HFSS. An example evanescent-mode cavity designed to resonate at a frequency of

2.83 GHz is depicted in Fig. 2.6. This cavity is designed with the use of substrate-integrated-waveguide (SIW) technology to be compatible with the standart PCB fabrication processes. The outer radius of the cavity is designed as $b = 4.85$ mm while the inner radius of the cavity is designed to be $a = 1.5$ mm.
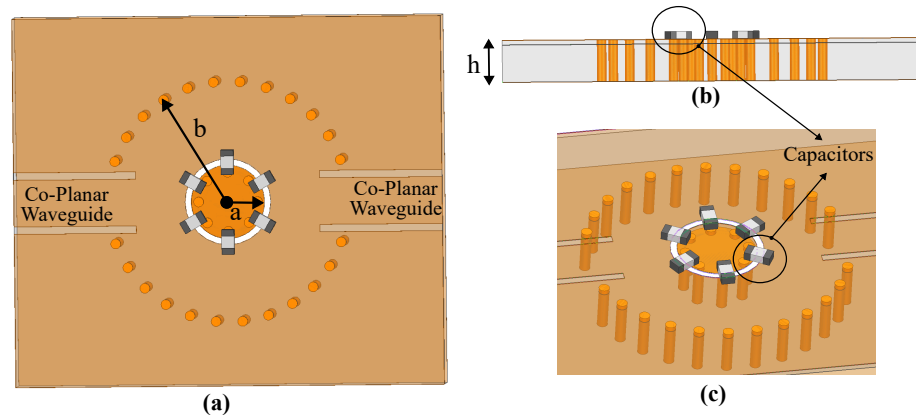
Figure 2.6: An example of an SIW based cavity resonator design. (a): Top view, (b): Side view, and (c): 3-D view.

This structure is different than the one in Fig. 2.5 in which the heavy loading is performed using a capacitive post. Instead of using a capacitive post, this design uses six surface mount capacitors of 1.1 pF on the top of the structure to perform the capacitive loading effect. As observed in Fig.2.6 (a), (b), and (c), the coaxial structure is obtained using copper-plated vias within two laminated substrates having a thickness of 1.52 mm and 0.17mm. The configuration shown in Fig. 2.6 shows a single resonator being weakly coupled to two co-planar-waveguide components of 50 Ω each for the measurement of its quality factor. This structure has its main mode at 2.83 GHz and two other modes at almost twice this frequency, at 5.64 GHz, as observed from Fig. (2.7).

Modes

| **I:** 2.83 GHz | **II:** 5.64 GHz | **III:** 5.66 GHz |
| **Q:** 250 | **Q:** 75 | **Q:** 75 |
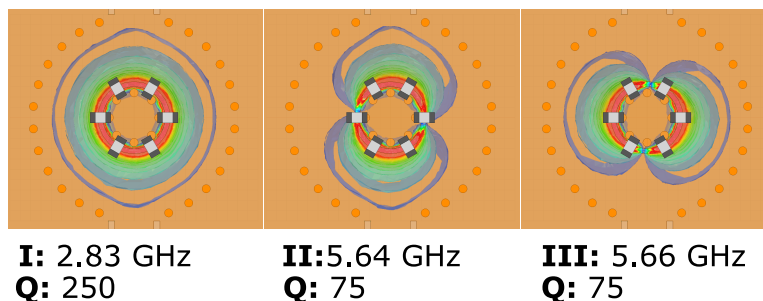
Figure 2.7: The first three resonant modes of the evanescent-mode cavity that is depicted in Fig. 2.6. This image is taken from the own publication of the author in [62].

The mode of interest in for designing a filter is in many cases the mode with the lowest resonance frequency. This is not a requirement and one can also utilize two modes of a cavity resonator such as the dual-mode patch resonator in [2]. However, the desire is to have the mode with the lowest resonance frequency to have the highest possible quality factor and the higher order (spurious) modes to have lower quality factor since these modes of the resonators couple with each other and create other undesired passbands. This will be revisited in Chapter 4 during the examples of the use of the coupling matrix.

2.5   Acoustic Wave Resonators

As discussed in the introduction, the acoustic-wave based resonators can have exceptional quality factor values with very small form factors, which make them suitable for on-chip integration. The SAW resonators are usually used for frequencies below 1 GHz while for S-band, the BAW resonators are used more ubiquitously. As the BAW resonators are more suitable to be used at the operating frequencies that are used in this dissertation, the theory of BAW resonators will be considered.

Designing and fabricating AW based resonators is a field of expertise and is not

the focus of this dissertation. For information about such, the readers are directed to [42]. On the other hand, this dissertation will include an extensive use of the AW based resonators to design microwave filters, therefore, one still needs to know the circuit models that define the frequency behavior of the device. In addition, it is important to understand the parameters and mechanisms for the design of the resonators to know the feasibility of designing a resonator with a certain foundry process workflow. Therefore, we start with the basics of the BAW resonators including the use of mechanical wave equations.

2.5.1   Mason Model of the BAW Resonator

A BAW resonator is formed by placing a piezoelectric material of thickness d_p, a relative permittivity of ϵ_r, a piezoelectric constant of e, a stiffness constant of c and a density of ρ between two conductive electrodes as depicted in Fig. 2.8 (a) and (b). In this context, the mechanical wavenumber is defined as:

$$k = \frac{\omega}{v_p}, \tag{2.34}$$

where $v_p = \sqrt{c/\rho}$ is the phase velocity of a mechanical wave within the slab. It should be realized that this structure creates a static capacitance due to the dielectric constant of the piezoelectric material, which can be calculated with the parallel-plate capacitor equation given by:

$$C_0 = \epsilon_0 \epsilon_r \frac{A}{d_p}, \tag{2.35}$$

where ϵ_0 is the free-space permittivity and A is the area of the conductors.
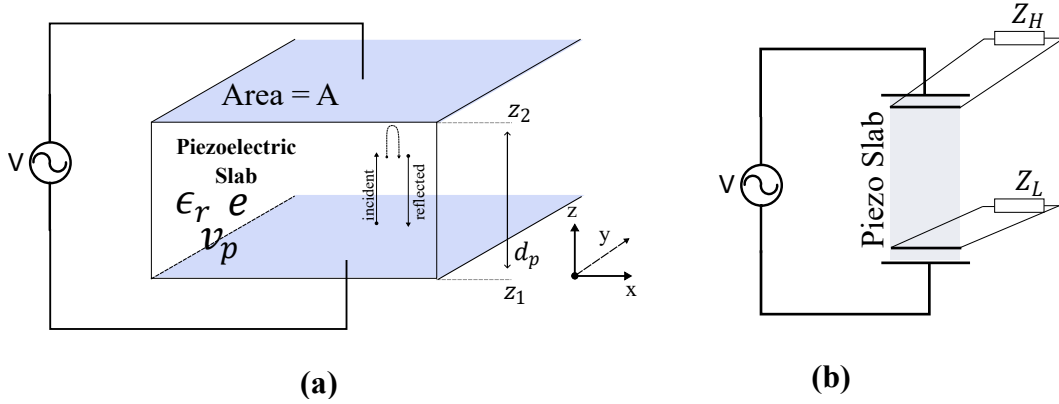
Figure 2.8: Drawing of an acoustic slab that acts like a mechanical waveguide. The propagation is in z-direction and the thickness of the slab is d_p.

In the presence of these variables, the Mason equivalent input impedance looking into a BAW resonator can be described as [42]:

$$Z_{in} = \frac{1}{j\omega C_0}\left(1 - \frac{k_t^2 \tan(\phi)}{kd_p\phi} \frac{\frac{Z_H+Z_L}{Z_p}\cos^2(\phi) + j\sin(2\phi)}{\frac{Z_H+Z_L}{Z_p}\cos(2\phi) + j(1 + \frac{Z_HZ_L}{Z_p^2})\sin(2\phi)}\right), \qquad (2.36)$$

where Z_H and Z_L are the mechanical loads at locations z_1 and z_2, as depicted in Fig. 2.8 (b). $\phi = kd_p/2$ and k_t^2 is the electromechanical coupling coefficient being dictated by the piezoelectric material between the electrodes, which is obtained as:

$$k_t^2 = \frac{e^2}{Z_p\epsilon_0\epsilon_r v_p}. \qquad (2.37)$$

Under the assumption of no mechanical loads at the mechanical ports, this equation can is simplified to:

$$Z_{in} = \frac{1}{j\omega C_0}\left(1 - \frac{k_t^2 \tan kd_p/2}{kd_p/2}\right). \qquad (2.38)$$

Analyzing the unloaded impedance, one can realize that the input impedance to the BAW approaches to infinity for $\tan(kd_p/2) \to \infty$, meaning that $kd_p/2 = \pi/2$. This

41

gives the parallel resonance frequency of the BAW as:

$$f_p = \frac{v_p}{2d_p}.$$ (2.39)

For the series resonance, the input impedance of the of the BAW should be zero, giving that:

$$\frac{k_t^2 \tan (kd_p/2)}{(kd_p/2)} = 1,$$ (2.40)

which gives the conclusion that:

$$k_t^2 = \frac{\pi}{2} \frac{f_s}{f_p} \cot \frac{\pi}{2} \frac{f_s}{f_p}.$$ (2.41)

As an example, the input impedance calculation of a mechanically unloaded BAW resonator including AlN as its piezoelectric with a plate capacitance of 3 pF and a k_t^2 of 6% is depicted in Fig. 2.9. As observed, the BAW produces a series and a parallel resonance frequency and the series resonance frequency is always lower than that of the parallel resonance [42].

It should be noted that the k_t^2 value of the material would only be achieved in the case of a mechanically unloaded BAW, which means that the mechanical impedances in Fig. 2.8 is only valid for the case where the mechanical ports in the z-direction are interfacing the air. This is of course, not possible since there needs to be metallic electrodes to act as a transducer to surround the piezoelectric material. In that scenerio, (2.36) can be used.
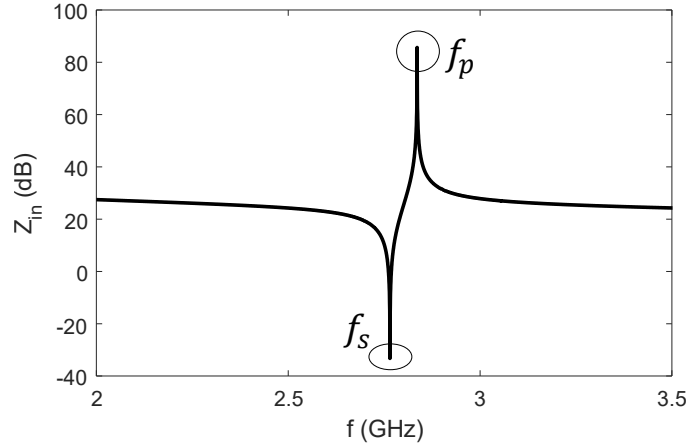
Figure 2.9: The input impedance of a mechanically unloaded BAW resonator with a k_t^2 of 6% and a static capacitance of 3 pF, found by (2.36).

In general, the effects of different electrode materials and also the presence of Bragg reflectors (used for confining the mechanical energy within the piezoelectric) [42, 66] will change the effective value of the k_t^2, which can also be called as k_{eff}^2. A very deep analysis of such effects can be found in [42].

2.5.2 Butterworth Van-Dyke Model

In contrast to the Mason model which can be used to understand the frequency behavior of the BAWs and can also be used for the design of them, the Butterworth Van-Dyke (BVD) model is designed to facilitate the use of the frequency behavior of the resonators to be modeled as an RLC based network.

The BVD model of a BAW resonator is depicted in Fig. 2.10. The extended model in Fig. 2.10 (a) shows the model that can include the spurious resonances whereas a simplified model is also depicted in Fig. 2.10 (b). In this model, the RLC network denoted by $C_m, L_m,$ and R_m is called as the motional branch, which models the acoustic wave resonances while the term C_0 is coming from the capacitor that is formed by the electrodes that are sandwitching the piezoelectric material.

43
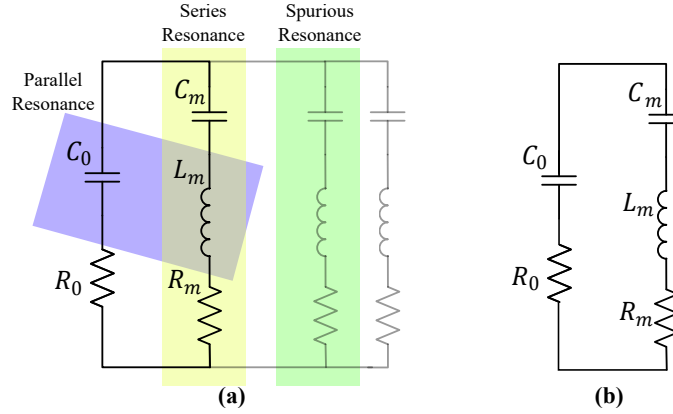
Figure 2.10: The Butterworth Van-Dyke model of the BAW resonators. (a) The extended model including the modeling of the spurious modes. (b): The simplified BVD model.

According to the simplified BVD model in 2.10 (b), the series resonance of the network can be obtained as:

$$\frac{1}{2\pi\sqrt{L_m C_m}} \tag{2.42}$$

and the parallel resonance of the network can be obtained as:

$$f_p = \frac{1}{2\pi}\sqrt{\frac{C_0 + C_m}{L_m C_m C_0}} = f_s\sqrt{1 + \frac{C_m}{C_0}}. \tag{2.43}$$

Furthermore, the series and the parallel quality factors of this resonator can also be modeled from the BVD parameters as:

$$Q_s \cong \frac{2\pi f_s L_m}{R_m + R_0} \text{ and } Q_p \cong \frac{2\pi f_p L_m}{R_m + R_0}. \tag{2.44}$$

It is also important to mention that the BVD parameters of a BAW resonator can be obtained using the measurement of the input impedance of a BAW resonator, with the knowledge of the static capacitance, which can be calculated from the dimensions of it. Based on the measurements of the input impedance, the BVD parameters can be

obtained as:

$$
\begin{aligned}
C_m &= C_0\Big(\frac{f_p^2}{f_s^2} - 1\Big), \\
L_m &= \frac{1}{(2\pi f_s)^2 C_m}, \\
R_m &= \frac{2\pi f_s L_m}{Q_s}, \text{ and} \\
R_0 &= \frac{2\pi f_p L_m}{Q_p} - R_m,
\end{aligned}
\tag{2.45}
$$

where Q_s and Q_p can be obtained from the reciprocal of the 3-dB fractional bandwidth of the measured peak and the dip of the input impedance, which was given for the series and parallel resonant circuits in Fig. 2.6.

2.5.3 Different Resonances of BAW Devices

The Mason model of BAW resonators, as briefly discussed in Section 2.5.1, predicts the resonance frequency of the BAW devices using the one dimensional mechanical wave equation and assumes that the lateral dimension is infinite in size. The resonance condition that was being referred to is the mechanical resonance in the thickness dimension and it was assumed that the wave propagation and the particle displacement are in the same direction, as shown in 2.11 (a). This type of resonances are referred to as thickness modes, however, in practice, the particle displacement also happens at the lateral dimensions as well [42]. When the particle displacement is in both the thickness and the lateral dimensions, this type of resonance is called as a *lamb mode*.
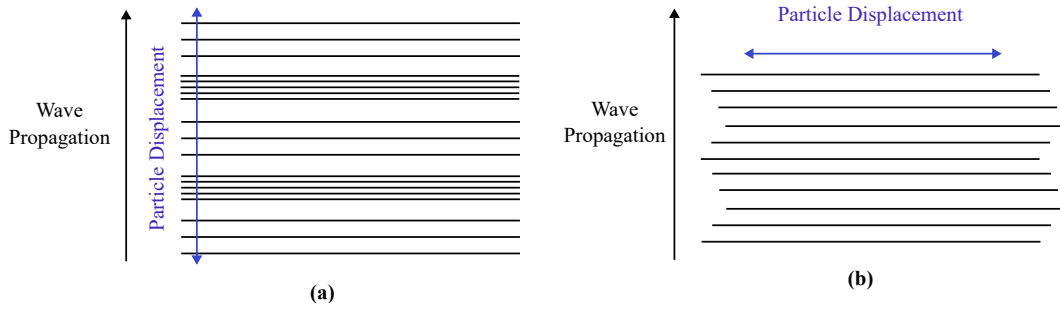
Figure 2.11: (a): The condition for the BAW resonators where the wave propagation and the particle displacement are in the same direction, (b): The condition where they are orthogonal to each other.

In addition to the longitudinal modes, the wave propagation and the particle displacement can be orthogonal to each other, as shown in Fig. 2.11 (b). The resonance of this is called as a shear resonance [42] and the excitation in the lateral dimension can be due to the leakage from the main mode. This type of resonances are one of the main causes of the spurious modes in BAW devices and can occur either between the main series and the parallel resonance frequencies, or beyond those resonance frequencies.
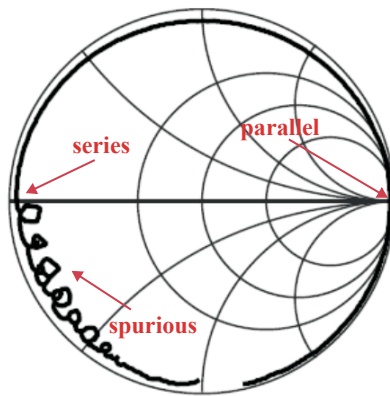
Figure 2.12: Spurious resonances of a BAW resonator on Smith Chart. (This figure is adapted from [42].

An example illustration of the electrical input impedance of a BAW resonator is depicted in Fig. 2.12. For this example, the spurious modes are below the series resonance frequency and this type of behavior is common for the BAW devices using AlN

46

material [67]. For BAW devices with ZnO material, the spurious modes can be observed between the series and the parallel resonance frequency and can have effects on the passband of the filters being designed with them.

2.5.4 Materials in BAW Design

There are multiple different piezoelectric materials that are used for the design of the BAW resonators including AlN, ZnO, PZT, and LiNbO$_3$. The mechanical properties of these materials are depicted in Table 2.1.

Table 2.1: Mechanical properties of the commonly used piezoelectric materials in AW based resonator technologies [42]. c_{33} is the stiffness constant, ρ is the density, e_{33} is the piezoelectric constant, ϵ_r is the relative dielectric permittivity, v_p is the phase velocity, Z_a is the acoustic impedance, and k_t^2 is the electromechanical coupling coefficient.

Material	$c_{33}(N/m^2)$	ρ (kg/m^3)	e_{33}	ϵ_r	v_p (m/s)	$Z_a(kg/m^2s)$	$k_t^2(\%)$
AlN	395	3260	1.5	10.5	11340	3.7e7	6.1%
ZnO	211	5680	1.32	10.2	6370	3.61e7	9.1
CdS	94	4820	0.44	9.5	4500	2.15e7	2.4

Among the four aforementioned piezoelectric materials, AlN is one of the most used one for the design of RF filters due to many different factors. These include the high acoustic velocity, high termal conductivity, low acoustic loss, and its chemical stability during manufacturing processes [68]. Considering the other materials, ZnO, PZT, and LiNbO$_3$ have larger k_t^2 values compared to AlN, however, none of the other materials are CMOS compatible. In addition, the high phase velocity of AlN makes the thickness of the piezoelectric layer to be thicker than the other materials, making it more stable.

One of the issues with the AlN material is the relatively low k_t^2 value, which makes

it difficult to be used in the filter applications. In order to increase this value, doping the AlN with Sc, which makes it AlScN is a common method [68]. Using this method, the k_t^2 value can be increased beyond 12% and conventional filter design methods can usually achieve FBW values at a similar value to the k_t^2 value of the resonator. Table 2.2 provides the properties of several AW resonators with different technologies of piezoelectric materials.

Table 2.2: Properties of several AW resonators with different piezoelectric materials from literature.

Ref	Piezoelectric	Technology	f (GHz)	k_t^2	Q
[69]	PZT	FBAR	1.6	15.9	53
[70]	LiNbO$_3$	FBAR	3	16.63	183
[71]	AlN	BAW	1.8	6.03	3685
	AlN	BAW	3.8	6.3	2589
[72]	Al$_{0.72}$Sc$_{0.28}$N	BAW	3.5	16	1070
[73]	Al$_{0.3}$Sc$_{0.7}$N	FBAR	3	18.1	213

As observed in table 2.2, achieving high k_t^2 values using PZT or LiNbO$_3$ is possible, however, they usually have too many spurious modes and the quality factor values may not be as good as those with AlN. Therefore, for the design of filters, AlScN material dominates the market [68].

2.6   Summary and Conclusions

In this chapter, the building blocks of the coupled-resonator based microwave/mmWave filters have been considered. Starting with a discussion on the lumped-element based resonators, the transmission-line-, cavity, and acoustic-wave resonators are examined

considering the achievable Q-factor values using each resonator. The cavity based resonators provide one of the highest Q values, however, they are not compatible for on-chip integration for the low-frequency microwave filter applications such as the applications for S-band where the wavelength of air is in the order of 15 cm. For such applications, the evanescent-mode cavity technology offers significant size reduction, however, the size of the resonators are still quite large for on-chip integration. Lumped-element resonators can be used for such applications with the use of high-resistivity silicon substrates to reduce the loss, however, the order of the quality factor that is achievable at this frequency range is still around 50, which is not enough to create higher order filters.

The acoustic-wave resonator technology has attracted a very significant attention due its capability of obtaining very high-Q values (of order 1000) at low frequencies with resonator dimensions of several micrometers. Discussions on the Mason model and the Butterworth-Van-Dyke model of the AW based resonators are also made and they are important in the design of filters based on AW resonators. Finally, the different material technologies in the design of the BAW resonators have been discussed and it has been emphasized that the Sc doped AlN is an important material for the design of filters based on AW resonators.

Chapter 3

Design of Generalized Chebyshev Functions

In Chapter 2, microwave resonators were examined, which are the building blocks of filters. To design filters, the resonators should be coupled together. One can realize filter responses that are based on Chebyshev functions by adjusting the strength and the nature of the coupling mechanisms (either E- or H-field) between the resonators and the source and the load terminations. To find the values of these coupling mechanisms, it is important to start with a polynomial Chebyshev response in the normalized frequency domain.

The polynomial based Chebyshev function should first be synthesized based on the desired order (N), ripple constant (ϵ) (this should not be confused with the dielectric permittivity), and the location of the finite-frequency transmission zeros (if any).

The reflection and the transmission response of a generalized Chebyshev function can be characterized using the polynomials having the *normalized* frequency variable s as:

$$S_{11}(s) = \frac{F(s)/\epsilon_r}{E(s)} \quad \text{and} \quad S_{21}(s) = \frac{P(s)/\epsilon}{E(s)},$$

$$\text{where} \begin{cases} \epsilon_r = 1, & N_{TZ} < N \\ \epsilon_r = \epsilon/\sqrt{\epsilon^2 - 1} & N_{TZ} = N. \end{cases} \tag{3.1}$$

In (3.1), N_{TZ} is the number of the finite-frequency transmission zeros and ϵ is the ripple constant which is defined as:

$$\epsilon = \frac{1}{\sqrt{10^{RL/10} - 1}} \left| \frac{P(s)}{F(s)/\epsilon_r} \right|_{s=\pm 1j}, \tag{3.2}$$

where RL is the desired return loss ripple in dB scale. In (3.1), the roots of the function $F(s)$ define the *reflection* zeros, the roots of $P(s)$ define the transmission zeros, and the roots of $E(s)$ define the poles of the Chebyshev function. For a function of order N with N_{TZ} finite-frequency transmission zeros, $F(s)$ and $E(s)$ should be of order N while $P(s)$ is of order N_{TZ}. The polynomials $F(s)$ and $E(s)$ can be written in terms of their coefficients as follows:

$$E(s) = e_0 + e_1 s + e_2 s^2 + ... + e_N s^N$$
$$F(s) = f_0 + f_1 s + f_2 s^2 + ... + f_N s^N \tag{3.3}$$

To start with the synthesis of the response in (3.1), one needs the information of the following:

- degree of the function,

- the locations of the finite-frequency transmission zeros, which are denoted as s_i, where $i \in [1, N_{TZ}]$, and

- the ripple constant ϵ.

Using these parameters, the polynomial fractions that define the normalized-frequency Chebyshev response can be synthesized by finding $P(\Omega)$ and switching to $P(s)$, then finding $F(\Omega)$ and switching to $F(s)$, and finally finding $E(\Omega)$ and switching to $E(s)$ using the algorithm that is explained in the following sections. It should be noted that the variable Ω is used to denote the normalized frequency variable. In the further chapters, ω will be used for actual frequency.

3.1 Finding P(s)

The polynomial function $P(s)$, which is the numerator of $S_{21}(s)$, is directly obtained from the desired transmission zero locations of the network, denoted as $s_i = j\Omega_i$. Initially, one needs to find it in the Ω-domain as:

$$P(\Omega) = \prod_{i=1}^{N_{TZ}} (\Omega - \Omega_i).$$ (3.4)

Once the polynomial $P(\Omega)$ is obtained, one can obtain P(s) by replacing Ω by s/j. The polynomial $P(s)$ needs to satisfy the orthogonality condition with $F(s)$, which is done by multiplying that polynomial by j or not, depending on the number of transmission zeros and the order of the filter [2, 4]. The orthogonality condition which determines whether to multiply $P(s)$ by j or not is depicted in Fig. 3.1 for all possible combinations of N and N_{TZ}.

Table 3.1: Orthogonality condition table demonstrating whether it is necessary to multiply $P(s)$ by j or not for different N and N_{TZ} conditions.

N	n_{fz}	$N - n_{fz}$	Mult. by j?
Odd	Odd	Even	Yes
Odd	Even	Odd	No
Even	Odd	Odd	No
Even	Even	Even	Yes

3.2 Finding F(s)

Finding $F(s)$ is more complicated than finding $P(s)$ and different algorithms have been proposed for this synthesis in literature [2]. $F(s)$ can be obtained from the roots of the function $C_N(\Omega)$ which is defined as:

$$C_N(\Omega) = \cosh\left[\sum_{n=1}^{N} \cosh^{-1} x_n(\Omega)\right], \tag{3.5}$$

where

$$x_n(\Omega) = \frac{1 - \Omega\Omega_n}{\Omega - \Omega_n}. \tag{3.6}$$

However, this is a complicated process and the common methodology to find the numerator of $C_N(\Omega)$ is the recursive algoritm given in [2]. In that algorithm, (3.5) is rewritten as:

$$C_N = \frac{1}{2}\left[G_N(\Omega) + G'_N(\Omega)\right], \tag{3.7}$$

where

$$G_N(\Omega) = \prod_{n=1}^{N}\left[\left(\Omega - \frac{1}{\Omega_n}\right) + \Omega'\sqrt{1 - \frac{1}{\Omega_n^2}}\right], \tag{3.8}$$

and

$$G'_N(\Omega) = \prod_{n=1}^{N}\left[\left(\Omega - \frac{1}{\Omega_n}\right) - \Omega'\sqrt{1 - \frac{1}{\Omega_n^2}}\right]. \tag{3.9}$$

In (3.8) and (3.9), Ω_n is the nth finite-frequency transmission zero and $\Omega' = \sqrt{\Omega^2 - 1}$.

The function $G_N(\Omega)$ can be obtained from $G_{N-1}(\Omega)$ at each step. At each iteration, it is possible to separate the terms with Ω and Ω' by defining two new functions given as:

$$G_N(\Omega) = U_N(\Omega) + V_N(\Omega) \text{ and}$$
$$G'_N(\Omega) = U_N(\Omega) - V_N(\Omega), \tag{3.10}$$

where $U_N(\Omega)$ and $V_N(\Omega)$ represent the terms of Ω and Ω' and can be written as:

$$U_N(\Omega) = u_0 + u_1\Omega + u_2\Omega^2 + ... + u_N\Omega^N \text{ and}$$
$$V_N(\Omega) = v_0 + v_1\Omega + v_2\Omega^2 + ... + v_N\Omega^N \tag{3.11}$$

This recursive algorithm is initiated by setting N to 1 and finding the initial functions as:

$$U_1(\Omega) = -\frac{1}{\Omega_1} + \Omega \text{ and}$$
$$V_1(\Omega) = \sqrt{1 - \frac{1}{\Omega_1^2}}. \tag{3.12}$$

Setting N to two, the functions for the second order are found as:

$$U_2(\Omega) + V_2(\Omega) = \left[\left(\Omega - \frac{1}{\Omega_2} + \Omega'\sqrt{1 - \frac{1}{\Omega_2^2}}\right)\right]\left[U_1(\Omega) + V_1(\Omega)\right],$$
$$\Rightarrow U_2(\Omega) = \Omega \cdot U_1(\Omega) - \frac{U_1(\Omega)}{\Omega_2} + \Omega' \cdot V_1(\Omega)\sqrt{1 - \frac{1}{\Omega_2^2}}, \text{ and} \tag{3.13}$$
$$\Rightarrow V_2(\Omega) = \Omega V_1(\Omega) - \frac{V_1(\Omega)}{\Omega_2} + \Omega' \cdot U_1(\Omega)\sqrt{1 - \frac{1}{\Omega_2}}.$$

This recursive algorithm can be used to continue until $U_N(\Omega)$ is found. However,

its analytical derivation is a tedious process with the increasing number of iterations. Instead, this algorithm can be coded to numerically calculate $U_N(\Omega)$.

Once the function $U_N(\Omega)$ is synthesized, the roots of this polynomial (Ω_i^r) should be obtained, which give the normalized frequency positions of the *reflection zeros*. Using the reflection zeros, one can convert them into s-domain using $s_i^r = j\Omega_i^r$ and finally, $F(s)$ can be obtained from the reflection zeros as:

$$F(s) = \prod_{i=1}^{N}(s - s_i^r).$$ (3.14)

Once $F(s)$ is obtained, the only remaining function to be found is $E(s)$ and it will be described in the next subsection.

3.3 Finding E(s)

The last function to be obtained in the synthesis of the generalized Chebyshev functions is the common denominator polynomial of $S_{11}(s)$ and $S_{21}(s)$, which is $E(s)$. This polynomial should be a Hurwitz Polynomial, meaning that the roots of $E(s)$ lie on the left half of the s-plane. It can be obtained using the *alternating pole method* [2]. With the prior knowledge of the functions $F(s)$ and $P(s)$, the equation of the conservation of energy can be written as:

$$S_{11}(s)S_{11}(s)^* + S_{21}(s)S_{21}(s)^* = 1 \text{ or}$$
$$\frac{F(s)F^*(s)}{\epsilon_r^2} + \frac{P(s)P^*(s)}{\epsilon^2} = E(s)E^*(s)$$ (3.15)

Considering the orthogonality condition between $P(s)$ and $F(s)$ in Table 3.1, (3.15) can be rewritten when $N - N_{TZ}$ is odd as:

$$\epsilon_r^2 \epsilon^2 E(s)E^*(s) = [\epsilon_r P(s) + \epsilon F(s)][\epsilon_r P(s) + \epsilon F(s)]^*, \qquad (3.16)$$

and when $N - N_{TZ}$ is even as:

$$\epsilon_r^2 \epsilon^2 E(s)E^*(s) = [\epsilon_r(jP(s)) + \epsilon F(s)][\epsilon_r(jP(s)) + \epsilon F(s)]^*. \qquad (3.17)$$

For responses of both even and odd order, the singularities of the term $E(\Omega)E(\Omega)^*$ are depicted in Fig. 3.1, being symmetrically located across the imaginary axis. This symmetry condition is due to the fact that $E(s)$ is a strictly Hurwitz polynomial [2].
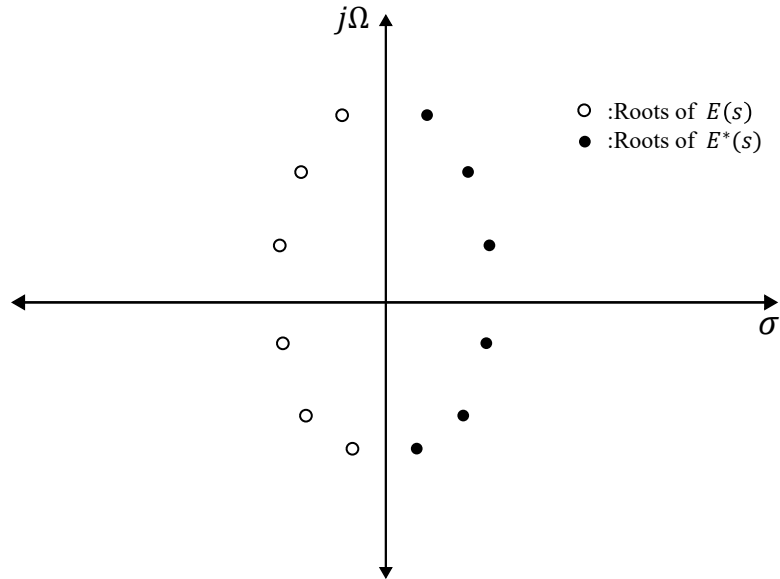
Figure 3.1: (a):Roots of the $E(s)E^*(s)$ polynomial on the complex plane

To simplify the synthesis of $E(s)$, (3.16) and (3.17) can be examined in the Ω plane,

which requires (3.15) to be rewritten as:

$$E(\Omega)E^*(\Omega) = \frac{\left[\epsilon_r P(\Omega) - j\epsilon F(\Omega)\right]}{\epsilon\epsilon_r} \cdot \frac{\left[\epsilon_r P(\Omega) + j\epsilon F(\Omega)\right]}{\epsilon\epsilon_r}. \tag{3.18}$$

To find the roots of $E(s)$, it is simplest to find the roots of one of the multiplicative terms on the right hand side (RHS) of (3.18). That provides half of the roots in Fig. 3.1, however, the distribution of the roots alternate between the positive and the negative side of the imaginary axis. As an example, the roots of the multiplicative terms on the RHS of (3.18) for a response of sixth-order are depicted in Fig. 3.2. It should be emphasized that the roots of (3.18) are in terms of the variable Ω and the roots in Fig. 3.2 correspond to these roots, when $\Omega = s/j$ conversion is made.
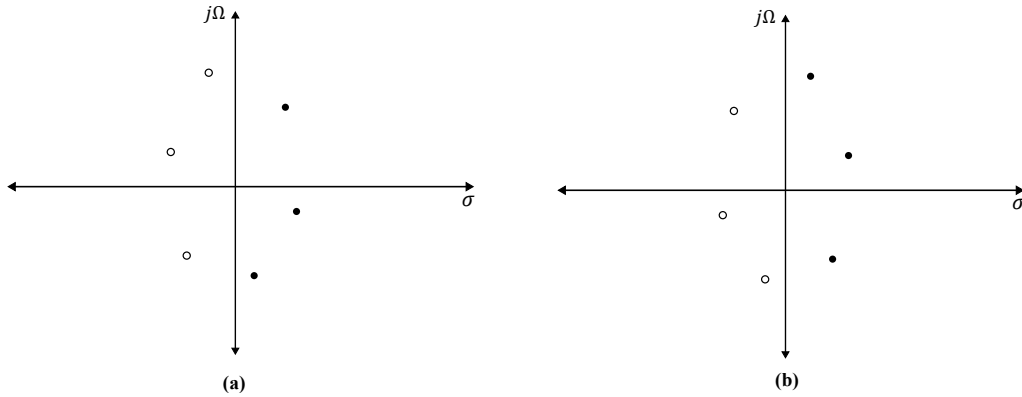
Figure 3.2: (a):Roots of $\left[\epsilon_r P(\Omega) - j\epsilon F(\Omega)\right]/\epsilon\epsilon_r$, after being transformed to the s-plane, and (b): Roots of $\left[\epsilon_r P(\Omega) + j\epsilon F(\Omega)\right]/\epsilon\epsilon_r$ after being transformed to the s-plane.

Once the roots of either $\left[\epsilon_r P(\Omega) - j\epsilon F(\Omega)\right]/\epsilon\epsilon_r$ or $\left[\epsilon_r P(\Omega) + j\epsilon F(\Omega)\right]/\epsilon\epsilon_r$, which produce the ones in Fig. 3.2 (a) and in Fig. 3.2 (b) in s-plane, are found, the ones on the right half plane should be mirrored to the left half plane. To make this simpler, one can simply find the roots of one of the two terms in Ω-domain, take the conjugate of the roots on the lower half of the real axis, and convert the roots into the s-domain by substituting $\Omega = s/j$.

3.4   Example Synthesis of a Chebyshev Response

Understanding the synthesis of the polynomials $F(s)$, $P(s)$, and $E(s)$ can be best understood with an example. As a starting point, a fully-canonical 21-dB Chebyshev response of order six will be synthesized in this section. An arbitrarily chosen set of transmission zero locations for the synthesis is given as $s_i = j[1.6, -1.2, -4, 4, -1.6, 1.2]$ rad/s and the value of the ripple constant is given as $\epsilon = 80$ and $\epsilon_r = 1.0001$.

The initial step of the synthesis is to obtain the transmission function $P(s)$, which can be synthesized as in Section 3.1, as:

$$P(s) = +js^6 + j(20)s^4 + j(68)s^2 + j(59).\qquad(3.19)$$

Then, the function $F(s)$ can be obtained using the recursive algorithm given in Section 3.2. Calculating $U_6(s)$ for this function gives the six reflection zero positions at $\pm 3307j, \pm 8008j \pm 9814j$ rad/s. Using these reflection zero positions, the function $F(s)$ can be obtained as:

$$F(s) = s^6 + 1.7s^4 + 0.79s^2 + 0.068\qquad(3.20)$$

Finally, the function $P(\Omega)/\epsilon - jF(\Omega)/\epsilon_r$ can be obtained and its roots are calculated. These roots are depicted in Fig. 3.3 (a) on the complex plane. As mentioned in Section 3.3, the complex conjugate of the roots in the lower half of the Ω plane are obtained to find the roots of $E(\Omega)$ for correction.
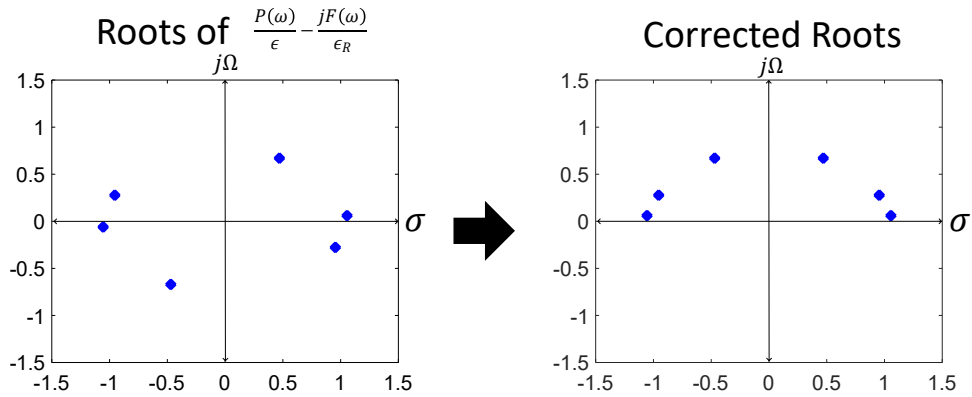
Figure 3.3: Obtaining the roots of $(P(\Omega)/\epsilon) - jF(\Omega)/\epsilon_R$ to use the alternating pole method. The Roots that are at the lower half of the s-plane are conjugated to obtain the correct roots.

The roots, after correction are depicted in Fig. 3.3 (b). These roots correspond to the left-half plane roots, when the s-plane is considered. Using the roots in Fig. 3.3 (b), the function $E(s)$ can be obtained as:

$$E(s) = s^6 + 2s^5 + 3.7s^4 + 4.1s^3 + 3.6s^2 + 2s + 0.74 \qquad (3.21)$$

Once $F(s)$, $P(s)$, and $E(s)$ are obtained in addition to ϵ and ϵ_r, the frequency response of the function is known and it can be plotted with respect to the normalized frequency variable Ω as depicted in Fig. 3.4.
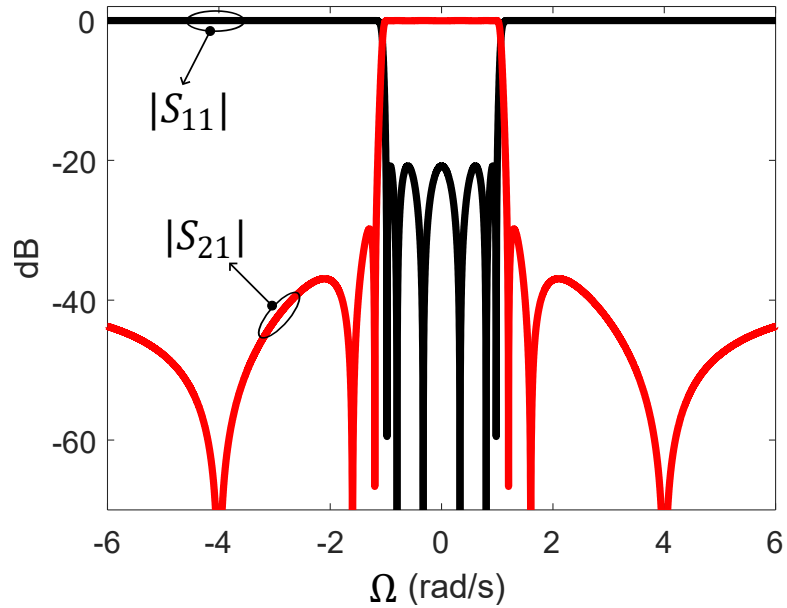
Figure 3.4: S-Parameters of the synthesized response in normalized frequency domain.

As observed in Fig. 3.4, the function has six poles and six transmission zeros, as prescribed initially. Considering the filter polynomials, it can be observed that both $P(s)$ and $F(s)$ are of order 6 with vanishing coefficients of odd-degree. This is a result of the function having transmission zeros that are located symmetrically around $\Omega = 0$ rad/s axis. It will be observed in the following sections that starting with completely symmetric functions like this is useful in simplifying the design of the microwave filter network.

This example concludes the synthesis of a generalized Chebyshev function in the normalized-frequency domain. This is the first step in the design of a microwave filter prototype. Based on the obtained Chebyshev response, a filter at an arbitrary center frequency and a fractional bandwidth can be designed. This design can be accomplished either using the coupling matrix based filter design methodology, or the more comprehensive circuit-synthesis and extracted-pole approaches. Both approaches will be examined in the following chapters.

3.5 Conclusions and Summary

In this chapter, the algorithm of obtaining a generalized Chebyshev function based on the desired number of finite transmission zero locations and the ripple constant is examined. This includes finding $F(s)$ and $P(s)$, which are the numerator polynomials of S_{11} and S_{21} polynomials, respectively. $P(s)$ is obtained from the locations of the transmission zeros while $F(s)$ is obtained using the recursive algorithm, as discussed in Section 3.2. The common denominator polynomial $E(s)$ is then obtained using the equation of conservation of energy and the alternating pole method. The resulting functions will be extensively used to form the coupling matrix and design filters with electromagnetic and acoustic-wave resonators.

Chapter 4

Coupling Matrix Based Filter Design

This chapter examines a very important tool in filter design, the *coupling matrix* (CM), which was introduced in early 1970s by Atia and Williams [74, 75]. In [75], a *narrow-band* microwave filter is referred to as a network comprising multiple cavities that are inter-coupled. Furthermore, in [75], a matrix that quantifies the strength of the coupling coefficients among these cavities is used to both analyze and *synthesize* a network to realize prescribed Chebyshev functions.

The coupling matrix based design methodology has become very popular within the last decade and it has been extended to be used for designing and analyzing microwave/mmWave filters realizing advanced filtering functions [2]. As such, this method has been used for the design of lossy filters [76–80], lossy-active filters [81], and acoustic-wave resonator based filters [56]. Furthermore, it is used for characterizing filter-amplifier configurations of RF front-end modules [82, 83], and even to design matching networks for microwave/mmWave power amplifiers [84].

In this chapter, the foundations of coupling matrix theory for the characterization of filters will be introduced. As a starting point, Section 4.1 will introduce the concept of multiple-coupled cavities and how to extract the frequency response of a filter from an admittance matrix or a coupling matrix. Then, Section 4.2 will examine the synthesis of the $(N + 2) \times (N + 2)$ *transversal* coupling matrix (the base coupling matrix) from

a prescribed Chebyshev function, which was described in Chapter 3. Section 4.3 will demonstrate the reconfiguration of the coupling matrix and Section 4.4 will demonstrate an example filter design using the reconfigured coupling matrix architectures.

4.1 Introduction and Analysis of the Coupling Matrix

4.1.1 N × N Coupling Matrix

The coupling matrix is a method to charecterize a multi-coupled-cavity configuration, which is demonstrated by a two-port RF network in Fig. 4.1 (a), which includes N resonators, as shown in Fig. 4.1 (b).

(a)

(b)
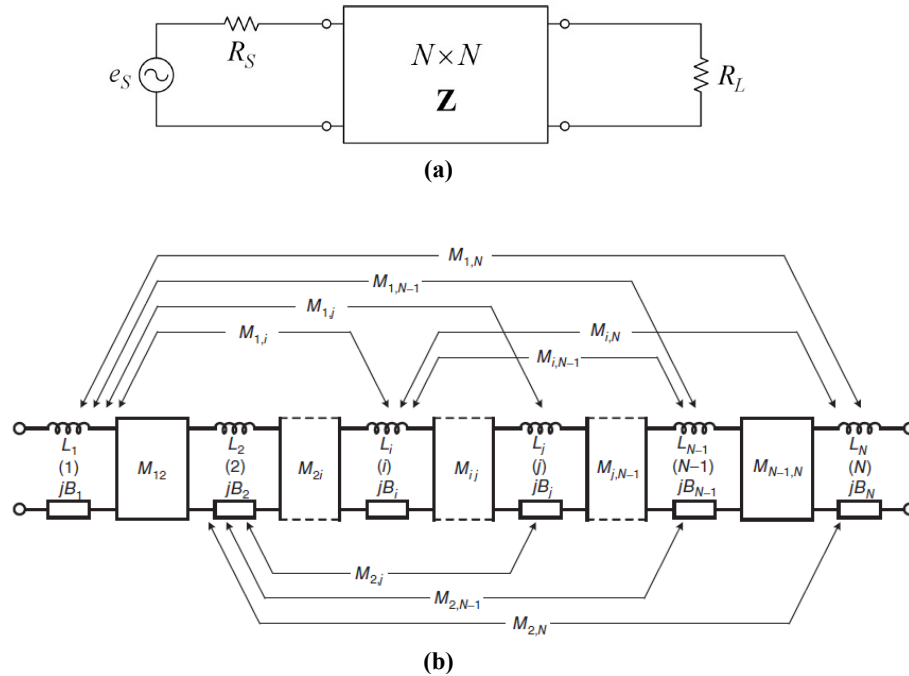
Figure 4.1: (a): Representation of a two-Port network with N resonators connected to a load of R_L and to a voltage source of e_s, and an internal resistance of R_S. (b): The view of multiple resonators connected to each other with coupling coefficients M_{mn}. These figures are taken from [2].

The network in 4.1 (a) is connected to a load with a resistance of R_L and a source

with a voltage e_s and an internal resistance R_S. This network has $N + 2$ current paths, which are denoted with i_n such that $n \in [1, N + 2]$ and each loop is *coupled* to another through a coupling coefficient of M_{mn}.

Considering that each inductor has a value of 1 H, The Kirchoff's voltage law (KVL) equations for each loop in matrix form can be written for the network in Fig. 4.1 (b) as:

$$
\begin{bmatrix} e_1 \\ 0 \\ \vdots \\ 0 \end{bmatrix} = \begin{bmatrix} R_S & 0 & \cdots & 0 \\ 0 & 0 & \cdots & 0 \\ \vdots & \vdots & \ddots & \vdots \\ 0 & 0 & \cdots & R_L \end{bmatrix} \begin{bmatrix} i_1 \\ i_1 \\ \vdots \\ i_N \end{bmatrix} + \begin{bmatrix} s & 0 & \cdots & 0 \\ 0 & s & \cdots & 0 \\ \vdots & \vdots & \ddots & \vdots \\ 0 & 0 & \cdots & s \end{bmatrix} \begin{bmatrix} i_1 \\ i_1 \\ \vdots \\ i_N \end{bmatrix} +
$$
$$
\begin{bmatrix} jM_{11} & jM_{12} & \cdots & jM_{1N} \\ jM_{21} & jM_{22} & \cdots & jM_{2N} \\ \vdots & \vdots & \ddots & \vdots \\ jM_{N1} & jM_{N2} & \cdots & jM_{NN} \end{bmatrix} \begin{bmatrix} i_1 \\ i_1 \\ \vdots \\ i_N \end{bmatrix}.
$$
(4.1)

Equation (4.1) can also be written as the following:

$$
\underline{\mathbf{E}} = ([\mathbf{R}] + [\mathbf{S}] + j[\mathbf{M}]) \cdot \underline{\mathbf{I}} = [\mathbf{Z}] \cdot \underline{\mathbf{I}},
$$
$$
\Rightarrow \underline{\mathbf{I}} = [\mathbf{Z}]^{-1} \cdot \underline{\mathbf{E}} = [\mathbf{Y}] \cdot \underline{\mathbf{E}}
$$
(4.2)

where $\underline{\mathbf{E}}$ and $\underline{\mathbf{I}}$ are the vectors denoting the phasor voltage and current in each loop respectively, $[\mathbf{R}]$ is the matrix that contains the source and the load resistances, $[\mathbf{S}]$ is the matrix that contains the frequency variable $s = j\Omega$, and $[\mathbf{M}]$ is the $N \times N$ *coupling matrix*. It should also be noted that the diagonal elements of $[\mathbf{M}]$ represent the frequency-independent-reactance (FIR) elements in Fig. 4.1 (b) such that $M_{nn} = B_n$ for $n \in [1, N]$. Furthermore, $[\mathbf{Z}]$ and $[\mathbf{Y}]$ denote the $N \times N$ impedance and the

admittance matrices of the N loops of the two-port filter network, respectively.

The $N \times N$ coupling matrix $[\mathbf{M}]$, along with the normalized source and load resistances R_S and R_L, is sufficient to characterize a generalized Chebyshev function of any order. This means that the frequency response of the network can be obtained from the coupling matrix and the source and load resistances. Considering that the transmission coefficient S_{21} of the network in Fig. 4.1 (a) is obtained from the output voltage and the input voltage, this can be extracted from the coupling matrix as:

$$S_{21} = 2\sqrt{\frac{R_s}{R_L}}\frac{v_N}{e_g} = 2\sqrt{\frac{R_s}{R_L}}R_L[[\mathbf{Y}]]_{N,1}$$

$$\Rightarrow \boxed{S_{21} = 2\sqrt{R_L R_S}[[\mathbf{Y}]]_{N,1}} \tag{4.3}$$

Furthermore, the reflection coefficient of the network can be calculated from the z-parameter Z_{11} of the network as:

$$S_{11} = \frac{Z_{11} - R_S}{Z_{11} + R_S} = 1 - \frac{2R_S}{Z_{11} + R_S}. \tag{4.4}$$

Considering that $Z_{11} = v_1/i_1$, the reflection coefficient of the filter can be obtained as:

$$\boxed{S_{11} = 1 - 2R_S[\mathbf{Y}]_{\mathbf{1,1}}} \tag{4.5}$$

The $N \times N$ coupling matrix is a good method to characterize the filter network, however, it requires the source and the load impedances for being complete. These impedances are also added to the matrix to form the $(N+2) \times (N+2)$ coupling matrix in the following subsection.

4.1.2 $(N + 2) \times (N + 2)$ Coupling Matrix

Instead of specifying the source and load impedances as in Fig. 4.1 (a), they can be absorbed into the coupling matrix. This can be done by starting with an $(N + 2) \times (N + 2)$ matrix as in Fig. 4.2 (a). The $(N + 2) \times (N + 2)$ matrix represents the network characterized by the $N \times N$ matrix being connected to two admittance inverters (coupling mechanisms) M_{S1} and M_{NL} at the input and the output of the network, as shown in Fig. 4.2 (b).
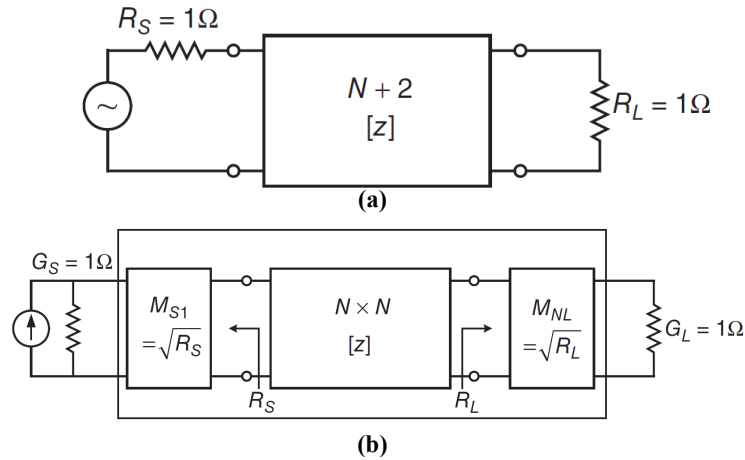
Figure 4.2: Embedding the source and the load terminations into the coupling matrix to create an $(N + 2) \times (N + 2)$ coupling matrix. (a): The network having $N + 2$ nodes being connected to a source and load of $1\,\Omega$ each. (b): Conversion of the series resistors at the input and output to parallel by using admittance inverters. This figure is taken from [2].

Use of the $(N + 2) \times (N + 2)$ coupling matrix absorbs the required non-unity source and load impedances into the input and the output of the filter. This is done using the admittance inverters and the kirchoff's voltage law (KVL) equations of the network are

now given as in the following:

$$
\begin{bmatrix} e_1 \\ 0 \\ 0 \\ \vdots \\ 0 \\ 0 \end{bmatrix} = \begin{bmatrix} 1 & 0 & 0 & \cdots & 0 & 0 \\ 0 & 0 & 0 & \cdots & 0 & 0 \\ 0 & 0 & 0 & \cdots & 0 & 0 \\ \vdots & \vdots & \vdots & \ddots & \vdots & \vdots \\ 0 & 0 & 0 & \cdots & 0 & 0 \\ 0 & 0 & 0 & 0 & 0 & 1 \end{bmatrix} \begin{bmatrix} i_1 \\ i_2 \\ i_3 \\ \vdots \\ i_{N+1} \\ i_{N+2} \end{bmatrix} + \begin{bmatrix} 0 & 0 & 0 & \cdots & 0 & 0 \\ 0 & s & 0 & \cdots & 0 & 0 \\ 0 & 0 & s & \cdots & 0 & 0 \\ \vdots & \vdots & \vdots & \ddots & \vdots & \vdots \\ 0 & 0 & 0 & \cdots & s & 0 \\ 0 & 0 & 0 & 0 & 0 & 0 \end{bmatrix} \begin{bmatrix} i_1 \\ i_2 \\ i_3 \\ \vdots \\ i_{N+1} \\ i_{N+2} \end{bmatrix} +
$$

$$
\begin{bmatrix} jM_{S,S} & jM_{S1} & jM_{S2} & \cdots & jM_{S,N+1} & jM_{S,L} \\ jM_{1,S} & jM_{11} & jM_{12} & \cdots & jM_{1N+1} & jM_{1,L} \\ jM_{2,S} & jM_{11} & jM_{22} & \cdots & jM_{2N+1} & jM_{2,L} \\ \vdots & \vdots & \vdots & \ddots & \vdots & \vdots \\ jM_{N+1,S} & jM_{1,1} & jM_{N,2} & \cdots & jM_{N,N+1} & jM_{N+1,L} \\ jM_{S,L} & jM_{L,1} & jM_{L,2} & \cdots & jM_{L,N+1} & jM_{L,L} \end{bmatrix} \begin{bmatrix} i_1 \\ i_2 \\ i_3 \\ \vdots \\ i_{N+1} \\ i_{N+2} \end{bmatrix}, \quad (4.6)
$$

which can again be written as:

$$
\underline{\mathbf{E}} = ([\mathbf{R}] + [\mathbf{S}] + j[\mathbf{M}]) \cdot \underline{\mathbf{I}} = [\mathbf{Z}] \cdot \underline{\mathbf{I}},
$$
$$
\Rightarrow \underline{\mathbf{I}} = [\mathbf{Z}]^{-1} \cdot \underline{\mathbf{E}} = [\mathbf{Y}] \cdot \underline{\mathbf{E}}, \tag{4.7}
$$

where $[\mathbf{R}]$, $[\mathbf{S}]$, $[\mathbf{Z}]$, and $[\mathbf{Y}]$ are all $(N + 2) \times (N + 2)$ and $[\mathbf{M}]$ is the $(N + 2) \times (N + 2)$ coupling matrix. Since both the source and the load have a unit impedance, the transmission and the reflection coefficients can be found as:

$$
\boxed{S_{21} = 2[[\mathbf{Y}]]_{N,1}} \text{ and}
$$
$$
\boxed{S_{11} = 1 - 2[[\mathbf{Y}]]_{1,1}}. \tag{4.8}
$$

When the frequency response of the network is being derived from the coupling

67

matrix, there are several important observations:

- The coupling matrix entries $M_{m,n}$, where $m \neq n$ represent the normalized admittance inverter values with respect to f_0 and Δ.

- The entries $M_{m,n}$, where $m = n$ represent the shunt-connected normalized FIR elements.

- For a lossless network, all entries of $[\mathbf{M}]$ are real.

- In order to observe the response of the network, the bandpass transformation can be performed as a change of variable:

$$\Omega \rightarrow \frac{1}{\Delta} \left[\frac{\omega}{\omega_0} - \frac{\omega_0}{\omega} \right], \tag{4.9}$$

where $\omega_0 = 2\pi f_0$ is the angular center frequency.

- To observe the response of the network when the resonators have finite quality factor values of Q_u, the frequency variable s can be replaced by $s + \delta$ where

$$\delta = \frac{\Delta}{Q_u}. \tag{4.10}$$

It should be noted that δ is a real variable which represents a shunt real conductance at each resonant node of the network.

The analysis equations of the coupling matrix are used to visualize the frequency response of a filter that is characterized by the coupling matrix. On the other hand, the coupling matrix can be used to *design* a filter network using an arbitrary prescribed Chebyshev function, as synthesized in Chapter 3.

4.2   Synthesis of the Coupling Matrix

In this section, the synthesis of the $(N+2) \times (N+2)$ coupling matrix will be examined using two different methods. The first method includes the use of the g-coefficients. This method is straightforward, however, it is limited to the filters with no finite-frequency transmission zeros. The second and more comprehensive method synthesizes the *transversal* coupling matrix which can characterize an arbitrary Chebyshev function, that is generated with the algorithm in Chapter 3.

4.2.1   Coupling Matrix Synthesis Based on g-coefficients

For inline all-pole filters of arbitrary orders, the g-coefficients can be used to synthesize the inline coupling matrix, as depicted in Fig. 4.3 (a) with the inline coupling-routing diagram shown as in Fig. 4.3 (b). For the coupling-routing diagram, the filled circles represent the *resonant nodes* (RN) meaning that they include an FIR element parallel connected to a capacitance. The empty circles (only the source and the load) represent the *non-resonant nodes* (NRN), which correspond to the nodes including an FIR element and a conductance, as depicted in Fig. 4.3 (c). It should be noted that for the source and the load terminations, this conductance is equal to the source or the load termination conductance. Finally, Fig. 4.3 (d) depicts the circuit diagram of the network that is characterized by the coupling matrix and the coupling-routing diagram.

For the inline coupling matrix of Fig. 4.3 (a), since all the diagonal elements are equal to zero, the FIR elements for each resonant and non-resonant node are also equal to zero. This is common for the responses that are symmetric, however, for certain responses, the FIR elements need to be nonzero for completeness. These will be considered in the next sections.

	S	**1**	**2**	**...**	**N − 1**	**N**	**L**
S	0	m_{s1}	0	...	0	0	0
1	m_{s1}	0	m_{12}	...	0	0	0
2	0	m_{12}	0	...	0	0	0
⋮	⋮	⋮	⋮	⋱	⋮	⋮	⋮
N − 1	0	0	0	...	0	$m_{N-1\,N}$	0
N	0	0	0	...	$m_{N-1\,N}$	0	m_{NL}
L	0	0	0	...	0	$m_{N\,L}$	0

(a)

(b)

(c)

(d)
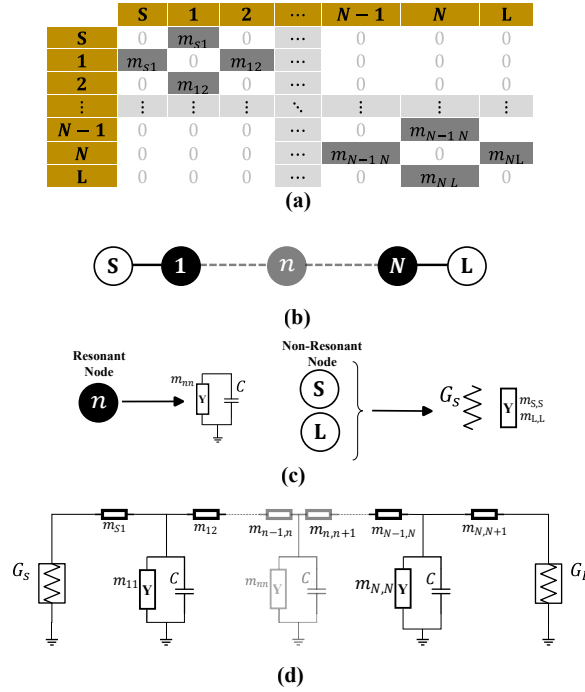
Figure 4.3: (a): The inline $(N + 2) \times (N + 2)$ coupling matrix. (b): Coupling-routing diagram of the inline coupling matrix in (a). (c): The normalized-frequency equivalent of the network that is characterized by the coupling matrix in (a). For this network, the capacitance values are all equal to 1 F. Furthermore, the FIR elements (m_{nn}) for the network in (c) are all equal to zero for the coupling matrix in (a).

The coupling matrix entries for the matrix in Fig. 4.3 (a) can be synthesized as:

$$m_{n,n+1} = \frac{1}{\sqrt{g_n g_{n+1}}} \quad n \in \{1, 2, ..., N\},$$

$$m_{s1} = \frac{1}{\sqrt{g_0 g_1}}, \quad m_{NL} = \frac{1}{\sqrt{g_N g_{N+1}}}. \tag{4.11}$$

When all the FIR elements are equal to zero, this means that each resonator is designed to resonate at the common center frequency. Furthermore, each resonator is coupled to the one next to it, meaning that no cross-coupling mechanisms are required.

However, it is not possible to synthesize the filters realizing finite-frequency transmission zeros with this method. That will be introduced in the design of the transversal coupling matrix topology.

4.2.2 Synthesis of the $(N+2) \times (N+2)$ Transversal Coupling Matrix

The transversal coupling matrix is one of the most comprehensive coupling matrices that can characterize an arbitrary Chebyshev function of any order and an arbitrary number of finite-frequency transmission zeros. This matrix is obtained from a generalized Chebyshev function whose S-parameter polynomials are defined by $S_{11}(s) = F(s)/(\epsilon_r E(s))$ and $S_{21}(s) = P(s)/(\epsilon E(s))$ as in (3.1) of Chapter 3.

To synthesize the coupling matrix, one needs to convert the scattering polynomials into admittance (y-) polynomials, which can be obtained as:

$$
\begin{aligned}
y_{22}(s) &= \frac{y_{22_n}(s)}{y_d(s)} = \begin{cases} n_1(s)/m_1(s) & N \text{ is even,} \\[2mm] m_1(s)/n_1(s) & N \text{ is odd,} \end{cases} \\[4mm]
y_{21}(s) &= \frac{y_{21_n}(s)}{y_d(s)} = \begin{cases} P(s)/\big[m_1(s) \cdot \epsilon\big] & N \text{ is even,} \\[2mm] P(s)/\big[n_1(s) \cdot \epsilon\big] & N \text{ is odd,} \end{cases}
\end{aligned}
\tag{4.12}
$$

where

$$
\begin{aligned}
m_1(s) &= \mathrm{Re}(e_0 + f_0) + j\mathrm{Im}(e_1 + f_1)s + \mathrm{Re}(e_2 + f_2)s^2 + \ldots \\
n_1(s) &= j\mathrm{Im}(e_0 + f_0) + \mathrm{Re}(e_1 + f_1)s + j\mathrm{Im}(e_2 + f_2)s^2 + \ldots,
\end{aligned}
\tag{4.13}
$$

As a reminder, e_i and f_i are the complex coefficients of the polynomials $E(s)$ and $F(s)/\epsilon_r$, respectively. The underlying theory for obtaining a transversal CM is that the admittance polynomials of the network can be written as a sum of multiple terms which contain resonating elements. This implies that an arbitrary Chebyshev function can be characterized as a parallel connection of a set of sub-circuits. To obtain these sub-circuits, a partial fraction expansion (PFE) on the admittance polynomials

can be performed as:

$$[\mathbf{Y_N}] = \begin{bmatrix} y_{11}(s) & y_{12}(s) \\ y_{21}(s) & y_{22}(s) \end{bmatrix} = \frac{1}{y_d(s)} \begin{bmatrix} y_{11n}(s) & y_{12n}(s) \\ y_{21n}(s) & y_{22n}(s) \end{bmatrix}$$

$$= \boxed{ j \begin{bmatrix} 0 & K_\infty \\ K_\infty & 0 \end{bmatrix} + \sum_{k=1}^{N} \frac{1}{s - j\lambda_k} \cdot \begin{bmatrix} r_{11k} & r_{12k} \\ r_{21k} & r_{22k} \end{bmatrix} } . \tag{4.14}$$

In (4.14), the encapsulated term should be examined carefully. First of all, K_∞ is a constant term which represents an additional admittance inverter to the sum of multiple terms in (4.14). It should be noted that K_∞ can be derived from the admittance polynomials as:

$$jK_\infty = \left. \frac{y_{21n}(s)}{y_d(s)} \right|_{s \to \infty} = (\epsilon/\epsilon_r)(\epsilon_r - 1). \tag{4.15}$$

It can be realized that as $\epsilon_r = 1$ for non-canonical responses, K_∞ is only nonzero for the non-canonical networks. Proceeding with the observation of the encapsulated term in (4.14), one should notice the similarity of the admittance matrix within the sum formula with the admittance matrix of the network given in Fig. 4.4.
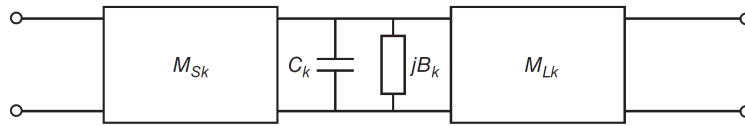
Figure 4.4: A single component of the partial fraction expansion for obtaining the transversal coupling matrix. This figure is adapted from [2].

The admittance matrix of the network, that represents a resonant node being connected to admittance inverters, in Fig. 4.4 can be written as follows:

$$[\mathbf{Y_k}] = \frac{1}{sC_k + jB_k} \cdot \begin{bmatrix} m_{Sk}^2 & m_{Sk}m_{Lk} \\ m_{Sk}m_{Lk} & m_{Lk}^2 . \end{bmatrix} \tag{4.16}$$

Comparing this term with the box encapsulated term in Fig. 4.14, it can be inferred that the overall filter network can be written in terms of the parallel connection of a number of N of the circuit of Fig. 4.4. As an addition, a parallel admittance inverter that represents K_∞ in (4.14) is also connected as depicted in Fig. 4.5.
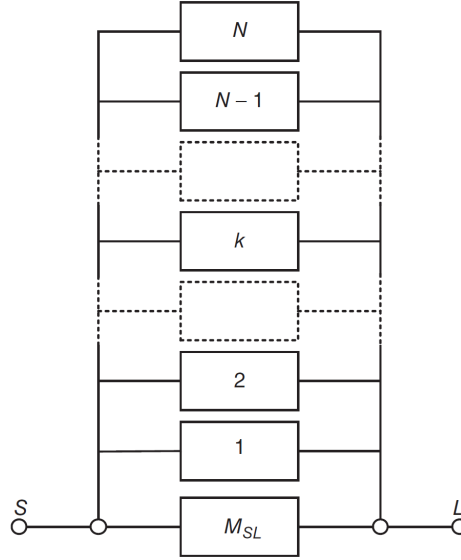
Figure 4.5: The transversal filter topology that represents the transversal coupling matrix. This figure is taken from [2].

The network topology in Fig. 4.5 is referred to as the transversal topology, whose admittance matrix can be written in terms of each individual lowpass element in Fig. 4.4 as:

$$
j \begin{bmatrix} B_S & m_{SL} \\ m_{SL} & B_L \end{bmatrix} + \sum_{k=1}^{N} \frac{1}{sC_k - jB_k} \cdot \begin{bmatrix} m_{Sk}^2 & m_{Sk}m_{Lk} \\ m_{Sk}m_{Lk} & m_{Lk}^2. \end{bmatrix}
\tag{4.17}
$$

	S	1	2	3	$\cdots$	k	$\cdots$	N−1	N	L
S	m_{SS}	m_{S1}	m_{S2}	m_{S3}	$\cdots$	m_{Sk}	$\cdots$	$m_{S,N-1}$	m_{SN}	m_{SL}
1	m_{1S}	m_{11}								m_{1L}
2	m_{2S}		m_{22}							m_{2L}
3	m_{3S}			m_{33}						m_{3L}
$\vdots$	$\vdots$				$\ddots$					$\vdots$
k	m_{kS}					m_{kk}				m_{kL}
$\vdots$	$\vdots$						$\ddots$			$\vdots$
N−1	$m_{N-1,S}$							$m_{N-1,N-1}$		$m_{N-1,L}$
N	m_{NS}								m_{NN}	m_{NL}
L	m_{LS}	m_{L1}	m_{L2}	m_{L3}	$\cdots$	m_{Lk}	$\cdots$	$m_{L,N-1}$	m_{LN}	m_{LL}

Figure 4.6: The transversal $(N + 2) \times (N + 2)$ coupling matrix. This figure is taken from [2].

It should be realized that the transversal network in Fig. 4.5 includes the shunt-FIR elements at the source and the load (B_S and B_L) in addition to each of the shunt resonators (resonant nodes) being coupled to the source and the load. Therefore, relating the equations (4.14) and (4.17), one can populate the transversal coupling matrix in Fig. 4.6 as follows [2]:

$$C_k = 1, \qquad B_k = m_{kk} = -\lambda_k$$

$$m_{Lk}^2 = r_{22k} \qquad \text{and} \qquad m_{Sk}m_{Lk} = r_{21k}, \qquad (4.18)$$

$$m_{Lk} = \sqrt{r_{22k}} \qquad \text{and} \qquad m_{Sk} = r_{21k}/\sqrt{r_{22k}}$$

These equalities finalize populating the $(N + 2) \times (N + 2)$ transversal coupling matrix. Although this topology forms the basis for obtaining the CM from an arbitrary Chebyshev function with an arbitrary number of finite-frequency transmission zeros, it is not very practical to realize as a circuit. Therefore, the manipulation and refonfiguration of the coupling matrix will be considered in the following sections.

4.3 Scaling and Reduction of the Coupling Matrix

As discussed in Section 4.2 and 4.2.2, the coupling matrix is a matrix that can be used to both design and analyze a microwave filter from a prescribed Chebyshev function. As such, there are infinitely many topologies and component values (i.e., capacitances and inductances) that can be used to realize a single prescribed response for an arbitrary center frequency and fractional bandwidth. This is possible with the scaling and the transformation of the coupling matrix.

4.3.1 Scaling of the Coupling Matrix

One of the strongest points of the coupling matrix is that the off-diagonal elements represent the *normalized* admittance inverters and the value of those inverters can be rescaled without altering the frequency response of the network that it characterizes. This operation is equivalent to adjusting the transformer ratios of the input and output to each resonant or to the non-resonant node such that the total transferred energy remains the same [2].

Considering the nth resonant node that is shown in Fig. 4.3 (c), for instance, the amount of energy passing through the inverter $m_{n-1,n}$ is represented by the *coupling coefficient* as:

$$k_{n-1,n} = \frac{m_{n-1,n}}{\sqrt{C_{n-1}C_n}}.$$ (4.19)

As long as this coupling coefficient between the nodes are kept constant, one has the freedom to change the capacitances and the value of the coupling matrix entry $m_{n-1,n}$, without altering the frequency response of the network. Therefore, considering that the new values of $C_{n-1}, C_n,$ and $m_{n-1,n}$, which are denoted by $C'_{n-1}, C'_n,$ and $m'_{n-1,n}$, respectively, the response remains unchanged as long as the following equality is satis-

fied:

$$k_{n-1,n} = \frac{m_{n-1,n}}{\sqrt{C_{n-1}C_n}} = \frac{m'_{n-1,n}}{\sqrt{C'_{n-1}C'_n}}. \tag{4.20}$$

This feature makes it possible to scale the coupling matrix in a way to multiply each row and the column with an arbitrary scaling coefficient α, without altering the response of the matrix. This is depicted in Fig. 4.7 (a). The updated coupling matrix, after the multiplied column and the row is updated, is depicted in Fig. 4.7 (b), which is denoted by an admittance matrix, and corresponds to $[\mathbf{S}] + j[\mathbf{M}]$, as in (4.7).
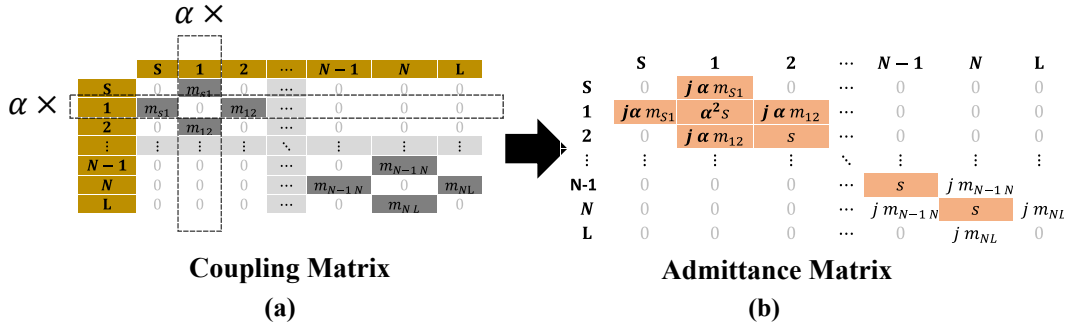
Figure 4.7: Scaling of the coupling matrix. (a): The $(N+2) \times (N+2)$ coupling matrix. (b): The scaled version of the coupling matrix, which is an admittance matrix.

Although replacing the coupling matrix with an admittance matrix as in Fig. 4.7 is not desirable, it will be shown in the synthesis of the extracted poles that this operation can also be performed on the non-resonating nodes without replacing the coupling matrix with an admittance matrix. In that sense, the scaling operation gives a lot of flexibility to the designer to obtain realizable capacitance and/or inductance element values, when required.

4.3.2 Similarity Transformations on the Coupling Matrix

The $(N+2) \times (N+2)$ coupling matrix, as discussed in Section 4.2.2, can be considered as the basis for characterizing an arbitrary Chebyshev function with a CM representa-

tion. However, the transversal coupling matrix and the transversal filter topology is not a practical topology for most applications due to the difficulty of achieving multiple branches of coupling from source to each resonator.

One of the most important realizations, which is widely used for the case of cavity based filter configurations, is the folded topology [15–17]. The coupling-routing diagram and an illustration of the possible non-zero coupling values in the CM of the folded topology are depicted in Fig. 4.8 (a) and (b), respectively.
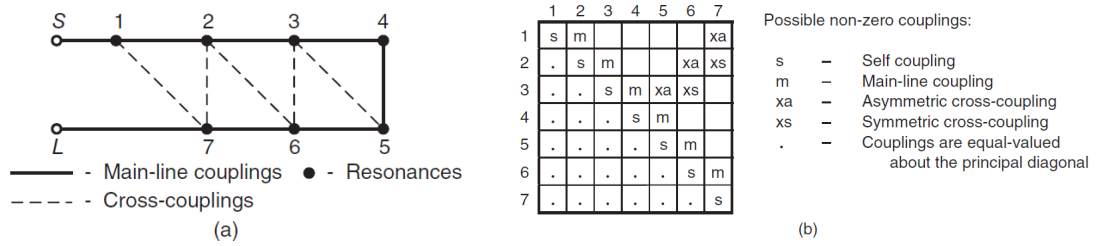
Figure 4.8: (a): The coupling-routing diagram of a seventh order folded topology. The dashed lines represent the possible non-zero coupling paths. (b): The CM representation of the folded topology in (a).These two images are taken from [2].

In order to convert the transversal filter topology into the folded form, one needs to use a set of similarity transformations on the matrix. These similarity transformations are performed in a way to annihilate the transversal connections. They also do not alter the eigenvalues, which result in the characterized response to remain unchanged [2].

The similarity transform on the coupling matrix at stage $(r - 1)$, which is denoted by ($[\mathbf{M_{r-1}}]$), is defined as:

$$[\mathbf{M_r}] = [\mathbf{R_r}] \cdot [\mathbf{M_{r-1}}] \cdot [\mathbf{R_r^T}], \qquad (4.21)$$

where $[\mathbf{R}]$ is the trigonometric rotation matrix with a pivot $[i, j]$ such that $i \neq j$ and a rotation angle θ_r. For the rotation matrices, $R_{ii} = R_{jj} = \cos\theta_r$ and $R_{ij} = -R_{ji} = \sin\theta_r$, given that $i, j \neq 1$ or N. An example rotation matrix with pivot $[3, 5]$ is illustrated for

a seven-by-seven matrix as :

$$
\begin{bmatrix}
1 & 0 & 0 & 0 & 0 & 0 & 0 \\
0 & 1 & 0 & 0 & 0 & 0 & 0 \\
0 & 0 & \cos\theta_r & 0 & \sin\theta_r & 0 & 0 \\
0 & 0 & 0 & 1 & 0 & 0 & 0 \\
0 & 0 & \sin\theta_r & 0 & \cos\theta_r & 0 & 0 \\
0 & 0 & 0 & 0 & 0 & 1 & 0 \\
0 & 0 & 0 & 0 & 0 & 0 & 1
\end{bmatrix},
\tag{4.22}
$$

The similarity transform in (4.21) can be applied on a matrix as many times as desired without altering the frequency response that it characterizes. Using a transform with a pivot $[i, j]$ on $[\mathbf{M_{r-1}}]$ annihilates the elements of $[\mathbf{M_{r-1}}]$ when the rotation angles are given as:

$$
\begin{aligned}
\theta_r &= \tan^{-1}(M_{ik}/M_{jk}) \text{ to annihilate } M_{ik} \\
\theta_r &= -\tan^{-1}(M_{jk}/M_{ik}) \text{ to annihilate } M_{jk} \\
\theta_r &= \tan^{-1}(M_{ki}/M_{kj}) \text{ to annihilate } M_{ki} \\
\theta_r &= -\tan^{-1}(M_{kj}/M_{ki}) \text{ to annihilate } M_{kj}
\end{aligned}
\tag{4.23}
$$

Using the rotation angles with the pivots in (4.23), one can reduce the $(N + 2) \times (N + 2)$ transversal coupling matrix to the folded canonical form in Fig. 4.8 (b) by annihilating the coupling coefficients with the order given in Fig. 4.9.

Figure 4.9: The annihilation sequence to convert a seven-by-seven (5 th order) transversal coupling matrix into the folded topology. This figure is taken from [2].

It should be noted that Fig. 4.9 shows the annihilation sequence of a coupling matrix of a fifth order fully canonical transversal coupling matrix, which includes all possible nonzero elements. The use of this sequence will also be used in the examples in the following subsections.

4.3.3 Interpretation of the Coupling Matrix and Bandpass Transformations

As the coupling matrix charactarizes a filtering response in normalized frequency domain, converting a coupling matrix into a circuit diagram requires one to denormalize the coupling coefficients and the self coupling elements (the FIRs) with respect to the desired center frequency and the fractional bandwidth. The denormalization procedure is achieved with a change of variable $\Omega \rightarrow (1/\Delta)(\omega/\omega_0 - \omega_0/\omega)$ and is derived for the inline filters in [6].

The circuit elements that are being represented by the coupling matrix are depicted in Fig. 4.10 with different color codes. First of all, the kth diagonal element, which is highlighted in red, corresponds to a resonant node and is realized with a parallel tank

circuit including a capacitance of C, an inductance of L, and the FIR element, which represents an admittance and is denoted as b, as observed. The capacitor-inductor pair can attain arbitrary element values as long as they resonate at the desired center frequency ω_0. However, it is best to keep the value of the capacitance (C) uniform among different resonators of the network since this value is required for the denormalization of different elements. This common capacitance value can be called as "reference capacitance". For the resonant node, an FIR has the effect of shifting its resonant frequency from the center frequency.
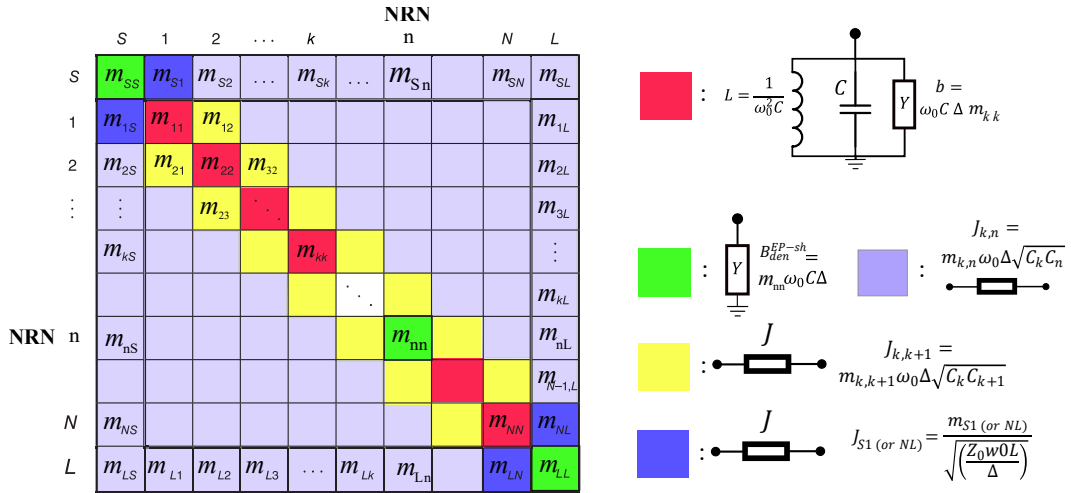
Figure 4.10: The interpretation of the coupling matrix nodes. Red entries indicate the resonant nodes, yellow entries are for inline coupling coefficients, green entries are for source and load admittances, and the purple ones represent the cross-coupling mechanisms. For the equations, ω_0 is the center frequency and Δ represents the desired FBW, and C_k represents the capacitance at the kth node.

In addition to the resonant nodes, the diagonal elements can also include non-resonant nodes (NRN). When there is an NRN, it should be clearly indicated in a way that is similar to the text "NRN" in Fig. 4.10. These nodes contain an FIR element, which is denormalized using the element m_{nn}. As the source and the load nodes are also NRNs, they are shown with green color, just as m_{nn}. In most of the filters, the FIR elements at the source and the load are equivalent to zero, however, it is possible for

80

them to have nonzero values, which is common for the design of the extracted-pole and acoustic-wave filters, in the following chapters.

The coupling coefficients, highlighted with yellow color represent the inline coupling mechanisms and are denormalized using the capacitor values at each end. Again, it is the best to keep these capacitances the same and equal to a single reference capacitance value. Likewise, the coefficients highlighted with purple denote the cross-coupling mechanisms and are denormalized similarly to the inline coupling mechanisms, as shown in Fig. 4.10. Finally, the coefficients that are connecting the elements to either the source or the load are shaded with dark blue and should be calculated separately, using the port impedances, as observed in Fig. 4.10.

4.4 An Example of a Filter Design Using the Coupling Matrix Approach

This example will illustrate the use of the coupling matrix to design an S-band filter using the heavily loaded evanescent-mode cavities that are introduced in Chapter 2. The design requirements for the filter are listed as:

- Bandpass filter having a bandwidth from 2.7 GHz to 3.1 GHz.

- Less than 1 dB of insertion loss within the passband.

- Two of such filters should fit into a square space of 2 inch $\times$ 2 inch,

- 30 dB of rejection at 4 GHz.
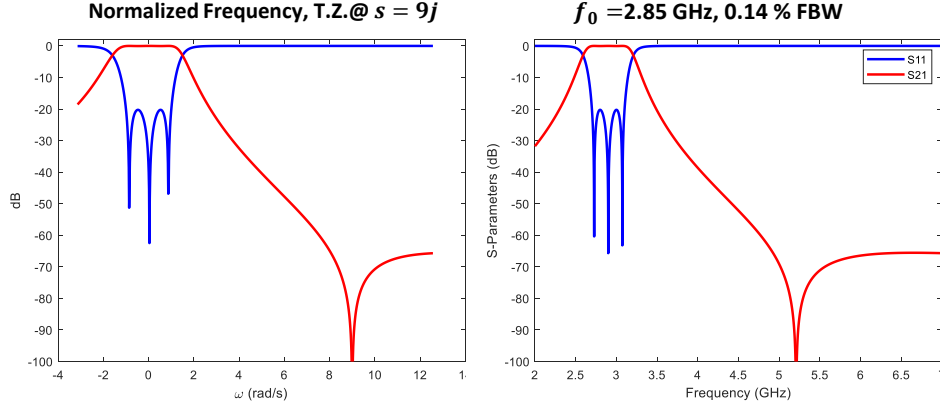
Figure 4.11: The response of the designed 3rd order Chebyshev function with a finite transmission zero at $s = j9$. (a): The normalized-frequency respnse and (b): the denormalized frequency response with $f_0 = 2.85 GHz$ and 14% FBW.

It has been shown in Chapter 2 that the heavily loaded evanescent-mode cavity resonator suffers the issue of the second mode at 5.64 GHz. This results in a second passband around that frequency with a higher insertion loss, which compromises the rejection of the filter. In order to suppress that, a third-order 20-dB equiripple filter response is designed with the algorithm in Chapter 3 to have a normalized-frequency transmission zero location at $s = j9$ rad/s. The S-polynomials of the response are given as:

$$F(s) = s^3 + (-0.056j)s^2 + (0.75)s - 0.028j,$$

$$P(s) = js + 9, \qquad (4.24)$$

$$E(s) = s^3 + (2.4 - 0.056j)s^2 + (3.6 - 0.21j)s + (2.5 - 0.36j),$$

with $\epsilon = 3.5$ and $\epsilon_r = 1$. The normalized-frequency response is provided in Fig. 4.11 (a). The same response is also denormalized for a center frequency of 2.85 GHz and a FBW of 14% and is depicted in Fig. 4.11 (b). The denormalized frequency point of the transmission zero is at 5.2 GHz, as observed. The admittance polynomials of this

network can be obtained using (4.12) and (4.13) as:

$$y_{11_n} = +1.2s^2 + j(-0.1)s + 1.3$$

$$y_{21_n} = +j(0.14)s + 1.3 \qquad (4.25)$$

$$y_d = +1s^3 + j(-0.056)s^2 + 2.2s + j(-0.19)$$

Having a partial fraction expansion on $y_{11}(s)$ and $y_{22}(s)$ makes it possible to write them as:

$$y_{11}(s) = \frac{0.3239}{s + 1.4852j} + \frac{0.2697}{s - 1.4513j} + \frac{0.5936}{s - 0.0896j}$$

$$y_{21}(s) = \frac{-0.3239}{s + 1.4852j} + \frac{-0.2697}{s + 1.4513j} + \frac{0.5936}{s - 0.0896j} \qquad (4.26)$$

Therefore, using the obtained poles and the residues, the transversal coupling matrix can be written as:

$$
[\mathbf{M_{transversal}}] =
\begin{array}{ccccc}
S & 1 & 2 & 3 & L \\
\left[\begin{array}{ccccc}
0 & -0.5691 & -0.5193 & 0.7704 & 0 \\
-0.5691 & 1.4852 & 0 & 0 & 0.5691 \\
-0.5193 & 0 & -1.4513 & 0 & 0.5193 \\
0.7704 & 0 & 0 & -0.0896 & 0.7704 \\
0 & 0.5691 & 0.5193 & 0.7704 & 0
\end{array}\right]
\begin{array}{c}
S \\ 1 \\ 2 \\ 3 \\ L
\end{array}
\end{array} . \quad (4.27)
$$

Following the transversal coupling matrix, the following set of similarity transformations with a rotation angle $\theta_r = \arctan(cM_{kl}/M_{mn})$ needs to be carried out to convert it into the folded topology:

- Annihilate $M_{S,3}$ with $k = 4$, $l = 4$, $m = 1$, $n = 3$, and $c = -1$,

- Annihilate $M_{2,3}$ with $k = 4$, $l = 3$, $m = 1$, $n = 2$, and $c = -1$,

- Annihilate $M_{3,5}$ with $k = 3$, $l = 5$, $m = 4$, $n = 5$, and $c = +1$,

After the annihilation of the elements, the folded CM is shown as:

$$[\mathbf{M_{folded}}] = \begin{matrix} & S & 1 & 2 & 3 & L & \\ \begin{bmatrix} 0 & 1.09 & 0 & 0 & 0 \\ 1.09 & 0.031 & -1.034 & 0.120 & 0 \\ 0 & -1.034 & -0.117 & -1.034 & 0 \\ 0 & 0.120 & -1.034 & 0.031 & 1.090 \\ 0 & 0 & 0 & 1.090 & 0 \end{bmatrix} & \begin{matrix} S \\ 1 \\ 2 \\ 3 \\ L \end{matrix} \end{matrix}. \qquad (4.28)$$

There are multiple points that need to be taken into consideration in the folded CM of (4.28). First of all, the diagonal elements are nonzero except for the source and the load. This means that the resonators should not be tuned to resonate at f_0. This is referred to as *asynchronous tuning* [2]. As observed, the FIR elements $m_{1,1}$ and $m_{3,3}$ are equivalent and positive in sign (capacitive) and $m_{2,2}$ is negative, meaning that it is inductive. It should also be noticed that the entries $m_{S,1}$ and $m_{1,2}$ have opposite signs, meaning that one of them should be an electric-field coupling while the other one should be a magnetic-field coupling. Having coupling mechanisms of opposite sign is referred to as *mixed coupling* in literature [2].
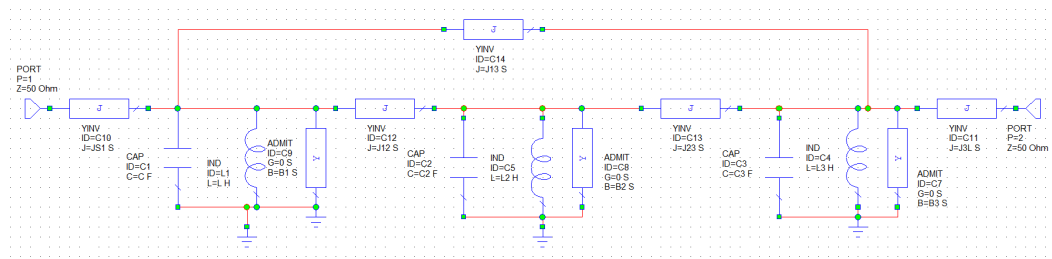
Figure 4.12: Circuit diagram obtained from the folded CM in 4.28 .

The folded coupling matrix can be converted into a filter network with $f_0 = 2.89$ GHz and $\Delta = 13.8\%$ as described in Fig. 4.10 and in Section 4.3.3. The circuit diagram of this filter network is constructed in Cadence AWR and is depicted in Fig. 4.12. For this folded filter network, the element values are calculated as follows:

- $C_i = 1$ pF (reference capacitance),

- $L_i = \frac{1}{\omega_0^2 C_i}$, for $i \in \{1, 2, 3\}$,

- $B_i = m_{i,i}\omega_0 C_i \Delta$, for $i \in \{1, 2, 3\}$,

- $J_{i,j} = m_{i,j}\omega_0 \Delta \sqrt{C_i C_j}$ for $i, j \in \{1, 2, 3\}$,

- $J_{S,1} = m_{S,1}/\sqrt{50 \cdot w_0 \cdot L_1/\Delta}$, and

- $J_{3,L} = m_{3,L}/\sqrt{50 \cdot w_0 \cdot L_3/\Delta}$.

While this network can be realized with lumped elements, the design is intended to be incorporated to the antenna laminate stackup of the Horus radar and is implemented within the Rogers 4350B layers of thicknesses 1.52 mm and 0.17 mm. More details of the radar and the laminates can be found in [62].

The resonator technology that is used for implementation is the described evanescent-mode-cavity based resonators in Chapter 2. According to the coupling matrix, three evanescent-mode cavities are designed. The first and the third resonators are set to resonate at 2.887 GHz while the middle resonator resonates at 2.916 GHz.

The Ansys HFSS simulation model of these three resonators are depicted in Fig. 4.13 (a). As observed in the exploded view in Fig. 4.13 (b), the input and output connections of the filter are ground-backed co-planar waveguide (GCPW) sections. These waveguide sections (slots) are extended into the cavity resonators as branching slotlines to realize the magnetic-field coupling between input-to-the-first-resonator and the
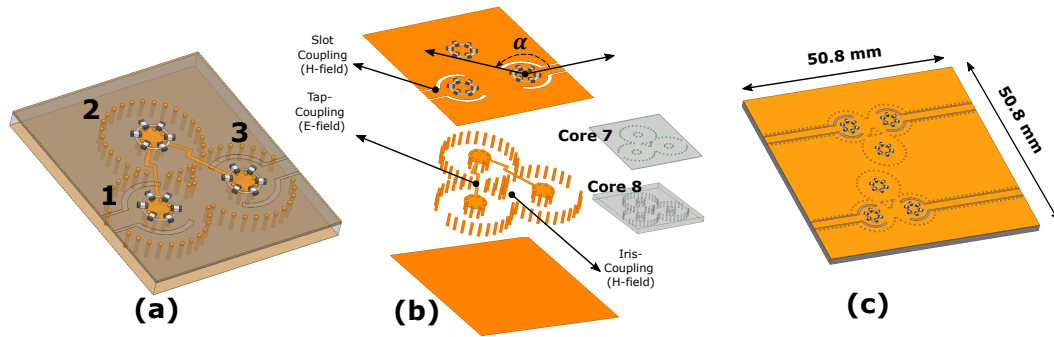
Figure 4.13: (a): The HFSS model of the designed third-order filter. (b): The exploded view of the filter. Core 7 and Core 8 correspond to the order of the antenna stackup layers in which the filter is placed. (c): Two filters fitted into a single element of the antenna panel. This image is taken from the publication of the author in [62].

output-to-the-third-resonator. The coupling strength can be adjusted by changing the angle α, which adjusts the extent to which the slots are extended into the cavity. The main-line coupling between resonators 1 and 2 and 2 and 3 are accomplished by tap-coupling, as observed in Fig. 4.13 (b). Finally, the cross-coupling between the resonators 1 and 3 is obtained with a narrow inductive iris between them, as also depicted in Fig. 4.13 (b). The magnetic coupling from the inductive iris has the opposite sign of the coupling between the main-line-coupling mechanisms, as enforced by the coupling matrix. Fig. 4.13 (c) demonstrates a pair of the designed third-order filters fitted within a single element of the bottom two layers of the Horus antenna panel.

As a proof of concept, the filter pair in Fig. 4.13 (c) is fabricated using two Rogers Corp. RO4350B substrates with thicknesses of 1.52 mm and 0.17 mm, which are patterned using photolithography and wet etching processes. The fabricated prototype is depicted in Fig. 4.14. For the discrete capacitors on the top post, surface-mount high-Q capacitors from AVX Corp. are used. As the excitation slots interfere with the resonant frequencies of the first and third resonators, the common capacitance value of the capacitors on the middle resonator is different than that of the first and third resonators. The common capacitance value is 0.55 pF on the first and third resonators, whereas the

middle resonator is loaded with 1.0 pF capacitors.
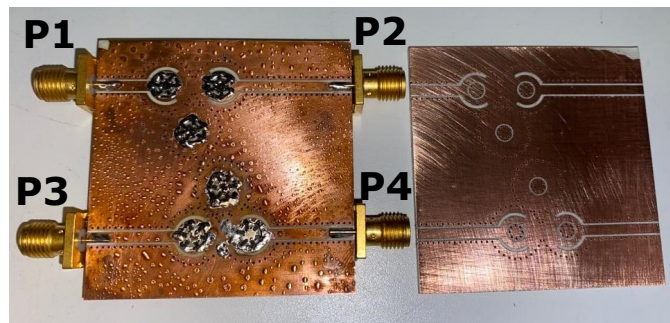
Figure 4.14: Fabricated prototype of the filter. To show the outcome of the lithography, another prototype without the loading capacitors and the SMA connectors is also depicted. P1–P4 denote the port numbers of the four port network in the single antenna element. This image is taken from the publication of the author in [62].

The measured results of the fabricated filter pair prototype are depicted and compared to the simulation results in Fig. 4.15. As observed, the magnitude response of the prototypes (denoted as channel 1 and channel 2) in Fig. 4.15 (a) agree well with the simulated results at the lower band edge, however, the bandwidth of the measured prototype is slightly narrower than in simulation. This is mainly due to the fabrication tolerance of the strips that are used for inter-resonator coupling. The undercut from wet etching results in thinner strips than expected, and that reduces the inter-resonator coupling between resonators 1-2 and 2-3. This yields a narrower bandwidth than expected. The insertion loss of the prototype is measured as 0.86 dB, which agrees well with that of the simulations.
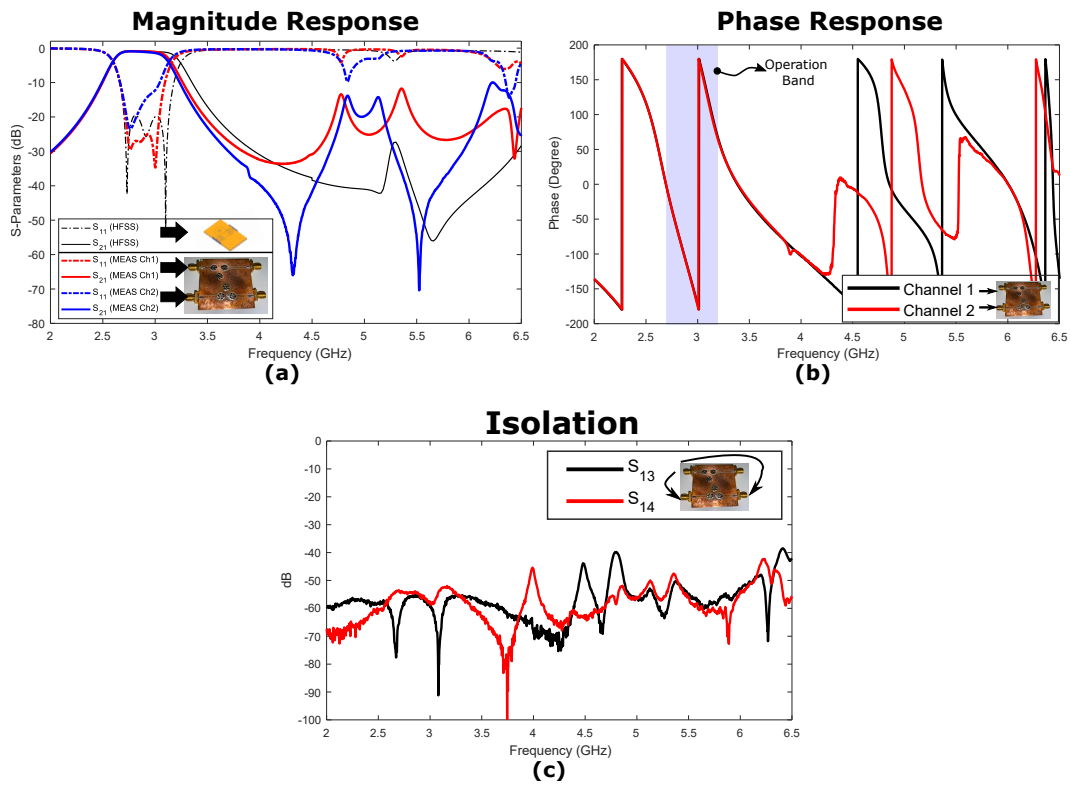
Figure 4.15: Summary of the achieved filter pair performance. (a) A comparison of the measured and simulated S-parameters of both channels of the filter pair. (b) The measured phase response of both channels with the operation band of the radar system highlighted. (c) The measured isolation between the separate channels of the filter pair. This image is taken from the publication of the author in [62].

As these filters are designed to be connected to the transceiver channels, proper phase matching is important for the phased array calibration. As observed in Fig. 4.15 (b), the measured phase responses of the both channels are in very good agreement within the frequency range of 2 GHz to 4 GHz, which covers the band of operation. Finally, the cross-coupling between the two channels needs to be as low as possible in order to prevent increased cross-polarization components. As observed in Fig. 4.15 (c), the isolation between the filter ports is better than 40 dB for the frequency range of 2 GHz to 6.5 GHz.

88

4.5 Summary and Conclusions

This chapter introduced the analysis and the synthesis of one of the strongest filter design methodologies, the coupling matrix theory. The methodology of obtaining the transversal coupling matrix has been discussed extensively and the methods to convert this topology to the more useful folded version is discussed. A real application example of the use of the coupling matrix for the design of a third-order filter with a single transmission zero for the Horus antenna panel is discussed.

The coupling matrix will be used extensively in the design of the filters based on acoustic-wave resonators and the *hybrid acoustic-electromagnetic (Hybrid-ACEM)* filters. Therefore, understanding what each coupling matrix entry means and the connection between the coupling matrix and a circuit prototype is important.

Chapter 5

Circuit and Extracted-Pole-Synthesis Methods

5.1 Introduction and Background

The folded and transversal based topologies form the basis of the CM-based microwave filter synthesis and many different filter topologies including Pfitzenmainer, Cul-de-Sac, arrow, can be synthesized from these two matrices using a series of similarity transformations, as described in Chapter 4.

However, not all the topologies can be obtained using matrix transformations. In addition to being obtained by matrix rotations, there are several other topologies realizing arbitrary-position transmission zeros, including trisections [85, 86] and N-tuplets [87, 88]. These all use N electromagnetic resonant nodes to realize the poles and inter-resonator coupling mechanisms to generate the transmission zeros. Furthermore, there are very limited studies to obtain these configurations from the transversal or the folded topologies by matrix rotations.

One approach that can achieve an arbitrary number of transmission zeros *without* using inter-resonator coupling is the use of extracted-poles [89–99]. The extracted pole method is one of the topologies which does not have an established algorithm to be obtained from the folded or the transversal CMs. The earliest works on this concept dates back to 1980s by John Rhodes and Richard Cameron, which included the use of

cavities [89]. This approach was also patented in 1982 [92].

In the most general terms, an extracted pole element is a network that includes a resonant node coupled to a non-resonant node. This element, as opposed to a single resonating node, produces a series and a parallel resonance, which is used to provide one pole and one transmission zero to a filter response. Therefore, the use of extracted poles is an alternative method to using cross-coupling to create transmission zeros in a microwave filter implementation. The advantage of that is to design *inline* filters of Nth order with an arbitrary number of transmission zeros up to N, which corresponds to the fully canonical case.
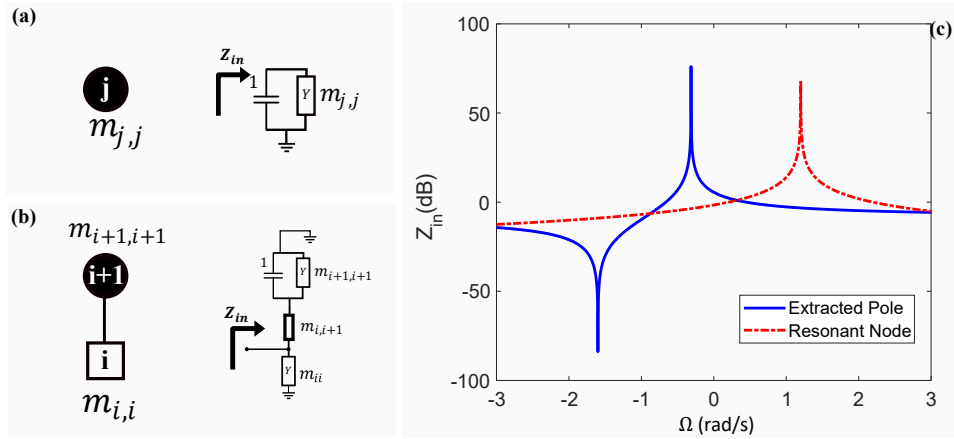
Figure 5.1: (a) and (b): Coupling-routing and normalized-frequency circuit representation of a resonant node and an extracted pole, respectively. (c): Normalized frequency response comparison of the EP and the resonant node.

As it has been extensively discussed in Chapter 4, the resonant nodes in the coupling matrix are the building blocks of a coupled-resonator filter. The coupling-routing diagram of a resonant node is depicted in Fig. 5.1 (a) along with its normalized-frequency circuit representation. An extracted pole is also depicted with its coupling-routing diagram and the normalized-frequency circuit in 5.1 (b). The input impedance to each of these networks are also shown in Fig. 5.1 (c). As observed, the resonator has a single peak impedance value at the resonant frequency whereas the extracted pole has a series

91

and a parallel resonance, depending on the values of the elements.

The following sections will consider how one can use the network-synthesis and the extracted-pole approaches to design filters with extracted poles.

5.2 Network-and-Extracted-Pole-Synthesis Approaches

The network-synthesis approach is based on obtaining the ABCD polynomials of the response from its S-polynomials and then extracting the resonant nodes and the cross-coupling mechanisms one-by-one until the last element in the network is extracted. The details and derivations of the extraction processes are examined in [2] and rather than focusing on the derivations, this chapter will examine the processes of extracting the nodes in a network.

The S-polynomials of a response were given in (3.1) in Chapter 3. In order to synthesize a network based on extracted poles, one should switch from the S-polynomials into the ABCD-polynomials, which can be characterized as:

$$[ABCD]_{Full}(s) = \frac{1}{jP(s)/\epsilon} \cdot \begin{bmatrix} A(s) & B(s) \\ C(s) & D(s) \end{bmatrix}, \qquad (5.1)$$

where, $A(s), B(s), C(s)$, and $D(s)$ correspond to the numerator of the ABCD polynomials, which have the common denominator $jP(s)/\epsilon$. These polynomials can be obtained from the polynomial coefficients of the functions $E(s)$ and $F(s)$. For even-

order case [2],

$$A(s) = jIm(e_0 + f_0) + Re(e_1 + f_1)s + jIm(e_2 + f_2)s^2 + ... + jIm(e_N + f_N)s^N,$$

$$B(s) = Re(e_0 + f_0) + jIm(e_1 + f_1)s + Re(e_2 + f_2)s^2 + ... + Re(e_N + f_N)s^N,$$

$$C(s) = Re(e_0 - f_0) + jIm(e_1 - f_1)s + Re(e_2 - f_2)s^2 + ... + Re(e_N - f_N)s^N,$$

$$D(s) = jIm(e_0 - f_0) + Re(e_1 - f_1)s + jIm(e_2 - f_2)s^2 + ... + jIm(e_N - f_N)s^N,$$

(5.2)

and for the odd-order case [2],

$$A(s) = Re(e_0 + f_0) + jIm(e_1 + f_1)s + Re(e_2 + f_2)s^2 + ... + Re(e_N + f_N)s^N,$$

$$B(s) = jIm(e_0 + f_0) + Re(e_1 + f_1)s + jIm(e_2 + f_2)s^2 + ... + jIm(e_N + f_N)s^N,$$

$$C(s) = jIm(e_0 - f_0) + Re(e_1 - f_1)s + jIm(e_2 - f_2)s^2 + ... + jIm(e_N - f_N)s^N,$$

$$D(s) = Re(e_0 - f_0) + jIm(e_1 - f_1)s + Re(e_2 - f_2)s^2 + ... + Re(e_N - f_N)s^N.$$

(5.3)

Obtaining the ABCD-polynomials of the network from the S-polynomials is the first step in the synthesis of a network. This will be followed by a sequence of extractions in the pathway of obtaining a normalized lowpass network from the polynomials.

5.2.1 Extraction of Circuit Elements

Once the ABCD polynomials are obtained, one needs to extract the circuit components for a normalized lowpass filter network to obtain the desired filter from it. In that sense, the extractions are carried out consequtively. At each step of extraction, the initial ABCD matrix is denoted as $[\mathbf{ABCD}]_\mathbf{I}$ and the matrix after the extraction is denoted as $[\mathbf{ABCD}]_{\mathbf{rem}}$, which is depicted in Fig. 5.2.

(a)   **(b)**

$$\begin{bmatrix} A(s) & B(s) \\ C(s) & D(s) \end{bmatrix}$$ $$\begin{bmatrix} A_{rem}(s) & B_{rem}(s) \\ C_{rem}(s) & D_{rem}(s) \end{bmatrix}$$
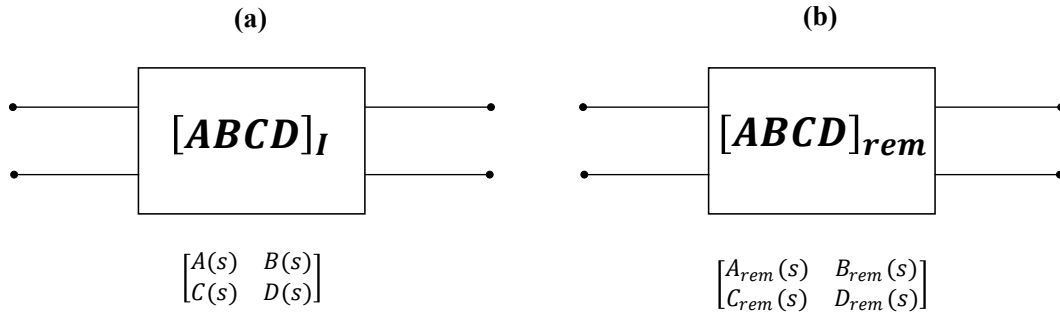
Figure 5.2: (a): The initial ABCD matrix to extract a circuit element from the network and (b): The remainder ABCD matrix after extracting the desired element from the network.

At step i, one can extract an admittance inverter with a value of Y_0, a capacitance of value C_i, an FIR element of value jB_i, or a cross-coupling inverter M_{cross} between the input and the output of the network section that is characterized by $[\mathbf{ABCD}]_{\mathrm{I}}$. These extractions are depicted in Fig. 5.3. Each extraction step modifies the polynomials $A(s), B(s), C(s), D(s)$ and possibly $P(s)$, depending on which element is being extracted. When an admittance inverter is being extracted, one can determine the value of the inverter as in Fig. 5.3 (a). However, the value of capacitance, FIR element, or cross coupling inverter cannot be arbitrarily chosen, as depicted in (b), (c), and (d) of the same figure. The remainder ABCD polynomials after the extraction of each element are also depicted in the same figure.

(a)

$A_{rem}(s) = A(s)\cos\phi - jC(s)\sin\phi/Y_0$
$B_{rem}(s) = B(s)\cos\phi - jD(s)\sin\phi/Y_0$
$C_{rem}(s) = C(s)\cos\phi - jA(s)Y_0\sin\phi$
$D_{rem}(s) = D(s)\cos\phi - jB(s)Y_0\sin\phi$
$P_{rem}(s) = P(s)$

When $\phi = \pi/2$ and $Y_0 = 1$ (a unit inverter), this simplifies to

$A_{rem}(s) = -jC(s)$
$B_{rem}(s) = -jD(s)$
$C_{rem}(s) = -jA(s)$
$D_{rem}(s) = -jB(s)$
$P_{rem}(s) = P(s)$

(b)

$C_i = \left.\dfrac{D(s)}{sB(s)}\right|_{s=j\infty} = \left.\dfrac{C(s)}{sA(s)}\right|_{s=j\infty}$

$A_{rem}(s) = A(s)$
$B_{rem}(s) = B(s)$
$C_{rem}(s) = C(s) - sC_iA(s)$
$D_{rem}(s) = D(s) - sC_iB(s)$
$P_{rem}(s) = P(s)$

(c)

$B_i = \left.\dfrac{D(s)}{B(s)}\right|_{s=j\infty}$ or $\left.\dfrac{C(s)}{A(s)}\right|_{s=j\infty}$

$A_{rem}(s) = A(s)$
$B_{rem}(s) = B(s)$
$C_{rem}(s) = C(s) - B_iA(s)$
$D_{rem}(s) = D(s) - B_iB(s)$
$P_{rem}(s) = P(s)$

(d)

$M_{ij} = \left.-\dfrac{P(s)}{B(s)}\right|_{s=j\infty}$

$A_{rem}(s) = A(s)$
$B_{rem}(s) = B(s)$
$P_{rem}(s)/\varepsilon = P(s)/\varepsilon + M_{ij}B(s)$

$C_{rem}(s) = C(s) + 2M_{ij}P(s)/\varepsilon + M_{ij}^2B(s)$
$D_{rem}(s) = D(s)$

Figure 5.3: The extraction process of the several network elements from the known ABCD polynomials of a Chebyshev function. (a): Extraction of an admittance inverter with a value of Y_0 and a phase length θ. (b): Extraction of a capacitance element, (c): Extraction of an FIR element, and (d): Extraction of a cross-coupling mechanism. This figure is taken from [2].

Using these extraction procedures for several circuit elements, the resonant nodes, non-resonant-nodes, and the extracted poles of the network can be obtained. The extraction is not performed randomly and it should be done following the rules that will be discussed in the next section.

5.2.2 Extraction of the Network

The extraction sequence of the network elements depend on N, N_{TZ}, the desired number of extracted-poles in the network, which is defined as N_{EP}, and the order of the elements in the network. The initial $A(s)$ and $D(s)$ are of degree $N - 1$, $B(s)$ is of degree N, $C(s)$ is of degree $N - 2$ except for the fully canonical case where $C(s)$ is of degree N [2]. N_{EP}, is determined by the designer. In addition, $P(s)$ is always of degree N_{TZ}.

As a clarification, M is used as the coupling coefficients during circuit extraction, m_{ij} is used solely for the coupling matrix entries, and J_{ij} is used to denote the denormalized admittance inverter values with respect to the center frequency and fractional bandwidth.

For the design of a network, the following rules need to be followed:

- Start the extraction from either source or the load nodes.

- If $N = N_{TZ} = N_{EP}$, all the nodes should be extracted poles.

- If $N > N_{TZ} = N_{EP}$, there will be resonators in the network in addition to extracted poles, however, no cross-coupling is needed.

- If $N > N_{TZ} > N_{EP}$ or $N = N_{TZ} = N_{EP}$, there will be both resonators and extracted poles in the network.

- If $deg(P(s)) = deg(B(s))$, one should extract either an EP or a cross-coupling inverter.

- Therefore, if $N = N_{TZ} = N_{EP}$ (fully canonical case including both resonators and EPs), a source-to-load coupling is required since $deg(P(s)) = deg(B(s))$ in the begining of the extraction process.
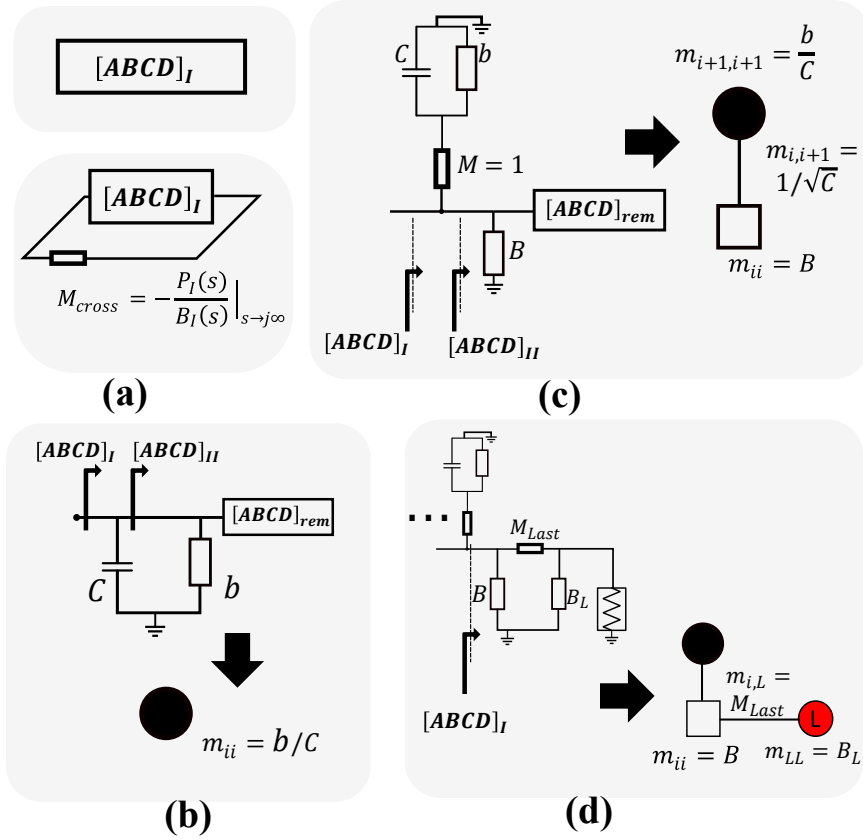
Figure 5.4: Summary of the extraction procedure: (a): The two-port network charecterized by its ABCD polynomials, that will be used for extraction. Also the extraction of a cross-coupling inverter. (b): Extraction of a resonant node. (c): Extraction of an EP section. (d): Extraction of the load and the last node, when the last section is an EP.

- For the shunt $sC + jB$ pairs (resonant nodes), extract the capacitance first.

- When the degree of $P(s)$ and $B(s)$ are equal, a cross coupling inverter should be extracted following the full extraction of a resonant node. Therefore, for the fully canonical filters, an S-L cross-coupling extraction is required first.

- If the last node before the load is a resonator, the last element should be a cross-coupling inverter.

- On the other hand, if the last node is an extracted pole, the extraction of the last node will be described in the following paragraphs with the help of Fig. 5.4 (d).

At each step, depending on whether a resonant-node, an EP, or the last node is being extracted, Fig. (5.4) depicts the required procedure. Considering that the network to start with at the current step of the extraction is characterized by $[ABCD]_I(s)$:

A cross-coupling inverter can be extracted as:

$$M_{cross} = -\frac{P_I(s)}{B_I(s)}\Big|_{s\to j\infty},$$ (5.4)

as observed in Fig. 5.4 (a). This operation can reduce the degree of $P(s)$ by either one or two (creating one or two zeros), latter being special for the case of symmetrical functions.

A resonant node as in Fig. 5.4 (b), can be extracted by obtaining the capacitance as:

$$C = \frac{D_I(s)}{sB_I(s)}\Big|_{s\to j\infty},$$ (5.5)

followed by the FIR element as:

$$b = \frac{D_{II}(s)}{B_{II}(s)}\Big|_{s\to s_{next}},$$ (5.6)

where s_{next} is the position of the transmission zero that will be implemented at the next step of the extraction. If the next node to be extracted after this resonant node is another resonant node, the transmission zero is at infinity and $s_{next} = j\infty$. If the next section is an EP, then s_{next} should attain the position of that finite transmission zero. To use the resonant node in a coupling matrix, it is required to normalize the capacitance to one, which results in the normalized FIR value of $m_{i+1,i+1} = b/C$. Furthermore, it is important to multiply each coupling element connected to this resonant node by $1/\sqrt{C}$ to make the node compatible with the coupling matrix.

An extracted-pole as in Fig. 5.4 (c), which produces a transmission zero at $s = s_i$

can be obtained from the residue of the pole given by:

$$r = \left.\frac{D_I(s)}{B_I^x(s)}\right|_{s=s_i}, \text{ where } B_I^x(s) = \frac{B_I(s)}{s - s_i}. \tag{5.7}$$

Using this residue, the extracted pole elements are obtained as:

$$C = \frac{1}{r} \text{ and } b = \frac{-s_i}{r}. \tag{5.8}$$

When converting these elements for coupling matrix representation, the node is scaled by the value of the capacitance, resulting in the FIR to obtain the value $-s_i$ and the coupling coefficient between the resonant and the non-resonant node in Fig. 5.4 (c) $(m_{i,i+1})$ to attain a value of $1/\sqrt{C}$.

The last element in the EP of Fig. 5.4 (c), being the shunt FIR (B) is obtained as:

$$B = \left.\frac{D_{II}(s)}{B_{II}(s)}\right|_{s \to s_{next}}, \tag{5.9}$$

where s_{next} is the normalized frequency point of the next transmission zero to be extracted.

The source has a nonzero admittance (B_S) if the first node is going to be an EP. That admittance is extracted using (5.9) and setting s_{next} as the normalized TZ position of the first extracted pole. However, if the first node is a resonant node, no source admittance is extracted.

The last node of the design is extracted depending on whether the last node before the load is an EP section or a resonant node. If the last node is a resonant node, there is no load admittance and the last node-to-load coupling can be extracted as a cross-coupling, as in Fig. 5.4 (a). On the other hand, if the last node is an EP, as in Fig. 5.4 (d), one needs to extract it as a cross-coupling element M_{Last} as follows: Extract a shunt

admittance at infinity (B in Fig. 5.4 (d)), flip the network (interchange $A(s)$ and $D(s)$), and extract another admittance at infinity, which obtains the load admittance (B_L).

Regarding the extraction procedure described throughout this section, the only way to understand it is through multiple examples to illustrate.

5.2.3   Examples for Illustration

This section will synthesize three different networks with and without the use of extracted poles. A 4th order 15-dB equiripple response will be used for synthesis and is characterized as:

$$F(s) = +1s^4 + 1.1s^2 + 0.16$$
$$P(s) = -1s^4 - 19s^2 - 41$$
$$E(s) = +1s^4 + 1.6s^3 + 2.4s^2 + 1.8s + 0.91$$

$$\text{with } \epsilon = 45.5 \text{ and } \epsilon_r = 1.0002.$$

(5.10)

These S-polynomials are converted into ABCD-polynomials, which can be shown as:

$$A(s) = +1.6s^3 + 1.8s$$
$$B(s) = +2s^4 + 3.5s^2 + 1.1$$
$$C(s) = +0.0002s^4 + 1.3s^2 + 0.75$$
$$D(s) = +1.6s^3 + 1.8s$$

(5.11)

It should be noticed that this is a symmetric and a fully-canonical response, which results in the odd-order coefficients in $P(s)$ and $B(s)$ to vanish. The following three different networks will be synthesized to realize this function:

1. Folded canonical network with no extracted poles.

2. Two extracted poles and two cross-coupling mechanisms, and

3. Four extracted poles and no cross-coupling mechanisms.

Example 1: Folded Canonical Synthesis

The initial topology that will be synthesized is the folded canonical prototype, which can also be obtained using the similarity transformations on the transversal coupling matrix. It will be synthesized with the network-synthesis approach only in order to show that it is also capable of obtaining this topology.
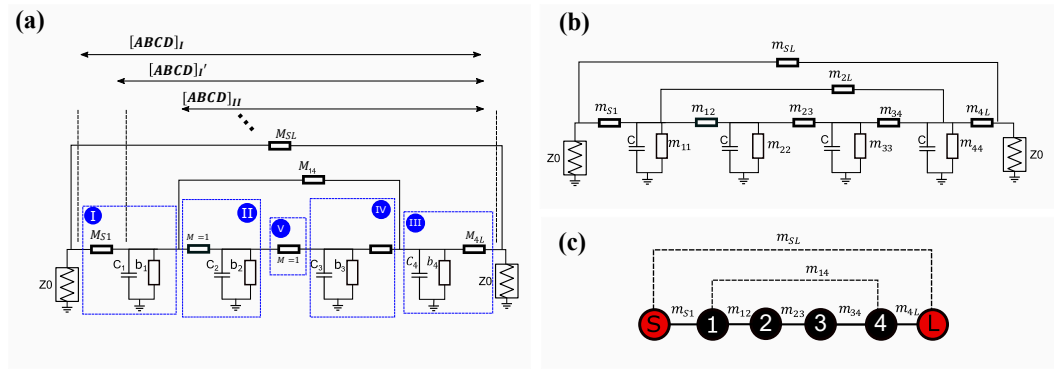
Figure 5.5: Extraction of Example 1. (a): The extraction sequence and the boxes for the folded-coupling matrix extraction. (b): The circuit diagram representing the CM to be synthesized, (c): The coupling-routing diagram.

The synthesis of this network is depicted in Fig. 5.5 (a) with the enumerated boxes. The steps of the synthesis are listed as follows:

- **S-L Coupling:** Since the response is fully canonical, $deg(P(s) = deg(B(s))$, therefore, an S-L coupling should be extracted using:

$$M_{SL} = -\frac{P_{initial}(s)}{B_{initial}(s)}\bigg|_{s=j\infty}. \tag{5.12}$$

101

The updated $P(s)$ after this operation is given as:

$$P_{updated}(s) = -17s^2 - 40, \tag{5.13}$$

which is of second degree. Normally, a single cross-coupling reduces the degree of $P(s)$ by one, however, for the special case of symmetric responses, it reduces that by two and produces a symmetric pair of transmission zeros.

- **Box I:** Extract unit inverter as described in Fig. 5.3 and obtain C_1, followed by the FIR b_1 using

$$C_1 = \left.\frac{D_I'(s)}{sB_I'(s)}\right|_{s=j\infty} \quad \text{and} \quad b_1 = \left.\frac{D_I''(s)}{B_I''(s)}\right|_{s=j\infty}, \tag{5.14}$$

where $D_I'(s)$ and $B_I'(s)$ are the D and B polynomials of the network once the unit inverter is removed and $D_I''(s)$ and $B_I''(s)$ refer to the ones after C_1 is extracted. Once C_1 and b_1 are extracted, $[ABCD]_{II}(s)$ is obtained. This gives $C_1 = 1.23$ F and $b_1 = 0$ S. After that, flip the network by exchanging $A(s)$ and $D(s)$ polynomials.

- **Box II:** With the flipped network, the propagation is from the load towards the source this time. Similar to Box I, extract a unit inverter M_{4L}, followed by C_4 and b_4, which gives $C_4 = 1.23F$ and $b_4 = 0$ S.

- **Cross-Coupling** After extracting Box IV, the ABCD polynomials are given as:

$$A(s) = -0.92s$$

$$B(s) = -1.3s^2 - 0.73$$

$$C(s) = -0.1s^2 - 1.1 \tag{5.15}$$

$$D(s) = -0.92s$$

$$P(s) = -17s^2 - 40,$$

which means that the degree of $P(s)$ and $B(s)$ are both two at this stage. There-fore, another cross-coupling extraction is needed to obtain M_{14}.

- **Box III:** Similar to Box I, extract a unit inverter, M_{14} and extract C_3 and b_3. Flip the network again to go towards Box II.

- **Box IV:** Similar to Box I, extract a unit inverter, M_{14} and extract C_3 and b_3.

- **Box V:** The final step in the extraction process is to obtain the value of the last admittance inverter using the extraction method of an inter-resonator coupling with a transmission zero at infinity, which is given as:

$$M_{23} = -\frac{P_V(s)}{B_V(s)}\bigg|_{s=j\infty}. \tag{5.16}$$

Once all the elements are extracted, the capacitance values are given as: $C_1 = C_4 = 1.23$ F, $C_2 = C_3 = 1.44$ F, the FIR element values are obtained as: $b_1 = b_2 = b_3 = b_4 = 0$ S. In addition, the coupling elements are given as $M_{S1} = M_{12} = M_{34} = M_{4L} = 1$ S. The non-unit inverters are the ones that are obtained using cross-coupling extraction, which are given as: $M_{SL} = 0.01$ S, $M_{24} = -0.28$ S, and $M_{23} = 1.072$ S. These values correspond to the elements that are given in Fig. 5.5 (a). Using these elements, the

admittance matrix of the network can be obtained as shown in (5.17).

$$[\mathbf{Y}] = \begin{array}{c} \\ \\ \\ \\ \end{array} \begin{matrix} & \times(1/\sqrt{C_1}) & \times(1/\sqrt{C_2}) & \times(1/\sqrt{C_3}) & \times(1/\sqrt{C_4}) \\ \mathbf{S} & \mathbf{1} & \mathbf{2} & \mathbf{3} & \mathbf{4} & \mathbf{L} \\ \begin{bmatrix} 0 & 1.00 & 0 & 0 & 0 & 0.01 \\ 1.00 & (1.23j)s & 1.00 & 0 & -0.28 & 0 \\ 0 & 1.00 & (1.44j)s & 1.07 & 0 & 0 \\ 0 & 0 & 1.07 & (1.44j)s & 1.00 & 0 \\ 0 & -0.28 & 0 & 1.00 & (1.23j)s & 1.00 \\ 0.01 & 0 & 0 & 0 & 1.00 & 0 \end{bmatrix} & \begin{matrix} \mathbf{S} \\ \mathbf{1} \rightarrow \times(1/\sqrt{C_1}) \\ \mathbf{2} \rightarrow \times(1/\sqrt{C_2}) \\ \mathbf{3} \rightarrow \times(1/\sqrt{C_3}) \\ \mathbf{4} \rightarrow \times(1/\sqrt{C_4}) \\ \mathbf{L} \end{matrix} \end{matrix} \quad (5.17)$$

In order to obtain the coupling matrix of the network, one needs to normalize all the capacitances to unity. This can be obtained using the scalability feature of the admittance inverters of the network. To normalize each of the capacitances, a node scaling is required at nodes 1, 2, 3, and 4. In other words, each row and column i of (5.17) should be multiplied by $1/\sqrt{C_i}$ for $i \in 1, 2, 3, 4$, as depicted in (5.17). After that, the folded canonical coupling matrix of the network is depicted in (5.18).

$$[\mathbf{M_{Folded}}] = \begin{matrix} \mathbf{S} & \mathbf{1} & \mathbf{2} & \mathbf{3} & \mathbf{4} & \mathbf{L} \\ \begin{bmatrix} 0 & 0.90 & 0 & 0 & 0 & 0.01 \\ 0.90 & 0 & 0.75 & 0 & -0.23 & 0 \\ 0 & 0.75 & 0 & 0.74 & 0 & 0 \\ 0 & 0 & 0.74 & 0 & 0.75 & 0 \\ 0 & -0.23 & 0 & 0.75 & 0 & 0.90 \\ 0.01 & 0 & 0 & 0 & 0.90 & 0 \end{bmatrix} & \begin{matrix} \mathbf{S} \\ \mathbf{1} \\ \mathbf{2} \\ \mathbf{3} \\ \mathbf{4} \\ \mathbf{L} \end{matrix} \end{matrix} \quad (5.18)$$

The normalized-frequency network and the coupling-routing diagram of (5.18) are depicted in Fig. 5.5 (b) and (c), respectively.

104

Example 2: Topology with EPs and Resonators

This topology is a different topology that includes both extracted poles, resonators, and cross-coupling to obtain the response. The possibility of having this approach is introduced in [90], however, no filter application or a fabrication was included. This section will demonstrate how to synthesize this topology and it will be a key synthesis in the design of the novel hybrid acoustic-electromagnetic filters in the following chapters.

The steps of the synthesis are depicted in Fig. 5.6 (a). To synthesize this network, again, one needs to check the ABCD parameters of the network which shows that the degree of $P(s)$ and $B(s)$ are equivalent. As the degree of both are equal to 4, again, the extraction starts with a cross-coupling inverter and has the same value as in the previous example.
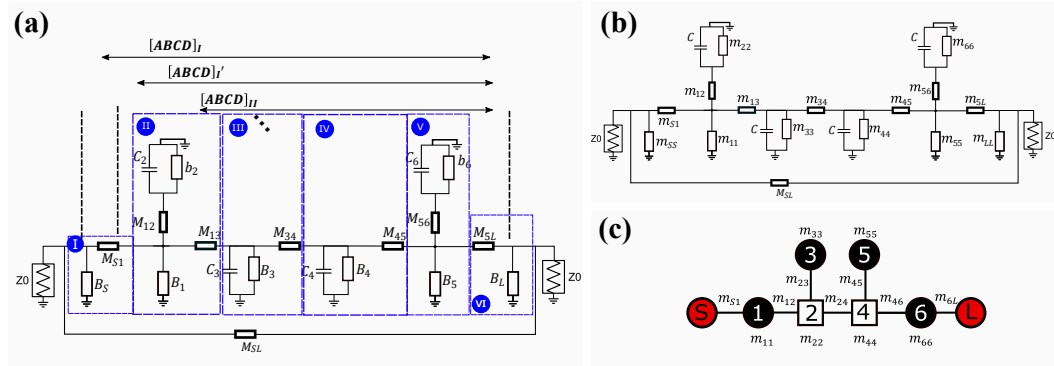
Figure 5.6: Extraction of Example 2. (a): The extraction sequence and the boxes for the folded-coupling matrix extraction. (b): The circuit diagram representing the CM to be synthesized, (c): The coupling-routing diagram.

The initial TZ positions are given as: $s_i = j[-4, 1.6, -1.6, 4]$ rad/s. There is also flexibility on choosing the initial values of the admittance inverters M_{S1}, M_{13}, M_{34}, and M_{45}, which are initially chosen to be $[-1, 1, -1, 1]$. The remaining inverter values will be coming out of the extraction. Once the S-L coupling is extracted, the updated $P(s)$ was given as $-17s^2 - 40$, which has the new roots at: $j[-1.55, 1.55]$ rad/s. These roots

are shifted from their original positions. Therefore, the new zeros that will be used in the extraction should be the updated positions of these two zeros. This situation was also discussed in [90] and it is not a significant problem as long as the new roots do not turn out to be complex. The consequences of that will become evident in the design of the hybrid acoustic-EM filters in the next chapters.

Once the S-L coupling is extracted, the steps of synthesis are provided as follows:

- The first and the last nodes of the network are extracted pole elements. Therefore, the source and the load admittances will be nonzero.

- **Box I:** Starting from the source side, extract the shunt source admittance, as described in Section 5.2.3 as:

$$B_S = \left. \frac{D_{II}(s)}{B_{II}(s)} \right|_{s \to j1.55}. \tag{5.19}$$

Then, extract the unit inverter M_{S1} with a value of -1, as previously determined.

- **Box II:** Obtain the elements of the extracted pole. It was determined that the zero that this extracted pole is responsible for is at j1.55 rad/s. Therefore, obtain the residue of the extracted pole as:

$$r = \left. \frac{D_{II}(s)}{B_{II}^x(s)} \right|_{s=j1.55}, \quad \text{where } B_{II}^x(s) = \frac{B_{II}(s)}{s - j1.55}. \tag{5.20}$$

Using this residue, the extracted pole elements are obtained as:

$$C_2 = \frac{1}{r} \text{ and } b_2 = \frac{-1.55j}{r}. \tag{5.21}$$

Then, considering that the next node will be a resonator, obtain B_1 using

$$B_1 = \left.\frac{D'_{II}(s)}{B'_{II}(s)}\right|_{s \to \infty}, \tag{5.22}$$

where $D'_{II}(s)$ and $B'_{II}(s)$ are the $D(s)$ and $B(s)$ polynomials after the elements C_2 and b_2 are extracted. Finally, extract a unit inverter $M_{13} = 1$, as chosen previously.

- **Box III:** Similar to the extraction of a resonant node in the previous example, obtain C_3, B_3, and extract $M_{34} = -1$.

- **Box IV:** Similar to the extraction of a resonant node in the previous example, obtain C_4, B_4, and extract $M_{45} = 1$.

- **Box V:** Similar to Box II, obtain C_6, b_6, and M_{56}.

- **Box VI:** For this case, the extraction of last node in Fig. 5.4 (d). Then, extract a cross coupling at infinity, which gives M_{5L}. Then, extract the shunt admittance at infinity (B_5), flip the network (interchange $A(s)$ and $D(s)$), and extract another admittance at infinity, which obtains the load admittance (B_L).

Once the synthesis of the network is completed, the obtained FIR values of the network are given as: $B_s = -0.755\,\text{S}$, $B_1 = -1.32$, S $b_2 = -1.55\,\text{S}$, $B_3 = -0.11\,\text{S}$, $B_4 = 0.11\,\text{S}$, $B_5 = 2.9\,\text{S}$, $b_6 = 1.55\,\text{S}$, and $B_L = 0.755$ S. Furthermore, the coupling element values are given as: $M_{S1} = -1, M_{13} = 1, M_{34} = -1, M_{45} = 1$. The remaining elements are given as: $M_{12} = 0.978, M_{56} = 1.45, M_{5S} = 1.4813$. Finally, the capacitance values are given as: $C_1 = 1.04\,\text{F}$ $C_2 = 2.13\,\text{F}$, $C_3 = 0.97\,\text{F}$, and $C_4 = 0.48\,\text{F}$.

$$
[\mathbf{M}] =
\begin{array}{c}
\begin{array}{cccccccc}
\mathbf{S} & \mathbf{1,N} & \mathbf{2} & \mathbf{3} & \mathbf{4} & \mathbf{5,N} & \mathbf{6} & \mathbf{L}
\end{array} \\
\left[
\begin{array}{cccccccc}
-0.76 & -1.00 & 0 & 0 & 0 & 0 & 0 & 0.01 \\
-1.00 & -1.32 & 0.98 & 0.68 & 0 & 0 & 0 & 0 \\
0 & 0.98 & -1.55 & 0 & 0 & 0 & 0 & 0 \\
0 & 0.68 & 0 & -0.11 & -0.69 & 0 & 0 & 0 \\
0 & 0 & 0 & -0.69 & 0.11 & 1.01 & 0 & 0 \\
0 & 0 & 0 & 0 & 1.01 & 2.90 & 1.45 & 1.48 \\
0 & 0 & 0 & 0 & 0 & 1.45 & 1.55 & 0 \\
0.01 & 0 & 0 & 0 & 0 & 1.48 & 0 & 0.76
\end{array}
\right]
\begin{array}{c}
\mathbf{S} \\
\mathbf{1,N} \\
\mathbf{2} \\
\mathbf{3} \\
\mathbf{4} \\
\mathbf{5,N} \\
\mathbf{6} \\
\mathbf{L}
\end{array}
\end{array}
\qquad (5.23)
$$

These values can be shown with an admittance matrix, however, once the capacitance values are normalized to unity, the coupling matrix of this network is provided in (5.23). The circuit diagram for the normalized-frequency network is depicted in Fig. 5.6 (b) and the coupling-routing diagram of the network is also shown in Fig. 5.6 (c).

Example 3: Topology with only EPs

The final example to realize the desired response is based on purely extracted poles. Therefore, in this example, there will be no cross-coupling extraction. The extraction process of the network is depicted in Fig. 5.7 (a).
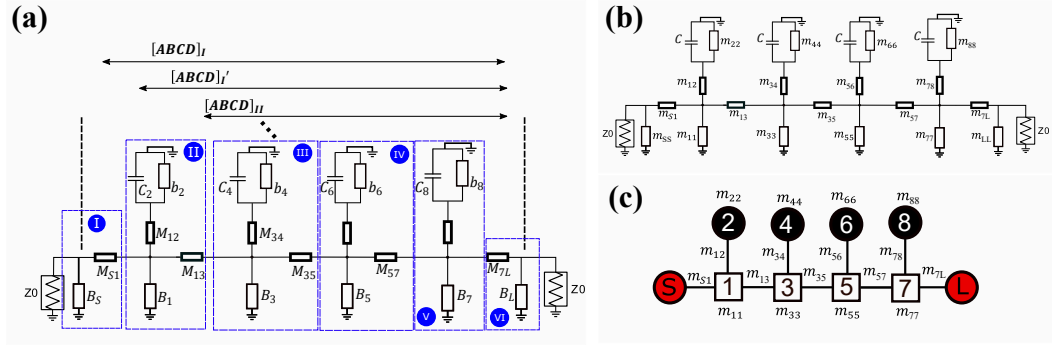
Figure 5.7: Extraction of Example 3. (a): The extraction sequence and the boxes for the folded-coupling matrix extraction. (b): The circuit diagram representing the CM to be synthesized, (c): The coupling-routing diagram.

To extract each element, similarly, one needs to determine the initial values of the inline inverter values M_{S1}, M_{13}, M_{35}, and M_{57}, which are chosen to be $[-1, 1, -1, 1]$ S, respectively. Furthermore, the order of the transmission zeros that will be used in the extraction should be determined, which is chosen as: $[s_1, s_2, s_3, s_4] = j - 4, 1.6, -1.6, 4]$ rad/s. The further steps for extraction are summarized as follows:

- **Box I:** The first and the last nodes of the network are extracted pole elements. Therefore, the source and the load admittances will be nonzero. Starting from the source side, one needs to extract the shunt source admittance, as described in Section 5.2.3 as:

$$B_S = \left. \frac{D_I(s)}{B_I(s)} \right|_{s \to s_1}, \tag{5.24}$$

Then, extract the unit inverter M_{S1} with a value of -1, as previously determined.

- **Box II:** Obtain the elements of the extracted pole. According to the chosen zero locations, obtain the residues of the EP as:

$$r = \left. \frac{D_{II}(s)}{B_{II}^x(s)} \right|_{s=j4}, \text{ where } B_{II}^x(s) = \frac{B_{II}(s)}{s - j4}. \tag{5.25}$$

109

Using this residue, the extracted pole elements are obtained as:

$$C_2 = \frac{1}{r} \text{ and } b_2 = \frac{-4j}{r}. \tag{5.26}$$

Then, considering that the next node will be a resonator and therefore, with a transmission zero at infinity, obtain B_1 using

$$B_1 = \left. \frac{D'_{II}(s)}{B'_{II}(s)} \right|_{s \to j1.6}, \tag{5.27}$$

where $D'_{II}(s)$ and $B'_{II}(s)$ are the $D(s)$ and $B(s)$ polynomials after the elements C_2 and b_2 are extracted. Finally, extract a unit inverter $M_{13} = 1$, as chosen previously.

- **Box III, Box IV, and Box V:** Similar to obtaining the extracted pole elements, obtain the values of the elements in these boxes.

- **Box VI:** Just as in Example II, find the element values in the last node.

After these extractions and normalizing the capacitances to unity, the coupling matrix of the full extracted-pole network is depicted in (5.28).

$$[\mathbf{M}] =$$

	S	1, N	2	3, N	4	5, N	6	7, N	8	L	
S	0.21	1.00	0	0	0	0	0	0	0	0	S
1, N	1.00	4.21	4.18	−1.00	0	0	0	0	0	0	1, N
2	0	4.18	4.00	0	0	0	0	0	0	0	2
3, N	0	−1.00	0	−1.60	1.44	1.00	0	0	0	0	3, N
4	0	0	0	1.44	−1.60	0	0	0	0	0	4
5, N	0	0	0	1.00	0	2.70	1.87	−1.00	0	0	5, N
6	0	0	0	0	0	1.87	1.60	0	0	0	6
7, N	0	0	0	0	0	−1.00	0	−2.49	3.21	0.77	7, N
8	0	0	0	0	0	0	0	3.21	−4.00	0	8
L	0	0	0	0	0	0	0	0.77	0	−0.21	L

$$(5.28)$$

It can be observed from the coupling matrix in (5.28) that the values of the FIR elements at the dangling resonators are given as: $m_{22} = 4, m_{44} = -1.6, m_{66} = 1.6$, and $m_{88} = -4$, which correspond to the location of the normalized-frequency transmission zeros in the desired order.

5.3 Summary and Conclusion

This chapter introduced the design of filters that use extracted poles in addition to the resonators. An extracted pole is defined as a non-resonating node coupled to a dangling resonator. This produces a series and a parallel resonance, just like the acoustic-wave resonators. The extracted pole synthesis methodology is an important technique to synthesize inline filters realizing fully canonical responses without the use of cross-coupling mechanisms. An extracted pole network can be obtained using

Chapter 6

Coupling Matrix Based Design of Narrowband Ladder-AW Based Microwave Filters

Both the EP networks and the AW resonators have series and parallel resonances and their input impedances have similarity, when considered for narrow fractional bandwidths. Due to that similarity, the EP based filter design is extended to the design of acoustic-wave filters, which attracted a significant amount of attention in the last decade. As such, one of the most solid efforts to synthesize the AW resonator based filters using the extracted-pole synthesis is provided in [56]. This was followed by [57–59] in a way to incorporate transversal sub-networks into the design which includes both extracted-pole synthesis and transversal coupling matrix synthesis approaches.

This chapter introduces the design of narrow-band AW based ladder filters from the synthesized full-EP based networks. The reason for using the term "narrowband" is because the conventional equations for converting the EP sections to BVD sections give accurate results for FBW values of up to approximately 10%. To correct for that, a new technique is also proposed in this section which will be used in the next chapter in the design of Hybrid-ACEM filters with FBW values of 30%.

6.1 Definition of Series-EP and Shunt-EP Sections

As a reminder, an extracted pole section can be characterized as an NRN coupled to a dangling resonator and the frequency response of the EP sections are dependent on the behavior of the FIR elements at the resonant and the non-resonant nodes of the network. Based on the inductive or capacitive nature of the FIR elements, this dissertation identifies the EP sections in two different categories, which are depicted in Fig. 6.1 as follows:

- **Shunt-EP:** For the case of the shunt-EP, both the FIR elements in the NRN and the resonant node (m_{ii} and $m_{i+1,i+1}$ in Fig. 6.1 (a)) are positive, in other words, they are capacitive.

- **Series-EP:** For the series-EP case, both the FIR elements in the NRN and the resonant node (m_{ii} and $m_{i+1,i+1}$ in Fig. 6.1 (b)) attain negative values, which corresponds to them being inductive.

It should be mentioned that there are no such terms in the literature, however, in [63], we refer to these sections as the series-EP and the shunt-EP sections. That is because their frequency- and bandwidth- denormalized frequency responses correspond to that of the series- and shunt-connected acoustic-wave resonator sections.
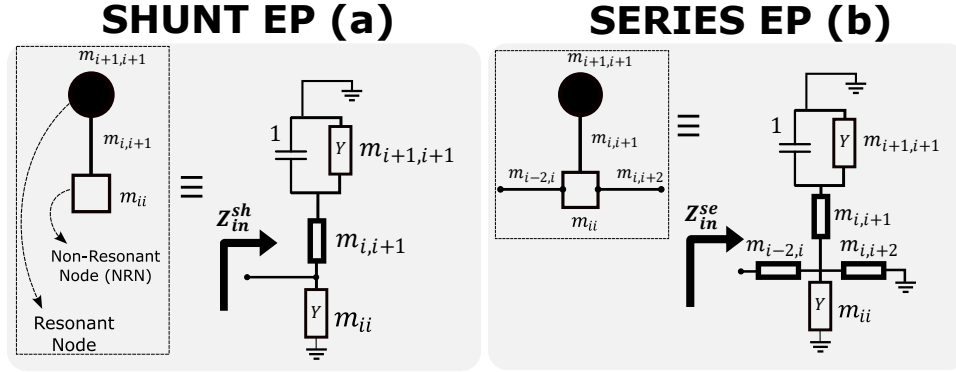
Figure 6.1: Extracted pole sections that are representing the shunt-connected and series-connected AW sections in the normalized frequency domain. The input impedances in (a) and (b) are used for calculating the series and parallel resonances of the resulting BVD sections in the denormalized bandpass frequency domain.

For the lowpass normalized-frequency domain, the impedance looking into the shunt- and series-EP sections in Fig. 6.1 (a) and (b) can be obtained as:

$$Z_{in}^{SH} = j \frac{\Omega + m_{i+1,i+1}}{m_{i,i+1}^2 - \Omega m_{i,i} - m_{i,i} m_{i+1,i+1}}$$

$$\text{and } Z_{in}^{SE} = \frac{j}{m_{i-2,i}^2} \frac{\Omega m_{i,i} + m_{i,i} m_{i+1,i+1} - m_{i,i+1}^2}{\Omega + m_{i+1,i+1}}. \tag{6.1}$$

Therefore, the normalized-frequency series and parallel resonant frequencies of the Shunt-EP section are found as:

$$\Omega_{se}^{SH-EP} = -m_{i+1,i+1} \text{ and}$$

$$\Omega_{pa}^{SH-EP} = \frac{m_{i,i} m_{i+1,i+1} - m_{i,i+1}}{m_{i,i}}, \tag{6.2}$$

while for the Series-EP section, the series and the parallel resonance frequencies can be obtained as:

114

$$\Omega_{se}^{SE-EP} = -m_{i+1,i+1} \text{ and}$$

$$\Omega_{pa}^{SE-EP} = \frac{m_{i,i}m_{i+1,i+1} - m_{i,i+1}}{m_{i,i}}. \tag{6.3}$$

It should be noticed that the *series* resonance frequency of the Shunt-EP section corresponds to the frequency at which the EP section pulls the signal to ground, meaning that it creates a transmission zero at that frequency. However, the *parallel* resonance of the series-EP section causes a high impedance at this frequency and again, it creates a transmission zero at that frequency.

To find the corresponding k_t^2 value for a given FBW of Δ and a center frequency of ω_0, the bandpass resonance frequencies of the shunt- and series-EP sections in Fig. 6.1 should be obtained using the lowpass-to-bandpass conversion as in [2]:

$$\Omega \rightarrow \frac{1}{\Delta}\left[\frac{\omega}{\omega_0} - \frac{\omega_0}{\omega}\right]. \tag{6.4}$$

One should reorganize this equation and find the solutions of the following equality:

$$\omega^2 - (\Delta\Omega\omega_0)\omega - \omega_0^2 = 0, \tag{6.5}$$

by setting $\Omega \rightarrow \Omega_{se}^{SH-EP}$ for the series resonance and $\Omega \rightarrow \Omega_{pa}^{SH-EP}$ for the parallel resonance, respectively. The *negative* roots of the solution for each case will give the denormalized resonance frequencies of the shunt-EP section, and will be denoted as ω_{se}^{SH-EP} and ω_{pa}^{SH-EP} respectively. Conversely, one should set $\Omega \rightarrow \Omega_{se}^{SE-EP}$ and $\Omega \rightarrow \Omega_{pa}^{SE-EP}$ and find the *positive* roots of (6.5) to get the series and parallel resonant frequencies of the series-EP section, which are denoted as ω_{se}^{SE-EP} and ω_{pa}^{SE-EP}. Once the denormalized resonance frequencies are found, the required k_t^2 of series- and shunt-

115

EP sections can be obtained as:

$$k_t^2 = \frac{\pi}{2} \frac{\omega_{se}}{\omega_{pa}} \cot \left(\frac{\pi}{2} \frac{\omega_{se}}{\omega_{pa}} \right). \tag{6.6}$$

The calculated k_t^2 in (6.6) is the k_t^2 of the BVD model assuming that the BVD model perfectly represents an extracted-pole, which is not true for large fractional bandwidths. Therefore, this value will be called as the k_t^2 *of the EP section* in this study since it is directly obtained from the extracted pole.

The next section will examine how one can translate the Shunt-EP and the Series-EP sections to their corresponding series-connected and shunt-connected AW based resonator sections using their BVD model.

6.2 Conversion Between EP to BVD Prototype

6.2.1 Conversion of the Shunt-EP Section

For this conversion, the useful property of the admittance inverters given in Fig. 6.2 should be kept in mind. It can be proven that a shunt impedance of Z_1 on one side of an admittance inverter of J can be transferred to the opposite side of it as an admittance with a value of $J^2 Z_1$, as observed.
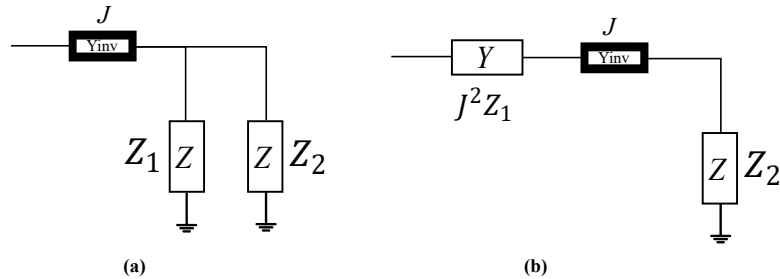
Figure 6.2: A property of admittance inverter to be used in the conversion of EPs to BVD sections.

Using this equivalence, the conversion of the shunt-EP section to the BVD prototype is quite straightforward and is explained in Fig. 6.3. In Fig. 6.3 (i), the coupling-routing diagram of the Shunt-EP section is depicted together with the denormalized Shunt-EP section. Once the elements of the resonant node are transferred towards the NRN, the network in Fig. 6.3 (ii) is obtained.
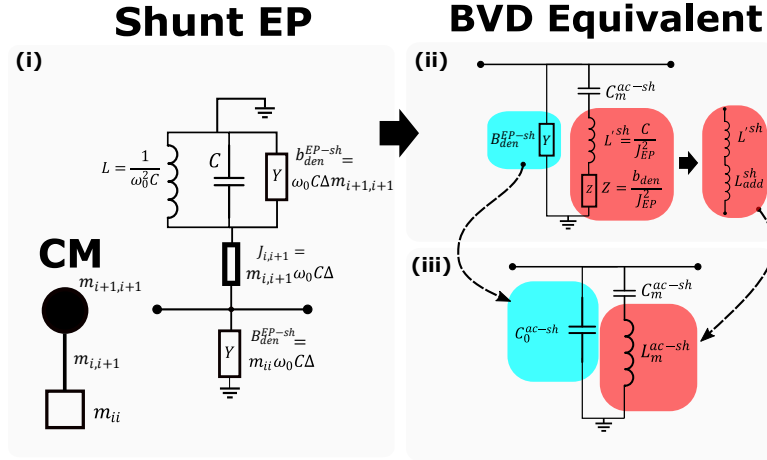
Figure 6.3: Conversion of the Shunt-EP section into the shunt-connected BVD prototype.

As observed, the equivalent circuit in Fig. 6.3 (ii) includes capacitance, inductance, and two FIR elements. These FIR elements can be converted into equivalent capacitance or inductances as observed in Fig. 6.2 (iii) and the values of the elements are given as:

$$C_m^{ac-sh} = J_{i,i+1}^2 L,$$
(6.7)

$$L_m^{ac-sh} = L'^{sh} + L_{add}^{sh} = \frac{C}{J_{i,i+1}^2} + \boxed{\frac{1}{\omega} \frac{b_{den}^{EP-sh}}{J_{i,i+1}^2}}, \text{and}$$
(6.8)

$$C_0^{ac-sh} = \boxed{B_{den}^{EP-sh}/\omega}.$$
(6.9)

The elements given by C_m^{ac-sh} and L_m^{ac-sh} correspond to the motional branch of the BVD prototype and the capacitance C_0^{ac-sh} corresponds to the plate capacitance of

the AW resonator. As observed, the equations (6.8) and (6.9) depend on the frequency variable ω. However, the BVD element values of the network should attain fixed values. For filters of narrow fractional bandwidth, including $\approx 1\% - 10\%$, replacing ω by ω_0 works well. However, for large FBW values, another wideband conversion is proposed in the following sections.

6.2.2 Conversion of the Series-EP Section

Converting the Series-EP section to its corresponding series-connected BVD model is slightly more complicated compared to converting the Shunt-EP section. This conversion is depicted in Fig. 6.4. As observed in Fig. 6.4 (i), the FIR elements of the frequency-and bandwidth-denormalized EP sections at the NRN and the resonator (B_{den}^{EP-se} and b_{den}^{EP-se}) should both be negative in order for that EP section to represent a series-connected acoustic wave BVD section. Furthermore, it should also be stated that the admittance inverters going into and out of the EP section (J_{out}) should have the same magnitude and the opposite sign of each other.
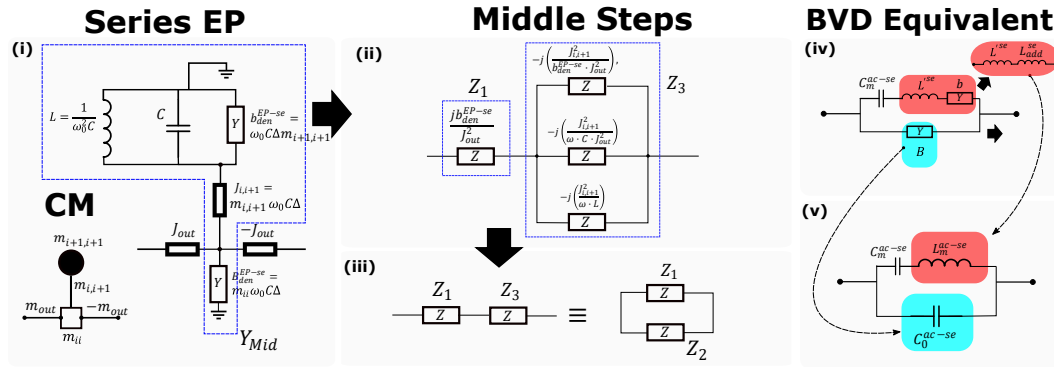
Figure 6.4: Conversion of the Series-EP into its BVD equivalent network. (i): The Series-EP and its bandpass transformation. (ii) and (iii): the middle steps for conversion, (iv) and (v): the final BVD equivalent networks.

To derive the equations to obtain the parameters of the series-connected BVD sec-

tion, the equivalent admittance of the boxed section in Fig. 6.4 (i) is called as Y_{mid}. In that case, the overall ABCD parameters of the EP section including the incoming and outgoing admittance inverters can be calculated as:

$$
[\textbf{ABCD}]_{\textbf{total}} = \left(\begin{bmatrix} 0 & j/J_{out} \\ jJ_{out} & 0 \end{bmatrix} \cdot \begin{bmatrix} 1 & 0 \\ Y_{mid} & 1 \end{bmatrix} \right) \cdot \begin{bmatrix} 0 & -j/J_{out} \\ -jJ_{out} & 0 \end{bmatrix}
$$
$$
= \begin{bmatrix} 1 & Y_{mid}/J_{out}^2 \\ 0 & 1 \end{bmatrix},
$$
(6.10)

where

$$
Y_{mid} = jB_{den}^{EP-se} + \frac{J_{i,i+1}^2}{jb_{den}^{EP-se} + j\omega C + 1/(j\omega L)}.
$$
(6.11)

It should be noted that $[\textbf{ABCD}]_{\textbf{total}}$ corresponds to the ABCD matrix of a series-connected impedance whose value is given by $(1/J_{out}^2)Y_{mid}$. This overall impedance value can also be decomposed into the circuit diagram in Fig. 6.4 (ii) with its impedance values given on that figure. In order to convert this network to the BVD prototype, one needs to separate the two series impedances Z_1 and Z_3, as encapsulated in Fig. 6.4 (ii), to an equivalent parallel combination. This is depicted in Fig. 6.4 (iii). It can be shown that in order for that series connected Z_1 and Z_3 pair to be equivalent to the parallel Z_1 and Z_2 pair, the following condition needs to be satisfied:

$$
Z_3 = -\frac{Z_1^2}{Z_1 + Z_2}.
$$
(6.12)

Therefore, to obtain the BVD equivalent element values in Fig. 6.4 (iv), which are

119

denoted as C_m^{se-ac}, L'^{se}, b, and B, the following equality should be solved:

$$\frac{jb_{den}^{EP-se}J_{out}^2}{J_{i,i+1}^2}+j\omega\frac{J_{out}^2 C}{J_{i,i+1}^2}+\frac{1}{j\omega}\frac{1}{LJ_{out}^2} = -\left(\frac{J_{out}^2}{b_{den}^{EP-se}}\right)^2\left(-j(\frac{1}{b}+\frac{1}{B})+\frac{1}{j\omega C_m^{ac-se}}+j\omega L'^{se}\right).$$

(6.13)

Equating the constant terms to the constant ones and the ones that have the frequency variable to the capacitance and inductance values, the BVD element values in Fig. 6.4 (v) can be found as:

$$C_m^{ac-se} = \frac{LJ_{i,i+1}^2 J_{out}^2}{\left(B_{den}^{EP-se}\right)^2},$$

(6.14)

$$L_m^{ac-se} = L'^{se} + L_{add}^{se} =$$

$$\frac{\left(B_{den}^{EP-se}\right)^2}{J_{i,i+1}^2 J_{out}^2} + \boxed{\frac{1}{\omega}\frac{\left(B_{den}^{EP-se}\right)^2}{J_{out}^2}\left(\frac{b_{den}^{EP-se} B_{den}^{EP-se}}{J_{i,i+1}^2} - 1\right)}, \text{ and}$$

(6.15)

$$C_0^{ac-se} = \boxed{-\frac{1}{\omega}\left(\frac{J_{out}^2}{B_{den}^{EP-se}}\right)}.$$

(6.16)

The three equations (6.14), (6.15), and (6.16), construct the BVD parameters of the series-connected acoustic-wave resonator section from the parameters of the Series-EP section which is denormalized for a fractional bandwidth of Δ and an angular center frequency of ω_0. As also mentioned for the case of the Shunt-EP section, the equations (6.15) and (6.16) include the frequency variable ω for this conversion while the BVD parameters need to attain fixed values. Therefore, this conversion is again valid only for narrow fractional bandwidth values.

6.3   Novel Wideband Corrections to the EP-to-BVD Conversion

In this subsection, the problems with the conventional conversion methodology from EP-to-BVD networks will be explained and an alternative method to fix this issue will

120

be introduced.

Thoroughout (6.7)–(6.16), the subscript "*den*" is used for denoting the denormalized version of the FIR elements. Furthermore, the reference capacitance C can be chosen arbitrarily in a way to adjust the values of the resulting parameters. It has been mentioned in Section 6.1.1 and 6.1.2 that the conversion of the FIR elements into inductances and capacitances requires the use of the frequency variable ω in (6.8) and (6.9) for shunt-AW and in (6.15) and (6.16) for series-AW sections (encapsulated in a box). It was also mentioned that, substituting the filter center frequency ω_0 for ω for (6.7)–(6.16) works very well for narrow bandwidths [56].

As an example, input impedances of a series-EP and a shunt-EP section are depicted in Fig. (6.5) (a) and (b), when they are denormalized for an f_0 of 2.461 GHz and a FBW of 5%. The component values of the Series-EP and the Shunt-EP sections are depicted in the figure. The same graphs also show the input impedance of their corresponding BVD equivalents, when ω_0 is used for ω in (6.7)–(6.16) and as observed, the impedances match very well for 5% FBW. For a FBW of 20% and an f_0 of 2.787 GHz, however, the input impedances of the original EP and the BVD equivalent using the conventional transformation do not match, as observed in Fig. (6.5) (b) and (d).
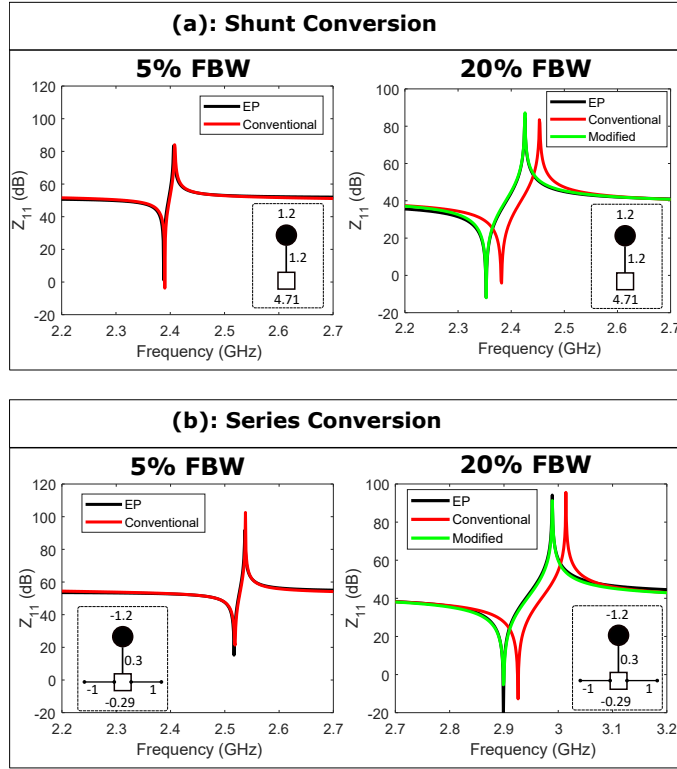
Figure 6.5: (a): Input impedance comparison of the conventional and proposed EP-to-BVD conversion for a shunt-EP section. (b): Conventional and proposed conversion of a series-EP section. For both (a) and (b), FBW values of 5% and 20% are depicted.

To restore this problem, one can convert these FIR elements to inductances and capacitances at frequencies that are different than ω_0. This can be done in a way to ensure that the BVD model of the AW resonators have the same series and parallel resonances as their corresponding EP sections. It will result in the encapsulated parts in (6.8), (6.9), (6.15), and (6.16) to be replaced. The proposed procedure for this correction is as follows:

- Calculate the series and parallel resonances for shunt (ω_{s-sh} and ω_{p-sh}) and for series (ω_{s-se} and ω_{p-se}) EP sections with respect to the desired center frequency and the fractional bandwidth using (6.2) and (6.3).

- The equations for the motional capacitances (6.14) and (6.7) do not change, as

122

these equations do not include a frequency variable.

- For a shunt resonator, force L_m^{ac-sh} to resonate with C_m^{ac-sh} at ω_s^{sh}, therefore,

$$L_{m_{new}}^{ac-sh} = \frac{1}{\omega_{s-sh}^2 C_m^{ac-sh}}. \qquad (6.17)$$

- Again for the shunt resonator, the static capacitance needs to resonate with the motional branch at ω_p^{sh}, therefore,

$$C_{0_{new}}^{ac-sh} = \frac{1}{\omega_{p-sh}^2 L_{m_{new}}^{ac-sh} - 1/C_m^{ac-sh}}. \qquad (6.18)$$

- Similarly, the motional inductance for the series resonator is found as:

$$L_{m_{new}}^{ac-se} = \frac{1}{\omega_{s-se}^2 C_m^{ac-se}}, \qquad (6.19)$$

- and the static capacitance for the series resonator is found as:

$$C_{0_{new}}^{ac-se} = \frac{1}{\omega_{p-se}^2 L_{m_{new}}^{ac-se} - 1/C_m^{ac-se}}. \qquad (6.20)$$

- Replace (6.8) and (6.9) with (6.17) and (6.18), respectively for shunt AW sections.

- Similarly, replace (6.15) and (6.16) with (6.19) and (6.20), respectively for series AW sections.

The proposed equations are tested to calculate the BVD parameters from the 20% shunt- and series-EP sections and the input impedance of the calculated BVD sections are shown in Fig. 6.5 (b) and (d) with the green trace, labeled as "modified" for 20%

fractional bandwidth. As observed, the series and parallel resonances of the both series- and shunt-BVD sections match well with that of the bandpass EP sections for large fractional bandwidth values as well, in contrast to the conventional conversion method which results in frequency shifts. It will be shown that this correction can produce wideband filters much more accurately.

6.4   Examples of Ladder-AW Based Filters

Until this point in this chapter, the conversion between the extracted-pole elements and their corresponding series- or shunt-connected BVD sections are extablished. Now, microwave filters with a specific FBW and center frequency with an arbitrary order can be synthesized using AW-based resonators.

To synthesize an AW based filter, the full-extracted pole based design in Chapter 6 should be considered. An important point of interest is to set the incoming and outgoing admittance inverters between the extracted poles to the same magnitude and alternating sign. The simplest way of doing so is to have them alternate between 1 and -1, initially. Furthermore, it is important to start the ladder network with a series-connected AW resonator. The reason for doing so is that initiating the network with a shunt-AW resonator will result in an additional admittance inverter between the source and the resonator. Some details of filters starting with shunt-AW sections are given in [100].

As an example, a seventh-order Chebyshev function with transmission zero locations given at $s_i = j[1.6, -1.6, 1.6, -1.6, 1.6, -1.6, 1.6]$ rad/s with an ϵ of 100 is designed. The return loss ripple is 17.77 dB. When the admittance inverters between the EP sections are obtained as $(-1)^{n-1}$ for $n \in [1, N-1]$, the full-EP based coupling matrix of the network is depicted as in the following:

	S	1,N	2	3,N	4	5,N	6	7,N	8	9,N	10	11,N	12	13,N	14	L	
	-0.77	1	0	0	0	0	0	0	0	0	0	0	0	0	0	0	S
	1	-0.99	1.04	-1	0	0	0	0	0	0	0	0	0	0	0	0	1,N
	0	1.04	-1.60	0	0	0	0	0	0	0	0	0	0	0	0	0	2
	0	-1	0	2.65	1.85	1	0	0	0	0	0	0	0	0	0	0	3,N
	0	0	0	1.85	1.60	0	0	0	0	0	0	0	0	0	0	0	4
	0	0	0	1	0	-1.66	1.63	-1	0	0	0	0	0	0	0	0	5,N
	0	0	0	0	0	1.63	-1.60	0	0	0	0	0	0	0	0	0	6
	0	0	0	0	0	-1	0	3.03	2.18	1	0	0	0	0	0	0	7,N
	0	0	0	0	0	0	0	2.18	1.60	0	0	0	0	0	0	0	8
	0	0	0	0	0	0	0	1	0	-1.66	1.63	-1	0	0	0	0	9,N
	0	0	0	0	0	0	0	0	0	1.63	-1.60	0	0	0	0	0	10
	0	0	0	0	0	0	0	0	0	-1	0	2.65	1.85	1	0	0	11,N
	0	0	0	0	0	0	0	0	0	0	0	1.85	1.60	0	0	0	12
	0	0	0	0	0	0	0	0	0	0	0	1	0	-0.99	1.04	-1	13,N
	0	0	0	0	0	0	0	0	0	0	0	0	0	1.04	-1.60	0	14
	0	0	0	0	0	0	0	0	0	0	0	0	0	-1	0	-0.77	L

$$(6.21)$$

In (6.21), it should be noticed that the element m_{22} is equal to -1.6, meaning that it implements the transmission zero at a normalized frequency of 1.6 rad/s. Therefore, this corresponds to a series-connected AW section, when denormalized. It should be realized that there will be 4 series- and 3 shunt-AW resonator sections in this network and as observed, the admittance inverters connecting the EP sections alternate in sign until the end.

Using the coupling matrix in (6.21), the denormalized full-extracted pole based network of seventh order is depicted in Fig. 6.6 (a). When the desired fractional bandwidth is Δ, the center frequency is f_0, and the source and the load impedances are 50 Ω each, the admittance inverter values between node i and j are calculated as:

$$J_{i,j} = m_{i,j}\omega_0\Delta\sqrt{C_iC_j}, \tag{6.22}$$

where C_i and C_j are the capacitances at node i and j. The inline coupling mechanisms have no capacitors that are directly connected on each side since they are between the

NRNs. However, these nodes are still coupled to the dangling resonators. Therefore, one still needs to include the capacitance values at each dangling resonator. For instance, the inverter value J_{13} is calculated as: $J_{1,3} = m_{1,3}\omega_0\Delta\sqrt{C_1 C_2}$ and similarly, $J_{11,13} = m_{11,13}\omega_0\Delta\sqrt{C_6 C_7}$. Although one can choose different values for these capacitances, it is best to set them to a single reference capacitance C_{ref}, just as in Chapter 4. The value of C_{ref} can be chosen arbitrarily to adjust the values of the other components. Furthermore, the inverters that are connected to the source and the load are calculated as:

$$J_{S,1} = m_{S,1}(1/\sqrt{50\omega_0 L_1/\Delta} \text{ and}$$
$$J_{14,L} = m_{13,L}(1/\sqrt{50\omega_0 L_1/\Delta},$$

(6.23)

where $L_1 = 1/\sqrt{\omega_0^2 C_{ref}}$.

During the denormalization, there is an important point to be considered. Because of the source and the load terminations, the equalities $J_{S,1} = -J_{1,3}$ and $J_{11,13} = -J_{13,L}$ are not satisfied, even though the coupling matrix satisfies $m_{S,1} = -m_{1,3}$ and $m_{11,13} = -m_{13,L}$. This prevents SE-EP1 and SE-EP4 to be converted to the SE-AW 1 and SE-AW 4 in Fig. 6.6.

In order to fix this issue, one can perform a node scaling at node 3, node 7, and node 11 with a value of $J_{S,1}/J_{1,3}$. This enforces the incoming and outgoing admittance inverters for the SE-EP sections in Fig. 6.6 (a) to have the same magnitude and the opposite sign, which makes it ready to be converted to the ladder-AW based network in Fig. 6.6 (b).
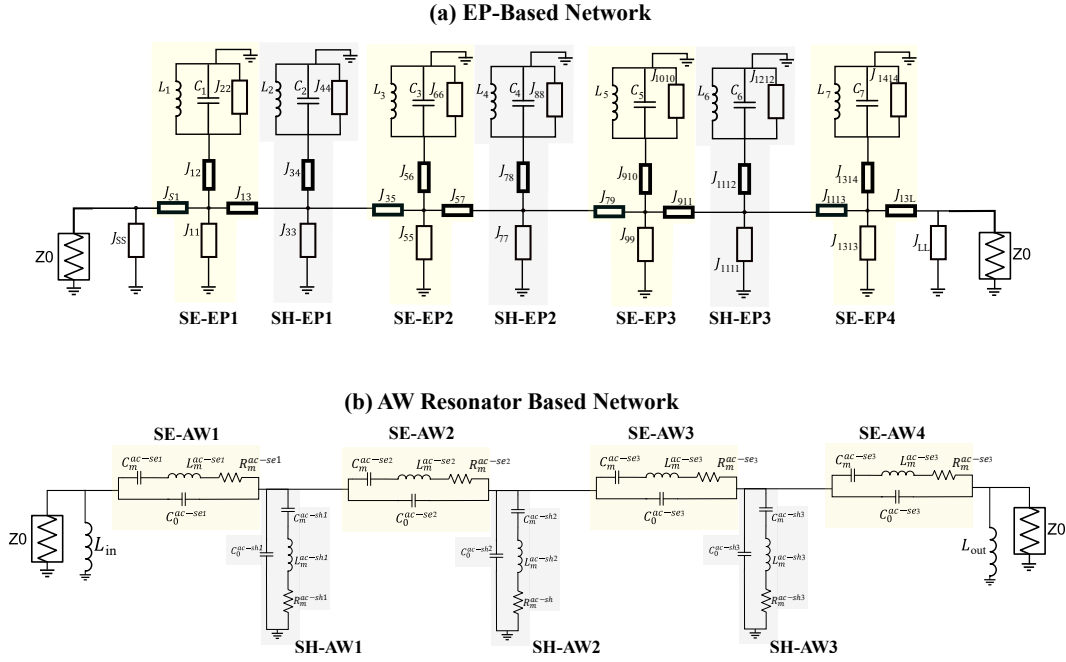
Figure 6.6: (a):The extracted-pole based network that is synthesized from the coupling matrix in (6.21). (b): The network that includes the BVD prototypes of the ladder-AW based design of seventh order.

Using either the classical or the proposed modified EP-to-BVD conversion, this network can be converted into the design with the BVD equivalents of the four series-connected and three shunt-connected acoustic-wave resonators, as depicted in Fig. 6.6 (b).

Using the CM in (6.21), the filter prototype is denormalized for two different applications. The first one is the 5g n41 band, which spans the band 2.496 GHz – 2.690 GHz (7.5%) and the second one is the 5g n77 band, which is spans 3.3 GHz– 4.2 GHz (24.4%). For these two examples, the BVD parameters of the seventh-order network in Fig. 6.6 (b) are depicted in Table 6.1. Using these values for the resonators, the simulation results of the filter network in Fig. 6.6 (b) are shown in Fig. 6.7 (a) and (b), for FBW values of 7.5% and 24.4%, respectively. The quality factor of the series resonance frequency is set to 1,200 for each resonator by adjusting the resistance at

each BVD section. As observed in Fig. 6.7, the responses have very roll-off and 40 dB

of OOB rejection.

Table 6.1: The BVD parameters of the seven AW based resonators from SE1 to SE4 for different fractional bandwidth values. The table depicts that for FBW values of 7.5% (5g n41) and 24.4% (5g n77). For the n41 example, $L_1 = L_2 = 4$ nH and for the n77 example, $L_1 = L_2 = 2.77$ nH. The values for n41 are obtained using the conventional EP-to-BVD conversion while the ones for the n77 band are obtained from the proposed conversion.

7.5% FBW	SE-1	SH-1	SE-2	SH-2	SE-3	SH-3	SE-4
C_0 (pF)	1.24	3.25	0.74	3.72	0.74	3.25	1.24
C_m (fF)	101.35	313.08	87.97	436.2	87.97	313.08	101.35
L_m (nH)	37.52	13.48	42.68	9.68	42.68	13.48	37.52
k_t^2 (%)	9.26	10.74	12.95	12.76	12.95	10.74	9.26
24.4% FBW	SE-1	SH-1	SE-2	SH-2	SE-3	SH-3	SE-4
C_0 (pF)	0.76	1.94	0.42	2.14	0.42	1.94	0.76
C_m (fF)	229.16	707.88	198.91	986.27	198.91	707.88	229.16
L_m (nH)	7.06	3.79	9.19	2.72	9.19	3.79	7.06
k_t^2 (%)	25.96	28.57	30.73	30.64	30.73	28.57	25.96

Considering the steep roll-off, low insertion loss, and 40 dB OOB rejection of both responses, it should be mentioned that they qualify for the requirements of the 5g bands that they are designed for. However, the practicality of these designs should be further considered. The initial observation regarding Table 6.1 is that the required values of the k_t^2 and C_0 varies across the resonators. When the design is switched from 7.5% FBW to 24.4% FBW, the required k_t^2 for each resonator drastically increases.

Regarding the design of the BAW resonators as described in Chapter 2, it should be recalled that the designer has control on the value of C_0 and the parallel resonance frequency. As the C_0 value is dependent on the conducting electrode size of the BAW, it can be scaled. However, the k_t^2 value is dependent on the piezoelectric substrate and

the k_t^2 values of the resonators should be uniformly distributed.
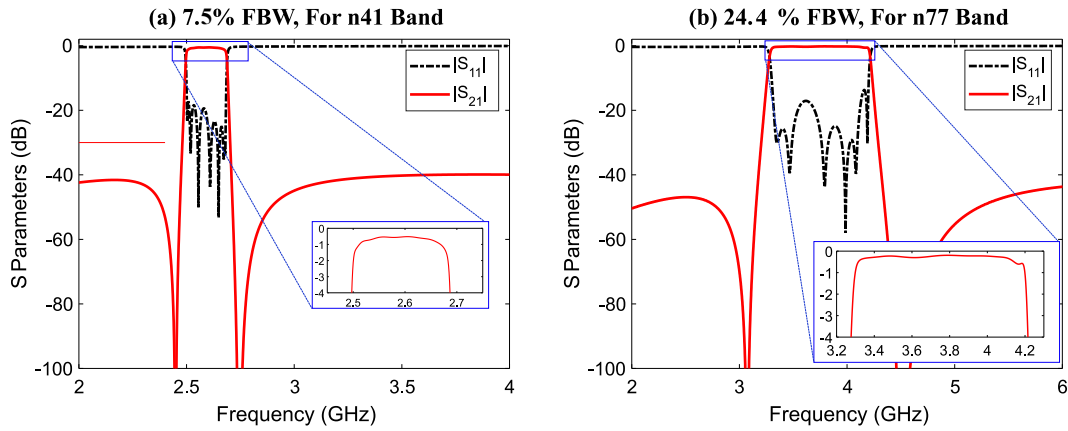
Figure 6.7: The simulation results of the ladder-AW based design in Fig. 6.6, when the parameter values in Table 6.1 are used. (a) The design for n41 band and (b): The design for n77 band.

For the synthesized ladder topology, the k_t^2 of each resonator is dependent on the following:

- The order of the filter,

- The position of the transmission zeros,

- The return loss of the design,

- The desired fractional bandwidth of the filter, and

- The position of the resonator within the network.

In order to have a uniform k_t^2 distribution, one can sweep the positions of the transmission zeros and the return loss value of the response [56]. It should also be noted that there is no such a guarantee that one can obtain a uniform set of k_t^2 values [56].

For this seventh-order network, reassigning the values of the transmission zeros to:
$s_i = j\{1.875, -1.73, 1.5, -1.5, 1.5, -1.73, 1.875\}$ rad/s and sweeping the return loss

value of the response produces the required k_t^2 values for the seven resonators as plotted in Fig. 6.8 (a) and (b) for the FBW values of 7.5% and 24.4%, respectively. It can be observed that for a return loss of around 20.64 dB, the required k_t^2 values are almost uniform for each example.
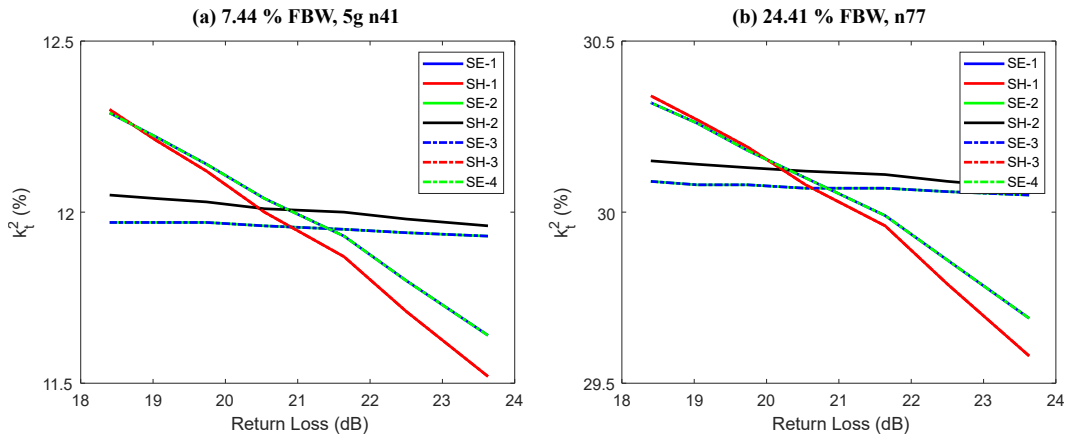
Figure 6.8: The k_t^2 distribution of the resonators in the seventh-order filter with respect to the return loss value. (a): The design with a FBW of 7.5% and (b): The design with a FBW of 24.4%.

The BVD parameter values of the two examples for which the k_t^2 values are made uniform by updating the TZ locations and setting the RL to 20.64 dB are depicted in Table 6.2. Comparing the k_t^2 values of the updated network with the ones of the same FBW in Table 6.1, one can realize the following: It is possible to design a network with a uniform set of k_t^2 values, however, the obtained common k_t^2 value is usually attained by increasing the values of the smaller ones in the design where all the transmission zeros are located symmetrically at the same normalized frequency.

Table 6.2: The BVD parameters of the seven AW based resonators from SE1 to SE4 for the two examples when the k_t^2 values are made uniform. The table depicts that for FBW values of 7.5% (5g n41) and 24.4% (5g n77). For the n41 example, $L_1 = L_2 = 5.09$ nH and for the n77 example, $L_1 = L_2 = 3.54$ nH. The values for n41 are obtained using the conventional EP-to-BVD conversion while the ones for the n77 band are obtained from the proposed conversion.

7.5% FBW	SE-1	SH-1	SE-2	SH-2	SE-3	SH-3	SE-4
C_0 (pF)	1.06	3.21	0.77	2.95	0.77	3.21	1.06
C_m (fF)	116.44	350.49	83.37	322.78	83.37	350.49	116.44
L_m (nH)	33.16	12.15	44.78	12.99	44.78	12.15	33.16
k_t^2 (%)	12.04	12	11.96	12.01	11.96	12	12.04
24.4% FBW	SE-1	SH-1	SE-2	SH-2	SE-3	SH-3	SE-4
C_0 (pF)	0.62	1.88	0.45	1.72	0.45	1.88	0.62
C_m (fF)	263.27	792.47	188.5	729.82	188.5	792.47	263.27
L_m (nH)	6.3	3.49	9.61	3.59	9.61	3.49	6.3
k_t^2 (%)	30.1	30.08	30.07	30.12	30.07	30.08	30.1

The new filter responses using the values of the parameters in Table 6.2 are depicted in Fig. 6.9 (a) and (b) for the 7.5% and the 24.4% FBW examples. It should be realized that the OOB rejection of the responses are still strong and they still satisfy the filter requirements of the corresponding 5g bands.

Considering the two design examples for n41 and n77 bands of 5g, the FBW values of 7.5% and 24.4% can be achieved with resonators with k_t^2 of approximately 12% and 30%, respectively. For different FBW values, the common k_t^2 of the AW resonators are depicted in Fig. 6.10. It can be observed that the required k_t^2 value for a particular FBW is always larger than the FBW value for this example.
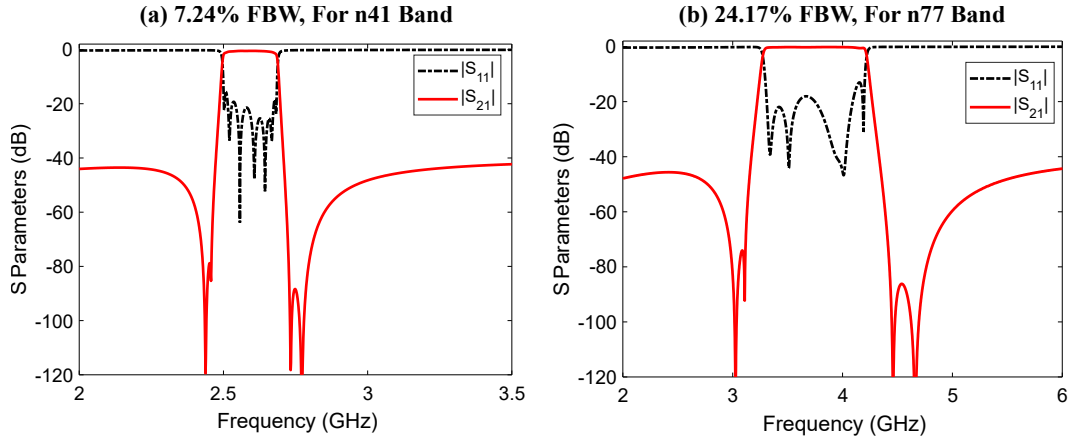
Figure 6.9: The simulation results of the ladder-AW based design in Fig. 6.6, when the parameter values in Table 6.2 are used. The results are for the case where the k_t^2 values are made uniform. (a): The design for n41 band and (b): The design for n77 band.

Considering the n41 example in this chapter, a k_t^2 of 12% is achievable with scandium doped AlN material, for instance [68]. However, achieving k_t^2 values of 30% is uncommon and has its own challenges such as weak temperature stability, low quality factor values, and not being CMOS compatible. This situation prevents one from designing on-chip filters for n77 band with the conventional ladder network that is described in this chapter.
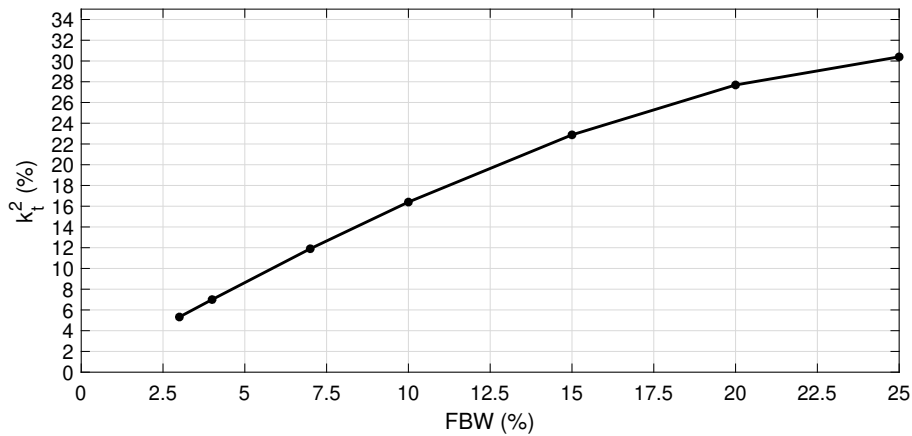
Figure 6.10: The graph of the achievable FBW with respect to the required k_t^2 of the resonators for the seventh-order example whose k_t^2 distribution is made uniform.

132

The increased data rates in telecommunication systems are already requiring front-end filters of 20% - 30%, such as the 5g n77 band. It is also projected that the future applications will require larger bandwidths in order to be able to accommodate the demand of the telecommunications networks. This is one of the largest challenges of the filters based on acoustic wave resonators.

6.5 Summary and Conclusions

In this chapter, the extracted pole and coupling matrix based design methods for the acoustic-wave ladder network based filters is examined. This is accomplished with a series of transformations from the newly defined Series-EP and Shunt-EP sections. Proceeding with that, the conventional methodology for converting the EPs to their corresponding BVD equivalents is examined with its limitations. It has been shown that this conversion gives inaccurate results when the desired FBW values are above 10%. Therefore, an alternative method for the derivation of the BVD parameters is proposed and the results of that conversion have been discussed. This conversion method will be used for the synthesis of wideband Hybrid-ACEM filters in the next chapter.

Apart from this conversion, the k_t^2 value distributions in a ladder AW based network has been discussed in detail for a seventh order response. Two different filter examples for the 5g n41 and 5g n77 bands are synthesized with the ladder topology. The methodology of obtaining a uniform k_t^2 value distribution is also depicted. Overall, this chapter builds all the background knowledge needed for designing the Hybrid-ACEM filters in the next chapter.

Chapter 7

Synthesis and Design of the Novel Hybrid

Acoustic-Electromagnetic Filters for Wideband Applications

The proper method of synthesizing AW resonator based microwave filters is considered in the previous chapter in detail. As described, the required k_t^2 values of the resonators can be made uniform for a desired center frequency and FBW by sweeping the positions of the transmission zeros and the prescribed return loss value of the filter by adjusting the parameter ϵ. For larger FBW values, such as 20%-30%, the required k_t^2 of the resonators typically go beyond 20% using this polynomial synthesis method [56–59, 61].

The limited achievable fractional bandwidth of the filters based on AW resonators has been a significant issue in the literature since the contemporary applications, i.e., WiFi 6, require FBW values of around 30% which cannot be achieved using AW resonators with the current achievable k_t^2 values. To solve this problem, many different methods have been proposed.

An intriguing approach uses inverting sections (coupled lines) to connect ladder-AW sections, which achieved filters with 20%–30% FBW with k_t^2 values of approximately 10% [54]. In order to increase the out-of-band (OOB) rejection performance, transversal sub-networks have been incorporated to the ladder architecture in [57–59].

The current state-of-the-art technique, as proposed in [61], is a transversal filter topology to reduce the dependency of the achievable FBW to the k_t^2 values of the resonators. In that study, a fully on-chip filter is designed for n77 band of 5g using AW based resonators with k_t^2 values of 13%.

There has been many studies to design wideband filters based on AW resonators, however, the main origin of not being able to achieve large fractional bandwidth values has not been mathematically well established. One of the main purposes of this chapter is to precisely define the problem with achiewing wide bandwidths using limited k_t^2 values. Once this problem is established and interpreted in the following section, the necessity and potential importance of introducing EM resonators within the AW based filters will become evident. In this regard, this chapter proposes a hybrid acoustic-electromagnetic (Hybrid-ACEM) topology with cross-coupling mechanisms to obtain the largest fractional bandwidth from the minimum possible k_t^2 values.

7.1 Precise Interpretation of the Problem

The precise connection between the achievable FBW value of the filter and the k_t^2 value of each resonator can be examined using an example synthesis. An example of a fully-canonical 7th order 15-dB equiripple response with normalized-frequency transmission zero locations at $[s_i] = j[1.6, -1.6, 1.6, -1.6, 1.6, -1.6, 1.6]$ rad/s is depicted in Fig. 7.1 (a), which can be realized with seven EP sections. Considering that the initial TZ is at a positive frequency, the network starts with a series-EP and alternates until the end, just as in the seventh order ladder examples in Chapter 6. The required k_t^2 values of the resonators for a bandpass ladder design with a center frequency of 2.5 GHz and a fractional bandwidth of 10% can be calculated from (6.6) and is given as: $[k_{t_i}^2] = [13.05, 15.11, 17.62, 17.38, 17.62, 15.11, 13.05]\%$, which is

a nonuniform set. To reduce the required k_t^2 values of all of the resonators while keeping the return loss the same, one can push the transmission zeros closer to the passband, to $[s_i] = j[1.2, -1.2, 1.2, -1.2, 1.2, -1.2, 1.2]$ rad/s and obtain another set $[k_{ti}^2] = [5.17, 7.33, 12.30, 12.59, 12.30, 7.33, 5.17]\%$. However, as observed from Fig. 7.1 (b), the 7th order 15-dB equiripple response now has more than 20 dB of out-of-band rejection degradation at $\Omega = \pm 6$ rad/s. To aim for larger fractional bandwidth values, or to have smaller k_t^2 values for the same FBW, one may need to push the zeros even closer to the passband which would only exacerbate the situation. Changing the return loss can reduce the k_t^2 values of some EP sections while increasing that of the others. Therefore, it is important to make the comparison for a fixed value of return loss.
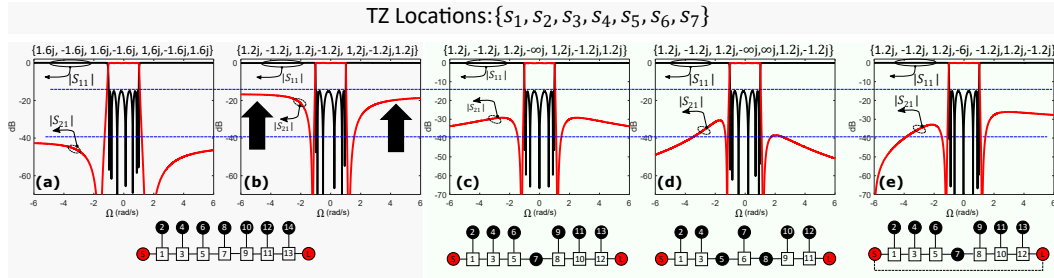
Figure 7.1: The problem definition and a proposed solution: Seventh-order equiripple responses: (a) and (b): Conventional canonical responses when the TZs are at $\pm 1.6j$ rad/s and $\pm 1.2j$ rad/s, respectively. The worsened out-of-band rejection in (b) is emphasized. (c) and (d): The responses when a single and two TZs are pushed to infinity, respectively. (e): The response when a single TZ is pushed toed to $-6j$ rad/s.

The problem in this situation is that the OOB rejection coming from each pole (20 dB/dec) is canceled above each transmission zero. Therefore, when the zeros need to be pushed closer to the passband to reduce the required k_t^2 values, that results in significantly weaker OOB rejection. In other words, for the response in Fig. 7.1 (b), all the poles are canceled at $\Omega = \pm 1.2$ rad/s and there is no other remaining pole or zero to suppress the transmission response after all the poles are canceled.

A non-canonical response, having just a single TZ at infinity can significantly recover the out-of-band rejection of the response, as given in Fig. 7.1 (c) while keeping all other TZs unchanged. As further observed, reducing the number of TZs by two gives an even better OOB rejection as in Fig. 7.1 (d). These two modifications will replace one or two EPs with a resonant node, which will require an EM resonator for realization. Finally, a TZ can also be moved to a much higher finite frequency instead of infinity, e.g., to $\Omega = -6$ rad/s, as observed in Fig. 7.1 (e) by keeping all the other zeros unchanged. This finite zero can be realized with a cross-coupling mechanism, as shown in the coupling-routing diagram in Fig. 7.1 (e), and will help with reducing the required k_t^2.
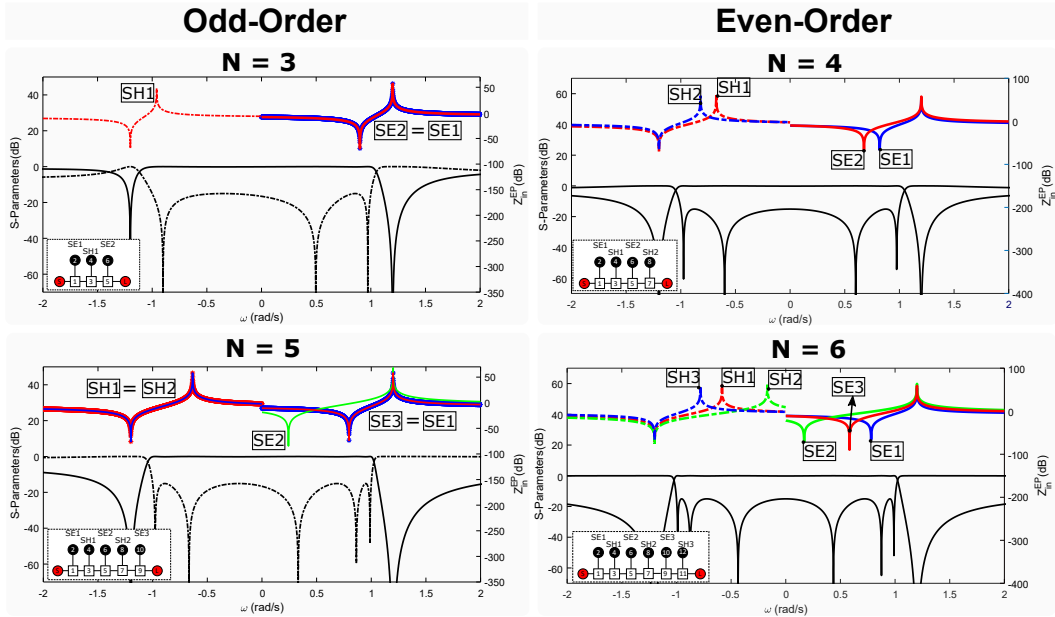
Figure 7.2: Resonance and anti-resonance distribution of the series and shunt EP sections for orders of 3, 4, 5, and 6. All of the responses belong to fully canonical, fully-EP based synthesis results.

It should be noted that replacing any EP with a resonant node in a fully canonical response having zeros close to the passband is beneficial for OOB rejection. However, replacing the EP with the highest k_t^2 (the one defining the middle of the passband) with

an EM resonator produces the greatest benefit.

To identify the EP sections that define the midband and the ones that define the band edges, the normalized-frequency impedances of each AW section (as derived in (6.1)) is plotted in Fig. 7.2 for 15-dB equiripple responses of different orders. For each case, the transmission zeros are located symmetrically at $s_i = j1.2(-1)^{i-1}$, where $i \in [1, N]$ and the order of the resonators are given as: [SE1,SH1,SE2,SH2,...]. As observed from the resonant peaks, the EP sections that are closer to the source and load terminations define the band edges while the ones that are in the middle of the network are responsible for the midband in each order. However, the distribution of the resonant peaks are different for different orders.

For the case of third and fifth orders in Fig. 7.2, reducing the number of zeros by one leaves the response symmetrical. As there are two series-EP sections for the third order (SE1 and SE2), replacing one of those with a resonant node results in a symmetrical network with the same k_t^2 values on the remaining EPs. For the fifth order, however, the SE2 section (middle most) resonator should be replaced with a resonant node as it defines the middle of the passband. For the case of even order, reducing the zeros by two is more beneficial as it leaves the response symmetrical. For the case of fourth order, the two resonators to be replaced are SE2 and SH1 whereas for the case of sixth order, these should be SE2 and SH2 (the middle most resonators).

It should be noted again, however, that replacing *any* EP section with a resonant node is beneficial for any order, if the zeros are close to the passband. However, there are additional benefits when replacing the EP section(s) with the highest k_t^2 value(s) with resonant node(s). This will also be demonstrated with the examples in the next sections.

7.1.1 The Proposed Topology

It has been established in the previous section that replacing the middle-most AW resonators of a ladder network with EM resonators and performing a source-to-load coupling can have the largest benefits in terms of reducing the required k_t^2 values for a desired fractional bandwidth. Therefore, the generalized Hybrid-ACEM topology can be depicted in Fig. 7.3.
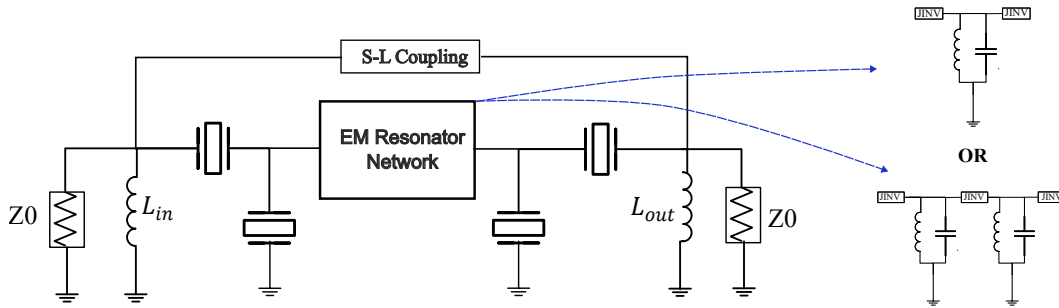
Figure 7.3: The generalized Hybrid-ACEM topology. The AW resonators are located towards the source and the load while the EM resonator network is in the middle of the topology. The EM resonator network can include one or two EM resonators.

As observed from Fig. 7.3, the EM resonator network in the middle can either be a single EM resonator that is coupled to the AW resonators, or it can be two EM resonators that are coupled to each other and to the surrounding AW resonators. The number of AW resonators can be increased or reduced in the same ladder pattern. Furthermore, an S-L coupling can be used to improve the OOB rejection, which, as a consequence can be used to increase the achievable FBW using a particular k_t^2.

In the following subsections, the rules to synthesize the Hybrid-ACEM topology will be defined and the proposed methods will be illustrated with several examples.

7.1.2 Synthesis of Wideband Hybrid-ACEM Filters

Using the extracted pole methodology and the coupling matrix, the challenge in obtaining wide fractional bandwidths using resonators with limited k_t^2 values has been

identified. The solution for this approach is to introduce a resonator technology change at the resonators with the largest required k_t^2 values in the design, which are typically the ones that are in the middle of the network. As an addition, we introduce cross-coupling mechanisms to further enhance the out-of-band rejection performance of the prototype function. The overall aim with this design is to obtain the desired FBW and the required selectivity/OOB rejection performance with the minimum possible k_t^2 value at the resonators. Once that is achieved, if the BAW technology has a k_t^2 value that is greater than that of the function-based synthesis, this will always work for the favor of the designer in that it will have better out-of-band rejection.

In order to design the Hybrid-ACEM filters with cross-coupling mechanisms for minimum possible k_t^2 values, the synthesis rules are reframed as follows:

1. Determine the coupling-routing diagram of the network, i.e., determine which section will be an EP and which section will be a resonant node.

2. Start with the overall polynomial ABCD matrix of the network, i.e., $ABCD_{Full}(s)$,

3. At each step, if $deg(P(s)) = deg(B(s))$ and if the number of the remaining EP sections to be extracted is less than $deg(P(s))$, extract a cross-coupling. Therefore, for hybrid canonical functions, the synthesis starts with a cross-coupling extraction.

4. Continue extracting the EP or resonant sections according to the coupling-routing diagram.

5. After each cross-coupling is extracted, find the roots of the resulting $P(s)$ and update the list of transmission zeros with these roots. The roots may or may not be the same as the initial transmission zero locations. This phenomenon is

also observed in [59] and [101], and will have important consequences in the design. Depending on the strength of the cross-coupling, the updated roots can become complex, which cannot be extracted using this method. If the roots are complex, neglect the real part of the roots. This assumption results in an error in the synthesized response, however, it can be tolerated in certain cases. This will be further explained in the examples.

6. At the end of the extraction process, the polynomials $A(s), C(s), D(s),$ and $P(s)$ should all be equal to zero and $B(s)$, should have a constant value.

7. Construct the coupling matrix with the extracted parameters throughout the steps 1-6.

8. Finalize the design by converting the extracted-pole sections into BVD models of AW sections using the *modified EP-to-BVD* conversion method as introduced in Chapter 6.

The proposed method will be illustrated using three different examples to demonstrate its strength and flexibilities. For the even-order case, a 6-pole-4-zero response with two EM resonators will be synthesized to demonstrate how the method is superior to the conventional method in terms of achieving large bandwidths with limited k_t^2 values. This is shown in Example 1. A 6-pole-6-zero hybrid canonical response extends the bandwidth enlargement capability of the 6-pole-4 zero response by introducing a single source-to-load coupling in Example 2. For the odd-order case, a 5-pole-4-zero response with one EM resonator is depicted in Example 3.

7.1.3 Examples of the Synthesis

Example 1: 6-Pole-4-Zero Symmetric Response

The initial response to be designed is an 18.2-dB equiripple 6-pole 4-zero symmetric function with transmission zero locations given by $[s_i] = j[1.2, -1.2, \infty, -\infty, -1.2, 1.2]$ rad/s. The S-polynomials of the design are provided as:

$$F(s) = s^6 + 1.8s^4 + 0.88s^2 + 0.086$$

$$P(s) = -s^4 - 2.9s^2 - 2.1$$

$$E(s) = s^6 + 1.8s^5 + 3.4s^4 + 3.6s^3 + \tag{7.1}$$

$$3.1s^2 + 1.7s + 0.7$$

$$\text{with } \epsilon = 3 \text{ and } \epsilon_r = 1.$$

This response can be synthesized as a hybrid network as in Fig. 7.4 (a) using the methodology given in Section II B. The initial observation regarding the transmission-zero set is that the first two zeros will need a series-shunt pair whereas the last two zeros result in a shunt-series pair, considering their signs. This transmission zero set is deliberately chosen to show the flexibility of the proposed hybrid response in that the first and the last resonators can be made as both series-AW sections in an even-order response, as opposed to the inability of doing so in a fully inline ladder AW filter of even order [102].
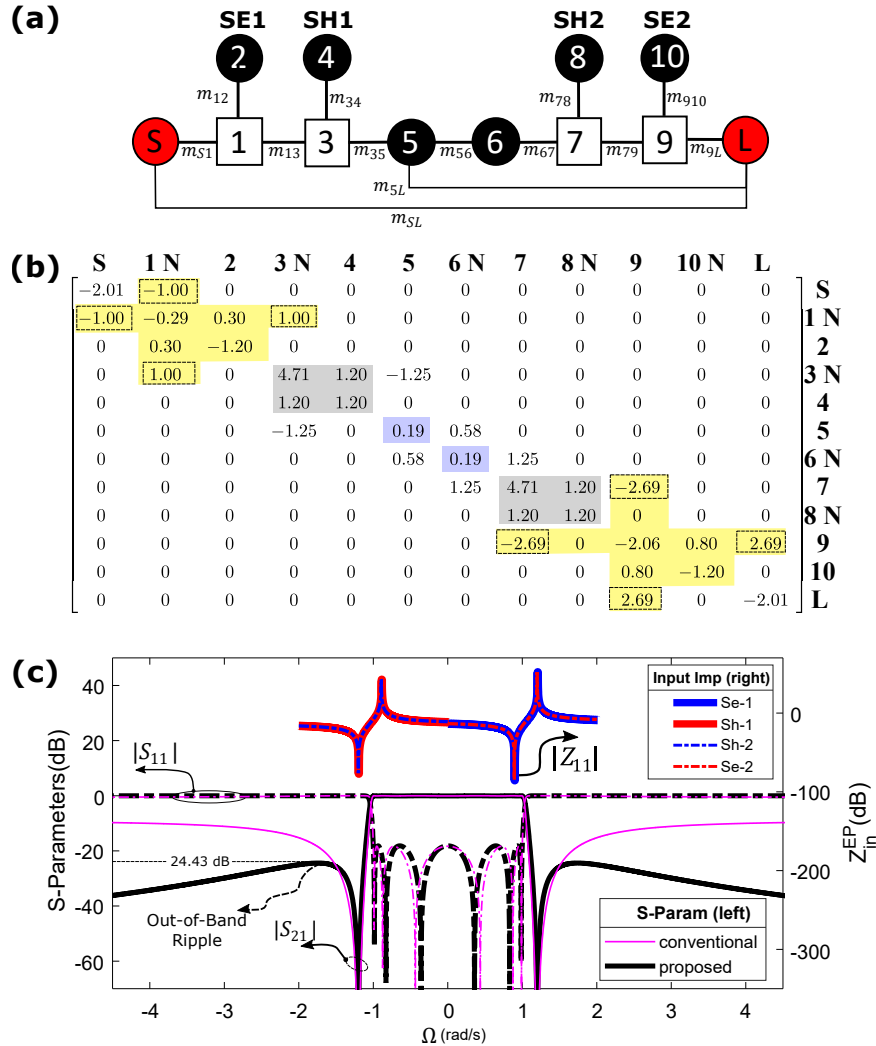
Figure 7.4: (a): The coupling-routing diagram for Example 1 and Example 2. m_{SL} and m_{5L} are equal to zero for Example 1. (b) and (c): The coupling matrix and the normalized frequency response of Example 1, respectively. The magenta trace depicts the response with the conventional method where all the sections are made of EPs when the response has the same return loss with this example (18.2 dB).

Since the response has 4 transmission zeros, four extracted pole sections can realize them, resulting in m_{SL} and m_{5L} to be equal to zero. The coupling matrix of the network is depicted in Fig. 7.4 (b) along with the normalized-frequency response of the network in Fig. 7.4 (c), labeled as "proposed". For this response, the out-of-band ripple (the

peak of $|S_{21}|$ in the out-of-band region as shown in the figure) is obtained as 24.43 dB. On the same graph, the frequency response of an 18.2 dB equiripple conventional 6th order ladder-EP with TZ locations at $j[1.2, -1.2, 1.2, -1.2, 1.2, -1.2]$ rad/s is also depicted in magenta. That is representative of the response that can be obtained with the conventional ladder-AW design. As observed, the out-of-band rejection of the proposed method is significantly stronger compared to the conventional design.

An important observation is that once the sixth-order fully-extracted pole response is converted to the non-canonical hybrid-inline prototype, the shunt and the series extracted-pole sections have the same resonant and anti-resonant points, irrespective of the return loss of the response, as observed in Fig. 7.4 (c). This is a very important corollary, which will result in a uniform k_t^2 distribution among the AW resonators once the design is hybridized. For instance, if denormalized for a FBW of 30%, the k_t^2 distribution of the EP sections are given as: $[k_{t_{SE1}}^2, k_{t_{SH1}}^2, k_{t_{SH2}}^2, k_{t_{SE2}}^2] = [10.78, 10, 78, 10.78, 10.78]\%$ (having four EP sections). This gives a Δ/k_t^2 of 2.78. For the conventional method, the set of k_t^2 values for a FBW of 30% is calculated as $[11.1, 15.4, 29.0, 29.0, 15.5, 11.1]\%$ (six EP sections). This gives a Δ/k_t^2 of 0.96 in addition to an unusable response for the conventional method. For good OOB rejection values, the zeros should be pushed farther away from the passband, which will further increase the required k_t^2 values.

Example 2: 6-Pole-6-Zero Hybrid-Canonical Response

In Example 1, increasing the return loss (in-band-ripple) results in a lower common k_t^2 for all four EP sections at the cost of worse OOB rejection. To strengthen the OOB rejection performance, a symmetric pair of transmission zeros can be added to the 6-pole-4-zero response, which are far away from the passband. These zeros can be realized with an S-L cross-coupling mechanism. This can achieve the same out-of-band

ripple as Example 1 with a better return loss of 20.27 dB and it will be observed that the k_t^2 values are reduced for the same FBW without compromising from the OOB rejection performance. The set of finite-frequency transmission zeros are given by: $[s_i] = j[1.2, -1.2, 3, -3, -1.2, 1.2]$ rad/s. The S-polynomials of the response to be considered are given as in the following:

$$F(s) = s^6 + 1.8s^4 + 0.9s^2 + 0.091$$

$$P(s) = -s^6 - 12s^4 - 28s^2 - 19$$

$$E(s) = s^6 + 2s^5 + 3.7s^4 + 4.1s^3+ \tag{7.2}$$

$$3.7s^2 + 2.1s + 0.94$$

with $\epsilon = 20$ and $\epsilon_r = 1.0013$.

The network for this response can also be charecterized with the coupling-routing diagram given in Fig. 7.4 (a). The initial step to synthesize this response is to extract a cross-coupling mechanism, which extracts the symmetric TZ pair at $\pm 3j$. As the response is symmetric, this operation reduces the order of $P(s)$ by two and the new transmission polynomial is given as:

$$P(s) = -0.46s^4 - 1.3s^2 - 0.91,$$

whose roots are given as: $[s_i^{new}] = [-0.031 + 1.188j, -0.031 - 1.188j, 0.031 + 1.188j, 0.031 - 1.188j]$, which are complex. Normally, as also presented in [90], a network for a response with complex roots cannot be obtained with the extracted-pole method. However, it can be observed that $|Im\{s_i^{new}\}| >> |Re\{s_i^{new}\}| \forall i$. In this case, the real part of each root can be neglected and the extracted-pole synthesis can continue with the new transmission zero set of $[s_i^{new}] =$

145

$j[1.188, -1.188, \infty, -\infty, -1.188, 1.188]$ rad/s. Once the transmission-zero set is updated after the cross-coupling extraction, the remaining network is synthesized just as in the 6-by-4 example.

Example 2, 6-Pole 6-Zero

(a)

	S	1 N	2	3 N	4	5	6 N	7	8 N	9	10 N	L
S	−2.94	−1.00	0	0	0	0	0	0	0	0	0	0.03
1 N	−1.00	−0.19	0.20	1.00	0	0	0	0	0	0	0	0
2	0	0.20	−1.19	0	0	0	0	0	0	0	0	0
3 N	0	1.00	0	6.50	1.16	−1.35	0	0	0	0	0	0
4	0	0	0	1.16	1.19	0	0	0	0	0	0	0
5	0	0	0	−1.35	0	0.15	0.62	0	0	0	0	0
6 N	0	0	0	0	0	0.62	0.18	1.34	0	0	0	0
7	0	0	0	0	0	0	1.34	5.48	1.09	−1.00	0	0
8 N	0	0	0	0	0	0	0	1.09	1.19	0	0	0
9	0	0	0	0	0	0	0	−1.00	0	−0.22	0.22	1.00
10	0	0	0	0	0	0	0	0	0	0.22	−1.19	0
L	0.03	0	0	0	0	0	0	0	0	1.00	0	−2.46

(b)
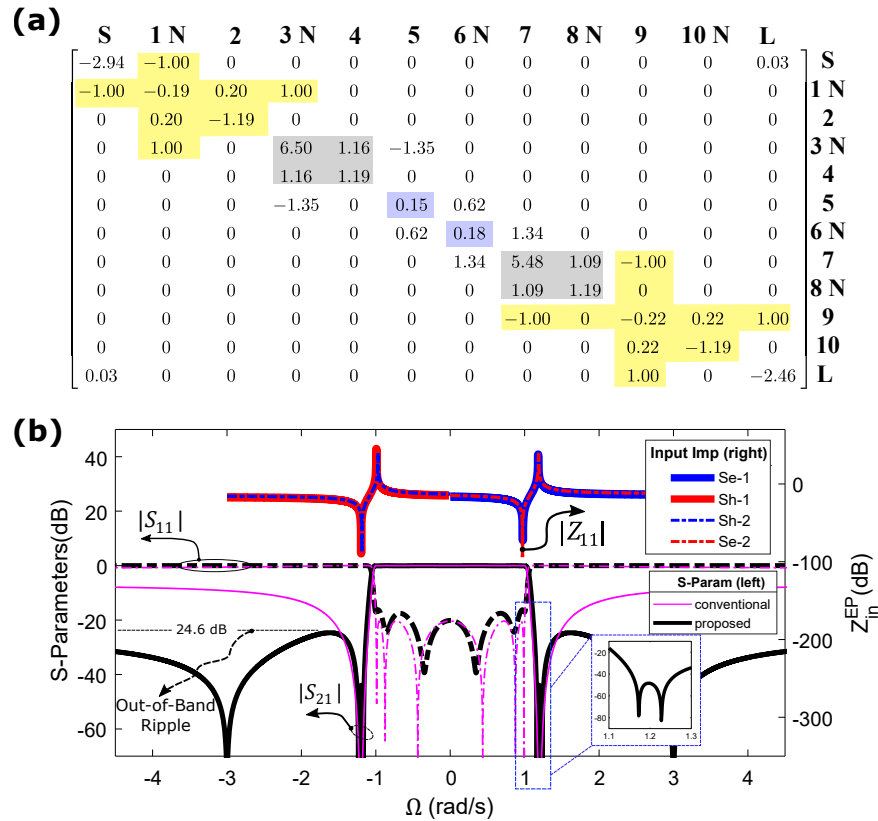
Figure 7.5: (a) and (b): The coupling matrix and the normalized frequency response of Example 2, respectively. The magenta trace depicts the response with the conventional method where all the sections are made of EPs when the response has the same return loss with this example (20.27 dB).

The coupling matrix representation and the normalized-frequency response of the synthesized network are depicted in Fig. 7.5 (a) and (b), respectively. It should be observed that the synthesized response is not a perfect Chebyshev function, especially considering the split transmission zeros at the band edges, since the real parts of the updated transmission zeros are neglected after the cross-coupling extraction. For such cases, it is observed that the magnitude of the complex parts of the updated zeros in-

146

crease when the transmission-zero pair that is added for out-of-band rejection enhancement ($\pm 3j$ rad/s for this example) are chosen closer to the passband. Neglecting the real parts of the updated zeros results in increased inaccuracies if they are large in magnitude. Therefore, it is important to choose such zeros sufficiently far away from the passband to minimize the inaccuracies. The good news is that these zeros are added only for out-of-band rejection improvement and therefore selecting them away from the passband is compatible with the idea behind using them.

With the improved return loss, the proposed 6-pole-6-zero response requires k_t^2 values of $[7.26, 7.26, 7.63, 7.63]\%$ when denormalized for a FBW of 30%, which is even lower than in Example 1, while having almost the same out-of-band ripple. This gives a Δ/k_t^2 of 4.13. Again, the 6-pole-6-zero hybrid-canonical response is compared with the conventional ladder-EP design having the same return loss (20.27 dB) and the TZ set of $j[1.2, -1.2, 1.2, -1.2, -1.2, 1.2]$ rad/s in Fig. 7.4 (e). For this return loss value, the required set of k_t^2 values for the conventional design is given as $[8.86, 12.11, 27.46, 27.46, 12.11, 8.86]\%$. As observed, the required k_t^2 for the conventional design is slightly lower than the case for 18.2 dB return loss, however, it should be noted that the OOB rejection gets worse for the conventional response. Furthermore, the proposed topology can achieve this bandwidth with much lower k_t^2 values.

Example 3: 5-Pole-4-Zero Response

As an odd-order example, a 5-pole-4-zero response is considered. As established in Section II A, employing a single EM resonator can reduce the required k_t^2 significantly compared to its fully-canonical counterpart. The response is an 15.72-dB equiripple with its transmission zeros at $[s_i] = j[1.2, -1.2, \infty, -1.2, 1.2]$ and is characterized by

the following polynomials:

$$F(s) = s^5 + 1.5s^3 + 0.55s,$$

$$P(s) = js^4 + j(2.9)s^2 + j(2.1),$$

$$E(s) = s^5 + 1.7s^4 + 2.8s^3 + 2.8s^2 + 1.8s + 1,$$

(7.3)

$$\text{with } \epsilon = 2 \text{ and } \epsilon_r = 1.$$

The coupling-routing diagram, the coupling matrix, and the normalized-frequency response of the network are depicted in Fig. 7.6 (a), (b), and (c), respectively.
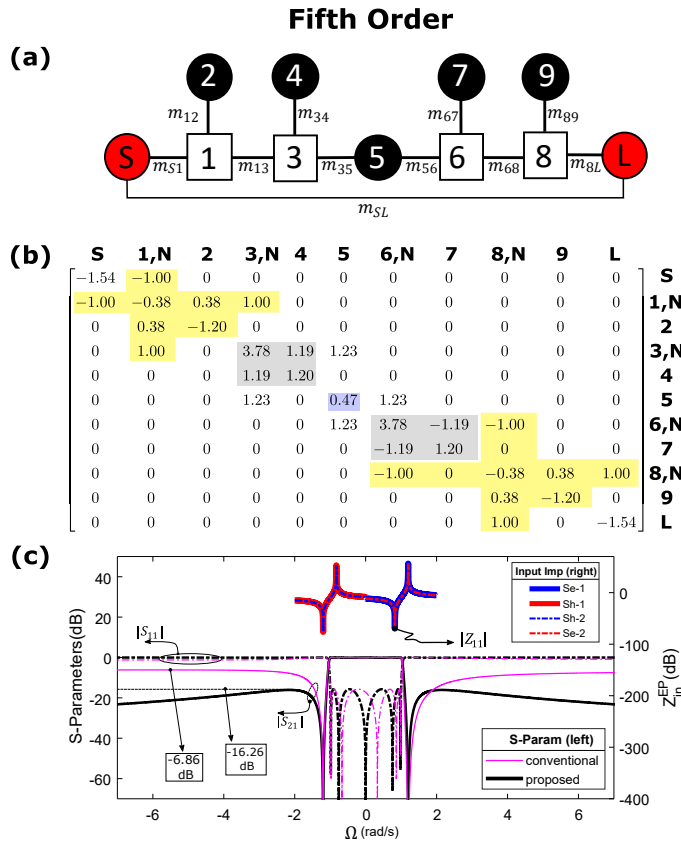
Figure 7.6: (a): The coupling-routing diagram for Example 3. m_{SL} is equal to zero for Example 3. (b) and (c): The coupling matrix and the normalized frequency response of Example 3, respectively. The magenta trace depicts the response with the conventional method where all the sections are made of EPs for each example, when the response has the same return loss with the corresponding example.

The response of a 15.72-dB fully-canonical, fully-EP based filter with TZ loca-

tions at $[s_i] = j[1.2, -1.2, 1.2, -1.2, 1.2]$ rad/s is included with the proposed fifth order response in Fig. 7.6 (d). As observed, the out-of-band rejection of the fully canonical filter, being at 6.86 dB, is much worse compared to the out-of-band ripple of the proposed design, being at 16.26 dB. Furthermore, if denormalized for a 20% FBW, the k_t^2 of the EP sections for the proposed design is calculated as $[8.80, 8.80, 8.80, 8.80]\%$, being lower compared to the one of the conventional design, which is $[8.89, 12.19, 20.14, 12.19, 8.89]\%$. Again, it needs to be mentioned that obtaining a similar out-of-band performance with the conventional design requires the TZ locations located further away from the passband which results in much larger k_t^2 values.

Considering the response of 5th order, it should be mentioned that the roll-off and the out-of-band rejection of this prototype is much less, compared to the sixth-order design, especially when the S-L coupling was included in Example 2. Therefore, this one can achieve reduced FBW values for a particular FBW value. However, the complexity of this one is less compared to the sixth-order since there is a single EM resonator in the network. For the simulations, the stronger case of sixth order design will be considered.

7.2 Simulation Results

The frequency- and bandwidth- denormalized network representation of the coupling matrices for Example 1 and Example 2 are shown in Fig. 7.7 (a) and referred to as the "EP based network". This network has the exact same response one can get by plotting the coupling matrix for a desired f_0 and FBW since the FIR elements are not converted into inductances or capacitances. Using the developed modified EP-to-BVD conversion methodology in Chapter 6, the EP based network can be converted to the Hybrid-ACEM network in Fig. 7.7 (b). The proposed method in Chapter 6 is needed to

149

avoid frequency shifting during this conversion because the conventional method has significant inaccuracies for wideband responses. This is detailed in Chapter 6.

In order to show the validity of the proposed method, both examples are designed for the specifications of 5g n77 band. This includes a maximum of 2 dB IL between 3.300 GHz–4.210 GHz, a minimum attenuation of 25 dB at 2.300 GHz–2.482 GHz and 5.150 GHz–5.925 GHz, 30 dB attenuation between 2.496 GHz–2.570 GHz and 10 dB of attenuation between 4.400 GHz–5.000 GHz bands [61]. The AW resonators in Fig. 7.7 (b) are designed to have a series-Q of 1,200 and the EM resonators are set to have a Q_u of 50. The ideal FBW value of this band (3.300 GHz – 4.210 GHz) is 24.4%, however, including the finite-Q of each resonator, all of the required specifications are met with a target design FBW of 29.1% and 30.49% for Example 1 and 2, respectively.

The circuit simulation of each example are performed in Cadence AWR and shown in Fig. 7.7 (c) and (d), respectively. In each figure, the requirements of the n77 band are also marked with the red lines, which show that the both examples achieve or exceed the required attenuation and IL specifications. The return loss of Example 2 is slightly asymmetrical, however, this is due to the errors in EP-BVD conversion and can be fixed with tuning. For comparison, the response of the non-lossy EP-based network in Fig. 7.7 (a) is also shown as a ground truth for each case.

(a) EP-Based

(b) Hybrid-ACEM

(c)

(d)

(e)

	Example 1, for 5g n77				Example 2, for 5g n77			
	SE1	**SH1**	**SE2**	**SH2**	**SE1**	**SH1**	**SE2**	**SH2**
C_0 (pF)	1.97	2.65	1.97	2.65	3.22	3.89	2.67	3.28
C_m (fF)	182.1	244.6	182.1	244.6	205.6	248.7	180.35	220.5
L_m (nH)	7.55	10.3	7.55	10.3	6.43	1.03	7.35	1.16
k_t^2 (%)	10.33	10.33	10.33	10.33	7.37	7.37	7.74	7.74
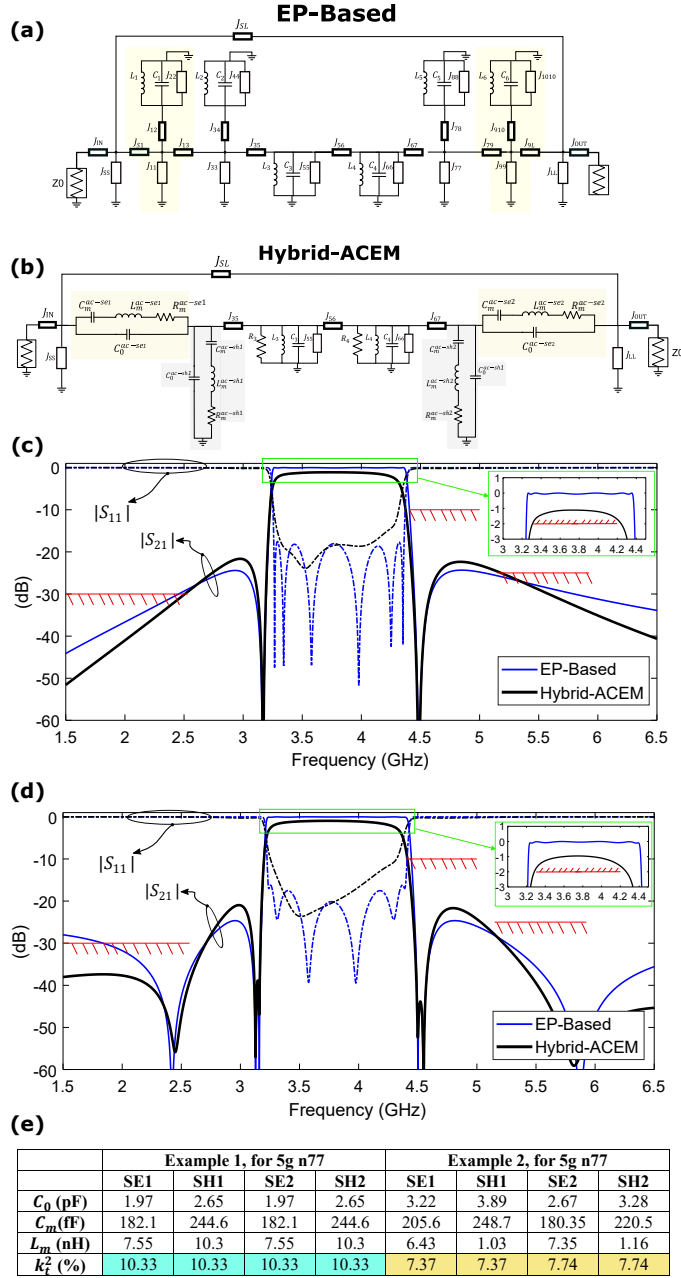
Figure 7.7: (a): The bandpass denormalization of Example 1 and 2, which gives the exact equivalent responses of the coupling matrices. (b): The Hybrid-ACEM network after the EP sections are converted to their BVD equivalents using the proposed conversion in Chapter 6. (c) and (d) : Comparison of the responses of the EP-based (ground truth) and the Hybrid-ACEM network for Example 1 and Example 2. The red lines depict the requirements of the 5g N77 band. The AW resonators have a series Q of 1,200 and the EM resonators are set to have a Q_u of 50. (e): The BVD parameters for the Hybrid ACEM responses in (c) and (d).

Finally, the parameters of the BVD networks in Fig. 7.7 (b) are depicted for each example in Fig. 7.7 (e). It should be realized that the target FBW of approximately 30%, which satisfies the effective bandwidth of 24% is achievable with AW resonators having k_t^2 values of 10.3% in Example 1 and 7.37% and 7.74% in Example 2. This shows that a FBW of up to 4 times the k_t^2 value of the AW resonators are achievable with the proposed study which still satisfies the stringent performance requirements of the 5g n77 band ($\Delta/k_t^2 \approx 4$).

At this point, the role of adding a single capacitive/inductive S-L coupling mechanism to Example 1 and switching to Example 2 should be rephrased. The importance of Example 1 is that for a Hybrid-ACEM network of 4 AW and 2 EM resonators in the middle, the required k_t^2 of all AW resonators are the same, being independent of the return loss. As a result, the required k_t^2 can be lowered by increasing the return loss from 18.2 dB to 20.27 dB. The weakening effect of this action on the OOB rejection can then be recovered to have the same OOB ripple as Example 1 by adding the S-L coupling mechanism, which produces the outer transmission zeros. It should be emphasized that this is not the case for the conventional full-AW based ladder prototype and one needs to sweep both the TZ locations and the return loss to converge on a uniform k_t^2 distribution [56].

To further elaborate on the findings in the previous paragraph, it should be stated that if the second example is forced to have a k_t^2 of 10.33%, just as in Example 1, the achievable FBW is approximately 42 %. This finding is demonstrated in Fig. 7.8. As observed, if one tries to increase the bandwidth of Example 1 (black trace) from 29.1% to 42 % by keeping the k_t^2 constant at 10.33%, the response produces worse OOB rejection, shown with the red trace. However, the S-L coupling mechanism in Example 2 can recover that OOB rejection and keep the OOB ripple at the same value. This means that the S-L coupling mechanism can be used to reduce/adjust the required

k_t^2 values without sacrificing from strong OOB rejection.
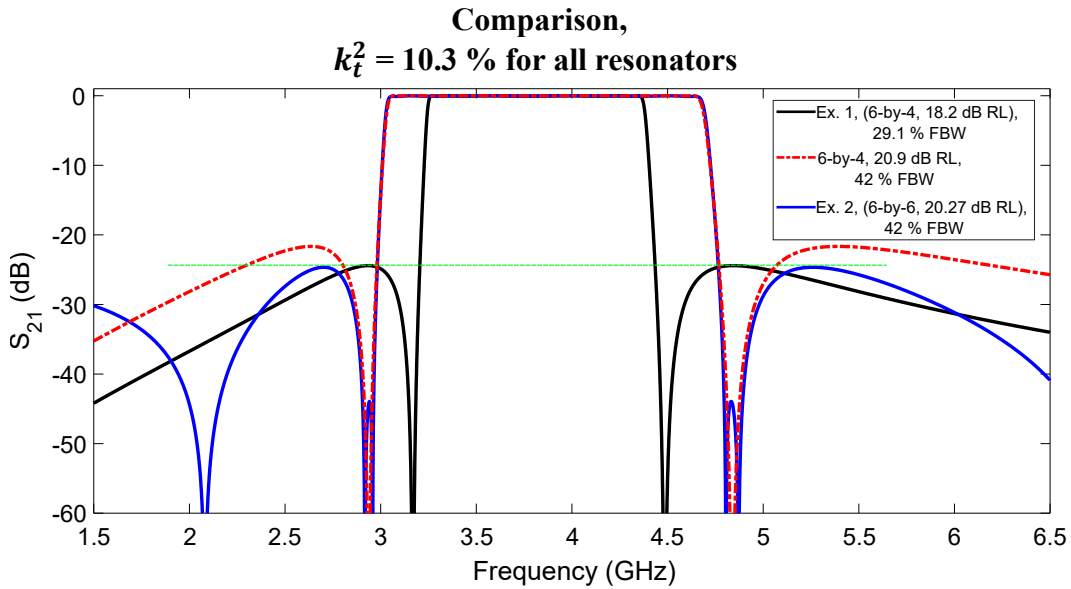
Figure 7.8: Comparison of Example 1 and Example 2 when the k_t^2 values of the resonators are forced to 10.3%. The black trace is the 29.1% FBW response of Example 1, which has 18.2 dB return loss. The red trace is Example 1 whose RL is readjusted to 20.9 dB with a FBW of 42%. The degradation on the OOB rejection should be noticed. The blue trace shows Example 2 with 42% FBW which again needs a k_t^2 of 10.3%. The OOB ripple of Ex.1 and Ex.2 are the same while Ex.2 can have a much larger FBW compared to Ex.1 with the same k_t^2.

7.2.1 Design Sensitivity to the Variations in Component Values

As the proposed Hybrid-ACEM method includes EM resonators which can be lumped- or distributed-element based, the sensitivity of the design for the component value variations is important. This is especially true in the presence of on-chip spiral inductors, which can magnetically couple to each other and have inductance variations. In order to test that behavior of the network, the inductors of the EM resonators in Fig. 7.7 (b) are changed 10% and 20% compared to their prescribed values to observe the effect on the design.

The filter responses when the value of L_3 and L_4 are increased 10% and 20% beyond

their original values are shown in Fig. 7.9, together with the original response.
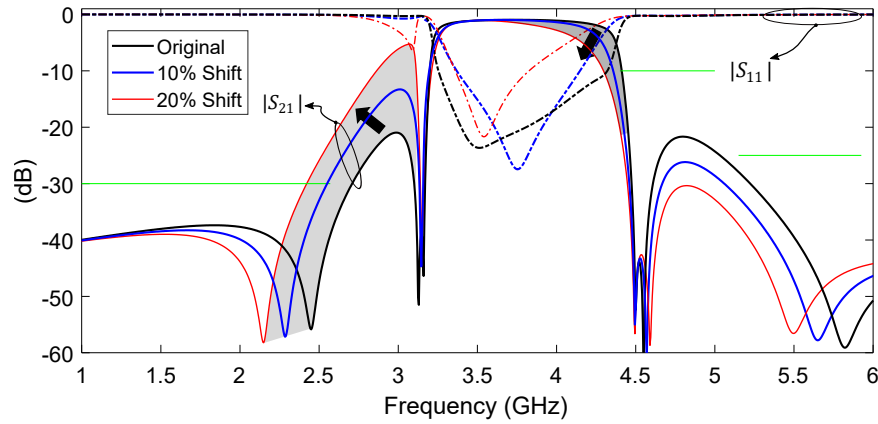
Figure 7.9: Effect of the variations on component values to the filter response. The original response of Example 2 is depicted with the blue trace. In red and the black traces, the inductance values at the EM resonators are varied by 10% and 20%, respectively.

It should be realized in Fig. 7.9 that having a 10% variation on the value of the EM resonaors can be tolerable, however, the effect becomes more severe with 20% variation. It should be realized that the designed filter may go out of the required specifications due to the mutual coupling effect between the inductors, which can cause component value variations.

7.2.2 Comparison with EM Filters

Although it is possible to design narrower bandwidth responses, this method is more beneficial for fractional bandwidth values of 10% or above. Since the design has the potential to be an on-chip filter which can include lossy lumped-element resonators for the EM resonators, the effect of their finite (and low) Q is very important for different FBW values. This effect is analyzed for the 6-pole-4-zero (Example 1) case by simulating the filter response when the Q of the EM resonators (Q_{EM}) are 50. The circuit diagram for this analysis is depicted in Fig. 7.10 (a). The series quality factor of each

AW resonator is chosen to be 1,200.

It has been mentioned that achieving such bandwidths (or having the claimed Δ/k_t^2 values is not possible with the conventional ladder-acoustic design using these low k_t^2 values, however, it is possible to obtain these responses with electromagnetic-only or lumped-element based filters. As a comparison, responses of sixth-order transversal filters (as in Fig. 7.10 (b) are designed using the transversal coupling matrix [5]. These filters have the same response polynomials as Example 1 and their responses are calculated when the Q of each resonator is 50.

The comparison of the filter responses of the fully EM and Hybrid-ACEM prototypes for FBW values of 15% and 25% are depicted in Fig. 7.10 (c). The observation is that the Hybrid-ACEM response always has less insertion loss, flatter passband, and sharper band edges compared to the full-EM response for the same FBW. At this point, it is convenient to define a measure, "usable bandwidth" which refers to the bandwidth at which the insertion loss of the filter increases 1 dB beyond its minimum value. Considering the 15% and 25% FBW values, the Hybrid-ACEM has 0.82 dB and 0.48 dB better IL performance when the minimum IL is considered, respectively. On the other hand, it should be realized that the usable bandwidth of the proposed design is significantly better, compared to the full-EM prototype. The usable bandwidth for a target bandwidth of 937 MHz (25% FBW) is 804 MHz for the Hybrid-ACEM and 640 MHz for the full-EM response. Similarly, for a desired bandwidth of 558 MHz (15% FBW), it is calculated as 463 MHz and 324 MHz for the Hybrid ACEM and the Full-EM responses, respectively.
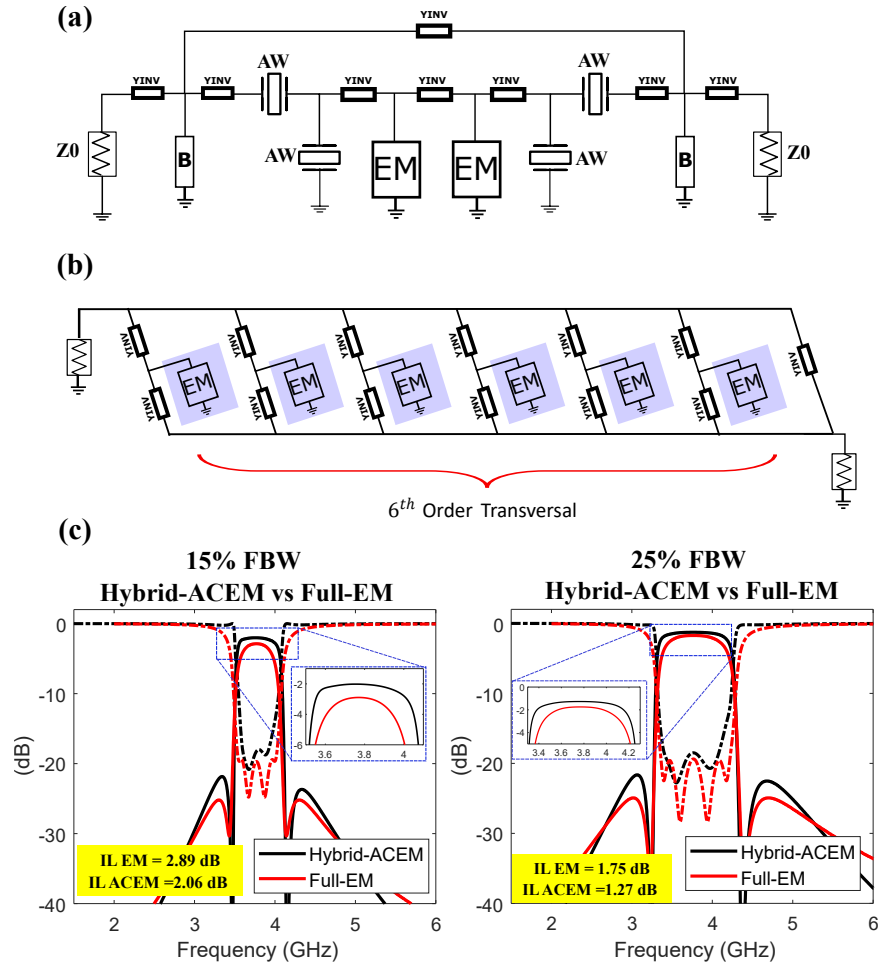
Figure 7.10: Effect of the finite EM resonator quality factor: (a): The EM and AW resonator equivalent circuits for introducing loss. (b): Hybrid-ACEM prototype. (c): Transversal full-EM network with loss. (d) Comparison of the responses for a FBW of 10% and (e): Comparison of the responses for 20%. The Hybrid-ACEM networks use the proposed EP-to-BVD conversion method.

7.3 Experimental Results

As a proof-of-concept, Example 2 is denormalized for a center frequency of 2.66 GHz and a FBW of 11.2%, which spans the frequency range of 2.52 GHz – 2.82 GHz. The designed bandwidth contains the 5g n41 band, however, it is larger than the requirement to show the wideband capability of the proposed method. The lower band-edge is aimed

at achieving a 30 dB attenuation at 2.42 GHz and the upper band is designed to have this attenuation within 100 MHz of the band edge. The determining factor on the choice of the filter frequency is the limited commercial availability of the BAW resonators at the desired resonant frequencies.
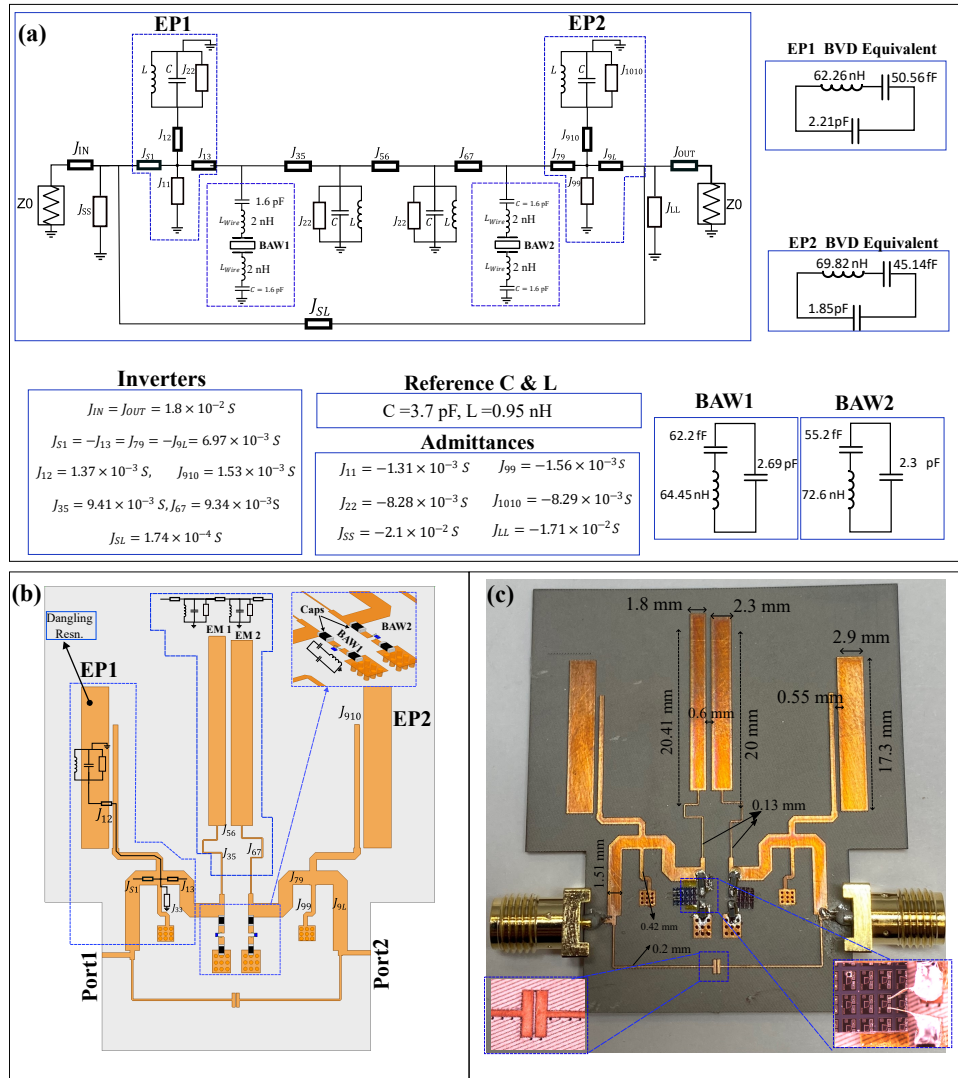
Figure 7.11: Fabricated prototype: (a): The network prototype that explains the fabricated example. The equivalent BVD models of EP1 and EP2 are also depicted as "EP1/EP2 BVD Equivalent". (b): The HFSS model of the fabricated prototype. (c): The fabricated prototype with a magnified view of one of the shunt-connected BAW resonators. (d): Comparison of the simulated and measured results.

The schematic diagram, the HFSS simulation model, and the photograph of the fabricated prototype are depicted in Fig. 7.11 (a), (b), and (c), respectively. To design the prototype with the microstrip technology, these results have been tuned after acquiring the initial values. For the lower band edge, two equivalent shunt-connected BAW resonators are used. These resonators are designed and fabricated by Texas Instruments, utilizing dual-Bragg acoustic mirrors at the bottom and on top of the resonant body [79]. The BAW resonator has a parallel resonance frequency of 2.53 GHz and a series resonance frequency of 2.497 GHz. Furthermore, the parallel quality factor is around 1,200, C_0 is 2.4 pF, and the k_t^2 is 3.5%. The probe measurements of the input impedance of this BAW resonator are depicted in Fig. 7.12 with the black trace. Wedge type bonding with a gold wire of diameter 25 μm is used with Indium pellets to connect the BAW resonator onto the copper layer of the printed-circuit board (PCB). 1.6 pF discrete capacitors from AVX corp. are connected in series to the wirebonded resonator to cancel the wirebond inductance, as depicted in Fig. 7.11 (a). This has an effect on the equivalent C_0, and therefore, the k_t^2 of the BAW. It should be mentioned that the added capacitors reduce the k_t^2 of the BAW from 3.5% to 2.1%. The input impedance of the wirebonded BAW resonator, including the 1.6pF capacitors are also shown in 7.12.

Due to the limited availability of BAW resonators for the upper band edge of the design, the series-AW resonators for the prototype are obtained using microstrip-realized extracted-pole sections. These are shown with EP1 and EP2 in Fig. 7.11 (a) and (b), which emulate series-connected AW based resonators. The BVD models of the series-connected AW resonators that are emulated by EP1 and EP2 are depicted in Fig. 7.11 (a). On the other hand, in order for a one-to-one conversion from EP-to-BVD, $J_{S1} = -J_{13}$ and $J_{79} = -J_{9L}$ should be satisfied. Since both of these inverters are realized with quarter wave transformers, negative coupling is not achieved. In order to fix this problem, the coupling matrix in Fig. 7.5 is scaled by -1 at both S and the L

nodes and to get rid of the negative sign again, scaled once more at node 9 by -1. In this case, the EP sections can be used to emulate the BVD sections.
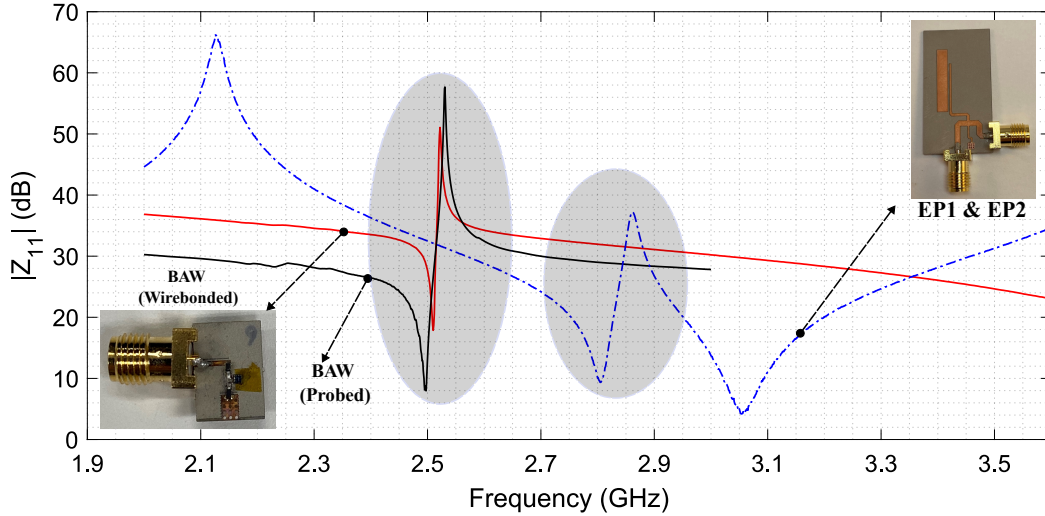
Figure 7.12: Input impedance measurements of the BAW resonator on-die (probed), the wirebonded BAW including the 1.6pF capacitors, and the EP section.

In order to create the EP sections, the dangling resonator in EP1 section in Fig. 7.11 (b) (shown as "Dangling Resn") is designed as a half-wave microstrip to emulate a shunt-connected RLC resonator. The inductance and capacitance of the RLC network are adjusted by tuning the characteristic impedance while the FIR element is adjusted by arranging the resonant frequency. Then, this section is connected to a shorted thin transmission line (depicted as J_{11}) in Fig. 7.11 (b) to complete the EP section. The input and the output inverters to the EP sections (J_{S1} and J_{13} for EP1 whereas J_{79} and J_{9L} for EP2) are realized with quarter-wave transformers. The microstrip-realized EP sections (EP1 and EP2) have a series resonant frequency of 2.809 GHz and a parallel resonant frequency of 2.859 GHz, which emulates a series-connected AW resonator with a k_t^2 of 4.24%. The input impedance measurements of the EP section are depicted in Fig. 7.12 with the blue trace.
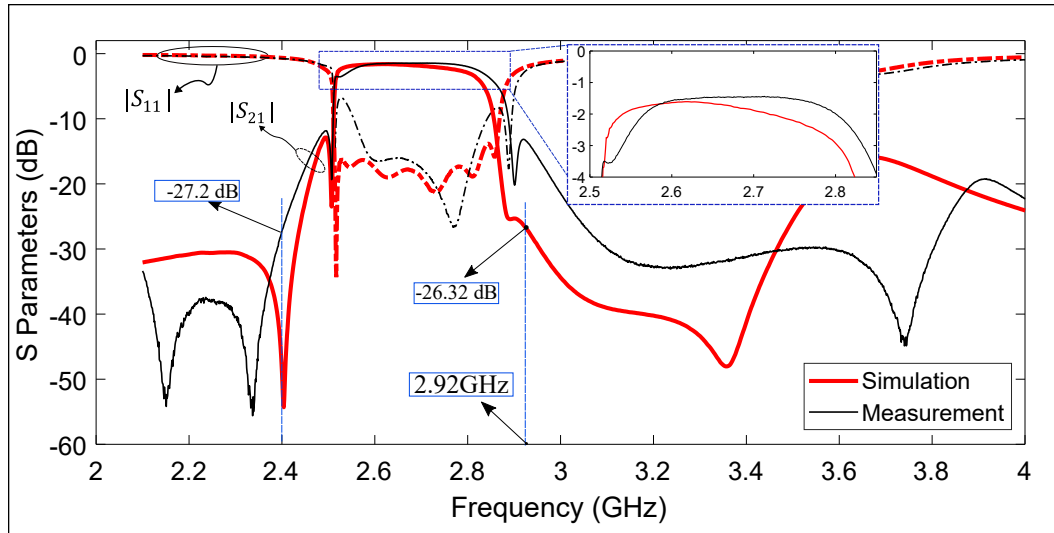
Figure 7.13: Comparison of the simulated and measured results.

The EM resonators (EM1 and EM2) in Fig. 7.11 (a) and (b) are realized with two half-wave microstrip resonators. Their design is carried out similarly to the dangling resonator of the EP sections. The inverters going into the two EM resonators (J_{35} and J_{67}) are realized using quarter-wave transformers while the inter-resonator coupling (J_{56}) is realized by magnetic edge-coupling.

Finally, the input and output admittances J_{SS} and J_{LL} are found redundant after tuning and are removed while J_{IN} and J_{OUT} are tuned for $0.02\,\mathrm{S} = 1/50\,\Omega$. This made it possible to realize these inverters directly with $50\,\Omega$ lines.

For the PCB design, a Rogers RO3010 substrate is patterned using an LPKF Proto-Laser U4 circuit board plotter. The measured S-parameters of the network are shown in Fig. 7.11 (d). It should be noted that the response of the design is sensitive to the inaccuracies at the dangling resonator sections of EP1 and EP2, therefore, care needs to be taken during the fabrication.

The simulation and measurement results of the design are depicted in Fig. 7.13. As observed from the simulation results, the lower band edge is designed to create a

TZ at 2.4 GHz, which is the upper band edge of n40 band. For the measured result, however, this is slightly shifted but there is still 27.5 dB of attenuation at 2.4 GHz. The lower band edge is defined by the shunt resonator and the initial dip at S_{21} as well as the overall rolloff is much stronger compared to the upper band edge. For the upper edge, the simulations were able to achieve 26.32 dB of attenuation at 2.92 GHz, which is 100 MHz above the desired bandedge frequency of 2.82 GHz. However, for the measured results, the upper band edge is slightly shifted. This is due to the strong effects of slight frequency shifts while fabricating the EP networks. The minimum insertion loss of the fabricated prototype is 1.45 dB and a flat passband at the midband region is observed.

7.4 Extension of the Design for Different Fractional Bandwidth Values and Comparison with the State-of-the-Art

As the Hybrid-ACEM method has been established with fabrication results that prove the concept, it is important to understand the limits of achievable fractional bandwidth values and also to consider the insertion loss levels for these FBW values. In that sense, the sixth order prototype with source-to-load coupling can achieve significantly wide FBW values in addition to having a common k_t^2 value among the AW based resonators. Therefore, this prototype will be considered for determining the limits of the design.
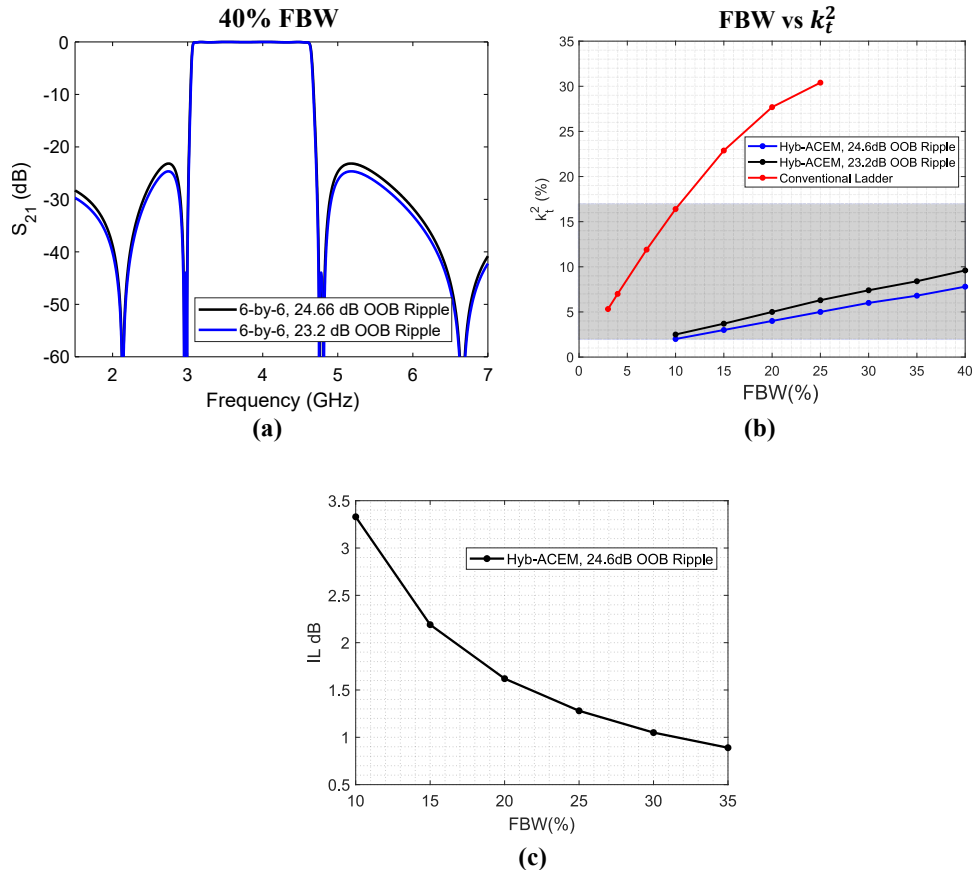
Figure 7.14: Extension of the design for larger FBW values. (a): Comparison of two responses with the same 6-pole-6-zero topology but having different OOB ripple values, when denormalized for 40% FBW. (b): Achievable FBW with respect to the required k_t^2 for the two Hybrid-ACEM responses in (a) (black and the blue traces), for the conventional ladder prototype of 7th order in Chapter 6, and the state-of-the art transversal-AW filter. (c): Insertion loss value of the sixth-order Hybrid-ACEM response with respect to the FBW, when the Q of the EM resonators are 50. The dark shaded region shows the practically achievable k_t^2 values of AW resonators.

Fig. 7.14 (a) depicts two different sixth-order hybrid-canonical responses that can be realized with the Hybrid-ACEM prototype. These responses have OOB ripple values of 24.66 dB and 23.2 dB and are denormalized for a FBW of 40%. For these two responses, the required k_t^2 values are plotted along with the desired fractional bandwidth in Fig. 7.14 (b). On the same graph, the achievable FBW is plotted with respect to the required k_t^2 for the conventional ladder prototype of 7th order, as explained in Chapter 6.

The shaded region on the graph demonstrates the practical values of k_t^2 that can be achieved today.

There are multiple observations regarding Fig. 7.14 (b). The first observation regarding this graph is that the OOB ripple and the return loss of the Hybrid-ACEM design can be adjusted to increase the Δ/k_t^2. For instance, for the case where OOB ripple is 24.6 dB, this ratio is around 4, however, if the OOB ripple is lowered to 23.2 dB, this ratio is approximately 5. Secondly, Δ/k_t^2 for the conventional seventh-order design is below 1, which gives an upper limit for the achievable FBW of around 15%. However, it can be observed that the achievable FBW is within the region of practical k_t^2 values for up to 40% FBW with the Hybrid-ACEM response.

Furthermore, the obtained insertion loss when the two EM resonators in the design have a Q value of 50 is also depicted in Fig. 7.14 (c) for visualization. The obtained insertion loss reduces with the increased fractional bandwidth, as observed from Fig. 7.14 (c), which works for the favor of the designer and can go below 1 dB for FBW values of 30%.

This analysis of the achievable FBW value with respect to the required k_t^2 values sets the metrics which can be used to compare the performance of two filters. It should be realized that a wideband response is only valuable to be achieved when it can provide a good out-of-band rejection.

In Table 7.1, the performance of the fabricated prototype in this study is compared with other significant studies which can be considered as the state-of-the art in terms of achieving large fractional bandwidth values.

In Table 7.1, the proposed study is included with the fabricated example of 11.2% FBW and using the simulated example which includes the n77 filter. Since the used AW resonators have different k_t^2 values in the studies, the FBW/k_t^2 can become an important metric as well. In order to have a fair comparison, the studies that include similar OOB

Table 7.1: A table of comparison with the related work in literature.

Ref	f0 (GHz)	Min. IL (dB)	RL (dB)	FBW (%)	OOB R. (dB) *	Ord	k_t^2	Tech	Δ/k_t^2
[54]	2.05	1.8	~15	17	>30	8	8.8	SAW & Cpl. ln	1.93
[61]	3.69	<=1	15	25	>30	4	13	Fully on-Chip	1.92
[55]	2.15	1.87	10	24.9	20	-	6.37	FBAR & Msp. ln	3.9
This	2.66	1.45	18	10.2	35	6	2.1& 4.24	BAW &EM	3.2
This, n77 Sim	3.77	0.94	15	30 (des), 24 (eff)	>35	6	7.3 & 7.7	Sim	4.05

* OOB Rej Refers to the out-of-band rejection which is obtained 300 MHz beyond the band edges.

rejection performances should be compared since it has been clearly shown in Fig. 7.8 that obtaining a larger FBW$/k_t^2$ is possible by having a weaker OOB rejection. For that, the OOB rejection performance that is 300 MHz beyond the band edges are considered. It can be observed that considering the designs having large FBW values that have better than 35 dB OOB rejection performances, our proposed study has the largest ratio which shows the maximum flexibility of having wideband filters in the presence of fixed k_t^2 values and while keeping the OOB rejection performance strong.

7.5 Conclusion and Discussion

In this chapter, the foundations of using EM (lumped or distributed) resonators within the design of BAW filters is presented with the aim of having significantly larger fractional bandwidth and out-of-band rejection performance while keeping a low insertion loss in the presence of low-k_t^2 resonators.

This study includes multiple contributions to the design of wideband microwave filters, compared to the introduction of this concept in [50]. Wide fractional bandwidths (such as 20%) are shown to be achievable using AW resonators with k_t^2 values of 5.8% or even lower. It has been shown the ladder AW resonator based conventional method-

ologies cannot achieve such fractional bandwidths and OOB rejection using AW resonators with such k_t^2 values. Responses of higher orders are considered and compared. The analysis on which and how many resonators in an inline EP-based filter to replace with EM resonators is performed. It has been shown that this can vary for designs of different orders. A simplification methodology for fully asymmetric responses is also provided. The analysis of the effects of finite-Q EM resonators is performed to give an insight on future on-chip implementation. It has been shown that including a single EM resonator can even have a significant advantage to accomplish much wider FBW values on certain filter orders. It has also been shown that using a cross-coupling to implement a pair of TZs can further reduce the required k_t^2 significantly while keeping the out-of-band ripple at the constant value.

As a proof-of-concept, it has been shown that an 11.2% FBW sixth-order, fully-canonical equiripple filter is achieved using a BAW resonator with a k_t^2 of 3.5% (effective value of 2.1%), which is not possible with the conventional ladder design methodologies. With the conceptual proof, the FBW and OOB limitations of AW-based filters are successfully mitigated using the hybrid concept.

Chapter 8

Summary, Conclusions, and Future Work

This dissertation can be considered as a technical and a methodological pathway for developing filters that can satisfy the growing demands of the next generation wireless transceivers. The summary of the work, the conclusions, the contributions and the future work will be discussed in this chapter.

8.1   Summary of the Work

The development of the dissertation starts with a discussion on the importance of the RF filters for wireless communication systems. As an example, the frequency spectrum allocation for 1.8 GHz to 7.125 GHz is shown in Fig. 8.1, which includes multiple operation bands. In order to prevent the interference and leakage from one band to another, the wireless transceivers need filters with high performance. For instance, a microwave filter operating at n41 band requires less than 2 dB insertion loss between 2.496 GHz–2.690 GHz and more than 30 dB attenuation at 2.4 GHz. This requires high-Q resonators ($Q_u > 1000$) and they need to have small form factors to fit inside of a chip. The high-Q EM resonators including cavities are too large to fit into integrated circuits and are not usable for such applications.

It has been discussed in Chapter 1 that the acoustic-wave filters dominate the on-
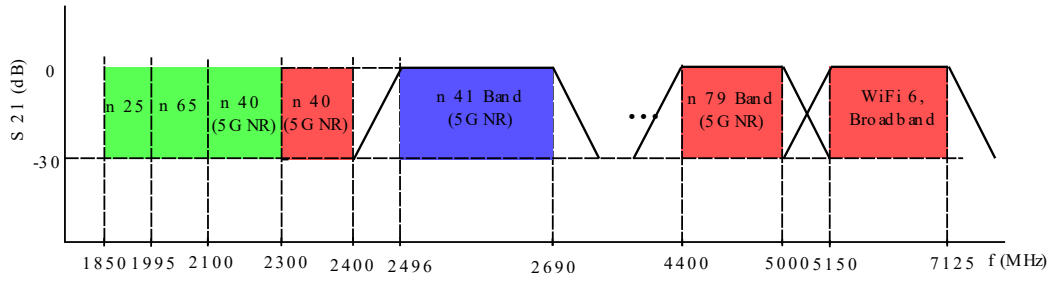
Figure 8.1: Wireless communication bands in the frequency spectrum between the frequencies 1850 MHz to 7125 MHz.

chip filter market due to their high quality factor values and chip-scale physical sizes. At present, there are studies that can achieve filters for n41 (7.5% FBW) band. Furthermore, a new state-of-the art filter is designed in [61] for n77 (24.4% FBW) band using AW resonators with k_t^2 values of 13.5%. However, the intrinsic parameter of k_t^2 puts an upper limit on the achievable fractional bandwidth with the AW based filters and the future applications, such as WiFi 6 will require ultra-large FBW values, such as 30%. This requires k_t^2 values above 30% with the conventional synthesis methods and such values are not practical to be achieved.

In Chapter 2, the resonators that are used at the microwave frequencies are considered. These include EM based and AW based resonators. This is followed by the development of a generalized Chebyshev function, the analysis and the synthesis of the coupling matrix of an arbitrary order, and the theory of the extracted-pole-synthesis methodology in Chapter 3, 4, and 5, respectively. Until that point, the strong theory of the coupled-resonator based filter design background has been established for the understanding and the solution of the bandwidth enlargement problem of the filters based on AW resonators.

In Chapter 6, the conversion methodologies from extracted-pole sections to the BVD equivalent network of the AW resonators is discussed. It has been argued that the conventional conversion methodology is not suitable for FBW values above 10%

and a new conversion methodology is proposed. Furthermore, the CM-based design of AW based filters is also discussed in this chapter. As an example, two seventh-order AW-based filters for n41 and n77 bands are synthesized, which require resonator k_t^2 values of 12% and 30% for FBW values of 7.5% and 24.4%, respectively. This gives Δ/k_t^2 values of around 0.62 and 0.81, respectively which is below 1. Considering that the achievable k_t^2 values with the state-of-the-art AlScN BAW resonators include 16% k_t^2 and a Q of 1070 [72], designing filters for wide bandwidths like n77 band is not possible with this method.

Chapter 7 starts with the precise interpretation of the reason for not being able to obtain wideband microwave filters using AW based resonators. This interpretation is based on the analysis of the Chebyshev functions that characterize the response and it is mathematically proven that the introduction of EM resonators at certain places within the network can provide significantly wider FBW values. This theory is backed with a new set of rules for the design of the novel Hybrid Acoustic-Electromagnetic (Hybrid-ACEM) filters. It has been theoretically shown that the sixth-order Hybrid-ACEM design can achieve the n77 band specifications with four AW resonators having k_t^2 values of approximately 7.5%. Considering that the target design FBW is 30.4%, the proposed method can achieve Δ/k_t^2 values of larger than 4. As a proof-of-concept, a sixth-order 11.2% FBW filter is designed, fabricated, and tested including BAW resonators with a k_t^2 of 3.5%. The measurement results demonstrate the validity and the significance of the developed method for the solution of this problem.

8.2   Conclusions and the Importance of the Work

In this study, it is hypothesized that the the maximum Δ/k_t^2 value for AW based filters can be achieved by incorporating EM resonators to the network while still complying

with the stringent insertion loss and the OOB rejection performance requirements of the wireless communication bands.

Throughout this study, this hypothesis is thoroughly investigated and a systematic methodology of maximizing the Δ/k_t^2 is described with real application examples such as the 5g n41 and 5g n77 bands. The proposed methodology is proven with the prototype filter design of sixth-order, which achieved a Δ/k_t^2 of 3.2. It is shown by simulations that the Hybrid-ACEM method can further achieve Δ/k_t^2 values above 4. To the knowledge of the author, this is the largest bandwidth enhancement in the literature. Improving the Δ/k_t^2 has the following benefits for the design of the AW based filters:

- It makes it possible to design wideband filters for the applications that need 30% or more FBW values.

- It reduces or eliminates the need for Sc doping process on the AlN substrate, which is an extra fabrication process.

- If the available k_t^2 is larger than the needed value by the Hybrid-ACEM design, enforcing the k_t^2 to a higher value will result in better OOB rejection performance.

These benefits provide significant flexibilities for the design of on-chip filters. Overall, the demonstrated method is an important candidate that can be extended for the design of wideband fully on-chip microwave filters and opens a pathway for the integration of the microwave filters on the system-on-a-chip applications.

8.3   Future Work

This dissertation includes the theoretical development of the methodology that opens a new pathway to reduce the limitations of the on-chip microwave filters and a proof-of-concept was designed using the available BAW resonators to the authors. The initial

future work of this study includes the design of a fully on-chip filter for a wideband application. An example circuit schematic diagram of a Hybrid-ACEM filter for on-chip integration is shown in Fig. 8.2. The it should be observed that the EM resonator network in the middle is completely converted into lumped components. The admittance inverters between the resonators are converted into π-networks made of capacitors and inductors and are absorbed into the adjacent resonators.
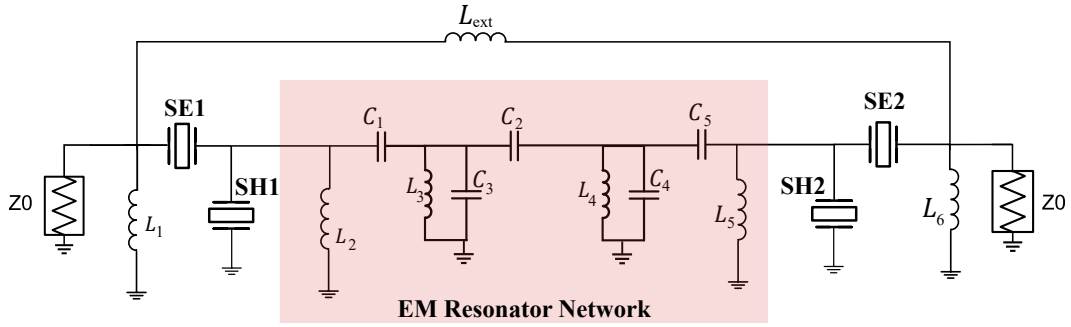
Figure 8.2: An example Hybrid-ACEM filter with lumped components for on-chipintegration. This example is designed for the 5g n77 band.

The circuit diagram for the on-chip implementation is aimed for the 5g n77 band and the values of the lumped components of the design are depicted in Table. 8.1. It should be realized that the values of the design are suitable for on-chip implementation, except for the S-L coupling inductor L_{ext}. This inductor has a value of 62.9 nH and can be placed off-chip. In addition to the values of the lumped elements, the BVD parameters of the BAW resonators are depicted in Fig. 8.2. It should be realized that the k_t^2 values of the resonators are about $8.27\% - 8.59\%$, which can be achievable with the AlN based BAW technology.

Table 8.1: Values of the lumped elements for the filter in Fig. 8.2

	1	2	3	4	5	6	Ext
C_i (pF)	1.23	0.42	1.13	1.30	1.08	-	-
L_i (nH)	0.93	1.57	0.73	0.73	1.57	1.03	62.9

Table 8.2: Values of the BVD parameters for the filter in Fig. 8.2

	SE1	SH1	SE2	SH2
C_0 (pF)	3.69	4.68	3.38	4.26
C_m (fF)	270.2	338.4	258.9	321.3
L_m (nH)	5.12	7.84	5.38	8.253
k_t^2 (%)	8.38	8.27	8.69	8.59
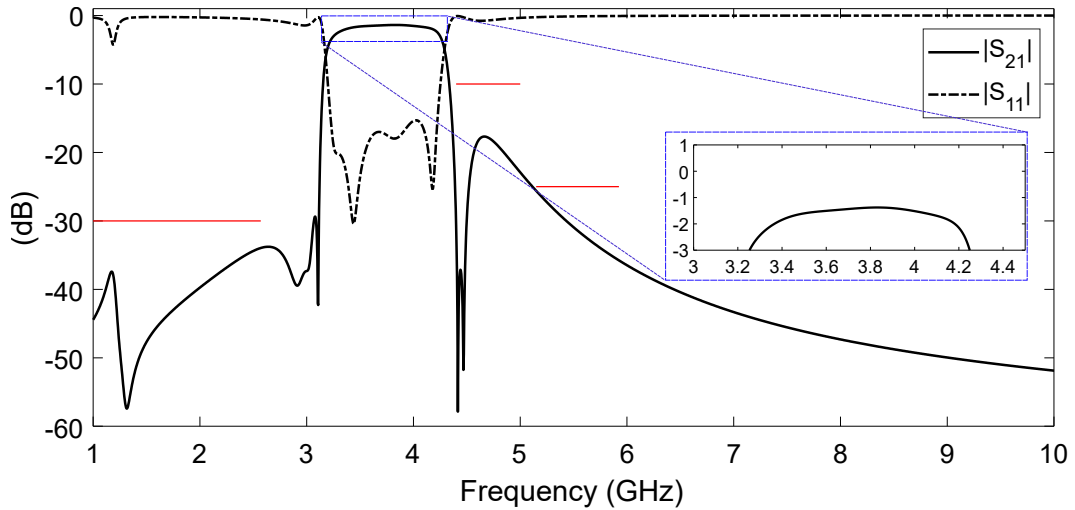
Figure 8.3: Simulation results of the designed Hybrid-ACEM filter for on-chip implementation.

The simulation results of the filter are depicted in Fig. 8.3. It should also be realized that the required rejection levels of the n77 band are marked with the red lines and the

simulated results meet the requirements. The quality factor of each inductor in the design is set to 50, which gives a minimum insertion loss value of 1.38 dB. In addition to the requirements of the n77 band, the simulation results also show strong rejection at the far out-of-band.

It should be mentioned that the simulation results observed here does not include electromagnetic simulations and are performed in Cadence AWR. Therefore, the coupling between the inductors and capacitors are not captured and this will require more work to be designed.

References

[1] M. LLC. "5g nr frequency bands." (2023), [Online]. Available: https://www.
rfwel.com/us/index.php/5g-nr-frequency-bands. (visited on 04/29/2023).

[2] R. Cameron, R. Mansour, and C. Kudsia, *Microwave Filters for Communication Systems: Fundamentals, Design and Applications*. Wiley, 2007.

[3] D. Pozar, *Microwave Engineering*. Wiley, 2011.

[4] R. Cameron, "General coupling matrix synthesis methods for chebyshev filtering functions," *IEEE Transactions on Microwave Theory and Techniques*, vol. 47, no. 4, pp. 433–442, 1999. DOI: 10.1109/22.754877.

[5] R. Cameron, "Advanced coupling matrix synthesis techniques for microwave filters," *IEEE Transactions on Microwave Theory and Techniques*, vol. 51, no. 1, pp. 1–10, 2003. DOI: 10.1109/TMTT.2002.806937.

[6] P. Jarry, *Advanced Design Techniques and Realizations of Microwave and RF Filters*. Feb. 2008. DOI: 10.1002/9780470294178.

[7] J.-S. Hong, *Microstrip Filters for RF/Microwave Applications*. 2001.

[8]   D. Peroulis, E. Naglich, M. Sinani, and M. Hickle, "Tuned to resonance: Transfer-function-adaptive filters in evanescent-mode cavity-resonator technology," *IEEE Microwave Magazine*, vol. 15, no. 5, pp. 55–69, 2014. DOI: 10.1109/MMM.2014.2321103.

[9]   A. Abbaspour-Tamijani, L. Dussopt, and G. Rebeiz, "Miniature and tunable filters using mems capacitors," *IEEE Transactions on Microwave Theory and Techniques*, vol. 51, no. 7, pp. 1878–1885, 2003. DOI: 10.1109/TMTT.2003.814317.

[10]   X. Liu, L. P. B. Katehi, W. J. Chappell, and D. Peroulis, "High-Q tunable microwave cavity resonators and filters using soi-based rf mems tuners," *Journal of Microelectromechanical Systems*, vol. 19, no. 4, pp. 774–784, 2010. DOI: 10.1109/JMEMS.2010.2055544.

[11]   S. Saeedi and H. H. Sigmarsson, "Miniaturized evanescent-mode cavity siw bandpass filter with spurious suppression," in *2018 IEEE Radio and Wireless Symposium (RWS)*, 2018, pp. 234–236. DOI: 10.1109/RWS.2018.8304996.

[12]   S. Saeedi and H. H. Sigmarsson, "Miniaturized evanescent-mode cavity siw bandpass filter with spurious suppression," in *2018 IEEE Radio and Wireless Symposium (RWS)*, 2018, pp. 234–236. DOI: 10.1109/RWS.2018.8304996.

[13]   S. Saeedi, G. Ariturk, and H. H. Sigmarsson, "Compact wide-stopband bandpass filter based on highly-loaded substrate integrated cavity resonators," in *2020 IEEE Radio and Wireless Symposium (RWS)*, 2020, pp. 145–147. DOI: 10.1109/RWS45077.2020.9050048.

[14] H. Joshi, H. H. Sigmarsson, S. Moon, D. Peroulis, and W. J. Chappell, "High-Q fully reconfigurable tunable bandpass filters," *IEEE Transactions on Microwave Theory and Techniques*, vol. 57, no. 12, pp. 3525–3533, 2009. DOI: 10.1109/ TMTT.2009.2034309.

[15] J. Rhodes, "A low-pass prototype network for microwave linear phase filters," *IEEE Transactions on Microwave Theory and Techniques*, vol. 18, no. 6, pp. 290–301, 1970. DOI: 10.1109/TMTT.1970.1127222.

[16] S. Alseyab, "A novel class of generalized chebyshev low-pass prototype for suspended substrate stripline filters," *IEEE Transactions on Microwave Theory and Techniques*, vol. 30, no. 9, pp. 1341–1347, 1982. DOI: 10.1109/TMTT. 1982.1131258.

[17] J. Rhodes, "The generalized direct-coupled cavity linear phase filter," *IEEE Transactions on Microwave Theory and Techniques*, vol. 18, no. 6, pp. 308– 313, 1970. DOI: 10.1109/TMTT.1970.1127224.

[18] Y. Wang *et al.*, "Half mode substrate integrated waveguide (hmsiw) band-pass filter," *IEEE Microwave and Wireless Components Letters*, vol. 17, no. 4, pp. 265–267, 2007. DOI: 10.1109/LMWC.2007.892958.

[19] B. Liu, W. Hong, Y.-Q. Wang, Q.-H. Lai, and K. Wu, "Half mode substrate integrated waveguide (hmsiw) 3-db coupler," *IEEE Microwave and Wireless Components Letters*, vol. 17, no. 1, pp. 22–24, 2007. DOI: 10.1109/LMWC. 2006.887244.

[20]   T. R. Jones and M. Daneshmand, "Miniaturized folded ridged quarter-mode substrate integrated waveguide rf mems tunable bandpass filter," *IEEE Access*, vol. 8, pp. 115 837–115 847, 2020. DOI: 10.1109/ACCESS.2020.3004116.

[21]   X. Wang, X.-W. Zhu, C. Yu, P.-F. Liu, and X.-S. Shi, "Design of the quarter-mode substrate integrated waveguide in-phase and out-of-phase filtering power divider," in *2018 IEEE MTT-S International Wireless Symposium (IWS)*, 2018, pp. 1–3. DOI: 10.1109/IEEE-IWS.2018.8400917.

[22]   C. Ma and C. Jin, "Compact triple-mode filter based on quarter-mode substrate integrated waveguide," in *2015 Asia-Pacific Microwave Conference (APMC)*, vol. 2, 2015, pp. 1–3. DOI: 10.1109/APMC.2015.7413195.

[23]   N. Delmonte, M. Bozzi, L. Perregrini, and C. Tomassoni, "Cavity resonator filters in shielded quarter-mode substrate integrated waveguide technology," in *2018 IEEE MTT-S International Microwave Workshop Series on Advanced Materials and Processes for RF and THz Applications (IMWS-AMP)*, 2018, pp. 1–3. DOI: 10.1109/IMWS-AMP.2018.8457166.

[24]   M. Nick and A. Mortazawi, "Low phase-noise planar oscillators based on low-noise active resonators," *IEEE Transactions on Microwave Theory and Techniques*, vol. 58, no. 5, pp. 1133–1139, 2010.

[25]   Y. Ishikawa, S. Yamashita, and S. Hidaka, "Noise design of active feedback resonator bef," *IEEE Transactions on Microwave Theory and Techniques*, vol. 41, no. 12, pp. 2133–2138, 1993.

[26] S. Saeedi, S. Atash-bahar, and H. H. Sigmarsson, "Active tunable substrate integrated evanescent-mode cavity resonator using negative resistance," in *2016 IEEE Radio and Wireless Symposium (RWS)*, 2016, pp. 87–90.

[27] C. .-. Chang and T. Itoh, "Microwave active filters based on coupled negative resistance method," *IEEE Transactions on Microwave Theory and Techniques*, vol. 38, no. 12, pp. 1879–1884, 1990.

[28] M. Ito, K. Maruhashi, S. Kishimoto, and K. Ohata, "60-ghz-band coplanar mmic active filters," *IEEE Transactions on Microwave Theory and Techniques*, vol. 52, no. 3, pp. 743–750, 2004.

[29] R. Kaunisto, K. Stadius, and V. Porra, "Active mmic filters with negative resistance compensation," *ELECTRONICS LETTERS*, vol. 34, no. 12, pp. 1236–1237, 1998.

[30] L. K. Yeung, X. Zou, and Y. E. Wang, "Parametric quality factor enhancement for highly-selective miniaturized bpfs," in *2020 IEEE Radio and Wireless Symposium (RWS)*, 2020, pp. 148–151.

[31] L. K. Yeung, X. Zou, and Y. E. Wang, "Bpfs with parametrically compensated passband insertion loss and selectivity," in *2020 IEEE International Microwave Symposium*, 2020, pp. 803–806.

[32] Y. Ishikawa, S. Yamashita, and S. Hidaka, "Noise design of active feedback resonator bef," *IEEE Transactions on Microwave Theory and Techniques*, vol. 41, no. 12, pp. 2133–2138, 1993.

[33] S. Lucyszyn and I. D. Robertson, "Monolithic narrow-band filter using ultrahigh-q tunable active inductors," *IEEE Transactions on Microwave Theory and Techniques*, vol. 42, no. 12, pp. 2617–2622, 1994. DOI: 10.1109/22.339805.

[34] L. Pantoli, V. Stornelli, and G. Leuzzi, "High dynamic range, low power, tunable, active filter for rf and microwave wireless applications," *IET Microwaves, Antennas & Propagation*, vol. 12, no. 4, pp. 595–601, 2018. DOI: https://doi.org/10.1049/iet-map.2017.0685.

[35] R. V. Snyder and D. L. Bozarth, "Analysis and design of a microwave transistor active filter," *IEEE Transactions on Microwave Theory and Techniques*, vol. 18, no. 1, pp. 2–9, 1970. DOI: 10.1109/TMTT.1970.1127126.

[36] Yue Wu, Xiaohui Ding, M. Ismail, and H. Olsson, "Rf bandpass filter design based on cmos active inductors," *IEEE Transactions on Circuits and Systems II: Analog and Digital Signal Processing*, vol. 50, no. 12, pp. 942–949, 2003. DOI: 10.1109/TCSII.2003.820235.

[37] G. Leuzzi, V. Stornelli, L. Pantoli, and S. Del Re, "Single transistor high linearity and wide dynamic range active inductor," *International Journal of Circuit Theory and Applications*, vol. 43, no. 3, pp. 277–285, 2015. DOI: https://doi.org/10.1002/cta.1938.

[38] W. Schwab and W. Menzel, "A low-noise active bandpass filter," *IEEE Microwave and Guided Wave Letters*, vol. 3, no. 1, pp. 1–2, 1993.

[39] Young-Hoon Chun, Sang-Won Yun, and Jin-Koo Rhee, "Active impedance inverter: Analysis and its application to the bandpass filter design," in *2002 IEEE*

178

MTT-S International Microwave Symposium Digest (Cat. No.02CH37278), vol. 3, 2002, 1911–1914 vol.3.

[40] W. Jutzi, "Microwave bandwidth active transversal filter concept with mesfets," *IEEE Transactions on Microwave Theory and Techniques*, vol. 19, no. 9, pp. 760–767, 1971.

[41] M. J. Schindler and Y. Tajima, "A novel mmic active filter with lumped and transversal elements," in *Digest of Papers.,Microwave and Millimeter-Wave Monolithic Circuits Symposium*, 1989, pp. 57–60.

[42] J. V. Tirado, "Bulk acoustic wave resonators and their application to microwave devices," Ph.D. dissertation, Universitat Autònoma de Barcelona, Barcelona, 2020.

[43] T. Kojima and H. Obara, "Two-port saw resonator using series connected idts," in *1998 IEEE Ultrasonics Symposium. Proceedings (Cat. No. 98CH36102)*, vol. 1, 1998, 81–86 vol.1. DOI: 10.1109/ULTSYM.1998.762104.

[44] M. Ueda *et al.*, "High-q resonators using fbar/saw technology and their applications," in *IEEE MTT-S International Microwave Symposium Digest, 2005.*, 2005, pp. 209–212. DOI: 10.1109/MWSYM.2005.1516561.

[45] D. Bell and R. Li, "Surface-acoustic-wave resonators," *Proceedings of the IEEE*, vol. 64, no. 5, pp. 711–721, 1976. DOI: 10.1109/PROC.1976.10200.

[46] A. A. Circuits. "What is bulk acoustic wave (baw) technology." (2023), [Online]. Available: https://www.allaboutcircuits.com/news/ti-introduces-two-

new - products - using - breakthrough - baw - resonator - technology/ (visited on 04/29/2023).

[47] D. Mo, S. Dabas, S. Rassay, and R. Tabrizian, "Complementary-switchable dual-mode shf scandium aluminum nitride baw resonator," *IEEE Transactions on Electron Devices*, vol. 69, no. 8, pp. 4624–4631, 2022. DOI: 10.1109/TED. 2022.3183963.

[48] Z. Schaffer, P. Simeoni, and G. Piazza, "33 ghz overmoded bulk acoustic resonator," *IEEE Microwave and Wireless Components Letters*, vol. 32, no. 6, pp. 656–659, 2022. DOI: 10.1109/LMWC.2022.3166682.

[49] J. Verdú, O. Menéndez, and P. de Paco, "Ladder-type filter based on bulk acoustic wave resonators with improved out-of-band rejection," *Microwave and Optical Technology Letters*, vol. 50, no. 1, pp. 103–107, 2008. DOI: https://doi.org/10.1002/mop.23013.

[50] G. Ariturk, N. R. Almuqati, Y. Yu, E. T.-T. Yen, A. Fruehling, and H. H. Sigmarsson, "Wideband hybrid acoustic-electromagnetic filters with prescribed chebyshev functions," in *2022 IEEE/MTT-S International Microwave Symposium - IMS 2022*, 2022, pp. 887–890. DOI: 10.1109/IMS37962.2022.9865475.

[51] S. Gong and G. Piazza, "Multi-frequency wideband rf filters using high electromechanical coupling laterally vibrating lithium niobate mems resonators," in *2013 IEEE 26th International Conference on Micro Electro Mechanical Systems (MEMS)*, 2013, pp. 785–788. DOI: 10.1109/MEMSYS.2013.6474360.

[52] D. Psychogiou, R. Gómez-García, R. Loeches-Sánchez, and D. Peroulis, "Hybrid acoustic-wave-lumped-element resonators (awlrs) for high-Q bandpass filters with quasi-elliptic frequency response," *IEEE Transactions on Microwave Theory and Techniques*, vol. 63, no. 7, pp. 2233–2244, 2015. DOI: 10.1109/TMTT.2015.2438894.

[53] R. Gómez-García, D. Psychogiou, R. Loeches-Sánchez, and D. Peroulis, "Bandwidth enlargement in acoustic-wave rf bandpass filters with planar transversal circuits," in *2015 European Microwave Conference (EuMC)*, 2015, pp. 426–429. DOI: 10.1109/EuMC.2015.7345791.

[54] X. Lu, K. Mouthaan, and Y. T. Soon, "Wideband bandpass filters with saw-filter-like selectivity using chip saw resonators," *IEEE Transactions on Microwave Theory and Techniques*, vol. 62, no. 1, pp. 28–36, 2014. DOI: 10.1109/TMTT.2013.2292041.

[55] H. Wu, Y. Wu, Z. Lai, W. Wang, and Q. Yang, "A hybrid film-bulk-acoustic-resonator/coupled-line/transmission-line high selectivity wideband bandpass fbar filter," *IEEE Transactions on Microwave Theory and Techniques*, vol. 68, no. 8, pp. 3389–3396, 2020. DOI: 10.1109/TMTT.2020.2989264.

[56] A. Giménez, J. Verdú, and P. De Paco Sánchez, "General synthesis methodology for the design of acoustic wave ladder filters and duplexers," *IEEE Access*, vol. 6, pp. 47 969–47 979, 2018. DOI: 10.1109/ACCESS.2018.2865808.

[57] Á. Triano, P. Silveira, J. Verdú, and P. de Paco, "Synthesis methodology for mixed-topology acoustic wave filters," in *2019 IEEE International Ultrason-*

ics Symposium (IUS), 2019, pp. 2568–2571. DOI: 10.1109/ULTSYM.2019.8925584.

[58] Á. Triano, J. Verdú, and P. de Paco, "Novel synthesis technique of mixed-topology extracted-pole resonators with parallel-connected structures for ladder-type acoustic filters," in *2019 IEEE MTT-S International Microwave Symposium (IMS)*, 2019, pp. 1019–1022. DOI: 10.1109/MWSYM.2019.8700990.

[59] Á. Triano, J. Verdú, and P. de Paco Sánchez, "A general synthesis technique of mixed-topology including parallel-connected structures for fully canonical ladder-type acoustic filters," *IEEE Transactions on Microwave Theory and Techniques*, vol. 67, no. 12, pp. 5061–5068, 2019. DOI: 10.1109/TMTT.2019.2948346.

[60] M. Iwaki, J. Tsutsumi, Y. Endo, H. Nakamura, and Y. Satoh, "An attenuation improvement technology for ladder saw/fbar filters and duplexers employing cancellation circuit," in *2011 41st European Microwave Conference*, 2011, pp. 751–754. DOI: 10.23919/EuMC.2011.6101733.

[61] J. Mateu *et al.*, "Acoustic wave transversal filter for 5g n77 band," *IEEE Transactions on Microwave Theory and Techniques*, vol. 69, no. 10, pp. 4476–4488, 2021. DOI: 10.1109/TMTT.2021.3091766.

[62] G. Ariturk, N. R. Almuqati, and H. H. Sigmarsson, "Element-level microwave filter integration in fully-digital phased array radar systems," in *2022 IEEE 22nd Annual Wireless and Microwave Technology Conference (WAMICON)*, 2022, pp. 1–4. DOI: 10.1109/WAMICON53991.2022.9786104.

[63] G. Ariturk, N. R. Almuqati, Y. Yu, E. T.-T. Yen, A. Fruehling, and H. H. Sigmarsson, "Exact synthesis of hybric acoustic electromagnetic filters for wideband chebyshev functions," *IEEE Transactions on Microwave Theory and Techniques*, 2023. DOI: UnderRevision..

[64] G. Craven and R. Skedd, *Evanescent Mode Microwave Components* (Artech House microwave library). Artech House, 1987.

[65] W. C. Chew and J. A. Kong, "Effects of fringing fields on the capacitance of circular microstrip disk," *IEEE Transactions on Microwave Theory and Techniques*, vol. 28, no. 2, pp. 98–104, 1980. DOI: 10.1109/TMTT.1980.1130017.

[66] E. T.-T. Yen *et al.*, "Integrated high-frequency reference clock systems utilizing mirror-encapsulated baw resonators," in *2019 IEEE International Ultrasonics Symposium (IUS)*, 2019, pp. 2174–2177. DOI: 10.1109/ULTSYM.2019.8925905.

[67] C. Enz and A. Kaiser, *MEMS-based Circuits and Systems for Wireless Communication*. Jan. 2013. DOI: 10.1007/978-1-4419-8798-3.

[68] L. Chen *et al.*, "Scandium-doped aluminum nitride for acoustic wave resonators, filters, and ferroelectric memory applications," *ACS Applied Electronic Materials*, vol. 5, no. 2, pp. 612–622, 2023. DOI: 10.1021/acsaelm.2c01409.

[69] P. Kirby, Q. Su, E. Komuro, Q. Zhang, M. Imura, and R. Whatmore, "Pzt thin film bulk acoustic wave resonators and filters," in *Proceedings of the 2001 IEEE International Frequncy Control Symposium and PDA Exhibition (Cat. No.01CH37218)*, 2001, pp. 687–694. DOI: 10.1109/FREQ.2001.956364.

[70] X. Bai *et al.*, "Mo/Ti multilayer Bragg reflector for LiNbO3 film bulk acoustic wave resonators," *Journal of Applied Physics*, vol. 128, no. 9, p. 094 503, Sep. 2020.

[71] M. D. Hodge *et al.*, "High rejection unii 5.2ghz wideband bulk acoustic wave filters using undoped single crystal aln-on-sic resonators," in *2017 IEEE International Electron Devices Meeting (IEDM)*, 2017, pp. 25.6.1–25.6.4. DOI: 10.1109/IEDM.2017.8268460.

[72] C. Moe *et al.*, "Highly doped alscn 3.5 ghz xbaw resonators with 16% k2eff for 5g rf filter applications," in *2020 IEEE International Ultrasonics Symposium (IUS)*, 2020, pp. 1–4. DOI: 10.1109/IUS46767.2020.9251412.

[73] J. Wang, M. Park, S. Mertin, T. Pensala, F. Ayazi, and A. Ansari, "A film bulk acoustic resonator based on ferroelectric aluminum scandium nitride films," *Journal of Microelectromechanical Systems*, vol. 29, no. 5, pp. 741–747, 2020. DOI: 10.1109/JMEMS.2020.3014584.

[74] A. Atia and A. Williams, "Narrow-bandpass waveguide filters," *IEEE Transactions on Microwave Theory and Techniques*, vol. 20, no. 4, pp. 258–265, 1972. DOI: 10.1109/TMTT.1972.1127732.

[75] A. Atia, A. Williams, and R. Newcomb, "Narrow-band multiple-coupled cavity synthesis," *IEEE Transactions on Circuits and Systems*, vol. 21, no. 5, pp. 649–655, 1974. DOI: 10.1109/TCS.1974.1083913.

[76] A. C. Guyette, I. C. Hunter, and R. D. Pollard, "Exact synthesis of microwave filters with nonuniform dissipation," in *2007 IEEE/MTT-S International Microwave Symposium*, 2007, pp. 537–540.

[77] Meng Meng and I. C. Hunter, "The design of parallel connected filter networks with non-uniform q resonators," in *2012 IEEE/MTT-S International Microwave Symposium Digest*, 2012, pp. 1–3.

[78] V. Miraftab and M. Yu, "Generalized lossy microwave filter coupling matrix synthesis and design using mixed technologies," *IEEE Transactions on Microwave Theory and Techniques*, vol. 56, no. 12, pp. 3016–3027, 2008.

[79] V. Miraftab and M. Yu, "Advanced coupling matrix and admittance function synthesis techniques for dissipative microwave filters," *IEEE Transactions on Microwave Theory and Techniques*, vol. 57, no. 10, pp. 2429–2438, 2009.

[80] M. Yu and V. Miraftab, "Shrinking microwave filters," *IEEE Microwave Magazine*, vol. 9, no. 5, pp. 40–54, 2008.

[81] G. Ariturk and H. H. Sigmarsson, "Lossy microwave filters with active shape correction," *IEEE Access*, vol. 9, pp. 35 075–35 087, 2021. DOI: 10.1109/ACCESS.2021.3061999.

[82] Y. Gao, J. Powell, X. Shang, and M. J. Lancaster, "Coupling matrix-based design of waveguide filter amplifiers," *IEEE Transactions on Microwave Theory and Techniques*, vol. 66, no. 12, pp. 5300–5309, 2018. DOI: 10.1109/TMTT.2018.2871122.

[83] Y. Gao *et al.*, "Substrate integrated waveguide filter–amplifier design using active coupling matrix technique," *IEEE Transactions on Microwave Theory and Techniques*, vol. 68, no. 5, pp. 1706–1716, 2020. DOI: 10.1109/TMTT.2020.2972390.

[84] J. A. Estrada, J. R. Montejo-Garai, P. de Paco, D. Psychogiou, and Z. Popović, "Power amplifiers with frequency-selective matching networks," *IEEE Transactions on Microwave Theory and Techniques*, vol. 69, no. 1, pp. 697–708, 2021. DOI: 10.1109/TMTT.2020.3020097.

[85] S. Amari, "Direct synthesis of cascaded singlets and triplets by non-resonating node suppression," in *2006 IEEE MTT-S International Microwave Symposium Digest*, 2006, pp. 123–126. DOI: 10.1109/MWSYM.2006.249409.

[86] W. Fathelbab, "Novel synthesis methodology of lowpass networks comprising generalized cascaded trisections," in *2021 IEEE 21st Annual Wireless and Microwave Technology Conference (WAMICON)*, 2021, pp. 1–4. DOI: 10.1109/WAMICON47156.2021.9443622.

[87] W. Fathelbab, "Novel synthesis methodology of lowpass networks comprising generalized cascaded trisections," in *2021 IEEE 21st Annual Wireless and Microwave Technology Conference (WAMICON)*, 2021, pp. 1–4. DOI: 10.1109/WAMICON47156.2021.9443622.

[88] S. Tamiazzo and G. Macchiarella, "An analytical technique for the synthesis of cascaded n-tuplets cross-coupled resonators microwave filters using matrix rotations," *IEEE Transactions on Microwave Theory and Techniques*, vol. 53, no. 5, pp. 1693–1698, 2005. DOI: 10.1109/TMTT.2005.847065.

[89] J. Rhodes and R. Cameron, "General extracted pole synthesis technique with applications to low-loss te/sub011/ mode filters," *IEEE Transactions on Microwave Theory and Techniques*, vol. 28, no. 9, pp. 1018–1028, 1980. DOI: 10.1109/TMTT.1980.1130213.

[90] S. Tamiazzo and G. Macchiarella, "Synthesis of cross-coupled prototype filters including resonant and non-resonant nodes," *IEEE Transactions on Microwave Theory and Techniques*, vol. 63, no. 10, pp. 3408–3415, 2015. DOI: 10.1109/TMTT.2015.2457421.

[91] A. Gimenez and P. de Paco, "A dual-tz extraction technique for the synthesis of cross-coupled prototype filters," *IEEE Microwave and Wireless Components Letters*, vol. 26, no. 10, pp. 777–779, 2016. DOI: 10.1109/LMWC.2016.2601295.

[92] R. et al., *Extracted pole filter*, US Patent 4,360793,207, Nov. 1982.

[93] S. Amari and G. Macchiarella, "Synthesis of inline filters with arbitrarily placed attenuation poles by using nonresonating nodes," *IEEE Transactions on Microwave Theory and Techniques*, vol. 53, no. 10, pp. 3075–3081, 2005. DOI: 10.1109/TMTT.2005.855128.

[94] G. Macchiarella and S. Amari, "Direct synthesis of prototype filters with non-resonating nodes," in *34th European Microwave Conference, 2004.*, vol. 1, 2004, pp. 305–308.

[95]   M. Yu and Y. Yang, "Unified extracted pole filter synthesis: Bridging the gap between em and circuit simulations," *IEEE Microwave Magazine*, vol. 21, no. 3, pp. 84–95, 2020. DOI: 10.1109/MMM.2019.2958163.

[96]   E. Guerrero, J. Verdú, and P. de Paco, "Synthesis of extracted pole filters with transmission zeros in both stopbands and nonresonant nodes of the same nature," *IEEE Microwave and Wireless Components Letters*, vol. 31, no. 1, pp. 17–20, 2021. DOI: 10.1109/LMWC.2020.3035848.

[97]   G. Macchiarella and S. Tamiazzo, "An application-oriented design procedure for cascaded-block extracted-pole filters," *IEEE Transactions on Microwave Theory and Techniques*, vol. 69, no. 1, pp. 647–658, 2021. DOI: 10.1109/TMTT.2020.3035367.

[98]   G. Macchiarella, M. Oldoni, and S. Tamiazzo, "Design of narrowband microwave filters with mixed-topology," in *2012 IEEE/MTT-S International Microwave Symposium Digest*, 2012, pp. 1–3. DOI: 10.1109/MWSYM.2012.6258271.

[99]   G. Macchiarella, M. Oldoni, and S. Tamiazzo, "Design of narrowband microwave filters with mixed-topology," in *2012 IEEE/MTT-S International Microwave Symposium Digest*, 2012, pp. 1–3. DOI: 10.1109/MWSYM.2012.6258271.

[100]   E. Guerrero, P. Silveira, J. Verdú, and P. de Paco, "Design guidelines for acoustic wave ladder filters starting in shunt resonator," in *2020 IEEE International Ultrasonics Symposium (IUS)*, 2020, pp. 1–4. DOI: 10.1109/IUS46767.2020.9251832.

[101] Á. Triano, J. Verdú, P. de Paco, T. Bauer, and K. Wagner, "Relation between electromagnetic coupling effects and network synthesis for aw ladder type filters," in *2017 IEEE International Ultrasonics Symposium (IUS)*, 2017, pp. 1–4. DOI: 10.1109/ULTSYM.2017.8091644.

[102] A. Triano, "Advanced synthesis techniques for parallel-connected and cross-coupled filters based on acoustic wave technologies," Ph.D. dissertation, Universitat Autònoma de Barcelona, Barcelona, 2020.

[103] M. Dishal, "Design of dissipative band-pass filters producing desired exact amplitude-frequency characteristics," *Proceedings of the IRE*, vol. 37, no. 9, pp. 1050–1069, 1949.

[104] J. Ni, J. Hong, and P. Martin Iglesias, "Compact microstrip if lossy filter with ultra-wide stopband," *IEEE Transactions on Microwave Theory and Techniques*, vol. 66, no. 10, pp. 4520–4527, 2018. DOI: 10.1109/TMTT.2018.2858781.

[105] J. Mateu *et al.*, "Synthesis of 4th order lossy filters with uniform q distribution," in *2010 IEEE MTT-S International Microwave Symposium*, 2010, pp. 1–1. DOI: 10.1109/MWSYM.2010.5517067.

[106] L. Szydlowski, A. Lamecki, and M. Mrozowski, "Design of microwave lossy filter based on substrate integrated waveguide (siw)," *IEEE Microwave and Wireless Components Letters*, vol. 21, no. 5, pp. 249–251, 2011. DOI: 10.1109/LMWC.2011.2119471.

[107] A. C. Guyette, I. C. Hunter, and R. D. Pollard, "The design of microwave band-pass filters using resonators with nonuniform$Q$," *IEEE Transactions on Microwave Theory and Techniques*, vol. 54, no. 11, pp. 3914–3922, 2006.

[108] A. C. Guyette, I. C. Hunter, and R. D. Pollard, "A new class of selective filters using low-q components suitable for mmic implementation," in *2004 IEEE MTT-S International Microwave Symposium Digest (IEEE Cat. No.04CH37535)*, vol. 3, 2004, 1959–1962 Vol.3.

[109] A. Basti, A. Périgaud, S. Bila, S. Verdeyme, L. Estagerie, and H. Leblond, "Design of microstrip lossy filters for receivers in satellite transponders," *IEEE Transactions on Microwave Theory and Techniques*, vol. 62, no. 9, pp. 2014–2024, Sep. 2014. DOI: 10.1109/TMTT.2014.2337285.

[110] R. Das, Q. Zhang, A. Kandwal, and H. Liu, "All passive realization of lossy coupling matrices using resistive decomposition technique," *IEEE Access*, vol. 7, pp. 5095–5105, 2019. DOI: 10.1109/ACCESS.2018.2887298.

[111] R. J. Cameron, "General coupling matrix synthesis methods for chebyshev filtering functions," *IEEE Transactions on Microwave Theory and Techniques*, vol. 47, no. 4, pp. 433–442, 1999.

[112] M. Nick and A. Mortazawi, "Low phase-noise planar oscillators based on low-noise active resonators," *IEEE Transactions on Microwave Theory and Techniques*, vol. 58, no. 5, pp. 1133–1139, 2010.

[113] Y. Ishikawa, S. Yamashita, and S. Hidaka, "Noise design of active feedback res-
       onator bef," *IEEE Transactions on Microwave Theory and Techniques*, vol. 41,
       no. 12, pp. 2133–2138, 1993.

[114] H. Ezzedine, L. Billonnet, B. Jarry, and P. Guillon, "Optimization of noise per-
       formance for various topologies of planar microwave active filters using noise
       wave techniques," *IEEE Transactions on Microwave Theory and Techniques*,
       vol. 46, no. 12, pp. 2484–2492, 1998.

[115] Y. Ishikawa, S. Yamashita, and S. Hidaka, "Noise design of active feedback res-
       onator bef," *IEEE Transactions on Microwave Theory and Techniques*, vol. 41,
       no. 12, pp. 2133–2138, 1993.

[116] D. Pozar, *Microwave Engineering*. Wiley, 2011.

[117]   Mini-Circuits. "Stabilizing network technical note." (2015), [Online]. Avail-
       able: https : / / www . minicircuits . com / app / AN60 - 064 . pdf (visited on
       09/30/2020).

[118] Keysight Technologies. "Noise figure measurement accuracy: The y-factor
       method." (2020), [Online]. Available: https://www.keysight.com/us/en/assets/
       7018-06829/application-notes/5952-3706.pdf (visited on 09/30/2020).

Appendix A

Acronyms

KVL: Kirchoff's Voltage Law,
CM: Coupling Matrix
AW: Acoustic Wave
AWR: Acoustic Wave Resonator
PFE: Partial Fraction Expansion
BVD: Butterworth Van-Dyke
EP: Extracted Pole
FBW: Fractional Bandwidth
FML: Filter with Moderate Loss
FHL: Filter with High Loss
RF: Radio Frequency
mmWave: Millimeter-Wave
NF: Noise Figure
SAW: Surface Acoustic Wave
BAW: Bulk Acoustic Wave
IDT: Interdigital Transducer
MEMS: Microelectromechanical Systems
NRN: Non-Resonant Node
SOC: System-on-a-Chip

Appendix B

Lossy-Active Filters and the Lossy-Active Coupling Matrix

In this chapter, a new approach of using active resonators within the concept of lossy filter design is presented. The objective is to recover the filter shape in the presence of moderate to highly lossy resonators. Unlike the common active filter approaches, where all the resonators are loss-compensated, the proposed design uses $N - 2$ active elements for the shape correction. Furthermore, the lossy coupling matrix in [80] is extended to propose the novel *lossy-active coupling matrix* for the first time. To prove the concept, two third-order 20 dB equiripple 5% fractional bandwidth (FBW) filters with different loss levels are designed and implemented. The first design recovers the shape of the filter with a Q_u of 100 at each resonator, whereas the second prototype, illustrating the use of highly lossy resonators, recovers the response at a Q_u of 28 at each resonator. This study is published in [81].

B.1 Lossy Microwave Filters and Lossy Coupling Matrix

Until this point of the introduction of the coupling matrix, we have always synthesized the coupling matrix to realize a Chebyshev response that has no attenuation in the pass-band, meaning that there is no insertion loss. Once the coupling matrix of the design is obtained, the resonators to realize the function are placed, the network results in a

response with a finite insertion loss and selectivity reduction based on the following three metrics: the quality factor of the resonators, the order of the filter, and the desired fractional bandwidth,

In many applications, a flat passband and good selectivity is required in the design, which cannot be obtained with the lossless coupling matrix and the use of finite-Q resonators.

In this regard, a different technique to recover the filter response is the design of lossy filters [76–80, 103–109]. In its essence, the concept is based on correcting the filter response and selectivity by accepting additional insertion loss (IL) within the passband. This technique was initially proposed in [103] as the classical method of predistortion, where the design is based on shifting the poles of the transfer function (S_{21}) on the complex plane to account for the losses. It was further enhanced in [107] by distributing the loss among the resonators using hyperbolic rotations and resistive cross-coupling among non-adjacent nodes. Two other examples that include filters with non-uniform dissipation are given in [76, 108].

Within the context of lossy filters, the *lossy coupling matrix* is introduced in [78–80]. In [80], the lossy filter is characterized as a lossless filter with an input and an output attenuator. The lossy coupling matrix is constructed by transferring the series resistances within the lumped element model of the attenuators towards the filter resonators. Drawing on that idea, the generalized lossy $N \times N$ and the transversal $(N + 2) \times (N + 2)$ coupling matrices (N being the filter order) are introduced in [78] and [79], respectively. In [78], the complex coupling matrix is synthesized from the lossy Chebyshev polynomials by considering its diagonalizability to its eigenvalue matrix. Following that, the transversal lossy coupling matrix is generated directly from the lossy admittance polynomials by using their residues in [79].

To distribute the losses evenly among the resonators or to manipulate the routing

194

topology of lossy filters, hyperbolic rotations are used in [78] and [79]. In that regard, performance metrics of inline and transversal lossy filter structures are compared in [109] and loss equalization methods are proposed in [105] and [110]. The hyperbolic matrix rotations produce purely imaginary and/or complex inter-resonator coupling mechanisms, which pose a challenge in terms of the practical implementation of lossy filters. While that issue is briefly addressed in [78], a more exact passive realization method based on resistive decomposition of the lossy coupling mechanisms is presented in [110].

To correct the shape of the filter response when the resonators have finite quality factors, an Nth order lossy filter is synthesized with the method in [80]. The design is based on the lossy synthesis method emulating the cascade of two attenuators at the input and output of the lossless filter, each of which has an attenuation factor of k, as depicted in Fig. 3 (a). The reflection and transmission responses of the lossy filter (S_{11}^{lossy} and S_{21}^{lossy}), are formulated in terms of those of the lossless one as:

$$
\begin{aligned}
S_{11}^{lossy} &= k^2 S_{11}^{lossless}, \\
S_{21}^{lossy} &= k^2 S_{21}^{lossless},
\end{aligned}
\tag{B.1}
$$

where k is the attenuation factor in linear scale. In (2), the lossless filter responses ($S_{11}^{lossless}$ and $S_{21}^{lossless}$) are characterized by the conventional polynomial synthesis method and are given as in the following [111]:

$$
|S_{21}^{lossless}|^2 = 1 - |S_{11}^{lossless}|^2 = \frac{1}{1 + \epsilon^2 |K_N(s)|^2},
\tag{B.2}
$$

where $|K_N(s)|$ is the Nth degree characteristic polynomial of the filter function and ϵ is the ripple factor.

Modeling the input and output attenuators as resistor-admittance inverter-resistor

cascade as in Fig. B.1 (b), shifting the series resistors towards the filter resonators as shunt conductances, and scaling the input/output inverters to unity as in [80], the circuit in Fig. B.1 (c) is obtained. The lossy coupling matrix and the coupling diagram of that filter are depicted in Fig. B.1 (d).

To achieve an attenuation factor of k with the attenuator model in Fig.B.1 (b), the admittance inverter and the pair of resistors need to have the following relation [80]:

$$J = \pm \frac{1}{\sqrt{1 - R^2}}, \quad k = \sqrt{\frac{1 - R}{1 + R}}, \quad \text{(B.3)}$$

where J is the value of the admittance inverter and R is the value of the resistor pair. The additional entries in the coupling matrix, including the shunt conductances at the non-resonating nodes (g'_S and g'_L) and at the lossy resonators (g'_1 and g'_N), are formulated as in the following:
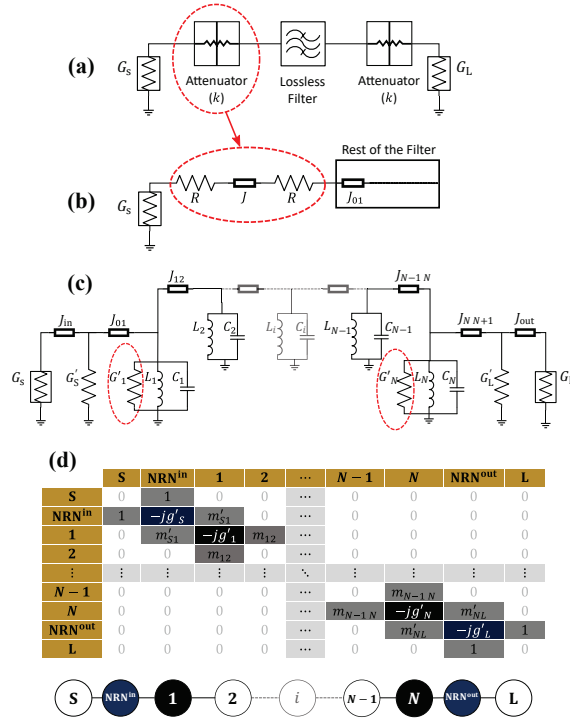
Figure B.1: (a): The lossy filter model in [80] as a starting point. (b): The resistor-admittance inverter-resistor based model of the attenuators in (a) with an attenuation factor of k in linear scale. (c): The synthesized lossy filter including loss in the input and output resonators[80]. (d): The $(N + 2) \times (N + 2)$ lossy coupling matrix and the coupling diagram of the filter in (c). In the coupling matrix and the diagram, *S* denotes the source, *L* denotes the load and *NRN* is for the non-resonating nodes.

$$g'_S = g'_L = R = \frac{1 - k^2}{1 + k^2},$$

$$m'_{S1} = \pm m_{S1}\sqrt{1 - R^2}, \quad m'_{NL} = \pm m_{NL}\sqrt{1 - R^2}, \tag{B.4}$$

$$g'_1 = Rm_{S1}^2, \quad g'_N = Rm_{NL}^2.$$

Considering (B.4), the initial parameter to be determined in the lossy filter design is the attenuation factor k, as it determines the required unloaded quality factors of the input and output resonators. To obtain the admittance inverter values in Fig. B.1

197

(c) from the coupling matrix entries, the entries need to be scaled according to the source/load resistances, the operating frequency, and the FBW of the bandpass filter. The required quality factors at the input/output resonators depend on the attenuation factor and the operating frequency.

Further observing Fig. B.1 (c) and (d), one can realize that there is no loss in the resonators through 2 to $N - 1$. With the use of hyperbolic rotations and resistive cross-coupling among different nodes, the loss could have been uniformly distributed among the resonators of the filter [77, 80, 107], however, that is beyond the scope of this study. Until this point, the resonators through 2 to $N - 1$ are still considered to be lossless.

B.2 Loss Compensation in Resonators

In Fig. B.2, an active resonator with a coupled feedback amplifier is depicted. The amplifier is coupled to the resonator with the external quality factors of Q_1 and Q_2 through the impedance inverters K_1 and K_2.
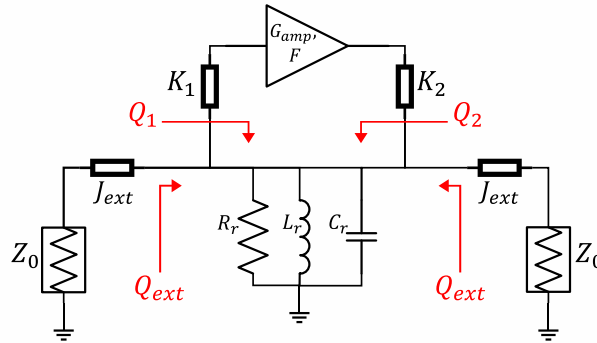
Figure B.2: Illustration of an active loss compensated resonator.

The external quality factors Q_1 and Q_2 are dependent on both the impedance in-

verter values K_1 and K_2 and the input/output impedances of the amplifier. Assuming that the input and output impedances of the amplifier are matched to 50 Ω, the external quality factors are given as:

$$Q_1 = \frac{K_1^2}{50\omega_0 L_r} \text{ and } Q_2 = \frac{K_2^2}{50\omega_0 L_r}. \tag{B.5}$$

With the external quality factors of the amplifier loop, the effective active negative resistance that is seen at the lossy resonator side can be calculated as [112]:

$$R_{negative} = \left(-\frac{\frac{K_2^2}{50}}{2G_{Amp}\frac{K_2}{K_1} - 1} \right) \| \left(\frac{K_1^2}{50} \right), \tag{B.6}$$

where G_{Amp} is the voltage gain of the amplifier in linear scale. As mentioned in [112], the full loss compensation at the lossy resonator is achieved when the negative resistance in (B.6) has the same magnitude as the resistance of the parallel resonator R_r. That equality will be achieved when the relationship between the amplifier gain (G_{Amp}), the unloaded quality factor of the resonator (Q_{u_r}), and the external quality factors Q_1 and Q_2 have the following relation [112]:

$$G_{Amp} = \frac{\sqrt{Q_1 Q_2}}{2} \cdot \left(Q_{u_r}^{-1} + Q_1^{-1} + Q_2^{-1} \right). \tag{B.7}$$

In addition to (B.7), it is important that the phase response of the amplifier feedback loop is an integer multiple of $360°$ for full loss compensation.

In the loss-compensated resonator, it is highly desirable to minimize the additional noise figure contribution of the active portion. It has also been discussed in [112–114] that the minimum noise with an active resonator can be achieved when the following relationship is satisfied:

$$Q_2 = G_{Amp}^2 Q_1. \tag{B.8}$$

Combining (B.7) and (B.8), one can obtain the following relationships between the external quality factors and the amplifier gain:

$$Q_1 = \frac{G_{Amp}^2 - 1}{G_{Amp}^2} Q_{u_r} \text{ and } Q_2 = (G_{Amp}^2 - 1)Q_{u_r}. \tag{B.9}$$

Therefore, it is important to satisfy the relations in (B.9) to have a fully loss compensated resonator with minimum additional noise figure from the amplifier. This design technique provides the flexibility of using resonators with arbitrary unloaded quality factors to start with as long as the impedance inverters providing the external quality factors (Q_1 and Q_2) are realizable. For convenience, the resonators 2 through $N - 1$ are chosen to be identical to the first and the last resonator of the filter in this study.

Apart from the input and output coupling of the amplifier (K_1 and K_2), the NF of the active resonator stage is determined by several factors. These include the external quality factors that are introduced to the resonator, the gain of the feedback amplifier, and most importantly, the unloaded quality factor of the passive resonator. Considering that the relations in (10) are satisfied for the active resonator in Fig. B.2, the minimum noise figure of the resonator stage is given by [112, 114]:

$$F_{min} = F_{passive} + \frac{Q_e}{Q_u}M, \text{ where}$$

$$M = \left(\frac{F - 1}{1 - \frac{1}{G_{Amp}^2}}\right) \text{ and } F_{passive} = 1 + \frac{Q_e}{2Q_u}. \tag{B.10}$$

In (B.10), M is the noise measure of the amplifier [112] and $F_{passive}$ is the NF of the passive resonator when the amplifier network (including K_1 and K_2) is not connected. A fundamental observation regarding (B.10) is that the noise figure of the active resonator has to be greater than $F_{passive}$ and it is highly dependent on the noise measure of the amplifier. The effect of slight variations of K_1, K_2, and the noise measure on

the noise figure of the resonator was thoroughly discussed in [112]. It is important to emphasize that the noise figure given by (B.10) is the noise figure of the single active resonator and not the overall filter. The effect of the noise figure of active resonators on the entire filter is dependent on different factors including the order of the resonators and the placement of the active resonator among them. Those factors were discussed and a noise figure estimate was done for a band-eliminate filter in [115].

B.3   The Lossy-Active Coupling Matrix

Having a coupling matrix representation of the filter makes the design more versatile. In this section, the new *lossy-active coupling matrix* is introduced as an extension to the lossy coupling matrix. The goal is to integrate the feedback amplifier network as an additional non-resonating node.

The circuit schematic in Fig. B.3 (a) depicts the final lossy-active filter when all resonators have the same unloaded quality factor and the resonators 2 through $N-1$ are loss-compensated with the method described in Section II-B. The new lossy-active coupling matrix is depicted in Fig. B.3 (b) and the routing diagram is given in Fig. 5 (c). The lossy-active coupling matrix has the same entries as the lossy coupling matrix except for the included loss at the resonators 2 through $N-1$ (highlighted in black) and additional active non-resonating nodes that include the amplifier loops as negative resistances. As all the resonators have the same Q_u without the loss compensation, $g_1' = g_2' = ... = g_N'$ should be satisfied. To be considered a coupling matrix entry, the negative resistances at the non-resonant nodes should be normalized with respect to the center frequency and the bandwidth. This is done by substituting the external quality factor values at the ith active resonator (Q_{1_i} and Q_{2_i}) in (6) for the non-normalized negative resistance in (7) and scaling it so that the ith resonator in Fig. 5 (a) resonates

at $\omega_0 = 1/\sqrt{L_i C_i}$ for $i \in \{2, 3, ..., N-1\}$. Therefore, each negative normalized conductance (g_{a_i}) in the lossy-active coupling matrix in Fig. B.3 (b) is found by:

$$g_{a_i} = \frac{1}{FBW}\left[\frac{1}{Q_{1_i}} - \frac{1}{Q_{2_i}}\left(2G_{Amp_i}\sqrt{\frac{Q_{2_i}}{Q_{1_i}}} - 1\right)\right], \tag{B.11}$$

$$\text{where } i \in \{2, 3, ..., N-1\}.$$

When the external quality factors Q_{1_i} and Q_{2_i} and the amplifier gain in each active resonator G_{Amp_i} satisfy the equality given in (B.11), it can be shown that the normalized negative conductance g_{a_i} has the exact same magnitude as g'_i in the lossy-active coupling matrix. For the lowest noise figure contribution, they also need to attain the values given in (10).
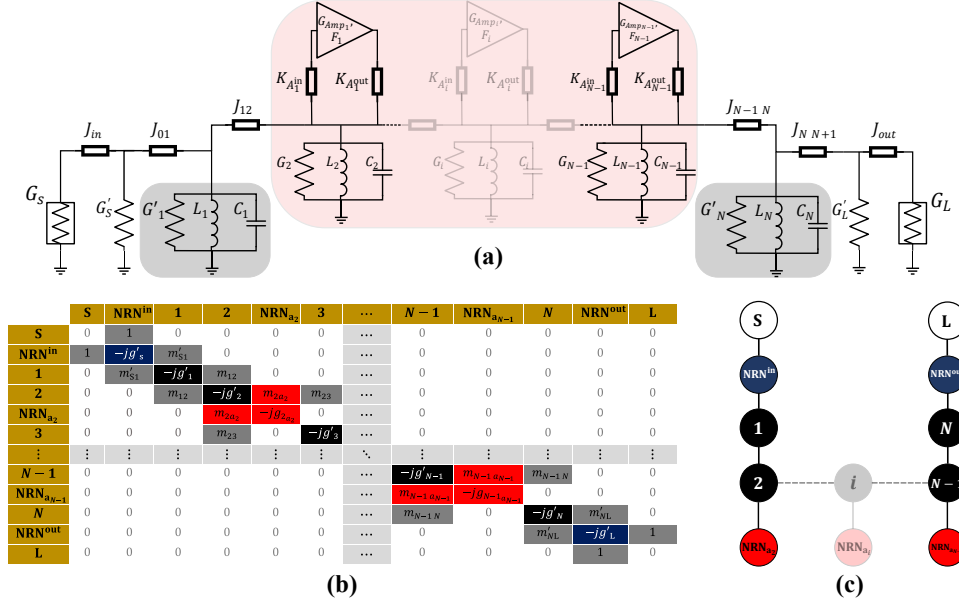
Figure B.3: (a): The lossy-active filter with loss compensation in the resonators 2 through $N-1$. (b): The lossy-active coupling matrix that characterizes the network in (a). (c): The routing diagram of the filter. NRN$^{\text{in}}$ and NRN$^{\text{out}}$ represent the non-resonant nodes at the input and output. NRN$_{a_i}$ denotes the ith amplifier loop as a single non-resonating node that acts like a negative resistance.

The value of the additional coupling coefficient, m_{ia_i} in Fig. B.3 (b), is also critical

for coupling each active non-resonant node to the resonating node of the ith active resonator. It can be found by considering the fact that the coupling matrix entries between the nodes are normalized admittance inverter values. In that regard, for the ith resonant node such that $i \in \{2, 3, ..., N-1\}$ to see the exact shunt negative conductance of (12), the value of the coupling coefficient is given as: $m_{ia_i} = \pm g_{a_i}$.

The lossy-active coupling matrix model that is proposed in this section models the input and output coupling of the amplifier as embedded within the active non-resonant node rather than considering them as separate coupling coefficients. An alternative model is given in the next section.

B.4 Alternative Representation of the Lossy-Active Coupling Matrix

Rather than considering the loss compensation network as a single node, the input and output nodes of the amplifier can also be considered as separate non-resonant nodes.
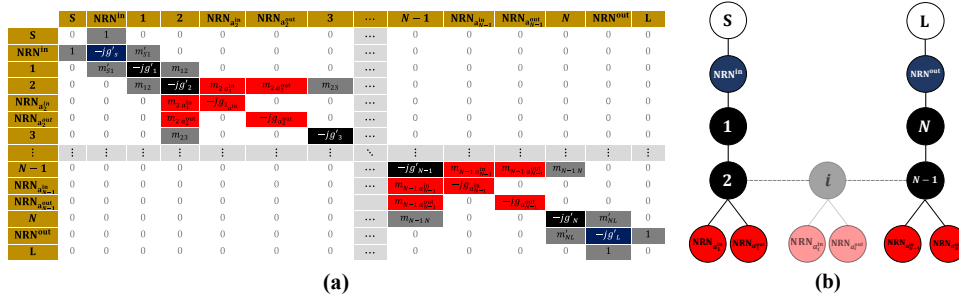
Figure B.4: (a): The alternative representation of the lossy-active coupling matrix and (b): the routing diagram for the coupling matrix in (a). This representation includes the input and output nodes of the amplifier as $\mathrm{NRN}_{a_i^{\mathrm{in}}}$ and $\mathrm{NRN}_{a_i^{\mathrm{out}}}$, respectively.

Splitting up the input and output nodes of the amplifier network, an alternative representation of the lossy-active coupling matrix is depicted in Fig. B.4 with a new routing diagram. The new nodes $\mathrm{NRN}_{a_i^{in}}$ and $\mathrm{NRN}_{a_i^{out}}$ in the routing diagram represent

the input and the output nodes of the ith feedback amplifier, such that $i \in \{2, 3, ..., N-1\}$. In this coupling matrix, the shunt conductances at the amplifier input and output are denoted as $g_{a_i^{in}}$ and $g_{a_i^{out}}$, respectively. Their values are found by separating the negative normalized conductance in (B.11) as:

$$g_{a_i^{in}} = \frac{1}{FBW \cdot Q_{1_i}},$$

$$g_{a_i^{out}} = -\frac{1}{FBW \cdot Q_{2_i}} \left(2G_{Amp_i} \sqrt{\frac{Q_{2_i}}{Q_{1_i}}} - 1 \right),$$

$$\text{where } i \in \{2, 3, ..., N-1\}. \tag{B.12}$$

The coupling coefficient between the amplifier input and its corresponding resonator is given by: $m_{ia_i^{in}} = \pm g_{a_i^{in}}$, whereas the coupling between amplifier output and the resonator is given by: $m_{ia_i^{out}} = \pm g_{a_i^{out}}$. It should be noted that the coupling configuration in Fig. B.4 does not take into account the coupling between the amplifier input and output, however, the effect of the input signal on the output is already embedded in (B.12).

B.5   Design and Analysis

To verify the proposed approach and demonstrate designs of different order, this section evaluates the performance of the method for different loss levels. For that purpose, filters of third-, fourth-, and fifth-order are designed using the circuit topology given in Fig. 5 (a).

The third-order filter examples include designs with resonator quality factor values of 200, 100, 50, and 28 which correspond to insertion loss values of 1.49 dB, 3 dB, 6.17 dB, and 12 dB, respectively. The fourth- and fifth-order design examples include

filters with insertion loss values of 3 dB and 12 dB. To have these insertion loss values, the corresponding quality factors are calculated as 108 and 31 for the fourth-order and 114 and 32 for the fifth-order filters. The designs are performed by denormalizing the lossy-active coupling matrix for a center frequency of 1 GHz and 5 % FBW.

The transmission and reflection responses of the filters are depicted in Fig. B.5 (a) for the third-order case and in Fig. B.6 (a) and (b) for the fourth- and fifth-order designs, respectively. The same figures also show the responses of the conventionally designed (i.e., using the g-coefficients) filters when each of their resonators has quality factors of 200, 100, 50, and 28 for the third-order, 108 and 31 for the fourth-order, and 114 and 32 for the fifth-order. Other parameters of the eight different designs, including the attenuation factor (k), noise figure, and insertion loss are listed in Table 1.
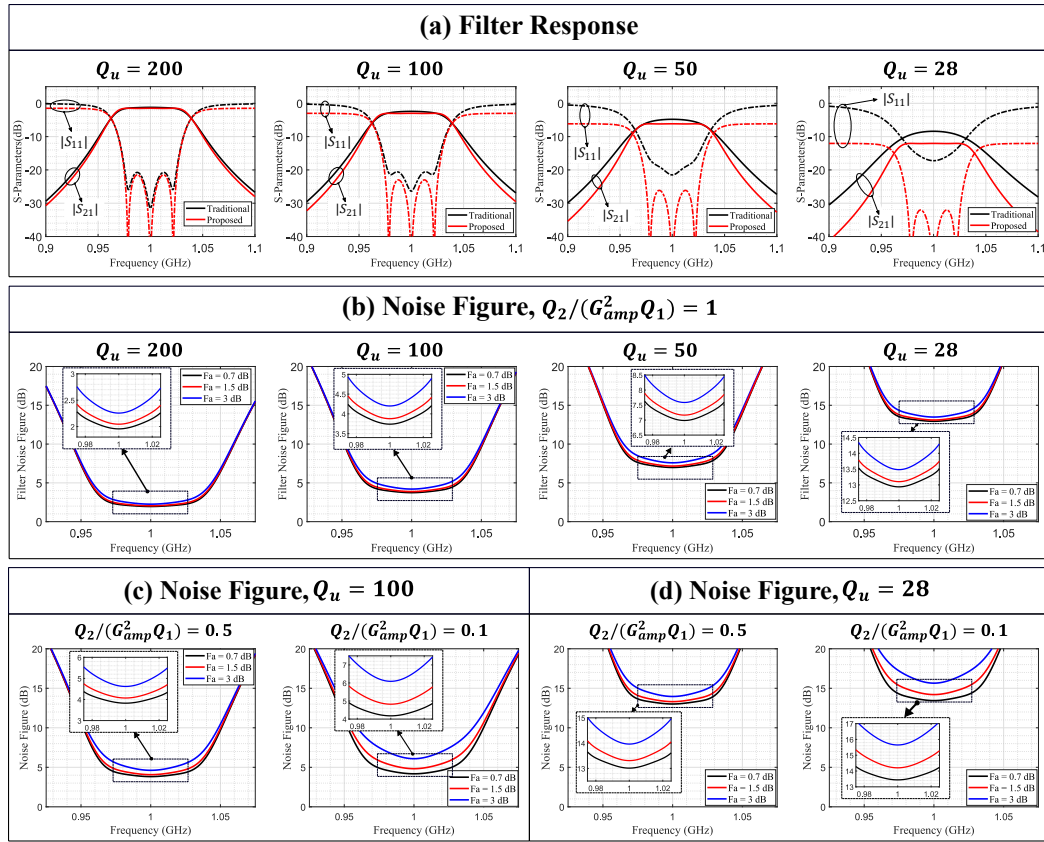
Figure B.5: (a): Recovery of the filter responses with the use of the proposed approach. Four different filter examples with quality factors of 200, 100, 50, and 28 in each resonator are depicted. For comparison, the responses of traditional design with the same quality factors on each resonator are also shown. The solid lines demonstrate $|S_{11}|$ and the dashed lines illustrate $|S_{21}|$ of each filter. (b): Theoretical noise figure responses of the proposed designs in (a). The figure shows the noise figures for an amplifier with different noise figure values. (c) and (d): Noise figure responses when the amplifier input and output coupling inverters are not properly tuned.
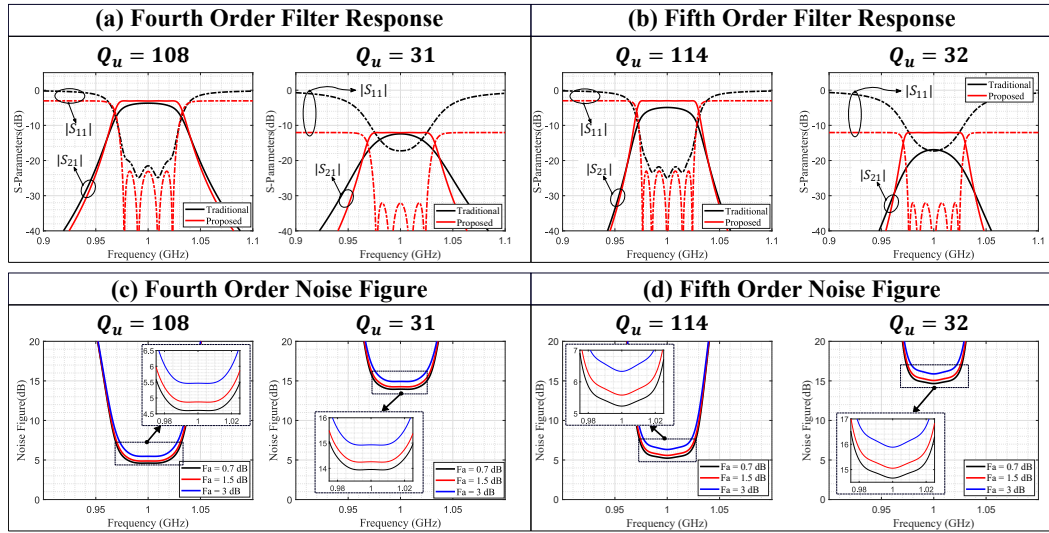
Figure B.6: Filter responses of the fourth- and fifth-order design examples are depicted in (a) and (b) whereas their noise figure responses are depicted in (c) and (d), respectively. As in Fig. B.6, the filter responses are compared with the corresponding design examples which have resonators of the same quality factors as in their lossy counterpart.

As observed in Fig. B.5 (a), the third-order filters designed with the proposed approach have the prescribed equiripple responses with the desired FBW and center frequencies. Not only can the proposed design reconstruct the response of the filter having a Q_u of 200 for each resonator, but it can also accomplish that for the severely perturbed transmission and reflection responses of the filter having a Q_u of 28 in each resonator. Further observing Fig. B.5 (a), it should also be noted that the shape recovery is achieved at the cost of additional IL for the third-order designs. This additional loss will be referred to as the accepted loss (AL) and is defined as the difference between the insertion loss of the traditional and the proposed designs. Comparing the responses in Fig. B.5 (a), it is observed that both the insertion loss and the accepted loss levels increase with the reduced resonator quality factors.

207

Table B.1: Parameters of the design examples of order three, four, and five. In the table, k denotes the attenuation factor, IL denotes the insertion loss, AL stands for the accepted loss, RcL is for recovered loss, and NF depicts the noise figure of the filters when amplifier external quality factors satisfy (9).

	Ord.	k	IL (dB)	Q_u	AL/RcL (dB)	NF (dB)
Ex.1	3	0.918	1.49	200	0.26 (A)	1.94
Ex.2 (FML)	3	0.841	3	100	0.57 (A)	3.75
Ex.3	3	0.701	6.17	50	1.33 (A)	7.16
Ex.4 (FHL)	3	0.500	12	28	3.63 (A)	12.94
Ex.5	4	0.841	3	108	0.38 (Rc)	4.60
Ex.6	4	0.5	12	31	0.26 (Rc)	13.95
Ex.7	5	0.841	3	114	1.93 (Rc)	5.23
Ex.8	5	0.5	12	32	4.92 (Rc)	14.66

The fourth- and fifth-order filter responses, which are designed to have insertion loss values of 3 dB and 12 dB, are shown in Fig. B.6 (a) and (b). As observed, these designs also have the prescribed filter responses. The shape perturbation in the conventional designs gets more severe as the filter order increases, which emphasizes the importance of the proposed method. While resonator quality factors at the order of 100 can produce acceptable filter responses using the traditional design of third-order, the same resonators yield significant filter shape degradation and additional insertion loss for the fourth- and fifth-order designs.

Unlike the third-order case, for the response of fourth- and fifth-order designs, the insertion loss of the proposed approach is *lower* than that of the conventional method. This is due to the fact that the number of loss-compensated resonators increases in the higher-order filters. In that case, the difference between the insertion loss of the traditional and the proposed approach is referred to as the *recovered loss* (RcL) in Table

1.

To examine the noise figure of the designs and the effect of the feedback amplifier noise figure on it, Fig. B.5 (b) depicts the simulated filter noise figures for three different amplifiers. These simulations are performed in AWR (Cadence Design Systems, San Jose, CA) design environment. The simulation models contain closed-form lumped and distributed elements. Furthermore, the compensation network uses the non-linear amplifier model with a flat gain of 15 dB within the frequency band of 0.5 GHz to 1.5 GHz. The input and output of the amplifier are matched to 50 Ω and the specified noise figure values in Fig. B.6 (b) are for a 50 Ω source.

For the amplifier noise figure values of 0.7 dB, 1.5 dB, and 3 dB, the simulated noise figures of the third-order designs are depicted in Fig 7 (b) when the external quality factors due to the amplifier (Q_1 and Q_2) satisfy the minimum noise condition in (9) and (10). As observed, an increase of 2.3 dB in the amplifier noise figure yields a filter noise figure increase of 0.54 dB and 0.46 dB when filter resonator quality factors are 28 and 100, respectively. Considering these results, it is seen that the increased amplifier noise figure has a minor impact on the overall noise figure of the third-order designs, as long as (9) is satisfied.

Another important point is that the external quality factors Q_1 and Q_2 greatly affect the overall filter noise figure. It was shown in [112–114] that slight external coupling variations that violate (9) yield significant filter noise figure degradations. To illustrate that, the third order designs with resonator Q_u values of 100 and 28 are simulated with detuned amplifier input and output coupling as given in Fig. B.5 (c) and (d). The corresponding S_{11} and S_{21} responses of the filters in Fig. B.5 (c) and (d) match the ones in Fig. B.5 (a) as Q_1 and Q_2 still satisfy the loss compensation condition given by (8). The effect of the increasing amplifier noise figure is exacerbated by the detuned coupling mechanisms. In particular, the 2.3 dB of amplifier noise figure increase yields

a noise figure increase of 0.79 dB when $Q_2/G_{amp}^2 Q_1 = 0.5$ and 1.9 dB when that ratio is 0.1 for the case of $Q_u = 100$. Therefore, this noise figure sensitivity should also be taken into account if the minimum noise figure is desired.

Finally, the noise figure responses of the fourth- and fifth-order designs are depicted in Fig. B.6 (c) and (d), respectively. It should be noted that the amplifiers at the active networks in each design are identical and have a gain of 15 dB as in the third-order case. The noise figures of the active filters increase further beyond their corresponding insertion losses, as the order of the filter increases. Furthermore, the sensitivity of the filter noise figure also increases when the noise figure of the amplifiers gets higher in the higher-order designs.

B.6   Methods of Implementation

Among the examples in the previous section, the third-order filters with resonator quality factors of 100 and 28 are implemented using microstrip technology. These prototypes are referred to as the filter with moderate loss (FML) and the filter with high loss (FHL), respectively. Their corresponding lossy-active coupling matrices are depicted in Fig. B.7. As observed, the lossy-active coupling matrices have negative imaginary entries at the diagonal elements, which represent the loss at each resonating and non-resonant node. Furthermore, each matrix also includes a diagonal entry with a positive imaginary term, representing the negative conductance at each active node. The magnitude of the normalized resistance at the second resonating node is equal to the magnitude of the active negative resistance, which corresponds to full loss compensation in the middle resonator of the lossy-active filter prototypes.

$$
M_{FML} = \begin{array}{cccccccc}
\text{S} & \text{NRN} & \text{1} & \text{2} & \text{NRN} & \text{3} & \text{NRN} & \text{L}
\end{array}
$$

	S	NRN	1	2	NRN	3	NRN	L	
	0	1	0	0	0	0	0	0	←S→
	1	$-0.171j$	1.067	0	0	0	0	0	←NRN→
	0	1.067	$-0.200j$	1.030	0	0	0	0	←1→
	0	0	1.030	$-0.200j$	0.200	1.030	0	0	←2→
	0	0	0	0.200	$0.200j$	0	0	0	←NRN→
	0	0	0	1.030	0	$-0.200j$	1.067	0	←3→
	0	0	0	0	0	1.067	$-0.171j$	1	←NRN→
	0	0	0	0	0	0	1	0	←L→

M_{FML}

	S	NRN	1	2	NRN	3	NRN	L
	0	1	0	0	0	0	0	0
	1	$-0.600j$	0.866	0	0	0	0	0
	0	0.866	$-0.703j$	1.030	0	0	0	0
	0	0	1.030	$-0.703j$	0.703	1.030	0	0
	0	0	0	0.703	$0.703j$	0	0	0
	0	0	0	1.030	0	$-0.703j$	0.866	0
	0	0	0	0	0	0.866	$-0.600j$	1
	0	0	0	0	0	0	1	0

M_{FHL}

Figure B.7: The lossy-active coupling matrices of the FML and the FHL. The matrices are denoted as M_{FML} and M_{FHL}, respectively. In the illustrations, the feedback amplifier network is considered as a negative resistance, as presented in Section II-C.

Using the lossy-active coupling matrices, the initial step in filter implementation is design of the lossy resonators, according to their lumped equivalents in Fig. B.3 (a). Considering that half-wave open-ended microstrip lines emulate parallel RLC resonators, the equivalent lumped impedance parameters are given as in the following [116]:

$$R_m = \frac{Z_0}{\alpha l}, \quad C_m = \frac{\pi}{2\omega_0 Z_0}, \quad L_m = \frac{1}{w_0^2 C}, \tag{B.13}$$

where $R_m, L_m,$ and C_m denote the equivalent resistance, inductance, and the capacitance of the microstrip resonator and α is the attenuation constant (Nepers/m). Using (B.13), the quality factor can be calculated as $Q_{u_m} = R_m/\omega_0 L_m$.

While the quality factor of 100 can be achieved with a microstrip resonator alone, the required Z_0 to get a Q_u of 28 is impractically high. Therefore, shunt resistors are used at both ends of the half-wave microstrip lines to reduce the Q_u of the resonators down to 28 for the FHL.

The inter-resonator coupling mechanisms are implemented using parallel edge-coupling and the desired coupling strength (M_{ij}) is achieved using:

$$M_{ij} = FBW \cdot m_{ij}, \tag{B.14}$$

where m_{ij} is the coupling coefficient between i^{th} and j^{th} resonator in the coupling matrix given by Fig. B.3 (b).

The input and output admittance inverters are realized using quarter-wave transformers in both designs. Their characteristic impedances are calculated by denormalizing the coupling matrix entries (m'_{S1}) and (m'_{3L}). The unit impedance inverters connected to the first and last resonators in the coupling matrix of Fig. B.3 (b) are scaled to have quarter-wave lines with realizable characteristic impedance values.
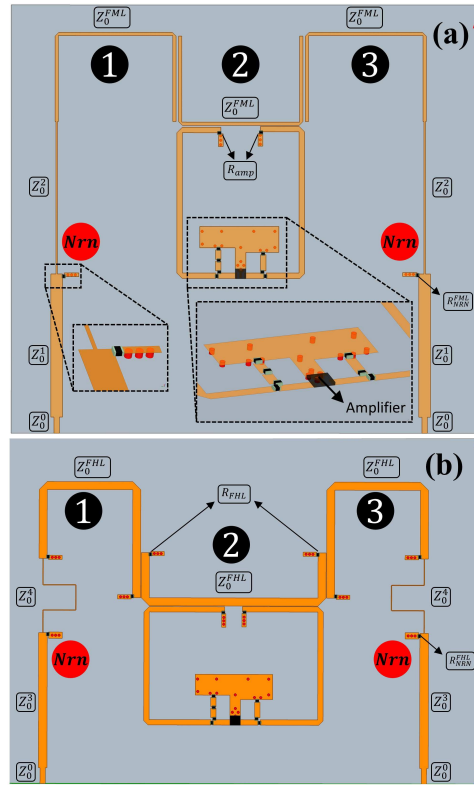
Figure B.8: The HFSS layouts of the filters. (a): Layout of the FML with magnified 3-D views at the non-resonant node and the amplifier network. (b): Layout of the FHL. The characteristic impedances, resonating and non-resonant nodes, and the resistors of both prototypes are marked and their values are shown in Table 2.

To implement the amplifier coupling at the middle resonator, edge coupling is used. The external quality factors Q_1 and Q_2 are calculated using (10). The amplifier for

Table B.2: The characteristic impedance and resistance values of the FML and FHL, as depicted in Fig. B.9.

Characteristic Impedances (Ω)						
Z_0^0	Z_0^1	Z_0^2	Z_0^3	Z_0^4	Z_0^{FML}	Z_0^{FHL}
50	29.9	98.6	36.8	125.4	67.6	38.4
Resistances (Ω)						
R_{amp}		R_{FHL}	R_{NRN}^{FML}		R_{NRN}^{FHL}	
50		1500	82		45	

achieving an infinite Q_u at the middle resonator is chosen to have a flat gain of 15 dB at the 0.8 to 1.2 GHz band.

The circuit-based simulations of the designs are carried out in AWR, whereas the electromagnetic (EM) simulations are done in HFSS Electromagnetic Suite (ANSYS, Cannonsburg, PA). The HFSS layouts of the prototypes are depicted in Fig. B.9. In that figure, transmission line impedances within the filter network are marked with the superscripts of Z_0. The characteristic impedances of the FML and FHL resonators are denoted as Z_0^{FML} and Z_0^{FHL}. Similarly, the termination resistors of the amplifier are denoted with R_{amp}, shunt resistors at non-resonating nodes of FML and FHL are shown as R_{NRN}^{FML} and R_{NRN}^{FHL}, and the shunt resistors to adjust the quality factors of FHL resonators are called as R_{FHL}, respectively. The values of these parameters after tuning are shown in Table 2.

The physical dimensions of the FML and FHL are given as (14.6 cm $\times$ 13.9 cm) and (14.6 cm $\times$ 11.3 cm), respectively. It should be noted that no attempts were made to miniaturize the prototypes as the goal of this study was to demonstrate the shape correction.

B.7 Fabrication and Measurements

To validate the proposed method, both prototypes were fabricated on a RO 4350B Lo-Pro (Rogers Corp., Chandler, AZ) 30-mil-thick substrate with a copper thickness of 17.5 μm. For precise board patterning, an LPKF ProtoLaser U4 (LPKF, Garbsen, Germany) was used. For the lumped capacitors at the amplifier network, multilayer ceramic capacitors from Murata Electronics (Kyoto, Japan) and for the RF-choke inductors, Murata spiral inductors were used. For the amplifiers of the loss compensation networks, PGA-103 low noise amplifier from Mini-Circuits (Brooklyn, NY) was used with its prescribed stabilization network [117].

The fabricated prototypes of the FML and the FHL are depicted in Fig. B.9 (a) and (b), respectively. To account for the discrepancies between simulated and actual resonator properties, a single resonator of each design was fabricated and measured. In order to measure the resonant frequencies and quality factors of the resonators, they are weakly coupled to the input and output ports using edge coupling, as depicted in Fig. B.9 (c) and (d). The measured quality factors of the single resonators at 1 GHz are 132.2 and 24.6 for the FML and FHL, respectively. After tuning for the slightly higher measured Q_u, it was observed in the simulations that the FML yields a response with approximately 4% of FBW at an insertion loss level of 3 dB. For the case of FHL, the measured quality factor was close enough to the simulated one, so it did not noticeably change the response.
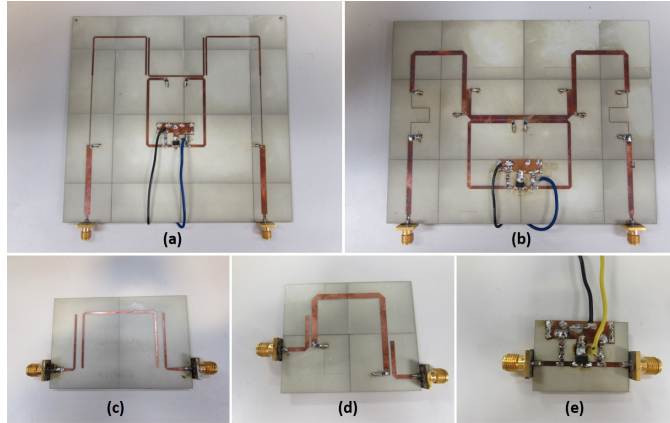
Figure B.9: The fabricated prototypes. (a): FML, (b): FHL, (c): A single resonator of FML, (d): A single resonator of FHL, and (e): The feedback amplifier in the loss compensation network.

To precisely determine the forward gain, phase contribution, noise figure, and the non-linearity of the amplifier, a single amplifier network is also fabricated and measured, as depicted in Fig. B.9 (e). The gain of the amplifier is measured to be approximately 15.6 dB and the noise figure is around 0.69 dB at a frequency of 1 GHz. To get accurate phase response measurements, the SMA connector lengths were de-embedded from the measured amplifier parameters in simulations. The 1-dB input and output compression points (IP1dB and OP1dB) of the amplifier are measured as 7.9 dBm and 22.5 dBm whereas the input and output third-order intercept points (IIP3 and OIP3) are measured as 26.5 dBm and 41.9 dBm. Furthermore, the DC power consumption of the prototypes are measured as 0.5 W. For an Nth order active filter using the proposed design technique, therefore, the power consumption is approximated as $(N - 2) \times P_{Amp}$, where P_{Amp} is the power consumption of the feedback amplifier within its linear operating region.

S_{11} and S_{21} measurements of the both prototypes are performed using an Agilent PNA N5225A (Keysight Technologies, Santa Rosa, CA) network analyzer. The noise figure measurements were taken with an Agilent PSA E4448A spectrum analyzer and

an Agilent 346B calibrated noise source. For the noise figure measurements, the Y-Factor method [118] was used with a measurement bandwidth of 1 MHz and 10 averages. Furthermore, an external LNA was cascaded to the network and the noise figure of a 15 dB attenuator is measured with the same setup to verify the accuracy of the measurements. IP1dB and OP1dB of the prototypes at 1 GHz are measured using an Agilent signal generator, the Agilent PSA E4448A spectrum analyzer, and a highly linear Mini-Circuits power amplifier (ZHL-10W-2G+) with 43.4 dB gain, 41.72 dBm OP1dB, and 53.5 dBm OIP3. The IIP3 and OIP3 levels of the prototypes are measured using the same signal source, power amplifier, and spectrum analyzer with 1 MHz tone spacing.

The theoretical and measured S-parameters for the FML and FHL are depicted in Figure 12. As observed, there is good agreement between the measured and theoretical responses for the FML. The measured insertion loss of FML is 2.92 dB at 1 GHz and its FBW is 4.2 %. The slightly narrower bandwidth is a result of re-tuning the design in order to account for the slightly higher measured quality factors than expected. For FHL, the measured and theoretical transmission responses are in good agreement with the fabricated prototype having an insertion loss of 11.82 dB. Considering the reflection response, the three pole locations are at the correct frequencies, however, the slightly detuned input and output coupling inverters cause a slight mismatch between the measured and theoretical responses. Overall, both prototypes have the desired filter response and selectivity.
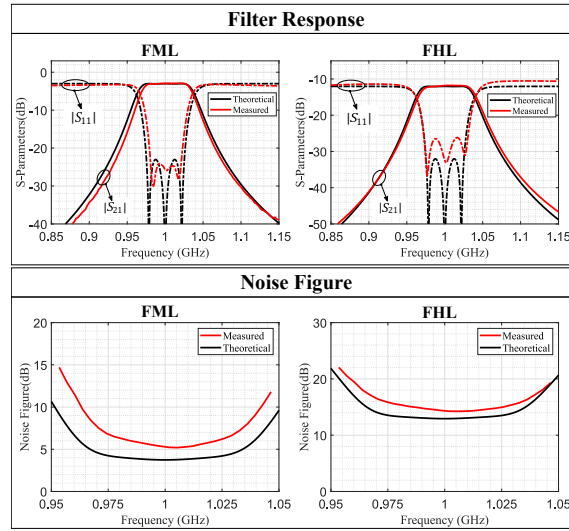
216

Figure B.10: Comparison of the theoretical and measured responses. The first row depicts the filter responses of FML and FHL whereas the second row demonstrates the noise figure responses. For the filter responses, the solid lines depict the $|S_{11}|$ and the dashed lines illustrate the $|S_{21}|$ of each filter.

Ref	Resonator Type	Techniques	Order	f_0 (GHz)/ FBW	Q_u	IL/IG (dB)	TZ	NF (dB)	IP1dB (dBm)	OP1dB (dBm)	IIP3 (dBm)	OIP3 (dBm)
[21]	Microstrip	Lossy, Non-Unif. Q	6	0.96/6.2%	250-80	7.2	Yes	*	**	**	**	**
[30]	Microstrip	Lossy, Equalized Q	4	1,11.5/%	200	3	Yes	*	**	**	**	**
[28]	Microstrip	Lossy, Non-Unif. Q	6	3.8/21%	95-57-35	2.5	Yes	*	**	**	**	**
[29]	double-layered coupled resn.	Lossy, Equalized Q	6	0.97/25.7%	120	3.4	Yes	*	**	**	**	**
[32]	Microstrip	Lossy, Equalized Q	4	0.925/9.2%	N/A	≈8.5	No	*	**	**	**	**
[26]	Combline Cavity	Lossy, Equalized Q	4	11.18/1%	1300	≈2.9	No	*	**	**	**	**
[4]	MMIC, λ/4 line	HEMT-Negative Resistance	2	60	***	2.8	Yes (I/O Cross-Coupl.)	10.5	8.8	5	***	***
[17]	MMIC, Lumped	Resonator Link with FET	3	1.9	***	12 (IG)	No	6.2	***	***	***	***
[14]	PCB Lumped Active Inductor	Class-AB BJT Active Inductor	2	0.7/5% (3-dB FBW)	***	7.2	No	10	***	12	***	***
[8]	Microstrip	Parametric Active	3	2.03/8%	***	0.22	No	3.7	***	17	***	26.5
[34]	SIW	Filtering Amplifier	2	10/5%	***	9 (IG)	No	≈ 3	≈ −5.5	≈ 5.5	***	***
FML	Microstrip	Hybrid	3	1/5%	131.2	2.89	No	5.19	38	34	46.94	44.05
FHL	Microstrip	Hybrid	3	1/5%	24.6	11.9	No	14.2	27	14	46	34.1

* Noise figure of passive filters will be equivalent to the reciprocal of their available power gain, or to their attenuation if perfectly matched at input and output.
** Passive filters are assumed to be linear and the information of P1dB and IP3 are not reported.
*** The data is not explicitly reported in the corresponding study.
IG: Insertion gain, TZ: Transmission zero.

Lossy Microwave Filters
Active Filters
Proposed Hybrid Lossy-Active Technique

Figure B.11: Table of comparison with other relevant studies in literature.

The theoretical and measured noise figures of the FML and the FHL are also depicted in Fig. B.10. The measured noise figure values of the designs are 5.19 dB for FML and 14.2 dB for FHL at 1 GHz, whereas the theoretical values are 3.76 dB and 12.97 dB, respectively. It should be noted that the theoretical noise figure results come

from the AWR simulations with closed-form lumped elements and do not take into account the losses due to the microstrip line inverters. The reason for including those simulation results was to demonstrate the theoretically achievable noise figure for both prototypes. Another reason for the discrepancies between the simulated and measured noise figures is the re-tuned input and output coupling inverters of the amplifier to achieve the best shape correction.

Finally, the non-linearity performances of the prototypes are depicted in the table of Fig. B.11. As both prototypes attenuate the input signal, the input-related non-linearity metrics (IP1dB and IIP3) and the output-related measurements (OP1dB and OIP3) are considered separately. As observed, the input compression point of FML is much higher than that of the FHL for a simple reason that the insertion loss difference between the amplifier ON and OFF states is much higher in FHL. In other words, a higher percentage of the energy is passing through the amplifier in FHL to compensate for the lower quality factor. An important point to be observed is that the input compression point and the third intercept of both prototypes are better than that of the amplifier that is used within the design of the prototypes. This is a result of the input power to the filter being shared within the resonators and the active network. This way, the amplifier is exposed to less power than the incoming input power to the active filter.

The table in Fig. 13 provides a comparison of several performance metrics of the related studies in the literature. The compared studies include the applications of active filters and lossy filters separately. To that end, the proposed method in this study is a hybrid implementation of lossy filters and active filters. Results of the two example prototypes show that the proposed design approach is realizable and the shape correction can be achieved using resonators with arbitrary quality factors. It should be noted that the shape correction is achieved at the cost of increased noise figure and non-linearity when the resonator quality factors are very low. Therefore, the initial

218

consideration with this design approach is to use resonators with the highest achievable quality factors within the design limits. Depending on the design, a pre-amplifier stage might be required to compensate for both the noise figure and the insertion loss if the available resonators have very low quality factors. This results in the prescribed filter selectivity with no insertion loss and reduced noise figure, which cannot be achieved by amplifying a perturbed filter response.

B.8   Conclusion and Discussion

Using the coupling matrix theory for highly lossy applications has always been a challenge for filter designers due to severe response shape degradations. In this study, a new method of synthesizing lossy filters with the use of an active quality factor enhancement method is presented. Unlike most active filter approaches, in which the active quality factor enhancement is used in every resonator, this study aims to minimize the number of active elements within the design.

For the design stage, a new concept of *lossy-active coupling matrix* is introduced. With that approach, this study represents an initial transfer of the lossy filter design theory to the highly lossy applications such as PCB-based or MMIC filters. Using the lossy-active coupling matrix and possible matrix rotations, higher-order filters can be designed using resonators with arbitrary quality factors. This will require future solutions including active inter-resonator coupling mechanisms. Therefore, the design theory in this study provides a new step towards implementing high selectivity filters with prescribed responses using resonators with limited quality factors. This proposed method facilitates the future integration of analog filters with improved performance into receiver front ends in system-on-a-chip applications.